

# **Cell Adhesion: Stochastic Receptor-Ligand Binding Under Force**

Ovidiu Bagdasar

Thesis submitted to the University of Nottingham  
for the degree of Doctor of Philosophy

May 2011

## Abstract

The adhesive interactions between cells and surfaces play a key role in many vital physiological processes, such as innate immune response, tissue formation, or wound healing, but also in targeted drug delivery and active control on the adhesion of viruses.

Adhesion is often mediated by specific intermolecular bonds, which generally function under considerable mechanical load. Bond properties can be explored by dynamic force spectroscopy, which measures the force required to separate two surfaces connected by small numbers of molecular bonds. Motivated by such experiments, the aim of this thesis is to investigate the adhesive effects of discrete, stochastic binding of clusters of intermolecular bonds, supported by a rigid or flexible substrate.

The stochastic adhesion of a cluster of bonds connecting a rigid disk and a flat surface is investigated within the framework of piecewise deterministic Markov processes. The model accounts for the rupture and rebinding of discrete bonds, depending on the disk's motion under applied force. Hydrodynamic forces in the thin layer of viscous fluid between the two surfaces are described using lubrication theory. Bonds are modeled as identical, parallel springs, and equally share the load. Monte Carlo simulations, capturing the stochastic evolution of clusters with few bonds, are complemented by various deterministic approximations, valid in the limit of a large number of bonds. Distinct regions in the parameter space spanned by force and drag are identified, where cluster's evolution is largely dictated by either bond kinetics, or enslaved to the disk's motion. The stability of the cluster is discussed for non-zero rebinding, while dynamic force spectroscopy experiments are mimicked under linearly ramped force.

The stochastic evolution of a bond population connecting a flexible membrane to a rigid wall within a fluid, is also formulated as a Markov process, and spatial effects are considered by allowing the vertical elastic bonds to differentially share the load, depending on their extension. The deterministic motion of the membrane, interrupted by stochastic binding and unbinding of bonds, is formulated as a partial differential equation, derived using lubrication theory. As shown by stochastic simulations and deterministic approximations, the volume and distribution of the liquid beneath the membrane, play a key role in the cluster's dynamics. The model provides preliminary evidence of the nature of peeling stochastic processes. Subsequently, the model predicts that the membrane and the bond population in clusters with sufficiently many bonds under rebinding, fluctuate near equilibria predicted by the deterministic approximation. The average population and extension of bonds are shown to be largely inversely correlated, using a wavelet-based semblance method.

# Acknowledgements

## A DREAM WITHIN A DREAM

Should you ask me how do I feel at the very moment I am writing this section I would answer: “Like an astronaut!!!”; although I have an oxygen mask on my face and intravenous serum in my two arms (just a serious metaphor, of course). So, allow me please to first thank God, for I seem to have pleased Him somehow, and so He granted me the power to eventually finish this PhD! Glory to Thee, my God, glory to Thee!

I warmly thank the European Commission for having funded my project as part of the MMBNOTT Early Training Research Programme in Mathematical Medicine and Biology, kindly hosted by the prestigious University of Nottingham. It’s been a great honor for me to be part of the staff of this University for three years.

THANK YOU PROFESSOR OLIVER JENSEN! Never had I hoped to get to live near a man like you. You are the first person ever to bring light into the mathematical chaos in my mind. Yet, our relationship was mutually beneficial, as I also managed to take Professor Jensen on higher peaks of patience with my ever postponed deadlines. You’ll always be a great example for me; I sincerely thank you for being not just an extraordinary teacher but also a friend in need!

Later on, my thanks go to Professor Frank G. Ball and Professor Phil M. Williams, my other two supervisors who’ve helped me at every step of this project.

I am most grateful to Archbishop John, my spiritual father and confessor, to whom the completion of the present work has special debts. I also thank Fr. Andreas Michailidis and Fr. Dan Ghindea for their persistence in interceding before Christ for me.

Ciprian Ionuț Duduială is the one who first told me of this project; he welcomed me when I arrived here and helped me with everything I needed. Ana Maria Gheorghe helped with the proofreading. Călin Miron showed me how to anchor my mathematical steps into the physical world. Igor Chernyavsky kindly explained many mathematical tips to me, and made my heart rejoice in the nights he was playing the guitar and we were singing. THANK YOU, GUYS!

---

Least but not last, I would like to thank my family: my mother and father, my super grandmother Ana, my grandfather, my parents-in-law, my brother and his family, my wife (Ioana Porodica) and especially my 6-months-old daughter Stefania (Fifi la Fourmi). They all spent the last year bossing me around in order to finish this project!

If I were to mention all those who prayed for me during my staying here, I would need to double the number of pages of this work, so it's better that I stopped here by saying a big THANK YOU to everyone!

# Contents

<b>List of Symbols</b>	<b>vii</b>
<b>1 Introduction</b>	<b>1</b>
1.1 Motivation . . . . .	2
1.2 Biological background . . . . .	4
1.2.1 Adhesion molecules and clusters . . . . .	4
1.2.2 Processes regulating the adhesive properties of clusters . . . . .	6
1.2.3 Experimental techniques . . . . .	7
1.3 Modeling cell adhesion . . . . .	12
1.3.1 Individual bonds: model and rupture . . . . .	12
1.3.2 Clusters . . . . .	15
1.3.3 Mechanical details of the models . . . . .	17
1.3.4 Deterministic models for the dynamics of bonds in a cluster . . . . .	18
1.4 Stochastic models for adhesion clusters . . . . .	21
1.5 Overview and structure of thesis . . . . .	24
<b>2 Adhesive molecular bond clusters between a disk and a surface</b>	<b>27</b>
2.1 A stochastic model for a cluster of elastic bonds . . . . .	28
2.1.1 Deterministic motion of the disk . . . . .	28
2.1.2 Dissociation and association rates . . . . .	30
2.1.3 Non-dimensional model . . . . .	31
2.1.4 Brownian and inertial effects in the disk's dynamics . . . . .	32
2.2 Methods . . . . .	34

2.2.1	Exact stochastic simulations . . . . .	34
2.2.2	Dynamics of the disk-bond system . . . . .	37
2.2.3	A deterministic approach . . . . .	41
2.3	Summary . . . . .	42
2.A	Thin film adhesion . . . . .	43
2.A.1	Lubrication equations . . . . .	43
2.A.2	Applications - adhesion near a flat rigid wall . . . . .	46
2.B	Stochastic hybrid systems: deterministic limits . . . . .	50
<b>3</b>	<b>Limiting drag approximations</b> . . . . .	<b>52</b>
3.1	Disk motion in the limiting drag cases . . . . .	53
3.2	Methods . . . . .	54
3.2.1	Master equation . . . . .	54
3.2.2	Deterministic approximation . . . . .	56
3.2.3	Gillespie Algorithm . . . . .	58
3.2.4	Fokker-Planck Equation (FPE) . . . . .	58
3.3	Results for constant force . . . . .	63
3.3.1	Vanishing rebinding . . . . .	63
3.3.2	Vanishing force: role of rebinding . . . . .	72
3.3.3	Finite force, finite rebinding . . . . .	75
3.4	Results for ramped force . . . . .	80
3.4.1	Loading regimes . . . . .	80
3.4.2	Mimicking DFS experiments . . . . .	83
3.5	Summary . . . . .	84
3.A	Normally distributed initial condition . . . . .	86
3.A.1	The zero-drag limit . . . . .	86
3.A.2	The infinite-drag limit . . . . .	87
3.B	Deterministic and stochastic approximations of cluster lifetime . . . . .	90
3.C	Validity domain of the FPE for zero force . . . . .	92

<b>4</b>	<b>Cluster dynamics under finite drag</b>	<b>95</b>
4.1	Constant force . . . . .	96
4.1.1	Preliminaries: local and global motion of the disk . . . . .	97
4.1.2	Testing stochastic simulations against other methods . . . . .	102
4.1.3	Non-zero rebinding: Critical force and equilibrium configurations	107
4.2	Cluster dynamics under ramped force . . . . .	113
4.2.1	Preliminaries . . . . .	113
4.2.2	Mimicking DFS experiments . . . . .	118
4.3	A possible PDE formulation of cluster dynamics . . . . .	120
4.3.1	The dCKE . . . . .	120
4.3.2	Solution along characteristics . . . . .	121
4.3.3	Validation of the solution against stochastic simulations . . . . .	123
4.3.4	Bivariate stochastic processes . . . . .	126
4.4	Summary . . . . .	128
4.A	Exact analytical solutions for $P_k(t; 0, h_0)$ . . . . .	130
4.B	The differential Chapman-Kolmogorov Equation (dCKE) . . . . .	134
4.B.1	The dCKE for the disk-bonds model . . . . .	134
4.B.2	Initial conditions . . . . .	139
4.B.3	Solution of the dCKE using the method of characteristics . . . . .	140
4.B.4	Qualitative behaviour of the dCKE solution: infinite-time limit . . . . .	142
4.B.5	Force and drag regimes . . . . .	146
<b>5</b>	<b>Adhesive molecular bond clusters between a membrane and a surface</b>	<b>148</b>
5.1	A stochastic model for clusters between a surface and a membrane . . . . .	149
5.1.1	The dimensional model . . . . .	149
5.1.2	Dimensionless model . . . . .	153
5.1.3	Membrane motion under vertical force at boundaries . . . . .	157
5.2	Solution of the model . . . . .	157
5.2.1	Numerical scheme for the deterministic motion of the membrane . . . . .	157
5.2.2	Exact stochastic simulation of the next rupture or rebinding . . . . .	158

5.2.3	A deterministic approach . . . . .	160
5.2.4	Time series comparison using wavelet-based semblance analysis . . . . .	161
5.3	Results: Membrane spreading . . . . .	162
5.3.1	Code validation using equilibria . . . . .	163
5.3.2	Membrane detachment in the absence of rebinding . . . . .	165
5.3.3	Membrane dynamics under rupture and rebinding of bonds . . . . .	170
5.3.4	Membrane vs. disk model dynamics under rebinding . . . . .	174
5.4	Results: Membrane dynamics under vertical force . . . . .	174
5.4.1	Code validation using equilibria . . . . .	175
5.4.2	Vanishing rebinding . . . . .	179
5.4.3	System dynamics under rupture and rebinding . . . . .	180
5.5	Analysis of single trajectories and peeling patterns . . . . .	183
5.5.1	Membrane fluctuations near the equilibrium . . . . .	183
5.5.2	Peeling patterns . . . . .	188
5.6	Summary . . . . .	192
5.A	Numerical solution of the membrane's steady states . . . . .	194
5.A.1	Steady states of the membrane: free fluid spreading . . . . .	194
5.A.2	Steady states of the membrane: vertically forced boundaries . . . . .	197
5.B	Membrane model accounting for lateral motion . . . . .	198
<b>6</b>	<b>Conclusions</b>	<b>202</b>
	<b>References</b>	<b>207</b>

# List of Symbols

$\alpha$	bond rupture rate scale in units of thermal energy / typical distance, page 30
$\beta$	bond rupture rate scale in units of thermal energy / typical distance, page 31
$\gamma$	dimensionless single-bond on-rate, page 30
$\Gamma$	Euler's constant, $\Gamma = 0.5772$ , page 90
$\delta(x)$	Dirac delta function, page 33
$\delta_{kn}$	Kronecker's symbol, page 22
$\kappa^*$	elastic modulus of bonds (assumed to behave as springs under force), page 15
$\lambda_{k \rightarrow k+1}(t)$	time dependent on-rate, page 34
$\lambda_{k \rightarrow k-1}(t)$	time dependent off-rate, page 34
$\mu$	dimensionless loading rate, page 31
$\mu^*$	liquid viscosity, page 28
$\mu_{H_D}$	mean displacement of a cluster at dissociation time, page 40
$\mu_{T_D}$	mean lifetime of a cluster, mean first passage time, page 40
$\mu_N(t)$	mean number of closed bonds, page 39
$\nu_D^*$	attempt frequency for barrier crossing in Kramers' theory, page 14
$\rho^*$	liquid density, page 28
$\sigma_{H_D}^2$	variance of the dissociation height, page 41
$\sigma_{T_D}^2$	variance of the cluster dissociation rate, page 40
$\sigma_N^2(t)$	variance of the number of closed bonds, page 39
$\phi(t)$	macroscopic evolution of the deterministic number of closed bonds, page 61
<b>A</b>	master equation ODE matrix, page 55
$A_{FPE}(x, t)$	drift term in the Fokker-Planck equation, page 59
<b>B</b>	dimensionless Brownian energy scale, page 33
$B(n, q)$	binomial random variable with parameters (n,q), page 73
$B_{FPE}(x, t)$	diffusion term in the Fokker-Planck equation, page 59
$c$	dimensionless drag coefficient, page 31
$D^*$	dimensional diffusion coefficient, page 33
$e^{\mathbf{A}}$	matrix exponential, page 56

$Ei(z)$	exponential integral, page 90
$\mathbb{E}$	step operator, page 55
$E_B^*$	height of the transition state barrier, page 13
$f$	dimensionless dissociating force per cluster, page 31
$\hat{f}$	scaled initial force per bond, page 58
$f_b$	dimensionless dissociating force per single bond, page 53
$f_c$	critical force for adhesion cluster stability, page 76
$f_X(t)$	density of the stochastic variable $X(t)$ , page 40
$F_k(t, h)$	state occupancy distribution for state with $k$ bonds at time $t$ , below height $h$ , page 39
$F^*$	dimensional force applied on the cluster, page 28
$F_0^*$	dimensional force scale, page 28
$F_b^*$	dimensional force per bond, page 30
$F_d^*$	dimensional drag force on the moving disk, page 29
$F_{el}^*$	dimensional elastic force, page 29
$F_{inertia}^*$	dimensional inertia force, page 28
$F_B^*$	dimensional Brownian force on the disk, page 32
$g(k)$	functional form of the forward (rebinding) rate (zero drag problem), page 56
$g_k(h)$	height dependent forward (rebinding) rate for the adhesion cluster, page 31
$g_d(N_d, H_d)$	deterministic on-rate, page 41
$G(x)$	scaled cluster on-rate in the Fokker-Planck equation, page 60
$h$	dimensionless displacement of the disk, page 31
$h_0$	dimensionless initial displacement of the disk, page 31
$h_{eq, k}$	equilibrium displacement of the disk with $k$ bonds attached, page 97
$h^*(t^*)$	dimensional time-dependent displacement of the disk, page 28
$H(t)$	dimensionless stochastic displacement of the disk at time $t$ , page 31
$H_k(t)$	dimensionless disk displacement with $k$ bonds attached at time $t$ , page 31
$H_d(t)$	deterministic mean displacement of the disk, page 41
$H_D(h)$	dissociation height, final bond extension (random variable) , page 40
$k$	number of closed bonds in the adhesion cluster, page 28
$k_B$	Boltzmann's constant, page 30
$k_0^*$	Kramer's off-rate, page 28
$k_{off}^*$	force-dependent single-bond off-rate, page 28
$k_{on}^*$	displacement dependent single-bond on-rate, page 30
$L^*$	biological bonds' rest length , page 28
$M_{disk}^*$	dimensional disk mass, page 32
$n$	cluster size, page 28
$N(t)$	number of closed bonds at time $t$ , page 31

$\widehat{N}(t)$	scaled mean number of closed bonds $\mu_N/n$ , page 58
$N_c$	number of closed bonds in the stationary state at critical force, page 76
$N_d(t)$	deterministic mean number of closed bonds, page 41
$N_{eq}$	number of bonds at equilibrium, page 75
$N_i(t)$	number of closed bonds in cluster $i$ at time $t$ , page 149
$N_s$	number of simulated stochastic trajectories, page 37
$\text{pln}(x)$	product logarithm, page 76
$p_k(t, h)$	state occupancy distribution for state with $k$ bonds at time $t$ and height $h$ , page 39
$P_k(t)$	state occupancy probability for state with $k$ closed bonds at time $t$ , page 22
$P_k^H(h)$	state occupancy probability for state with $k$ closed bonds at height $h$ , page 38
$P(x, t)$	solution of the Fokker-Planck equation, page 58
$\mathbf{P}(t)$	solution of the ME, page 55
$r(k)$	functional form of the backward (rupture) rate (zero drag problem), page 56
$r_k(h)$	height dependent backward (rupture) rate for the adhesion cluster, page 31
$r_d(N_d, H_d)$	deterministic off-rate, page 41
$R(x)$	scaled cluster off-rate in the Fokker-Planck equation, page 60
$Re$	Reynolds number, page 28
$R^*$	disk radius, page 28
$S$	sojourn time in a state with a fixed bond population, page 35
$S_{w_1, w_2}$	semblance of datasets $w_1$ and $w_2$ , page 162
$t$	dimensionless time, page 31
$t^*$	dimensional time, page 28
$T_d$	deterministic cluster lifetime, page 41
$T_D(t)$	cluster lifetime (random variable), page 40
$T_0^*$	physiological temperature, page 30
$T^*$	temperature, page 14
$U(a, b)$	uniform distribution of parameters $a, b$ , page 35
$U^*(x^*)$	energy landscape for Kramers' theory, page 13
$V^*$	dimensional disk velocity scale, page 33
$x_{BIF}$	bifurcation coordinate, page 109
$x^*$	reaction coordinate, position of the Brownian particle in Kramers' theory, page 13
$x_0^*$	typical displacement along the rupture coordinate, page 30
$x_B^*$	position of the transition state barrier in $U^*(x^*)$ , page 13
$x_C^*$	position of the bound state in $U^*(x^*)$ , page 13

## List of Abbreviations

AFM	atomic force microscope, page 8
BFP	biomembrane force probe, page 8
CAMs	cell adhesion molecules, page 1
CWT	continuous wavelet transform, page 161
dCKE	differential Chapman-Kolmogorov equation, page 134
DFS	dynamic force spectroscopy, page 7
DNA	deoxyribonucleic acid, page 11
FPE	Fokker-Planck Equation, page 58
ICAMs	intercellular adhesion molecules, page 4
IFM	intermolecular force microscopy, page 11
LOT	laser optical tweezers, page 11
ME	Master Equation, page 22
ODE	ordinary differential equation, page 33
PDE	partial differential equation, page 25
SDE	stochastic differential equation, page 33
VCAMs	vascular adhesion molecules, page 4

## List of Definitions

cluster of bonds	collection of identical receptor-ligand bonds, page 1
dissociation of bonds	rupture/breakage of receptor-ligand bonds, page 1
association of bonds	formation/(re)binding of receptor-ligand bonds, page 1
cluster lifetime	time when the last remaining bond in a cluster dissociates, page 40
cluster dissociation height	last remaining bond's extension at dissociation, page 40

# Introduction

THE LIFE of our bodies is a symphony of as many as  $10^{13}$  individual cells, grouped into around 200 different cells types with distinct, specific functions, of which nearly half are involved in adhesive interactions [4]. These can influence the shape, adhesion and migration of cells, which in turn are essential elements for many important physiological processes such as morphogenic movements, metastasis, tissue formation and maintenance [77], inflammation [2], or wound healing [51].

*Cellular adhesion* consists of the specific binding of a cell to a surface, the extracellular matrix or another cell using surface ligands called *cell adhesion molecules* (CAMs). These molecules recognize each other and bind specifically on a key-lock principle, the two binding sides being called *receptors* and *ligands* [4]. CAMs are of vital importance for biological life and they appear in most organisms, from bacteria and viruses to human beings. Plant cells also associate with their neighbours not only through interactions between their cell walls, but also through specialized junctions between their plasma membranes [4, 9, 24].

Adhesion of cells occurs at specialized sites spread over the plasma membrane, where *clusters* of specific ligands physically link the extracellular transmembrane adhesion receptors to intracellular structural and signaling proteins. The clusters exhibit a great diversity of structures and functions. They generally have to function under considerable mechanical force which can be exerted from outside or from within the cell and is known to influence the *stochastic* formation and rupture of bonds [10].

This thesis concerns the mathematical modelling of the stochastic adhesion of biological clusters under force. The applications motivating this work are presented in §1.1. The biological background is reviewed in §1.2. In §1.3 we overview existing modelling approaches for cell adhesion. In §1.4 we discuss some mechanical details of modelling the cell membrane. The organization of the thesis chapters is detailed in §1.5.

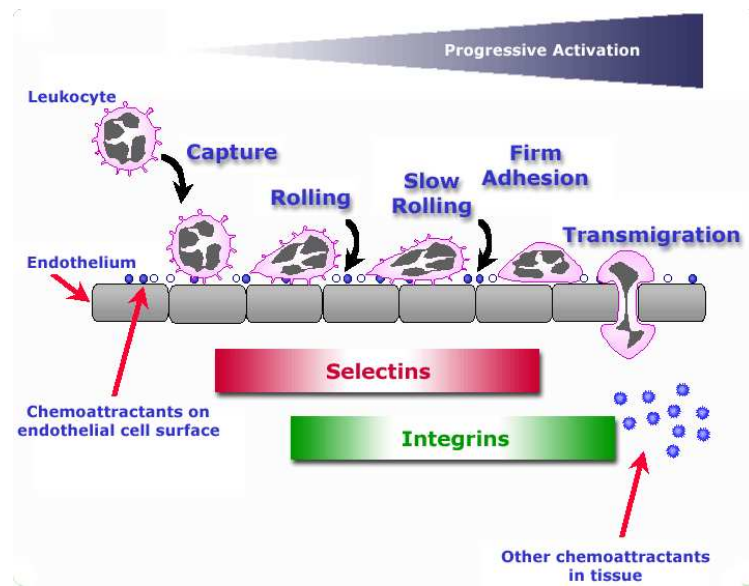


Figure 1.1: Leukocyte adhesion cascade: <http://bme.virginia.edu/ley/>.

## 1.1 Motivation

### Innate immune response and the leukocyte adhesion cascade

Adhesion plays a key role in the leukocyte adhesion cascade, which is a crucial step in the innate immune response of our body to an infection. When a tissue is invaded by infectious micro-organisms, it generates specific signals attracting leukocytes (which usually patrol throughout our organism in order to eliminate potentially harmful agents or dead cells) to escape from the blood vessel towards the site of infection. The process occurs mainly in the post-capillary venules, where haemodynamic shear forces are minimal due to small radius (usually  $8 - 100 \mu\text{m}$ ), and can be understood in several steps including *chemoattraction*, *rolling adhesion*, *tight adhesion* and (*endothelial*) *transmigration*, as presented in Fig. 1.1.

During the “chemoattraction” step, upon recognition of and activation by pathogens, resident macrophages in the affected tissue release cytokines such as interleukins (IL-1), tumor necrosis factors (TNF- $\alpha$ ) and chemokines. IL-1 and TNF- $\alpha$  cause the endothelial cells of blood vessels near the site of infection to express cellular adhesion molecules, including selectins. Circulating leukocytes are localized towards the site of injury or infection due to the presence of chemokines.

In the “rolling adhesion” phase, carbohydrate ligands on the circulating leukocytes bind to selectin molecules on the inner wall of the vessel with marginal affinity. The white cells present in the blood flow, having a typical velocity of several hundreds of

$\mu\text{m/s}$ , are then tethered through selectin ligands borne by their membranes and they begin rolling with 50 to 100-fold decreased velocity due to the rapid formation and dissociation of selectin-ligand bonds [4, 15].

A “firm adhesion” phase follows, that results in the complete cell arrest due to an interaction between integrin receptors (on white cells) and ligands such as ICAM-1 on endothelial cells. The chemokines released by macrophages activate the rolling leukocytes and cause surface integrin molecules to switch from the default low-affinity state to a high-affinity state. The activated integrins bind tightly to the complementary receptors expressed on endothelial cells, with high affinity, causing the immobilization of the leukocytes, despite the shear forces of the ongoing blood flow [24].

The last step in this succession is the “transmigration”. The cytoskeletons of the leukocytes are reorganized in such a way that the leukocytes are spread out over the endothelial cells. In this form, leukocytes extend pseudopodia and pass through the gaps between endothelial cells. The leukocytes secrete proteases that degrade the basement membrane, allowing them to escape the blood vessel in a process known as *diapedesis*. Once in the interstitial fluid, leukocytes migrate along a chemotactic gradient towards the site of injury or infection [24].

Recent papers have also identified additional steps in the adhesion cascade such as slow rolling, adhesion strengthening, intraluminal crawling, paracellular and transcellular migration [88].

### **Pathologies**

Adhesion molecules contribute to normal biological processes and disease states such as *cancer* (invasion and metastasis), *inflammatory disorders* (rheumatoid arthritis and autoimmune diabetes) and *cardiovascular diseases* (heart attack and stroke) [93]. Palacios *et al.* have proven that *breast cancer* could be identified by relations between the expression of the P- and E-cadherins [107], while tumor cell progression and metastasis were found to be dependent on the ability of a tumor cell to adhere to the proteins of the extracellular matrix and survive at the distant location [29]. Recent studies have shown that understanding the ability of the integrins in fibroblasts to interact with the extracellular matrix, apply force and remodel the matrix, may provide better insight into the pathology of diseases such as *fibrosis and cancer* that are commonly associated with *aberrant integrin signaling* and matrix formation [60].

## Drug development

Adhesion has also found applications in *drug design*, where it is manipulated to produce agents with *strong recognition and affinity to specific markers on cancer cell surfaces*, as suggested by Kortt *et al.* [81]. In chronic inflammatory diseases, the CAMs include E-selectin, intercellular adhesion molecule-1 (ICAM-1) and vascular adhesion molecule-1 (VCAM-1); they serve to slow and ultimately arrest leukocytes and may overreact to such a degree that their activity itself becomes harmful. Pharmaceutical agents reducing the induced expression of one or more of the cell adhesion molecules are expected to attenuate the inflammatory process [58, 86]. The adhesion cascade is halted whenever any of the mentioned steps is suppressed [4, 15], generating severe infections. Active control of the adhesion of viruses to host cells to reduce viral replication rate, using specifically engineered drugs, was achieved by English & Hammer [63].

## 1.2 Biological background

---

### 1.2.1 Adhesion molecules and clusters

#### First steps in cell adhesion

Moscona's experiments from the early 50's, where disrupted chick embryos regained their initial shape, brought to light the existence of cell adhesion molecules [100]. Using the single molecule experiments available since the mid-80's, it was found that CAMs bear highly diversified molecular, structural and topological properties. Even at present we can notice new molecules, mechanisms and functions that are continuously emerging, and there are novel technologies that allow a more detailed study of all these.

#### Main classes of adhesion molecules

The CAMs can be divided into four major groups: *selectins*, *integrins*, *immunoglobulins (Ig)* and *cadherins*, sketched in Fig. 1.2. They are embedded in the membrane that surrounds the cell, and most have sections that are extracellular, transmembraneous, and intracellular. The length of the extracellular domain of the molecule is typically 2 – 50 nm, the transmembrane domain is typically 6 – 8 nm in length, roughly the thickness of the membrane [66].

The *selectins* represent a class of cell-surface CAMs that mediate the adhesion between leukocytes, platelets and endothelial cells under blood flow in the vascular system. The selectin family is made up of three members: L-selectin (expressed on leukocytes), E -

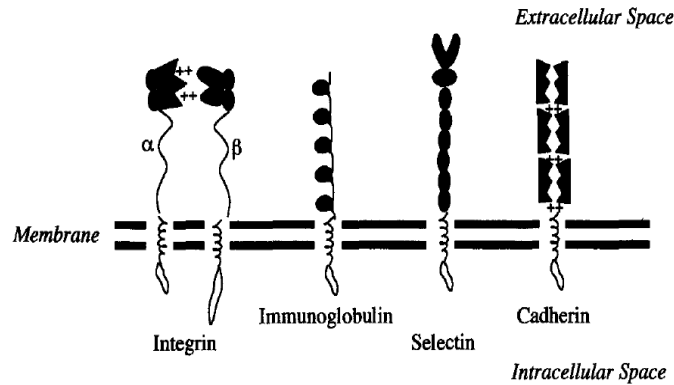


Figure 1.2: Sketch of classical CAMs, as depicted in [66].

selectin (expressed on endothelial cells) and P-selectin (expressed on platelets) [9, 24].

The *integrins* are a large family of CAMs, able to bind to a large variety of ligands and being key mediators for the cell-matrix adhesions. An example is the formation of the stable adhesions in leukocyte arrest, in which integrins on the surface of leukocytes bind to intercellular adhesion molecules (ICAMs), which are members of the Ig superfamily, expressed on the surface of endothelial cells [9, 24, 71, 72].

The *immunoglobulin superfamily* (IgCAMs), consists of glycoproteins mediating either cell-cell or cell-matrix adhesions during early development and in the adult period. Members of the Ig superfamily can mediate both *heterophilic* (e.g. with integrins) and *homophilic* interactions - in which an adhesion molecule on the surface of one cell binds to the same molecule on the surface of another cell. For example, the homophilic binding between N-CAMs (Ig molecules expressed on nerve cells) contributes to the formation of selective associations between nerve cells during their development. There are more than 100 members of the Ig superfamily, which mediate a wide variety of cell-cell interactions [9, 24].

The *cadherins* can be classified into four main subfamilies: classical cadherins, desmosomal cadherins, protocadherins and cadherin-like proteins. There are about twenty types of classical cadherins, such as N-cadherin (neural cadherin), R-cadherin (retinal), VE-cadherin (vascular endothelial) and P-cadherin (placental cadherin) that mediate selective adhesion of other cell types [79]. Cadherins are also the main responsible for the formation of stable junctions between cells in tissues and they play a fundamental role in cell-fate regulation and development. For example, homophilic interactions between E-cadherins lead to the selective adhesion of epithelial cells to one another. In addition, the protocadherins are expressed in the central nervous system where they seem to play a role in neuronal synapses adhesion [4, 9, 24].

There are also new types of surface protein increasingly involved in cell adhesion and whose functions are still far from being understood. This is the case for the heparan sulfate proteoglycans (HSPGs), which mediate a variety of cell-cell, cell-matrix and cell-microorganism adhesions, and the metalloprotease-disintegrins (ADAMs) involved in processes as myogenesis, neurogenesis and sperm-egg adhesion and fusion [9].

### **Collective behaviour of adhesion molecules**

Cell-cell interactions in which the cytoskeletons of adjacent cells are not linked to one another are called *transient*. Important examples of transient interactions can be found between the cells of the immune system, in the leukocyte adhesion cascade, and they are generally mediated by selectins, integrins, and members of the Ig superfamily [24].

When adhesive interactions also involve cytoskeletons of cells they are called *stable junctions*, and they are divided in four groups. The first two are the *adherens junctions* and *desmosomes*, where cadherins or related proteins (desmogleins and desmocollins) are linked to actin bundles and respectively intermediate filaments [4, 9, 24]. The specific adhesive properties of desmosomes led to the introduction of the term *hyper-adhesion* [51].

Initially wrongly described as apparent fusion between the outer leaflets of plasma membranes, *tight junctions* are the closest known contacts between adjacent cells and form seals that prevent the free passage of molecules (including ions) between the cells of epithelial sheets. *Gap junctions* serve as direct connections between the cytoplasm of adjacent cells. They provide open channels through the plasma membrane, which allow ions and small molecules (less than approximately a thousand daltons  $\simeq 1.66 \times 10^{-24}$  kg) to freely diffuse between neighboring cells, but prevent the passage of proteins and nucleic acids. Most cells in animal tissues - including epithelial cells, endothelial cells, and the cells of cardiac and smooth muscle - communicate by gap junctions. In electrically excitable cells, such as heart muscle cells, the direct passage of ions through gap junctions couples and synchronizes the contractions of neighboring cells [24].

### **1.2.2 Processes regulating the adhesive properties of clusters**

The adhesion of cells in a fluid environment is complicated by the multitude of biological structures, chemical reactions or physical mechanisms, all of which can regulate, inhibit or facilitate the stochastic formation and rupture of bonds.

### Cell motion

The specific motion of cells can significantly influence the pattern of the adhesion between cells and a substrate. In the rolling stage of the leukocyte adhesion cascade, the formation and breaking of molecular bonds happens at the front and at the back of the contact region between the leukocytes and the endothelium [15, 115], enabling the cells to resist the haemodynamic forces and to roll on the vessel wall. As mentioned earlier, this step is mediated by CAMs from the selectin family.

### Cell membrane deformations

Deformation of cells affects the area of contact between the cell and the substrate, the number of bonds that can form, hence the adhesive forces. An example in this sense is the transition from the rolling to the arrest of the leukocytes in the leukocyte adhesion cascade [4]. As suggested by Fig. 1.1, cell's arrest may be caused not only by the stronger integrin bonds, but also by the leukocyte's deformation which allows an increase in the number of adhesive bonds. Other receptors able to exert forces onto the cell's structure are the desmosomes, which help cells resist shearing forces [51].

### 1.2.3 Experimental techniques

CAMs are tiny and delicate objects, subject to pN forces and nm displacements [15], so accurate measurement of the physical properties of individual bonds had to wait for the discovery of appropriate instruments. Current single-molecule manipulation capacity spans six orders of magnitude in length ( $10^{-10}$  –  $10^{-4}$  m) and force ( $10^{-14}$  –  $10^{-8}$  N) and gives new insight into previously ignored features such as rupture force, or force spectra, providing a measure of bond energies, lifetimes, and more recently, entire energy landscapes [15, 16]. Viscoelastic properties can also be measured on short length scales and in small volumes, such as within cells [103].

Adhesion bonds in cells usually have to operate under force. To understand the behaviour of adhesion clusters it is thus vital to investigate bond failure under an applied force, this being the main idea of the *dynamic force spectroscopy* (DFS) [41, 103]. This technique has been used in the study of many important biological bonds including biotin-avidin, integrin [89], cadherin [8, 109] and selectins [40, 42, 48]. Typically, one end of the molecule under study is attached to a surface, while the free end is attached to a device through which force is applied. This setup inspired many models analyzing the stochastic detachment of surfaces connected by clusters of bonds.

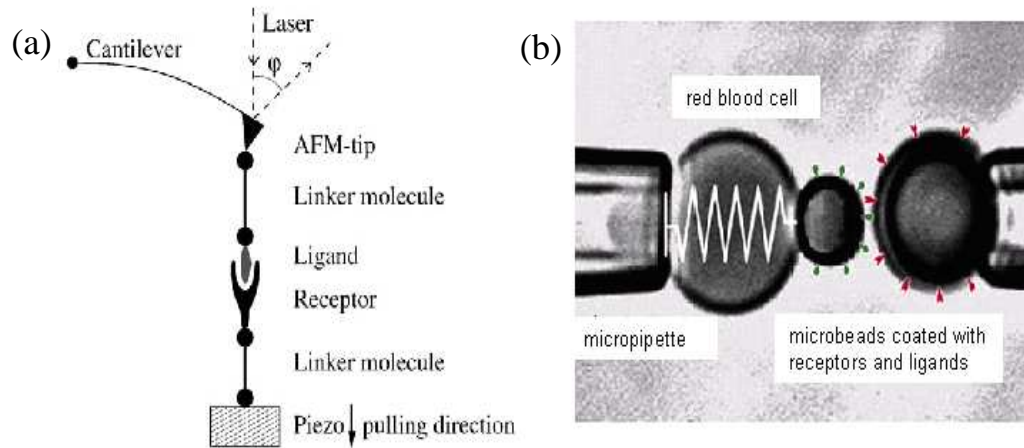


**Figure 1.3:** (a) Scheme of an AFM experiment of the forced unbinding of receptor-ligand bonds. (b) Sketch of a biomembrane force probe (BFP) experiment [42]. The biotinylated red blood cell is an elastic element which carries a microbead to which the ligands are attached. The bead on the right is held by a second pipette and is functionalised with the receptors.

### Single bond experiments

Ideally, the bonds at the surface and at the probe should specifically bind the ends of the molecule, support infinite loads and not affect the mechanical or biological properties of the attached molecule [103]. However no such thing happens in the complex biological situation, and it is generally difficult to interpret the data from applied force experiments. The elastic structure of the cell cytoskeleton yields a non-trivial stress-strain relation [12], which makes it difficult to exert force on adhesion sites in a controlled way. Also, cells react to external stresses and adhesion clusters change their structure under the influence of applied force, as has been proved by Riveline [120]. The solution is then to examine mechanical properties in *single molecule experiments*.

The *atomic force microscopy* (AFM) experiments on biotin-avidin bonds by Gaub and coworkers [101], enabled the investigation of forced unbinding of single molecules. Avidin can bind four biotin molecules with an unusually high binding energy of around  $20 k_B T$ . After the biotin-coated tip of an AFM-cantilever is stuck to the biotinylated agarose bead surface and the ligand-receptor pair is bound, the soft, elastic cantilever tip is retracted at a constant speed with piezo elements leading to a linear increase of force on the bond with separation, as illustrated in Fig. 1.3 (a).

The *biomembrane force probe* (BFP) is a popular technique developed by Evans *et al.* in 1991 [37], and has the possibility to measure bond-forces of only 5 pN with loading-rates from 0.05 – 60 nN/s (in contrast to the AFM measurements, where the measured bond-forces were around 100 – 300 pN). In the BFP, the CAMs are carried by a mi-

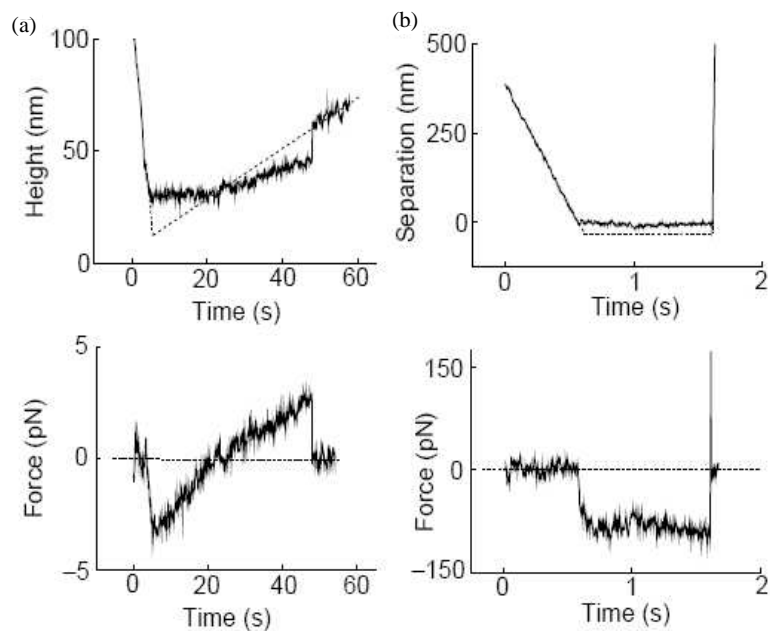


**Figure 1.4:** BFP tip-substrate distance and force versus time for cycles of approach-touch-separation with formation and rupture of a bond. (a) Loaded at extremely slow rate, a bond held the tip to the surface for 24 s and broke at  $\sim 3$  pN as the piezo retracted the transducer (dashed trajectory). The fluctuations in tip position (solid curve) were due to thermal excitations of the BFP. Stretch of the PEG polymers that linked the bond to the glass surfaces is shown by the slight upward movement ( $\sim 15$  nm) under force before detachment. (b) Loaded at extremely fast rate, a bond held the tip to the surface for  $\sim 0.003$  s (spike in force) and broke at  $\sim 170$  pN as the piezo retracted the test surface (dashed trajectory). The force fluctuations were due to position uncertainties and BFP stiffness (see Merkel *et al.* [95]).

crobead and then attached to a lipid vesicle or a red blood cell as sketched in Fig. 1.3 (b). The vesicle is aspirated in a micropipette at large aspiration pressure. The ligands are carried on a second bead which is directly held by a pipette. Single molecule binding is achieved by using a very small concentration of receptors. The sketched spring indicates that the red blood cell behaves to a very good approximation as an elastic spring. The force constant is determined by the tension of the vesicle which is directly determined by the aspiration pressure in the pipette [96]. The separation of the vesicles is analyzed under a microscope, and video is recorded to calculate the rupture force. In addition, receptor and ligands may be attached to their substrate through elastic tethers, usually polymeric linker molecules. It was shown that generally, a linear relation between displacement and force on the bond results. The most common loading protocol is the linear ramp of force in which the transducer is retracted at constant speed and force increases linearly in time with a constant loading rate [38].

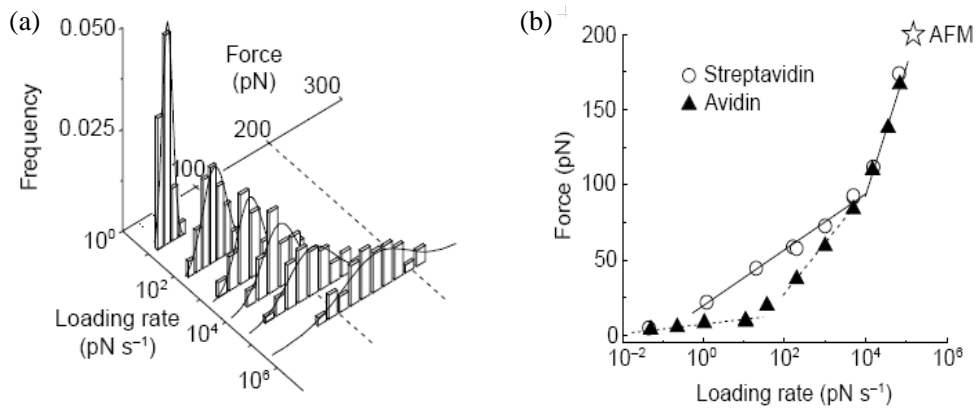


**Figure 1.5:** Biotin-streptavidin bond strengths. (a) Force histograms from tests of single biotin-streptavidin bonds demonstrate shift in peak location and increase in width with increase in loading rate. Gaussian fits used to determine the most frequent rupture force or bond strength are shown. As  $\sigma_f$  increased from  $\pm 1$  pN at the slowest rate to  $\pm 60$  pN at the fastest rate, the standard error in mean force (the statistical measure for error in strength) ranged from  $\pm 0.3$  pN to  $\pm 5$  pN. (b) Dynamic strength spectra for biotin-streptavidin (circles) and biotin-avidin (triangles) bonds. Consistent with the high-strength regime is the biotin-streptavidin strength (☆ AFM) measured recently by atomic-force microscopy (AFM) (see Merkel *et al.* [95]).

Fig. 1.4 shows results of BFP experiments on biotin-avidin bonds from the paper of Merkel [95], in which the loading rate  $k_f v_t$  was changed over several orders of magnitude by setting the BFP force constant  $k_f$  in the range  $0.1 - 3$  pN nm<sup>-1</sup>, and piezo retraction speed  $v_t$  in the range  $1 - 20000$  nm s<sup>-1</sup>. The time dependence of the piezo displacement and force in a typical experiment, is obtained for small (Fig. 1.4 (a)) and large (Fig. 1.4 (b)) loading rates. The experiment consists of three steps. Initially the binding sites are pressed together to facilitate binding. Then the pipette carrying the microbead with the ligands is retracted and the force increases linearly until it vanishes as the bond breaks. The elasticity of the transducer and the linker molecules holding the adhesion bonds has an important influence on the interpretation of the results, because it determines the actual loading rate on the bond [39].

The time-scale for bond rupture decreases with the increasing loading rate while the rupture force increases Fig. 1.5 (a). Also, the histograms show a sharp peak at small forces for slow loading and a broad distribution with a maximum at large forces for fast loading. The dynamic force spectrum depicted in Fig. 1.5 (b), plots bond strength as function of the logarithm of loading rate and shows a sequence of linear regimes with increasing slopes for biotin-avidin and biotin-streptavidin, respectively. This points to the presence of three and two energy barriers along the unbinding pathway, respectively [95].

In the same general DFS framework, along with the AFM and the BFP, other techniques have been applied to exert forces on single molecules and investigate bond strengths, e.g. *laser optical tweezers* (LOT) [76], *magnetic tweezers* [130], and more recently *intermolecular force microscopy* (IFM) [136]. In LOT experiments the molecules are tethered to a dielectric bead which is trapped in the force field of the focus of a single laser beam. Force is exerted on the adhesion bond by moving the bead with the laser beam. This technique was applied to measure force-extension curves of the muscle protein titin [76]. Magnetic tweezers use paramagnetic beads instead of dielectric ones which are held in a magnetic force field and used in the same way as optical tweezers. They have been applied, e.g. to investigate DNA elasticity [130]. The IFM was reported to give signal-to-noise ratios 30-fold higher than the AFM, with force resolution to the sub-picoNewton level and response time of sub-millisecond level by using a flexible glass microneedle. This was used to analyze the different bound states of paired nectin and cadherin molecules, where each bound state was found to have a unique lifetime and bond length [136].

### **Experiments on adhesive clusters**

The use of DFS in the analysis of biological clusters was attempted in a study related to the binding of T-lymphocytes and human umbilical vein endothelial cells (HUVECs), which is mediated by several types of adhesion molecules such as E- and P-selectins, intercellular adhesion molecule-1 (ICAM-1), and vascular adhesion molecule-1 (VCAM-1) [145]. An analytical treatment of the behaviour of multiple bonds in DFS experiments was recently proposed by Williams [144], where zipper and parallel loading scenarios are considered and analyzed with the aid of Poisson statistics. However, the collective behaviour of clusters of biological bonds is still far from being understood and serious effort is currently made in this direction.

The binding properties of molecular bonds can also be investigated with *flow chambers*, where a receptor-bearing cell or particle is driven along a ligand-coated surface in a laminar shear flow. Using a very dilute concentration of ligands on the wall allows one to observe transient adhesion events which are mediated by single adhesion bonds. Such attempts led to the first known experimental single bond rupture, performed by Harry Goldsmith in 1986 [135], and then used by Alon *et al.* for the study for leukocyte rolling [5]. Changing the flow velocity, or the viscosity of the fluid, allows the control of the force acting on these bonds. The advantages and limitations of this method have been exposed in the recent review of Bongrand [16].

### Recent experimental advances

In a different approach, multi-wavelength *X-ray diffraction* methods were used to obtain the specific structure of ligand-receptor pairs with ångström precision [54].

However, despite of the accuracy of the measurements, recent research emphasized that a proper calibration of the instruments requires a deeper theoretical understanding of the experimental setup, as suggested by Nassoy [102]. Such detailed theoretical analyzes have been recently done by Heinrich for BFP experiments [68], and by Clarke *et al.* for AFM experiments [20].

## 1.3 Modeling cell adhesion

---

Knowledge about single bond behaviour under force has to be integrated into an appropriate description of adhesion clusters of multiple bonds under force, where the particular details of the situation (rebinding of ruptured bonds, number of bonds involved, loading scenarios, hydrodynamic effects, membrane mechanics and cell dynamics) become important for the formulation of an appropriate model, ideally encompassing both deterministic and stochastic effects.

### 1.3.1 Individual bonds: model and rupture

As found by the BFP experiments of Evans & Ritchie [38], the maximum force that a single bond can withstand not only depends on the physical properties of the bonds, but also on the loading rate by which the bond is probed.

#### Bond models

The cornerstone in modelling cell adhesion is the appropriate description of single bonds. Inspired from the properties of generic polymers and confirmed in various experiments involving a number of adhesion molecules, the *elastic spring* model gives a good approximation for the complex behavior of the adhesion proteins, and also captures the effects of force and displacement in the dynamics of the cluster [87]. Refined versions of the linear spring behaviour of clusters, including a *multiple-spring* model for the receptor-ligand interaction have also been considered by Schwarz *et al.* [126].

Anticipated in 1988 by Dembo [28], *catch-bonds* exhibit an increase in lifetime under applied force. The existence of the first catch-bond was revealed 15 years later, by the experiments on selectin-mediated bonds under low force performed by Marshall *et al.* [94], while in 2008, a group lead by Sokurenko proved that catch-bond properties

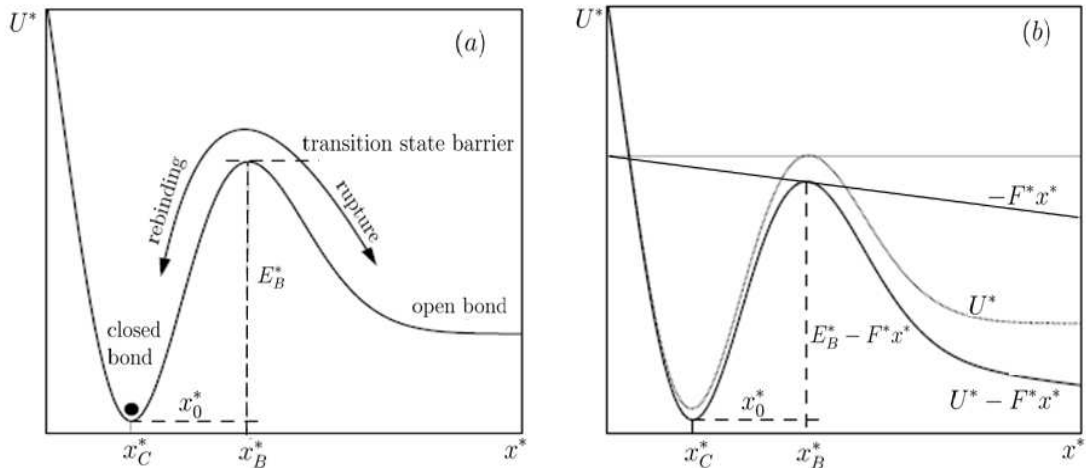


**Figure 1.6:** (a) Energy landscape  $U^*(x)$  along the 1D reaction coordinate  $x^*$ . Rupture and re-binding of molecular bonds correspond to transitions of the Brownian particle (black dot) over the transition state barrier. The bound state (“closed bond”) at  $x_C^*$  is separated by the transition state barrier at  $x_0^*$  from the unbound state “open bond”). (b) Original potential  $U^*(x)$  tilts under force with the addition of a new potential  $-F^*x^*$ .

are likely widespread [132]. It was suggested to call *slip bonds* the molecular bonds which (as expected) display a shorter lifetime under disruptive forces. Studies by the teams of Evans and Hammer [40, 42, 65] suggested that the catch behaviour could also be induced by the way force is applied, since the same molecules can exhibit both catch and slip behaviour for different force (or shear) regimes [7]. Other models for the behavior of CAMs, such as worm-like chains [35], or non-Hookean elastic springs (FENE) models used in the study of polymers [47], have been proposed.

### Stochastic rupture of single bonds under force

The stochastic dissociation of single bonds under force is a key issue in cell adhesion. Most commonly used models for bond adhesion assume that receptors and ligands are elastic springs which interact via a reversible chemical process



to form bond complexes, themselves having spring-like properties, where  $k_{on}^*$  and  $k_{off}^*$  are the forward and reverse reaction rates. Using a thermodynamic approach, Bell [10] and Dembo *et al.* [28] proposed two such models based on the interaction energies between free, bound and transition states.

A breakthrough was made by Bell in the late 70’s [10]. He estimated that the force required to separate two cells is much greater than the expected electrical forces between

cells, and the reaction rates for membrane-bound reactants would increase exponentially when force is applied, as in

$$k_{off}^*(F^*) = k_0^* \exp(F^*/F_0^*), \quad (1.3.2)$$

where  $k_0^*$  is the individual bond off-rate in the absence of force,  $F^*$  the applied force and  $F_0^* = k_B T^*/x_0^*$  a force scale for bond strength ( $k_B$  the Boltzmann constant and  $T^*$  the absolute temperature), where  $x_0^*$  represents a unit displacement along the rupture coordinate (a typical scale in (1.3.2) being  $F_0^* \simeq 4$  pN, for  $x_0^* \simeq 1$  nm).

The above rate was obtained by describing the rupture of bonds in the framework of Kramers' theory [67, 82, 138], as a thermally activated escape from a potential well. The main idea behind this approach is to replace the various states of a molecule (in adhesion closed and open bonds) with a "reaction coordinate"  $x^*$ , representing the distance between both fragments. Assuming the bond molecule undergoes Brownian motion in the  $x^*$ -direction, the rupture of biological bonds can be modelled as the escape of the particle sketched in Fig. 1.6 (a), from the potential well of coordinate  $x_C^*$ .

An imposed dissociating force  $F^*$  modifies the initial energy landscape to  $U^*(x^*) - F^*x^*$ . If the barrier is very sharp, its height  $E_B^*$  reduces in proportion to the product of  $F^*$  and the "reactive compliance"  $x_0^* = x_C^* - x_B^*$ , where  $x_C^*$  and  $x_B^*$  are the coordinates of the bottom of the well and the barrier. For sharp transition barriers, Kramers' theory applies and the particle has to jump over a barrier of height  $E_B^* - F^*x_B^*$ , as sketched in Fig. 1.6 (b). In the notation of [38], the rupture rate under force is

$$k_{off}^* = \nu_D^* e^{-(E_B^* - F^*x_B^*)/k_B T^*} = \nu_D^* e^{-E_B^*/k_B T^*} e^{F^*x_B^*/k_B T^*} = k_0^* e^{F^*/F_0^*},$$

so formula (1.3.2) is obtained, where  $\nu_D^*$  has the dimension of an inverse time and is determined by the shape of the potential.

The one-step model for single bond rupture under force was generalized and put in a firm theoretical basis by Evans and Ritchie [38] for barriers of finite width, where the shape and the position of bound state and barrier changes with force. This leads to an algebraic force dependence of  $\nu_D^*$  and to corrections in the dependence of the barrier height on  $F^*$ . Despite its simplicity and the flaws generated by its use in inappropriate situations [125], Bell's model is still widely used with good results. At present, intensive effort is made to establish a theoretical base for the rupture of single bonds, accounting for different bounding states and protein unfolding.

Dembo *et al.* [28] refined the model proposed by Bell [10], for the transition rate of Hookean springs under force, and obtained the formula

$$k_{off}^*(F^*) = k_0^* \exp \left\{ \left[ \frac{\kappa_{TS}^*}{\kappa^*} (L_{TS}^* - L^*) F^* + \frac{\kappa^* - \kappa_{TS}^*}{2(\kappa^*)^2} (F^*)^2 \right] / k_B T^* \right\}, \quad (1.3.3)$$

where  $L^*$  is the unstressed bond length and  $\kappa^*$  its stiffness, and the subscript TS denotes “transition state”. The association rate is derived through an affinity coefficient  $k_a^* \equiv k_{on}^*/k_{off}^*$ , which represents the relative chance of a bond forming or breaking and is assumed to form the Boltzmann distribution. Dembo’s model for the transition rate of Hookean springs under force predicts a rate

$$k_a^*(F^*) = k_a^*(0) \exp\left(-\frac{(F^*)^2}{2\kappa^*k_B T^*}\right), \quad (1.3.4)$$

where  $k_a^*(0)$  is the binding affinity in the absence of force. In particular, for  $\kappa_{TS}^* = \kappa^*$ , from (1.3.4) one recovers Bell’s formula (1.3.2) for an elastic spring

$$k_{off}^*(F^*) = k_0^* \exp\{[(L_{TS}^* - L^*) F^*]/k_B T^*\}. \quad (1.3.5)$$

Writing the force exerted on the bond as  $F^* = \kappa^*(h^* - L^*)$ , and substituting  $L_{TS}^* = L^*$  in (1.3.4), one obtains the most common version of Dembo’s rate

$$k_{off}^*(h^*) = k_0^* \exp\left(\frac{\kappa_{TS}^* - \kappa^*}{2k_B T^*} (h^* - L^*)^2\right). \quad (1.3.6)$$

More models used in bond kinetics are reviewed in [146].

### 1.3.2 Clusters

Most dynamic interactions between cells and substrates involve clusters of 2-100 adhesion molecules [15], which collectively share the mechanical load.

#### Bond population structure and position

A first problem in the study of clusters is to select the types of bonds involved. Most models consider homogeneous populations bond populations, and depending on the simulated experiment, bonds can be parallel to the direction of the force [31, 35, 49] (as for the DSF experiments), or they can be tilted to an angle [115] (as in the case of flow chambers). If two different species of adhesion bonds are present in the membrane, e.g. with different length, the membrane has to bend between two unlike adhesion bonds. This additional energy for bending can induce different dynamic regimes with clearly distinct patterns of stickers and repellers at intermediate times separation between the different species of molecules, as suggested by theoretical analysis from [143].

#### Mechanical loading scenarios

Of the same importance is the distribution of force between the bonds of the cluster. Experiments performed on heterogeneous clusters suggested that the pulling force may not be distributed evenly among the bonds [145], and this may be the reason why

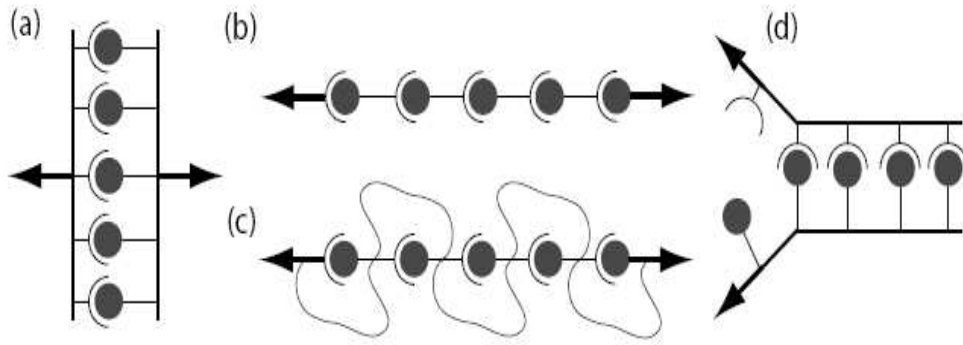


**Figure 1.7:** Loading scenarios for adhesion clusters. The direction of the force is indicated by arrows. (a) parallel bonds, (b) serial bonds (c) unfolding bonds and (d) zipper-like arrangement with sequentially loaded bonds [36].

most models involve homogeneous clusters. Multiple bonds can act as cooperative (simultaneous breakage) bonds in cadherin or as uncooperative bonds (bonds rupture sequentially) in nectin [136]. Another difference of clusters compared to single bonds is that the bonds can be *loaded* to different extents (sometimes even a fraction loaded while the rest unloaded) and that *rebinding* of broken bonds becomes important, being facilitated by the remaining intact bonds which keep the binding sites in close vicinity.

In regard to the distribution of force between the bonds and the behaviour upon bond breakage, different loading scenarios can be distinguished for multiple bonds as shown in Fig. 1.7. In the case of parallel bonds depicted in Fig. 1.7 (a), the force is redistributed among the intact bonds but the cluster as a whole remains intact until the last bond breaks. This scenario can be applied for diverse cellular adhesion clusters and for many DFS experiments on multiple bonds. Serial bonds sketched in Fig. 1.7 (b), individually feel the force applied to the whole chain and the breakage of the first bond disrupts the whole cluster as in the case of protein filaments such as actin. In the case of unfolding presented in Fig. 1.7 (c), bond breakage only extends the chain and the loading process starts anew, as in the case of proteins like the muscle protein titin in which several folded protein domains unfold and extend upon loading. In the zipper-like arrangement shown in Fig. 1.7 (d), the first bond of the chains is subject to the whole force and as soon as it breaks, the next bond is loaded. This model can be used as a model for RNA or DNA unzipping [90], or to examine the peeling of a cell off a surface [70]. In general (and for more dimensions), combined scenarios are conceivable.

### Association and dissociation of bonds in a cluster

Dissociation and association dynamics of parallel adhesion clusters was first discussed by Bell [10]. Although it is clear that force leads to accelerated cluster dissociation, it is usually not known how it is distributed over the different closed bonds in different situations of interest. In many cases, most prominently in rolling adhesion, only a few of the different bonds are loaded to an appreciable degree, thus dissociation occurs in a peeling fashion [28, 62]. However, due to geometrical reasons, even in this case there will be a subset of bonds which are loaded to a similar extent.

Factors as the initial number of closed bonds, the physical properties of the bonds (rest length, elastic constant, affinity, extensibility), the local geometry (flat or curved surface), the membrane properties (rigid or elastic) and the binding range (constant or variable) have a significant influence on the association rates for clusters, which in turn have a deep impact on cluster's lifetime and stability [10, 31, 35, 38].

### 1.3.3 Mechanical details of the models

#### Hydrodynamics

Because of the scales involved in cell adhesion, we generally deal with *low Reynolds number* flows, so there is negligible inertia [114]. The first to introduce hydrodynamics to the problem of cell adhesion were Hammer & Laffenburger [61], who exploited classical solutions (Goldman, Cox & Brenner [55, 56]) for the force and torque on a smooth rigid sphere rolling in a shear flow over a flat plane at zero Reynolds number. They balanced hydrodynamic forces on the cell with adhesive forces arising from distributed bonds in a small region at the base of the cell, close to the plane, employing Bell's (1978) kinetic model, to determine the number and strength of receptors required for adhesion. The membrane-fluid-surface interaction is usually addressed using thin film theory, and non-linear drag forces arise [70]. A *non-zero slip* boundary condition for the fluid-substrate interaction could eventually be considered [142], since the widely used no-slip boundary condition is not very suitable for modelling submicron and especially nanoscale flows, while surface roughness is another issue one should account for [139], when modelling cell adhesion.

#### Membrane mechanics

The adhesive behaviour of cells or capsules in a liquid environment is complicated by their mechanical properties like bending stiffness or shear elasticity, as highlighted by e. g. Pozrikidis [112, 113], Hodges & Jensen [70], or Reboux *et al.* [116]. As a result,

the members of the biotechnology community are now examining the mechanics of thin elastic shells under contact forces (a well known topic in civil and mechanical engineering), and recently, many man-made micro- or nano-capsules have found a wide range of industrial applications [116].

In BFP experiments, the lipid vesicles are typically under strong tension and often, the vesicles are only used as elastic force transducers while the bonds are attached to rigid microbeads. At the same time, adhesion receptors in clusters are densely packed (relative distances are in the range of nm) and are attached firmly to the cytoskeleton of the cell. Therefore, effects of membrane fluctuations are small and can be neglected in the context of tight adhesion clusters (cadherin-mediated, for example). However the situation changes in the case of transient bonds and different models analyzing the *peeling* [28, 70] (where bending and stiffness of the membrane are key parameters) or *rolling* of leukocytes [70, 115] have been proposed.

The most commonly used models for membranes with negligible bending stiffness are discussed by e.g. Risso & Carin [119] or Wan *et al.* [140], but experimental validation proved a very difficult task as shown by Smith *et al.* [131]. A more in-depth review of cell mechanics is presented in [116].

### 1.3.4 Deterministic models for the dynamics of bonds in a cluster

In addition to the rupture rate (1.3.2), Bell also proposed a deterministic model for the non-equilibrium dissociation of adhesion clusters under force [10]. He emphasized that “a little patience will suffice” for individual biological bonds to rupture even in the absence of force, but the situation changes dramatically if the bonds are linked together in a cluster, because the probability for all the receptors to be simultaneously unbound is very small. The equilibrium properties of adhesion clusters under rebinding were also discussed in [10].

#### Thermodynamic models

Soon after, a series of *thermodynamic models* for describing adhesion between two cells or between a cell and a surface was developed by Bell *et al.* [11], integrating details about the complementary receptors on the two surfaces (e.g. lateral mobility, heterogeneity, total number per cell), the cell-cell bridges that mediate adhesion (e.g. spring constant, length, binding constant), the repulsive forces between cells (e.g. compressibility of the glycocalyx, thickness of the glycocalyx, lateral mobility of the glycocalyx), and notions about the purely geometrical parameters of adhesion (e.g. maximum contact area, total surface areas of the two cells, heterogeneity vs. uniformity of contact distance). A

strong limitation of thermodynamic models is that they say nothing about the kinetic process involved in reaching equilibrium. The deterministic Bell-model has also been extended by Seifert [127, 128] to treat the linear loading of a cluster of adhesion bonds, which usually is applied in DFS experiments.

### **Point attachment model**

The framework proposed by Bell was used to analyze *leukocyte rolling in shear flow* by Hammer *et al.* in 1987 [61], in a model referred to as the “point attachment model” because it considers the contact area between the cell and the surface to be a small, homogeneous region that mediates the initial attachment of the cell to the surface. The cell is modelled as a rigid sphere and the receptors at the surface of the cell are assumed to convect and to diffuse into the contact area. The main finding is that the adhesion parameters, such as the bond formation rate, the receptor-ligand affinity, the fluid mechanical force, the receptor mobility, the number of receptors and the contact area may significantly enhance the peeling of the cell from the substrate. A key result is that there are two regimes in which different chemical and physical forces dominate: increasing bond formation rate means fewer receptors are required for adhesion at a fixed dimensionless dissociation constant, and an increasing dissociation constant means more receptors are required for adhesion at a fixed bond formation rate.

### **Membrane peeling**

A famous model for the behaviour of bonds under force was proposed by Dembo *et al.* [28], who found different expressions for the binding rates, assuming that the differences between the transition state and the bonded state illustrated in Fig. 1.6, can be described by a change in the spring constant only, as seen in (1.3.3). He also used the transition state theory but in the specific context of Hookean potentials. In his model, a piece of a thin, inextensible membrane is attached to a fixed wall and a pulling force is exerted on one end, while the other end is held fixed, in the so called “peel test”. The attachment and detachment under force is analyzed by coupling the equations for deformation of the membrane with equations for the chemical kinetics of the CAMs. Dembo also related bond stress to bond strain and the chemical rate constants of the adhesion molecules to bond strain, and derived a formula for critical tension, finally predicting that force does not necessarily increase dissociation rate, but could actually decrease it, postulating that applied force could entrap a dissociating ligand, in what we call now a catch-bond. His prophecy was found to be true 15 years later [94].

### **Membrane spreading and peeling**

On the same vein, a detailed analysis of *spreading and peeling interactions* between cells and substrates, mediated by clusters of bonds was performed by Hodges & Jensen in 2002 [70]. The cell is modelled as an extensible membrane under tension containing fluid of constant volume. In the rapid binding kinetics regime, the authors model the sedimentation of the cell onto the plane under adhesive forces (spreading), followed by removal of the cell from the plane under the action of an external force (peeling), using lubrication theory to describe the thin-film flow between the cell and the plane. It is shown that these events are dominated respectively by quasi-steady spreading and peeling motions. Also, a relation between cell rolling speed and shear rate is determined: at low speeds it is linear and independent of the viscosity of the suspending fluid; at higher speeds it is nonlinear and viscosity-dependent.

### **Bond tilting and sliding friction**

A continuation of this work was done by Reboux *et al.* [115]. The cell adhering to a biological interface is modelled as a rigid cylinder moving in a viscous shear flow near a wall. Adhesion forces arise through intermolecular bonds between receptors on the cell and their ligands on the wall, which form flexible tethers that can stretch and tilt as the base of the cell moves past the wall. A microscale calculation (for two parallel sliding plates) reveals a nonlinear force-speed relation arising from bond formation, tilting and breakage. Two distinct types of macroscale cell motion are then predicted: either bonds adhere strongly and the cell rolls (or tank treads) over the wall without slipping, or the cell moves near its free stream speed with bonds providing weak frictional resistance to sliding. The model predicts bistability between these two states, implying that at critical shear rates the system can switch abruptly between rolling and free sliding, and suggesting that sliding friction arising through bond tilting may play a significant dynamical role in some cell adhesion applications.

### **Multiscale modelling: continuum approaches**

An effective *multiscale computational approach* for the study of the adhesion of cells was proposed by N'Dri *et al.* [104]. The cellular level model consists of a continuum representation of the field equations and a moving boundary tracking capability to allow the cell to change its shape continuously. At the receptor-ligand level, a bond molecule is modelled as an elastic spring. Communication between the macro/micro- and nanoscale models is interactive during the computation. The computational model is assessed using an adherent cell, rolling and deforming along the vessel wall under imposed shear flows. The intracellular viscosity and interfacial tension are found to

directly affect the rolling of a cell while the presence of a nucleus increases the bond lifetime, and decreases the cell rolling velocity. Furthermore, it is found that a cell with a larger diameter rolls faster, and decreases the bond lifetime. This study shows that cell rheological properties have significant effects on the adhesion process, contrary to what has been hypothesized in most literature.

## 1.4 Stochastic models for adhesion clusters

---

A main issue in cell adhesion is to find the right coupling between the deterministic descriptions of the cell and environment with the stochastic behaviour of clusters consisting of few bonds. Also, an important issue is to examine the accuracy of the well-established deterministic models in the small number of bonds limit.

### Limitations of deterministic models

Since the deterministic limit could only describe the dynamics of the cluster in the large number of bonds limit (see e.g. [10], [28], [15]), a stochastic approach is required for the study of the fluctuations in the life of small clusters. When the stochastic models account for both rupture and reformation of broken bonds, analytical formulas are difficult to obtain, so results are explored mainly via Monte Carlo (and related) stochastic simulation algorithms.

As in the case of deterministic models, specially designed stochastic model are also developed to evaluate specific experiments, for example the binding probability between ligands and receptors on opposing surfaces as a function of contact time [146]. A stochastic version of the Bell-model has been introduced and studied in the large system limit and for specific parameter values by Cozens-Roberts *et al.* [26], who extended the model proposed by Dembo *et al.* [28] to obtain probabilities for the formation of bonds.

### Adhesive dynamics

Another important contribution of Hammer was the introduction of *adhesive dynamics* (AD) in 1992 [62], a computational method to simulate the adhesion of cells to surfaces. The method involves solving the equation of motion for a cell, and incorporates molecular properties such as bond kinetics and compliance. It has been successful at simulating the dynamics of cell adhesion under flow, and for predicting how dynamic states of adhesion follow from molecular properties. It has also been used to simulate virus-cell interaction, the aggregation of cells in linear flows, and the detachment of cells from surfaces. *Brownian adhesive dynamics* (BRAD) was a novel technique in-

roduced by Hammer *et al.* [63, 64] to simulate viral attachment to surfaces, which coupled Brownian motion simulations and adhesive dynamics. The method is capable of simulating multiple ligand/receptor pairs between the virus and cell, extendable to any geometry, and to any virus/cell system.

### **Purely stochastic models: parallel clusters of bonds under constant and linear force**

In an interesting approach towards the analysis of the stochastic dynamics of cell adhesion clusters, Tees *et al.* [134] made use of the survival functions inspired from the theory of reliability engineering of electric components and networks and the Bell model for bond rupture under applied force. They derived closed-form expressions for the probability distribution of the break-up time with multiple-independent or interacting bonds (and compared them with Monte Carlo simulations), showing that the average lifetime of  $n$  bonds scales with the  $n$ -th harmonic number multiplied by the lifetime of a single bond. Bond reformation was not analyzed, but identified in reliability theory as “maintained system”, while a method for addressing the non-uniform distribution of force between connected bonds was proposed.

In several papers, Erdmann & Schwarz use a stochastic version of the Bell model to analyze the stochastic dynamics of parallel clusters of bonds under constant [31], or linearly ramped force [32], with rebinding. Neglecting most mechanical aspects, the model has three dimensionless parameters: the cluster dimension  $n$  (total number of binding sites), the dissociating force  $f$  (or ramping coefficient for ramped force) and the rebinding coefficient  $\gamma$ . The state of the system is completely characterized by the number of closed bonds and the stochastic dynamics of the cluster are given by the one-step Master Equation (ME):

$$\frac{dP_k}{dt} = r_{k+1}P_{k+1} + g_{k-1}P_{k-1} - [r_k + g_k]P_k, \quad k = 0, \dots, n; \quad P_k(0) = \delta_{kn}, \quad (1.4.1)$$

where  $P_k(t)$  is the probability to have  $k$  closed bonds at time  $t$ , while  $r_k$  and  $g_k$  represent the stochastic rupture and rebinding rates for the clusters having  $k$  closed bonds. The ME is obtained from the analysis of the probability flux at the states  $k = 0, \dots, n$  [50, 138]. Different boundary conditions for the birth and death process involving the bond population are considered [122, pp. 194]. An *absorbing boundary* condition for the completely dissociated state for a cluster (zero bonds), is inspired from DSF experiments, where receptor and ligand are usually retracted by an elastic recoil of the linker molecules and rebinding is impossible. The state with zero bonds is called *reflecting* if rebinding is still possible.

Using a deterministic approximation for the ME the authors identify the relevant scaling  $f/n$  and identify three forcing regimes. In the low force regime, the cluster decays

exponentially, while in the intermediate force regime the decay is much faster and there is a sequential rupture of bonds (in the no rebinding case). In the large force limit, the model predicts a catastrophic rupture regime because the dissociation of the first bond leads to the instant dissociation of the cluster.

Once the ME (3.2.2) is solved (either analytically or numerically), many relevant quantities can be calculated. In the particular cases of zero force or no rebinding the ME can be solved even analytically. In the general case with force and rebinding the authors determine the critical force for dissociation analytically, while the solution of the ME is computed from stochastic simulations using the Gillespie algorithm [53]. A special focus was on the comparison between the deterministic and stochastic approximations for the solution of the ME and it is found that the deterministic approach only works well for low force and no rebinding, since it includes neither effects of fluctuations, nor the effect of an absorbing boundary.

### **Effects of receptor-ligand distance in clusters at equilibrium**

Another model proposed by Erdmann and Schwarz is used to assess the impact of *receptor-ligand distance* (considered constant) on cluster stability [35]. A one-step ME is derived which incorporates the effect of cooperative binding through a finite number of polymeric ligand tethers, of fixed length. The authors also consider Fokker-Planck and mean field equations [50, 117], as continuum limits of the ME. Polymers are modeled either as harmonic springs or as worm-like chains. In both situations the authors find bistability between bound and unbound states for intermediate values of receptor-ligand distance and calculate the corresponding switching times. For small cluster sizes, stochastic effects destabilize the clusters at large separation, as shown by a detailed analysis of the stochastic potential resulting from the Fokker-Planck equation.

### **Adhesion clusters between elastic substrates**

Employing the same ME approach, Gao *et al.* [49] analyzed an idealized *stochastic-elasticity model* of two elastic bodies joined by a cluster consisting of multiple molecular bonds, using elastic descriptions of adhesive contact on large scales and statistical descriptions of single-bond behaviors on small scales. The coupled stochastic-elasticity governing equations were solved numerically using Monte Carlo simulations. The aim was to investigate how the lifetime and strength of a molecular cluster are influenced by the adhesion size, the bond rebinding rate, and the elastic stiffness of the cell-substrate system. It was showed that depending on the adhesion size and the relative stiffness of the surrounding elastic media with respect to the adhesion cluster, there is a transition between uniform and crack-like singular distributions of interfacial traction.

For a given adhesion size, the average cluster lifetime approaches infinity asymptotically as the applied load is reduced below a critical value, defined as the strength of the bond cluster. Finally, the initial growth of a small cluster tends to stabilize adhesion as a result of collective effects in a stochastic process, in agreement with [31].

## 1.5 Overview and structure of thesis

---

The aim of this thesis is to propose and validate simple models addressing the validity of deterministic approximations, and to examine the importance of stochastic effects, for discrete adhesive molecular clusters with few bonds, which rupture and rebinding with rates depending on the motion of a rigid, or flexible substrate. The thesis is laid out as follows.

### Chapter 2

Here we develop a stochastic model for the evolution of a cluster of molecular bonds, connecting a flat surface to a rigid disk moving in a viscous fluid, under the influence of an applied force. The state of the system is characterized by the number of bonds and their extension at time  $t$ . Bonds are modelled as elastic springs under force, which rupture under force according to the Bell formula (1.3.2), and rebind with height-dependent rates. Between the rupture and rebinding events, the disk moves deterministically along curves depending on cluster population, force and drag. Bond and disk properties are incorporated in a dimensionless drag coefficient spanning over several orders of magnitude, which justifies a detailed treatment of the limiting cases of zero- and infinite-drag. The model dynamics is formulated in the framework of piecewise-deterministic Markov-processes proposed by Davis in 1984 [27, 111], and we derive an exact stochastic algorithm for simulating individual trajectories. A deterministic framework is also proposed.

As the model's main purpose is the development of tools suitable for studying the coupling between a continuous motion and the stochastic rupture and rebinding of bonds, the mechanical details are simple. Among other limitations, the model only accounts for the vertical motion of the disk, thin-film conditions are assumed to be valid for the entire cluster lifetime (and beyond), and no spatial effects generated by the rupture of various bonds (assumed identical) are considered. However, despite the model's simplicity, the methods we have developed allow the tackling of much more complex problems. In this work for example, spatial effects are addressed in Chapter 5, where the bonds attached to a flexible membrane are differentially stretched.

### Chapter 3

In this Chapter we analyze the zero-drag limit, where we recover the models proposed by Erdmann & Schwarz [31, 33], and the infinite-drag problem, which together give a good idea about the range of cluster's lifetime and decay profile. The time-independent transition rates greatly simplify cluster dynamics described by a ME (3.2.2), which is solved using analytic formulas, a Fokker-Planck equation (FPE), the Gillespie algorithm and deterministic approximations. Two parameter maps give a quantitative estimation of the constant force and loading rate regimes predicted by [31, 33]. The ratio  $f/n$  which fully characterizes the deterministic cluster decay, is found to have a limited relevance in the stochastic dynamics of the cluster, as direct solutions of the ME reveal that larger clusters decay faster than smaller ones, at same  $f/n$ . However, with rebinding, larger clusters may again survive longer for the same value of  $f/n$ .

### Chapter 4

This Chapter presents the drag-induced dynamics. The patterns of disk's detachment under constant force and drag are summarized in a parameter map. For small drag, the disk jumps between fixed positions, with the bonds breaking while the disk is stationary. In the intermediate drag regime, the bonds break as the disk moves between the equilibria. For large drag the disk moves little, and the bonds rupture due to thermal fluctuations. The region where the Erdmann & Schwarz model assumptions are valid is localized near the zero-drag boundary, while the "catastrophic" failure of bonds predicted in [31], does not happen anymore in the presence of drag. The distribution of cluster lifetimes and extension is examined using simulated trajectories. The cluster decay profiles confirm the force and drag regimes identified earlier. Stochastic simulations are validated against probability functions obtained from an analytical formula, and we also present results involving probabilities in time and height coordinates. For the problem with rebinding, we present a phase plane analysis of the deterministic equation, which identifies the stable and unstable equilibria, as well as of saddle points for the number of bonds and disk's displacement. The second part of the Chapter is dedicated to the study of the cluster's dynamics under ramped force, where we identify three distinct loading-rate regimes. For this case we develop simulations aimed at mimicking the DFS experiments, with an emphasis on cluster size, and drag.

In the third part of the Chapter we examine a possible PDE formulation for the time-evolution of the probability density of the bivariate stochastic process having the bond population and disk displacement as variables, following the work of Lipniacki [91]. A solution based on the method of characteristics is developed and compared against

stochastic simulations. For large drag ( $c \sim 100$ ) the transition rates are time-independent and the estimates of  $P_k(t)$  representing the probability of having  $k$  bonds at time  $t$  are in good agreement, in contrast with the results obtained for  $c \sim 1$ . A possible cause is suggested by the analytical solutions for the probabilities  $P_k$  computed in Appendix 4.A, which show that  $P_1$  is a  $n$ -dimensional integral with time-dependent limits. As this indicates that the problem may even not admit a PDE formulation, we formulate integro-differential forward and backward equations for the evolution of the density, whose solutions are to be checked against stochastic simulations.

## Chapter 5

Further we extend the results obtained for the vertical motion of a disk, to the vertical motion of a thin, flexible membrane connected to a planar surface via adhesion clusters, in the presence of hydrodynamic effects and vertical forces at the membrane boundaries. The variable gap between the two surfaces differentially stretches the bonds, assumed to behave as elastic springs under force. The bonds are also allowed to form and break at discrete binding sites spread over the membrane. The dynamics of the membrane-clusters system are addressed in the framework of piecewise deterministic Markov processes, and an exact stochastic algorithm is developed for the simulation of individual trajectories. The coupled evolution of adhesion clusters and the membrane's displacement is approximated by a differential equation whose solution is compared against results obtained from averages of the stochastic simulations. The membrane detachment time is strongly affected by the liquid volume underneath, by the bond population, and by the forces acting at the boundaries. The membrane displacement and bond populations are related using a wavelet-based semblance analysis.

The main conclusions of the thesis are reviewed in Chapter 6, where we also discuss potential further work.

# Adhesive molecular bond clusters between a disk and a surface

THE COUPLING between the cell's motion and the stochastic formation and dissociation of biological bonds represents a core interest in cell adhesion. Intensive research has been done considering detailed descriptions of cell's mechanics and continuous bond densities [28, 70, 115], or purely stochastic bond dynamics [31].

In this chapter we formulate a simple theoretical model coupling the stochastic evolution of discrete bonds to a simple motion between two surfaces, inspired from the DFS experiments [38, 95], presented in Chapter 1. To this end, we consider a cluster of bonds connecting a flat surface and a thin rigid disk moving vertically under force, in a fluid environment. The specific length-scales make thin-film effects important, while the small Reynolds number at cellular level ensures inertia can be neglected [114]. Following Bell [10], we consider a cluster of parallel and identical bonds, which act cooperatively and equally share the mechanical load. The bonds are modeled as elastic springs under force [98], which rupture and rebind due to thermal fluctuations. Bell's model is used for modelling the rupture rate of single bonds under force (1.3.2), while the rebinding of ruptured bonds depends on cluster's extension.

In §2.1 we formulate a detailed statement of the model, derive the equation of motion for the disk and propose appropriate rebinding and rupture rates. We then present a non-dimensional version of the model, and assess the role played by Brownian effects. In §2.2 we detail the methods involved in our study. Cluster dynamics are addressed in the framework of continuous-time Markov processes, and an exact stochastic algorithm is developed for simulating individual trajectories of the system. We also formulate a differential equation model for the coupled evolution of the bond population and the cluster's extension. In §2.3 we analyze the model and few possible extensions.

## 2.1 A stochastic model for a cluster of elastic bonds

In this section we formulate the full statement of the problem, discuss the rupture and rebinding rates, and then derive the non-dimensional version of the model. The effects of inertia and Brownian forces on the vertical motion of the disk are also discussed.

### 2.1.1 Deterministic motion of the disk

We consider a cluster of  $n$  biological bonds, connecting a fixed flat surface and a thin disk of diameter  $2R^*$ , which moves in a liquid of viscosity  $\mu^*$  and density  $\rho^*$ , under the action of a time-dependent dissociating force  $F^*(t^*)$  at time  $t^*$ . It is assumed that the bonds in the cluster are identical, parallel, equally share the load when connected, and behave under force as elastic springs of unstressed length  $L^*$  and elastic modulus  $\kappa^*$ . The length of the bonds at time  $t^*$  is denoted by  $h^*(t^*)$  (also representing the displacement of the disk, which does not tilt). The bonds rupture and rebind due to thermal fluctuations and the stress induced by their extension. A schematic of the model is sketched in Fig. 2.1, and the values of the parameters are displayed in Table 2.1.

For a disk of density  $\rho^*$  and vertical velocity  $v^*$  (same order of magnitude as the velocity of in-flow or rolling leukocytes) given in Table 2.1, the Reynolds number is

$$Re = \frac{\rho^* v^* (2R^*)}{\mu^*} \sim 10^{-3}, \quad (2.1.1)$$

suggesting that inertia can be safely neglected in our problem ( $F_{inertia}^* \simeq 0$ ) [114].

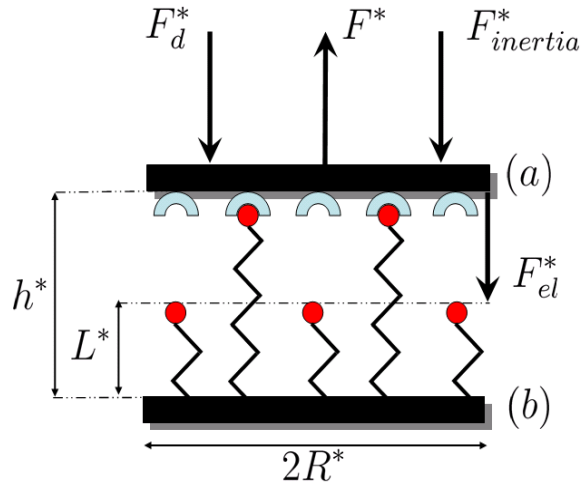


**Figure 2.1:** Elastic springs in an aqueous environment (dimensional): Cluster with  $n = 5$  bonds ( $k = 2$  connected) of rest length  $L^*$  attached to a thin disk (a) and a substrate (b), separated by the distance  $h^*(t^*)$  at time  $t^*$ . The disk moves subject to elastic force  $F_{el}^*$ , drag force  $F_d^*$  and dissociating force  $F^*$ .

Parameters	Values	References
Total number of bonds/cluster, $n$	2-100	[15]
Factor of rebinding rate, $\gamma$	1-100	[31]
Temperature, $T_0^*$	298 K	[10, 49, 78]
Rest length of bond, $L^*$	10-100 nm	[11]
Unstressed bond off-rate, $k_0^*$	$2.8 \text{ s}^{-1}$	[78]
Cell radius, $R^*$	$4 \mu\text{m}$	[78]
Single bond stiffness, $\kappa^*$	$0.01 - 5 \text{ dyn cm}^{-1}$	[15, 115]
Viscosity of surrounding liquid, $\mu^*$	$10^{-3} \text{ Pa s}$	[78]
Density of surrounding liquid, $\rho^*$	$1 \text{ g/cm}^3$	[78]
Force scale in bond dissociation, $F_0^*$	$4 \text{ pN}$	[10, 31, 49]
Leukocyte flow velocity, $v_F^*$	$100 \mu\text{m s}^{-1}$	[15]
Leukocyte rolling velocity, $v_R^*$	$1 - 2 \mu\text{m s}^{-1}$	[15]

**Table 2.1:** Range of relevant parameters for the disk motion in a liquid, and bond dynamics.

The disk's motion can be obtained from the balance of the forces acting on the disk,

$$F_d^* + F_{el}^* - F^* = 0, \quad (2.1.2)$$

where  $F_d^*$  is the drag force exerted by the surrounding liquid over the disk's surface,  $F_{el}^*$  is the elastic force in the stretched bonds and  $F^*$  is the dissociating force. Effects of inertia and Brownian forces on the disk's vertical motion are addressed in §2.1.4.

From the values given in Table 2.1, we obtain the ratio  $L^*/R^* \approx 0.01 \ll 1$ , so hydrodynamic adhesive effects are very important. The (nonlinear) drag force on the moving disk is derived in Appendix 2.A (2.A.15), using thin film theory [1]

$$F_d^* = \frac{3\pi\mu^*(R^*)^4}{2h^{*3}} \frac{dh^*}{dt^*} \quad (2.1.3)$$

where a no-slip boundary condition was considered. Although slip at the boundaries is likely to occur in the nm range [139], the equations for the drag force do not change significantly, therefore the no-slip boundary is sufficient for the purpose of this work. Formulae of the drag force on a one-dimensional plate moving vertically are also presented in Appendix 2.A, for no-slip (2.A.9) and slip (2.A.12) boundary conditions.

The elastic force in  $k$  connected and stretched bonds is

$$F_{el}^* = k\kappa^*(h^* - L^*). \quad (2.1.4)$$

Substituting the expressions of drag and elastic force in (2.1.2), the equation for the displacement of the disk with  $k$  bonds attached to it is

$$\frac{3\pi\mu^*(R^*)^4}{2(h^*)^3} \frac{dh^*}{dt^*} = F^* - k\kappa^*(h^* - L^*), \quad h^*(0) = h_0^* > 0. \quad (2.1.5)$$

Since the bonds break and rebind, the displacement of the disk is a piecewise deterministic stochastic variable, with the disk moving along solutions of (2.1.5) for the time intervals between the rupture/rebinding events.

### 2.1.2 Dissociation and association rates

Thermally activated rupture and rebinding of single molecular bonds are stochastic events, so the adhesion clusters' dynamics has to be described as a stochastic process. Usually, cell adhesion molecules function under force. The influence of a mechanical force on the rupture kinetics of biomolecular bonds was first discussed by Bell [10], who modelled the rupture of molecular bonds in the framework of Kramers' theory [67, 82], as a thermally activated escape over a transition-state barrier. Bell's formula for the single bond dissociation (rupture, breakage) rate under force is

$$k_{off}^*(F_b^*) = k_0^* e^{F_b^*/F_0^*}, \quad (2.1.6)$$

where  $k_0^*$  is the individual bond off-rate in the absence of force,  $F_b^*$  the applied force per bond and  $F_0^* = k_B T_0^*/x_0$  a force scale depending on the structure of the bond, which determines a force scale for bond strength ( $k_B$  is the Boltzmann constant and  $x_0^*$  is the displacement along the rupture coordinate). For the typical values  $x_0^* \simeq 1$  nm and physiological temperature  $T_0^* \simeq 300$  K, the force required to enhance the biological bond's rupture is  $F_0^* \simeq 4$  pN.

Equation (2.1.6) suggests that rupture occurs even in the absence of force, due to thermal fluctuations. Back to our problem, the bonds are modelled as linear springs, so the force acting per single bond is  $F_b^* = \kappa^*(h^* - L^*)$ . For estimating typical elastic bond forces, it is reasonable to consider that weak bonds are longer, while stiff bonds are shorter. Under this assumption, the values in Table 2.1 give

$$\kappa^* L^* \sim 1 - 50 \text{ pN}. \quad (2.1.7)$$

While the dissociation rate  $k_{off}^*$  mainly depends on the internal structure of the bond, the association (rebinding) rate  $k_{on}^*$  includes the formation of an encounter complex and depends on the details of the situation under consideration [31]. Since displacement is a key factor in the formation of the encounter complex [108], the association rate  $k_{on}^*$  is assumed to decay exponentially with the extension of the cluster, as in the formula

$$k_{on}^*(h^*) = k_0^* \gamma e^{\alpha(1-h^*/L^*)}, \quad (2.1.8)$$

where parameters  $\gamma$  and  $\alpha$  are intrinsic properties of the adhesion molecule, accounting for the affinity of the bond at its rest length and it's scaling with displacement variations, respectively.

### 2.1.3 Non-dimensional model

It is convenient to define the non-dimensional length  $h = (L^*)^{-1}h^*$ , time  $t = k_0^*t^*$ , applied force  $f = F^*/(\kappa^*L^*)$ , loading rate  $\mu = F^*/(\kappa^*L^*k_0^*t^*)$  and initial displacement of the disk  $h_0 = (L^*)^{-1}h^*(0)$ . To denote both constant and ramped force, we use the notation  $f(t)$ . The non-dimensional version of (2.1.5) is

$$v = \frac{dh}{dt} = -\frac{1}{c}h^3 [kh - (f(t) + k)], \quad h(0) = h_0, \quad (2.1.9)$$

representing the disk velocity with  $k$  bonds attached, at time  $t$  and height  $h$ , where

$$c = \frac{3\pi \mu^* k_0^* (R^*)^4}{2 \kappa^* (L^*)^3}, \quad (2.1.10)$$

is a non-dimensional drag coefficient. For the values of  $\kappa^*$ ,  $k_0^*$ ,  $R^*$  and  $L^*$  from Table 2.1, the range of the drag coefficient is obtained as  $0.01 \leq c \leq 10^4$ .

The solution of (2.1.9) for  $t \geq u$  is denoted by  $h = H_k(t; u, h_u)$ , where  $h_u$  represents the displacement of the disk at time  $t = u$ . When  $f$  is constant, (2.1.9) is autonomous and  $H_k(t; u, h_u) = H_k(t - u; 0, h_u)$ , with the initial condition  $H_k(0; 0, h_u) = h_u$ .

The stochastic variables  $N(t) \in \{0, 1, \dots, n\}$  (discrete) and  $H(t) \in [0, \infty)$  (continuous), representing the number of closed bonds (the remaining  $n - N(t)$  are open) and the disk's displacement respectively, completely determine the state of the system at time  $t$ . The state  $N = n$  is the number of binding sites in the cluster, and represents a *reflecting* (the next event is rupture) boundary for the stochastic variable  $N(t)$ . The state  $N = 0$  can be either *absorbing* or *reflecting* depending on whether rebinding after complete dissociation is possible (small displacement or force) or not (large force or displacement).

From (2.1.6), a single bond dissociates with the rate  $k_{off}^*/k_0^* = e^{\beta(h-1)}$ , where

$$\beta = F_{cl}^*/F_0^* = x_0^* \kappa^* L^* / (k_B T_0^*). \quad (2.1.11)$$

The estimates for  $\kappa^*L^*$  (2.1.7) predict the range  $1 \leq \beta \leq 15$ . The height-dependent rupture rate for the time segment when clusters have  $k = 0, \dots, n$  closed bonds is therefore given by

$$r_k(h) = ke^{\beta(h-1)}. \quad (2.1.12)$$

Using (2.1.8), the dimensionless rebinding rate for a single molecule is  $k_{on}^*/k_0^* = \gamma e^{\alpha(1-h)}$ . In a cluster with  $n$  binding sites, rebinding is assumed proportional to the number of open bonds [10, 61]. The rebinding rate for clusters having  $k = 0, \dots, n$  closed bonds is

$$g_k(h) = \gamma(n - k)e^{\alpha(1-h)}. \quad (2.1.13)$$

The rebinding rates used at  $N = 0$  for the *stochastic birth and death process* [122, p.372], are  $g_0 = \gamma n e^{\alpha(1-h)}$  for reflective, and  $g_0 = 0$  for absorbing boundaries, respectively.

In summary, we have developed a new stochastic model for the evolution of clusters of biological bonds connecting a disk and a surface. The stochastic rupture (2.1.12) and rebinding (2.1.13) rates depend on the position of the disk moving under the influence of the force  $f$ , along solutions of the deterministic equation (2.1.9). The parameters in our system are  $n$ ,  $f$  (or  $\mu$  for ramped force) and  $c$ , together with  $\alpha, \beta$  and  $\gamma$ , which are intrinsic properties of the bond.

#### 2.1.4 Brownian and inertial effects in the disk's dynamics

For the specific problem of cell adhesion, preliminary studies found that adherent cells (rigid disk and flat surface in our problem) can be distinguished from the ones not adhering to a surface, as they do not undergo significant Brownian oscillations [84].

As mentioned in Table 2.1, the disk's length scale is in the  $\mu\text{m}$  range, the bond length in the 10 nm range, while the timescale of molecular collisions is on the order of  $10^{-12}$  s and the lengthscale of molecular mean free paths is on the order of  $10^{-10} - 10^{-9}$  m. The tiny length- and time- scales suggest a deeper investigation of the role played by Brownian forces acting on the disk in the vertical direction, in our particular model.

Our results reflect the findings from the DFS experiments performed by Merkel *et al.* [95], discussed in §1.2.3. As depicted in Fig. 1.4, the thermal excitation induced fluctuations of the probe were about 2 – 5 nm, compared to the dissociating force induced displacement, which was of 30 – 40 nm at slow, and 500 nm at fast loading rates, respectively.

When accounting for the disk's mass and Brownian motion, the dimensional equation for the displacement of the disk is

$$M_{disk}^* \frac{dh^{*2}}{dt^{*2}} + G^* \frac{dh^*}{dt^*} = F^*(t^*) - F_{el}^*(t^*) + F_B^*(t^*), \quad (2.1.14)$$

where  $M_{disk}^*$  is the mass of the disk,  $G^*$  the coefficient of  $dh^*/dt^*$  in (2.1.3),  $F_B^*$  a stochastic force induced by external fluctuations, and  $F^*$  is the applied force on the disk. The deterministic component of the right-hand member in the previous equation will be denoted by  $F_{det}^* = F^* - F_{el}^*$ .

The Brownian force  $F_B^*$  is an irregular and unpredictable stochastic process, but its average properties are simple. The average vanishes, and because  $F_B^*(t^*)$  is caused by the collisions of the individual molecules of the surrounding liquid (the water molecule is about 0.1 by 0.2 nm in size) and varies rapidly, we can postulate that

$$\begin{aligned} \langle F_B^*(t^*) \rangle &= 0, \\ \langle F_B^*(t_1^*) F_B^*(t_2^*) \rangle &= \Gamma_B \delta(t_1^* - t_2^*), \end{aligned} \quad (2.1.15)$$

where  $\Gamma_B$  is a constant and  $\delta$  represents the Dirac function. The idea is that each collision is practically instantaneous and that successive collisions are uncorrelated [138, Chapter IX].

Balancing the first two terms in (2.1.14), and the Brownian noise on the disk, we obtain the scalings

$$\frac{M_{disk}^* h^*}{(t^*)^2} \sim \frac{G^* h^*}{t^*} \sim F_{det}^*. \quad (2.1.16)$$

From this equation, the relaxation time following a collision is found to scale as

$$t^* \sim \frac{M_{disk}^*}{G^*}.$$

Denoting by  $h^*$  the disk displacement length scale,  $V^*$  the velocity scale and  $k_B T^*$  the thermal energy, we obtain

$$h^* \sim V^* t^*, \quad k_B T^* \sim M_{disk}^* (V^*)^2. \quad (2.1.17)$$

Einstein [30], predicted that Brownian motion of a particle in a fluid at a thermodynamic temperature  $T^*$  is characterized by a diffusion coefficient  $D^*$ , and as shown in [18], the root mean square displacement in any direction after a time  $t^*$  is  $\sqrt{D^* t^*}$ . As a consequence of this fact, as well as from (2.1.16) and (2.1.17) we obtain

$$D^* \sim \frac{(h^*)^2}{t^*} \sim (V^*)^2 t^* \sim \frac{k_B T^*}{M_{disk}^*} t^* \sim \frac{k_B T^*}{G^*}. \quad (2.1.18)$$

The scales from (2.1.16) and (2.1.18) can be written as

$$\frac{1}{t^*} \sim \frac{F_{det}^*}{G^* h^*} \sim \frac{D^*}{(h^*)^2}. \quad (2.1.19)$$

Finally, from (2.1.18) and (2.1.19) we obtain the non-dimensional number

$$B = \frac{h^* F_{det}^*}{D^* G^*} = \frac{G^*}{k_B T^*} h^* \frac{F_{det}^*}{G^*} = \frac{h^* F_{det}^*}{k_B T^*}, \quad (2.1.20)$$

representing the ratio between the work done by deterministic forces and the thermal energy in the system. In the  $B \gg 1$  limit, Brownian effects can be neglected. Rewriting the right-hand side of (2.1.20) and using  $\beta \sim .25 - 12.5$ ,  $h \geq 1$ ,  $f \geq 0$  and  $L^*/x_0^* \sim 10 - 100$  (see Table 2.1), we obtain

$$B = \beta h (f - 1) \frac{L^*}{x_0^*} \gg 1, \quad (2.1.21)$$

for even relatively small forces, so Brownian effects are negligible for small forces.

A more accurate model accounting for the disk's fluctuations under Brownian forces, can be formulated using a stochastic differential equation (SDE)[69], rather than the ordinary differential equation (ODE) (2.1.9), which currently describes the motion of the disk. Nonetheless, the stochastic process would not be piecewise deterministic anymore, but system's trajectories can still be simulated.

## 2.2 Methods

In this section we present the notations and methods used to address the cluster dynamics. First, the behaviour of the cluster under force is formulated in the framework of inhomogeneous continuous-time Markov processes. An exact stochastic algorithm is derived, which allows the simulation of individual trajectories of the disk with bonds attached to it. Trajectories are then processed to obtain various probabilities, expected values for the number of closed bonds in the cluster, as well as estimates for the cluster lifetime and final extension of the bonds. A deterministic approximation for the simultaneous evolution of the number of closed bonds and displacement is then derived.

Despite being computationally expensive, stochastic simulations are the most reliable method, able to render the stochastic fluctuations in clusters with few bonds. These are compared against deterministic approximations and analytical solutions, when the latter are available.

### 2.2.1 Exact stochastic simulations

When clusters have few bonds, stochastic fluctuations become important. The problem is first formulated as a Markov process and then we derive a stochastic algorithm for the simulation of random variables  $N(t)$  and  $H(t)$ . The individual trajectories are then processed to obtain frequency functions which approximate (in the limit of a large number of individual trajectories) the marginal distributions for the Markov process.

The number of closed bonds  $N(t) \in \{0, 1, \dots, n\}$  evolves stochastically through the rupture or rebinding of a single bond, while height evolves deterministically between the rupture events. Once the process reaches the absorbing state  $N = 0$  (for absorbing boundary at  $N = 0$ ) or a certain value of time (for reflecting boundary at  $N = 0$ ), we stop the simulation. Let  $t_i$  ( $i \geq 0$ ) be the time of the  $i$ -th rupture or rebinding event, and let  $k = N(t_i)$ ,  $H_i = H(t_i)$ . Suppose that  $k \geq 1$ . The process  $\{N(t)\}_{t \geq t_i}$ , starting at the initial height  $H_i$  is an inhomogeneous continuous time Markov process, with finite state space  $E = \{k - 1, k, k + 1\}$  and time-dependent transition rates

$$\lambda_{k \rightarrow k-1}(t) = r_k(H(t)), \quad (k > 0), \quad (2.2.1a)$$

$$\lambda_{k \rightarrow k+1}(t) = g_k(H(t)), \quad (k < n), \quad (2.2.1b)$$

where  $H(t) = H_k(t; t_i, H_i)$ , for  $t \in [t_i, t_{i+1}]$  and  $r_0(H(t)) = g_n(H(t)) = 0$ .

The simulation of the next rupture or rebinding (referred to as an ‘‘event’’) is done in two distinct steps. The first step is to identify the time of the next event  $t_{i+1}$ , while the second is to identify whether the event is a rupture or a rebinding.

**Step 1: Next event time**

The total transition rate from the state  $N(t) = k$  at time  $t$  is denoted by

$$\lambda_k(t) = \lambda_{k \rightarrow k-1}(t) + \lambda_{k \rightarrow k+1}(t).$$

We calculate the distribution of the time spent in the state with  $k$  closed bonds starting at time  $t_i$  (the sojourn time), defined as

$$S = \inf\{\tilde{t} > 0 : N(t_i + \tilde{t}) \neq k\}. \quad (2.2.2)$$

Let

$$Q(\tilde{t}) = \Pr\{S > \tilde{t} | N(t_i) = k\}.$$

Clearly  $Q(0) = 1$  and as  $\Delta\tilde{t} \downarrow 0$ , by the Markov property we obtain

$$Q(\tilde{t} + \Delta\tilde{t}) = Q(\tilde{t}) (1 - \lambda_k(t_i + \tilde{t})\Delta\tilde{t}) + o(\Delta\tilde{t}).$$

This gives

$$\frac{dQ}{d\tilde{t}}(\tilde{t}) = -\lambda_k(t_i + \tilde{t}) Q(\tilde{t}),$$

with the solution

$$Q(\tilde{t}) = \exp\left\{-\int_0^{\tilde{t}} \lambda_k(t_i + u) du\right\}.$$

The cumulative distribution function of  $S$  is, for  $\tilde{t} > 0$ ,

$$\begin{aligned} F_S(\tilde{t}) &= \Pr\{S \leq \tilde{t} | N(t_i) = k\} = 1 - \Pr\{S > \tilde{t} | N(t_i) = k\} \\ &= 1 - Q(\tilde{t}) = 1 - \exp\left\{-\int_0^{\tilde{t}} \lambda_k(t_i + u) du\right\}. \end{aligned} \quad (2.2.3)$$

Considering the uniformly distributed variable  $\xi \sim U(0, 1)$ , the sojourn time satisfies  $S \sim F_S^{-1}(\xi)$ , thus we need to solve  $F_S(S) = \xi$ , which is equivalent to

$$\exp\left\{-\int_0^S \lambda_k(t_i + u) du\right\} = 1 - \xi. \quad (2.2.4)$$

Denoting by  $K$  the hazard function of the distribution  $Q$  [122, Chapter IX] defined as

$$K(\tilde{t}) = \int_0^{\tilde{t}} \lambda_k(t_i + u) du, \quad (2.2.5)$$

we can write (2.2.4) as  $\exp\{-K(S)\} = 1 - \xi$ , hence

$$K(S) = -\log(1 - \xi) \Leftrightarrow S = K^{-1}(-\log(1 - \xi)).$$

Since we also have  $1 - \xi \sim U(0, 1)$ , the time is simulated from

$$S = K^{-1}(-\log(\xi)). \quad (2.2.6)$$

As  $K^{-1}$  cannot be obtained analytically, (2.2.6) is solved numerically together with the motion of the disk from the system

$$\frac{dh}{dt} = -\frac{1}{c}h^3[kh - (f(t) + k)], \quad h(0) = H_i, \quad (2.2.7a)$$

$$\frac{dK}{dt} = \lambda_k(t), \quad K(0) = 0, \quad (2.2.7b)$$

which is integrated until  $K(t)$  hits the value  $-\log(\xi)$ .

The time of the next event is obtained as  $t_{i+1} = t_i + S$ .

### Step 2: Next event nature

To simulate the next state visited by  $\{N(t)\}$ , note that

$$\Pr \{N(t) = j \mid N(t_i) = k, S = t\} = \frac{\lambda_{k \rightarrow j}(t)}{\lambda_k(t)}, \quad (j = k - 1, k + 1).$$

For our problem, the event happening at time  $t_{i+1}$  is a rupture if

$$\zeta \leq \frac{\lambda_{k \rightarrow k-1}(t_{i+1})}{\lambda_k(t_{i+1})} = \frac{r_k(H(t_{i+1}))}{r_k(H(t_{i+1})) + g_k(H(t_{i+1}))}, \quad (2.2.8)$$

and rebinding otherwise, where  $\zeta \sim U(0, 1)$  and  $\xi$  are independent. The above procedure is repeated from the new state  $N(t_{i+1}), H(t_{i+1})$ .

In the case when more events are possible at a given time, we can use the following result. If  $X_1, \dots, X_m, m \leq 2$  are independent exponentially distributed random variables with rate parameters  $\lambda_1, \dots, \lambda_m$ , then

$$\min\{X_1, \dots, X_m\}$$

is also exponentially distributed, with parameter  $\lambda_1 + \lambda_2 + \dots + \lambda_m$ . The index of the variable which achieves the minimum is distributed according to the law

$$\Pr \{X_k = \min\{X_1, X_2, \dots, X_m\}\} = \frac{\lambda_k}{\sum_{i=1}^m \lambda_i}. \quad (2.2.9)$$

A proof of this classical result can be found in [122].

For our model, we define

$$S_k = \begin{cases} 0, & k = 0 \\ \lambda_1 + \dots + \lambda_k, & k = 1, \dots, m, \end{cases}$$

and the next event is chosen to be  $X_k$ , if  $\xi \in [S_{k-1}, S_k]$ , where  $\xi \sim U(0, 1)$ .

## General observations

The above algorithm is exact in principle, the only sources of inaccuracy being the choice of the random number generator, the precision used for solving (2.2.7) and the finite number of trajectories used to estimate various statistics.

### 2.2.2 Dynamics of the disk-bond system

The interaction between the number of bonds and the moving disk can be assessed using various statistics. Here we define various types of probability densities and distributions, average number of closed bonds, mean cluster lifetime, as well as other relevant statistics. In this chapter all disk trajectories start from the same initial height  $H(0) = h_0$ , while the influence of randomness in the initial height (normally distributed initial disk displacement) is analyzed in Appendix 3.A.

#### Probability of having $k$ bonds at time $t$

The output  $N(t)$  of many individual simulations is used to estimate the probability

$$P_k(t; 0, h_0) = \Pr\{N(t) = k \mid H(0) = h_0\}, \quad (2.2.10)$$

of having  $k$  bonds at time  $t$ , for  $k = 0, \dots, n$ .

Counting how many simulations out of  $N_s$  satisfy  $N(t) = k$ , we obtain the relative frequency functions

$$P_k^{(N_s)}(t; 0, h_0) = \frac{\{\text{number of simulations with } N(t) = k \mid H(0) = h_0\}}{N_s}. \quad (2.2.11)$$

The above functions satisfy the conservation property

$$\sum_{k=0}^n P_k^{(N_s)}(t; 0, h_0) = 1, \quad t > 0, \quad (2.2.12)$$

and in the large number of simulations limit we have, by the strong law of large numbers, almost surely, that

$$\lim_{N_s \rightarrow \infty} P_k^{(N_s)}(t; 0, h_0) = P_k(t; 0, h_0),$$

with the rate of convergence being in general of order  $1/\sqrt{N_s}$  (using the central limit theorem) [75].

The above probabilities exist for all values of the parameters (including the problem with rebinding) and provide an accurate description of the evolution of the number of bonds (mean, variance) and cluster lifetime, but give no information about the bonds'

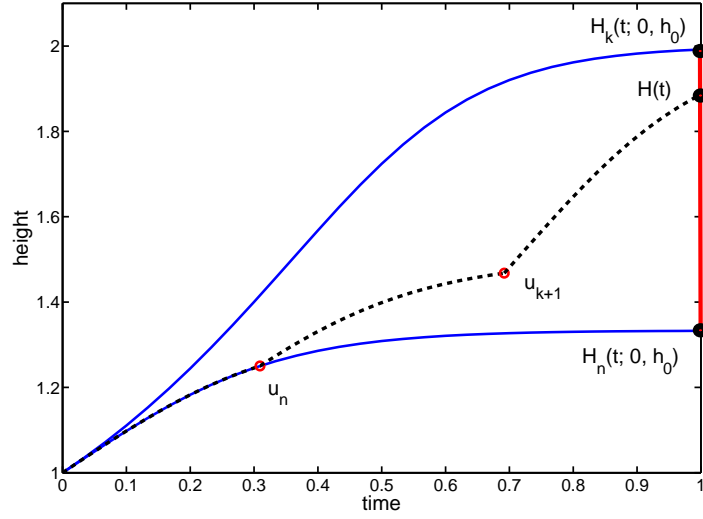


**Figure 2.2:** Simulated trajectory of the disk (dashed line) realized for  $n = 5$ ,  $k = 3$ ,  $h_0 = 1$ ,  $\gamma = 0$ ,  $\beta = 0$  and  $f = 1$  in the  $(t, h)$  space. The disk moves along  $H_n(t; 0, h_0)$  until  $u_n$ , the time when the  $n$ -th bond breaks. The time when the  $k$ -th bond ruptures is  $u_k$ .

extension. In the absence of rebinding, the bonds rupture sequentially and the trajectory is uniquely determined by the rupture times  $u_n, \dots, u_1$ . In this particular case the trajectories contributing to  $P_k(t; 0, h_0)$  are subject to specific geometrical constraints  $H(t) \in [H_n(t; 0, h_0), H_k(t; 0, h_0)]$ , as shown in Fig. 2.2.

These geometrical properties of the disk's trajectories are used in Appendix 4.A to derive analytical formulas for the probabilities  $P_k(t; 0, h_0)$ , which are used in Chapter 4 to validate the stochastic simulations.

### Probability of having $k$ bonds at height $h$

When  $H(t)$  is strictly monotonic (e.g. in the case of vanishing rebinding), a one-to-one correspondence between time and height can be established for a single simulation. We can consider then probabilities of having a certain number of bonds at a given height, to obtain important information about the evolution of the cluster under force with the displacement of the disk. Denoting  $T_h = \inf\{t \geq 0 : H(t) = h\}$ , we can define

$$P_k^H(h; 0, h_0) = \Pr\{N(T_h) = k \mid H(0) = h_0\}, \quad (2.2.13)$$

representing the probability of having  $k$  bonds at height  $h$ . These probabilities give an idea about the most likely height where the rupture events occur, and the computations are similar to those for  $P_k(t; 0, h_0)$ . The displacement  $H(t)$  is monotonic for  $h_0 = 1$  and zero rebinding.

### Probability densities and cumulative distributions over $h$ , of having $k$ closed bonds at time $t$

Both  $N(t)$  and  $H(t)$  can be used to estimate the distribution functions

$$F_k(t, h; 0, h_0) = \Pr\{N(t) = k, H(t) < h \mid H(0) = h_0\}, \quad (2.2.14)$$

of having  $k$  bonds at time  $t$ , and within the range  $[0, h)$ , for  $k = 0, \dots, n$ .

In the absence of rebinding, a single trajectory contributes to  $F_k(t, h; 0, h_0)$  if  $N(t) = k$  and  $H(t) \in [H_n(t; 0, h_0), h]$ . The relative frequency function for this event is obtained as

$$F_k^{(N_s)}(t, h; 0, h_0) = \frac{\{\text{no. of simulations for which } N(t) = k, H(t) < h, H(0) = h_0\}}{N_s}. \quad (2.2.15)$$

Clearly,  $\lim_{h \rightarrow \infty} F_k^{(N_s)}(t, h; 0, h_0) = P_k^{(N_s)}(t; 0, h_0)$  and in the large number of simulations limit we have that almost surely

$$\lim_{N_s \rightarrow \infty} F_k^{(N_s)}(t, h; 0, h_0) = F_k(t, h; 0, h_0).$$

The density function, defined as

$$p_k(t, h; 0, h_0) = \lim_{\delta h \rightarrow 0^+} \frac{\Pr\{N(t) = k, H(t) \in (h, h + \delta h) \mid H(0) = h_0\}}{\delta h} = \frac{\partial F_k(t, h; 0, h_0)}{\partial h}, \quad (2.2.16)$$

can be explored obtained either directly from simulations (using selected height bins), via numerical differentiation of (2.2.14), or by using kernel density estimation (see e.g. Silverman [129]). These functions illustrate how probabilities  $P_k(t; 0, h_0)$  are distributed along the height coordinate, and are illustrated in Appendix 3.A and §4.3.

### Expected number of closed bonds and variances

Quantities of practical interest are the expectation and variance of  $N(t)$ , which can be obtained as

$$\mu_N(t; 0, h_0) = \sum_{k=0}^n k P_k(t; 0, h_0), \quad (2.2.17a)$$

$$\sigma_N^2(t; 0, h_0) = \sum_{k=0}^n k^2 P_k(t; 0, h_0) - \mu_N^2(t). \quad (2.2.17b)$$

When no confusion is possible, the usual notations for these quantities will be  $\mu_N(t)$  and  $\sigma_N^2(t)$ . To approximate the above quantities at time  $t$ , we run a number of simulations, for which we estimate the state  $N(t)$ . In the large number of simulations limit, the average and variance of the states  $N(t)$  converge almost surely to  $\mu_N(t)$  and  $\sigma_N^2(t)$ , respectively. The analysis of  $\mu_N$  and its approximations will highlight the decay of clusters under various force regimes.

### Cluster dissociation time (“cluster lifetime”)

In the absence of rebinding or for an absorbing boundary at  $N = 0$ , the cluster dissociates and the stochastic variable  $T_D(t)$  representing the *time of dissociation* (the time when the last bond breaks or the cluster lifetime) can be defined. The density of  $T_D$  is

$$f_{T_D}(t) = \frac{dP_0(t; 0, h_0)}{dt}, \quad (2.2.18)$$

for the probabilities  $P_0(t; 0, h_0)$  defined in (2.2.10). Clearly, as  $P_0(0; 0, t) = 0$ , we have

$$\int_0^u f_{T_D}(t) dt = \int_0^u \frac{dP_0(t; 0, h_0)}{dt} dt = P_0(u; 0, h_0),$$

which should satisfy  $\lim_{u \rightarrow \infty} P_0(u; 0, h_0) = 1$ , when the cluster dissociates.

Of particular importance is the mean dissociation time  $\mu_{T_D}$ , defined as

$$\mu_{T_D} = \int_0^{\infty} t f_{T_D}(t) dt.$$

From  $N_s$  simulations, this can be estimated by

$$\hat{\mu}_{T_D} = \frac{\sum_{i=1}^{N_s} T_i}{N_s}, \quad (2.2.19)$$

where  $T_i$  is the moment when the  $i$ -th trajectory hits the absorbing boundary  $N = 0$ .

The standard deviation  $\sigma_{T_D}$  can also provide useful information about the cluster behaviour and can be estimated by

$$\hat{\sigma}_{T_D} = \sqrt{\frac{\sum_{i=1}^{N_s} (T_i)^2}{N_s} - \hat{\mu}_{T_D}^2}. \quad (2.2.20)$$

### Cluster dissociation height

When the cluster dissociates in finite time, the stochastic variable  $H_D(h)$  representing the dissociation height (disk displacement at dissociation) can be defined. When the probabilities  $P_k^H(h; 0, h_0)$  exist, the density of  $H_D$  is given by

$$f_{H_D}(h) = \frac{dP_0^H(h; 0, h_0)}{dh}. \quad (2.2.21)$$

Of practical interest is the mean displacement of the disk at dissociation, defined as

$$\mu_{H_D} = \int_0^{\infty} h f_{H_D}(h) dh.$$

This can be estimated from  $N_s$  individual simulations as

$$\hat{\mu}_{H_D} = \frac{\sum_{i=1}^{N_s} H(T_i)}{N_s},$$

where  $T_i$  is the time when the  $i$ -th trajectory hits the absorbing boundary  $N = 0$  and  $H(T_i)$  is the value of the random variable  $H$  at that time (for this particular realization).

Important information is obtained from the standard deviation  $\sigma_{H_D}$ , estimated by

$$\hat{\sigma}_{H_D} = \sqrt{\frac{\sum_{i=1}^{N_s} H^2(T_i)}{N_s} - \hat{\mu}_{H_D}^2}.$$

### 2.2.3 A deterministic approach

When the cluster has sufficiently many bonds, the rupture of an individual bond has a small effect on the behaviour of the cluster as a whole, and the number of closed bonds can be assumed to vary continuously. Denoting by  $N_d(t)$  the (continuous) number of closed bonds, we consider the continuous approximations of the discrete rates (2.1.12) and (2.1.13) in terms of two independent variables

$$\begin{aligned} r_d(N_d, H_d) &= N_d e^{\beta(H_d-1)} \\ g_d(N_d, H_d) &= \gamma(n - N_d) e^{\alpha(1-H_d)}, \end{aligned} \quad (2.2.22)$$

obtained by replacing  $k$  and  $h$  with their deterministic analogues  $N_d$  and  $H_d$ . The balance between the deterministic rupture and rebinding rates (2.2.22), together with (2.1.9), can be used to write down a system of deterministic equations for the simultaneous evolution of  $H_d(t)$  and  $N_d(t)$  as

$$\frac{dN_d}{dt} = \underbrace{-N_d e^{\beta[H_d-1]}}_{\text{Rupture}} + \underbrace{\gamma(n - N_d) e^{\alpha(1-H_d)}}_{\text{Rebinding}}, \quad (2.2.23a)$$

$$\frac{dH_d}{dt} = -\frac{1}{c} \left[ N_d H_d^4 - (f + N_d) H_d^3 \right], \quad (2.2.23b)$$

with the initial conditions  $H_d(0) = h_0$ , and  $N_d(0) = n$ . When the number of closed bonds is large, we examine the parameter values for which we have  $N_d(t) \rightarrow \mu_N(t)$ . In the case of no rebinding the cluster dissociates in finite time, with the rates given by (2.1.12). Moreover, in the large  $N_d$  limit, where the lifetime of the last remaining bond is very short compared to the lifetime of the cluster, the latter can be approximated with the scalar value  $T_d$  (in contrast to  $T_D(t)$ , which is a random variable) satisfying  $N_d(T_d) = 1$ . Asymptotic approximations of  $T_d$  provide essential information about the relevant scalings in the model as done by Erdmann *et al.* [31]. The performance of the  $T_d$  in estimating the median of the densities of  $T_D$  is illustrated in Fig. 4.3 for constant force and in Fig. 4.17 for linearly ramped force.

Although intuitive, the deterministic limit can also be derived rigorously as shown in Appendix 2.B, in the framework of stochastic hybrid systems discussed in [106] by Pakdaman *et al.*, who prove a law of large numbers with exponential convergence.

## 2.3 Summary

---

In this chapter we have introduced a new model for the stochastic behaviour of clusters of biological bonds under force and rebinding. Several experiments confirmed the elasticity of bonds under force [98], for example the length of fibronectin in response to applied force may increase 5- to 6-fold [73]. The extension of bonds is coupled to the nonlinear motion of a disk under force, which represents a significant extension over models assuming a constant displacement using polymeric spacers [35].

As the bonds in the clusters are short compared to the lengthscale of the contact region, the adhesion of clusters is enhanced by hydrodynamic effects. In our model, the deterministic motion of the disk (2.1.9), predicts that the external force initiating the motion is not entirely transmitted to the bonds, being mediated by drag. In the zero-drag limit (discussed in Chapter 3) we will recover the models proposed by Erdmann & Schwarz for constant [31, 32], and linear forces [33], respectively.

As a result of the low Reynolds number (2.1.1), inertia is neglected in this model [114]. The role played by the Brownian forces on the vertical motion of the disk with bonds attached was also proven to be negligible even for small forces in §2.1.4. The model can be further improved to encompass the disk's Brownian oscillations, by replacing the nonlinear ODE describing the motion of the disk (2.1.9), with a SDE.

The problem was formulated as a piecewise deterministic, bivariate, continuous-time Markov process, accounting for the number of closed bonds in a cluster  $N(t)$ , and their extension under force  $H(t)$ . The increase in complexity introduced by the movable disk, comes at the cost of having time-dependent transition rates (2.2.22).

A stochastic algorithm for simulating single trajectories of the system was proposed in §2.2.1, used to estimate several cluster statistics (lifetime, various probability functions, decay profile), detailed in §2.2.2. Finally, a deterministic approximation was proposed in §2.2.3, which is used in Chapter 4 for the study of cluster dissociation time (2.2.18) and extension (2.2.21).

A generalization of the model which addresses the behaviour of clusters of biological bonds connecting a fixed, flat surface to a moving and flexible membrane is presented in Chapter 5. The methods are also based on extensions of the ones presented in §2.2 for the disk-bonds model.

# Appendix

## 2.A Thin film adhesion

---

The adhesion of cells to a rigid surface is enhanced by adhesive effects generated by the thin-film of fluid between, which can be described using lubrication theory. The key feature of thin-film theory is that one dimension is much larger than the other. An example of such problem is a coin stuck tightly to a surface by putting a small amount of water between the two, when a surprisingly large force is required to pull the coin away from the table. This is possible because compared to the diameter of the coin, the height of the film of water is very small and as such is amenable to lubrication analysis. In this Appendix we present the Reynolds' lubrication equation, together with some applications relevant to the study of cell adhesion, based on [1].

### 2.A.1 Lubrication equations

The general Navier-Stokes equation are used to derive the 2D and 3D versions of the classical Reynolds' lubrication equations [1, 80]. To derive the lubrication equations assume that a curved surface having velocity components  $(U, V, W)$  sits on a thin film of fluid as shown in diagram 2.3 and the horizontal velocity components of the surface  $U$  and  $V$  are of the same magnitude. We use the notations  $L$  and  $h$  for the typical horizontal  $(x, y)$  and vertical  $(z)$  dimensions. The changes in the  $z$  direction are expected to be large compared to those in the  $x$  and  $y$  directions

$$\frac{\partial}{\partial x'} \frac{\partial}{\partial y} \sim O\left(\frac{1}{L}\right) \ll \frac{\partial}{\partial z} \sim O\left(\frac{1}{h}\right) \implies \delta = \frac{h}{L} \ll 1.$$

The velocity vector is  $\mathbf{u} = \left(u(x, y, z, t), v(x, y, z, t), w(x, y, z, t)\right)$ , while the pressure is  $p(x, y, z, t)$ . The density is  $\rho$ , the viscosity is  $\mu$  and kinematic viscosity is  $\nu = \mu/\rho$ . Assuming steady flow, the Navier-Stokes equation can be written as

$$\nabla \cdot \mathbf{u} = 0, \quad \frac{\partial \mathbf{u}}{\partial t} + \mathbf{u} \cdot \nabla \mathbf{u} = -\frac{\nabla p}{\rho} + \nu \nabla^2 \mathbf{u}, \quad (2.A.1)$$

where the first part is also known as the continuity equation. Assuming no slip boundary conditions at the interface between the fluid and the two surfaces ( $\mathbf{u} = 0$  at  $z = 0$  and  $z = h$ ),  $u$  and  $v$  must change by an amount of  $U$  as  $z$  varies over a distance  $h$ . The sizes of the terms in (2.A.1) can be obtained as

$$t \sim \frac{L}{U}, \quad \frac{\partial u}{\partial x} \sim \frac{U}{L}, \quad \frac{\partial^2 u}{\partial x^2} \sim \frac{U}{L^2}, \quad \frac{\partial u}{\partial y} \sim \frac{U}{L}, \quad \frac{\partial^2 u}{\partial y^2} \sim \frac{U}{L^2}, \quad \frac{\partial u}{\partial z} \sim \frac{U}{h}, \quad \frac{\partial^2 u}{\partial z^2} \sim \frac{U}{h^2},$$

with similar estimates for the derivatives of  $v$  and  $w$ .

From the continuity equations we obtain

$$\nabla \cdot \mathbf{u} = \frac{\partial u}{\partial x} + \frac{\partial v}{\partial y} + \frac{\partial w}{\partial z} = 0 \implies \frac{\partial w}{\partial z} \sim O\left(\frac{U}{L}\right) \implies w \sim O\left(\frac{Uh}{L}\right),$$

which leads to the estimates

$$\begin{aligned} \frac{\partial \mathbf{u}}{\partial t} &\sim \left( O\left(\frac{U^2}{L}\right), O\left(\frac{U^2}{L}\right), O\left(\frac{U^2 h}{L^2}\right) \right), \\ \mathbf{u} \cdot \nabla \mathbf{u} &\sim \left( O\left(\frac{U^2}{L}\right), O\left(\frac{U^2}{L}\right), O\left(\frac{U^2 h}{L^2}\right) \right), \end{aligned}$$

and

$$\nabla^2 \mathbf{u} \sim \left( O\left(\frac{U}{h^2}\right), O\left(\frac{U}{h^2}\right), O\left(\delta \frac{U}{h^2}\right) \right).$$

The above expressions suggest that

$$\left| \frac{\partial \mathbf{u}}{\partial t} \right|, |\mathbf{u} \cdot \nabla \mathbf{u}| \ll \nu |\nabla^2 \mathbf{u}| \quad \text{if} \quad \delta^2 \left( \frac{UL}{\nu} \right) \ll 1,$$

so the terms  $\partial \mathbf{u} / \partial t$  and  $\mathbf{u} \cdot \nabla \mathbf{u}$  in (2.A.1) neglected.

The quantity  $R = UL/\nu$  defines the Reynolds number, while  $R_m = \delta^2 R$  is referred to as the modified Reynolds number.

It is sensible to non-dimensionalize by setting

$$x = LX, \quad y = LY, \quad z = hZ, \quad u = U\hat{u}, \quad v = V\hat{v}, \quad w = \frac{Uh}{L}\hat{w},$$

where the vertical scales come from the continuity equation found in the first part of (2.A.1). The pressure scale is determined from the estimate

$$\frac{\partial p}{\partial x} \sim \mu \frac{\partial^2 u}{\partial z^2},$$

suggesting that  $p \sim \mu UL/h^2$ , so we can write  $p = (\mu UL/h^2)\hat{p}$ .

Substituting in equation (2.A.1), we obtain

$$\begin{aligned} R_m [\hat{u}\hat{u}_X + \hat{v}\hat{u}_Y + \hat{w}\hat{u}_Z] &= -\hat{p}_X + \delta^2 \hat{u}_{XX} + \delta^2 \hat{u}_{YY} + \hat{u}_{ZZ}, \\ R_m [\hat{u}\hat{v}_X + \hat{v}\hat{v}_Y + \hat{w}\hat{v}_Z] &= -\hat{p}_Y + \delta^2 \hat{v}_{XX} + \delta^2 \hat{v}_{YY} + \hat{v}_{ZZ}, \\ R_m^2 [\hat{u}\hat{w}_X + \hat{v}\hat{w}_Y + \hat{w}\hat{w}_Z] &= -\hat{p}_Z + \delta^4 \hat{w}_{XX} + \delta^4 \hat{w}_{YY} + \delta^2 \hat{w}_{ZZ}, \\ \hat{u}_X + \hat{v}_Y + \hat{w}_Z &= 0. \end{aligned} \tag{2.A.2}$$

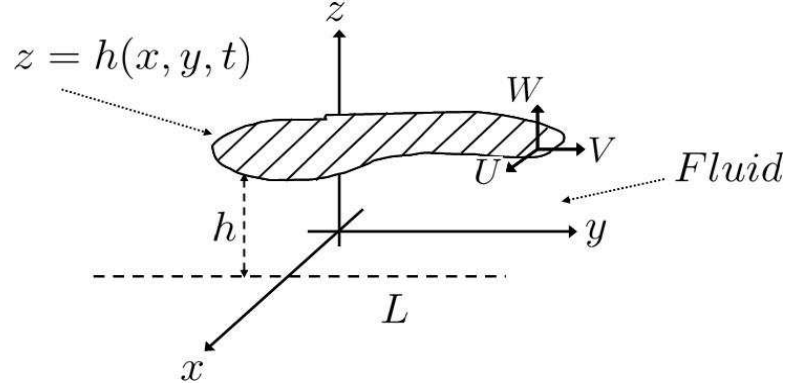


**Figure 2.3:** Diagram of the length scales in a thin film of liquid, situated between the fixed surface  $z = 0$  and the mobile surface  $z = h(x, y, t)$ .

In the limit  $\delta \rightarrow 0$  and  $R_m \rightarrow 0$  and restoring the dimensions we obtain the reduced set of equations

$$\begin{aligned} 0 &= -p_x + \mu u_{zz}, \\ 0 &= -p_y + \mu v_{zz}, \\ 0 &= -p_z, \\ u_x + v_y + w_z &= 0, \end{aligned} \tag{2.A.3}$$

with boundary conditions

$$u = v = w = 0 \text{ on } z = 0; \quad u = U, v = V, w = W \text{ on } z = h(x, y, t).$$

It is clear that there is no vertical pressure gradient, so  $p = p(x, y, t)$ . We integrate the first two equations of (2.A.3) twice with respect to  $z$  and obtain

$$u = \frac{1}{2\mu} p_x (z^2 - zh) + \frac{Uz}{h}, \tag{2.A.4}$$

$$v = \frac{1}{2\mu} p_y (z^2 - zh) + \frac{Vz}{h}. \tag{2.A.5}$$

Integrating the continuity equation, the vertical velocity component is found from the equation

$$-w = \int_0^z (u_x + v_y) dz,$$

which for  $z = h$  becomes

$$-W = \int_0^h (u_x + v_y) dz = \frac{\partial}{\partial x} \int_0^h u dz + \frac{\partial}{\partial y} \int_0^h v dz - Uh_x - Vh_y.$$

Using the expressions for  $u$  and  $v$  and integrating, the three-dimensional version of the Reynolds lubrication equation is obtained as

$$\frac{\partial}{\partial x} \left[ h^3 \frac{\partial p}{\partial x} \right] + \frac{\partial}{\partial y} \left[ h^3 \frac{\partial p}{\partial y} \right] = 6\mu (-Uh_x - Vh_y + 2W). \tag{2.A.6}$$

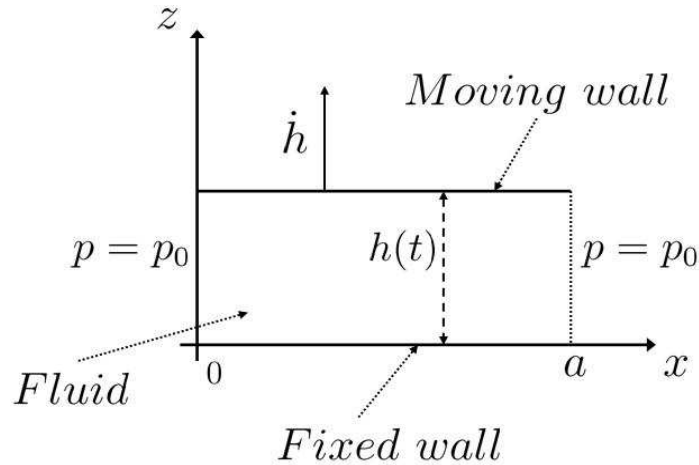


**Figure 2.4:** Diagram of the length scales in a thin film of liquid, situated between the fixed surface  $z = 0$  and the mobile surface  $z = h(x, t)$ .

### 2.A.2 Applications - adhesion near a flat rigid wall

Since the biological bonds are of a much smaller length compared to the cell scales, the cells subject to adhesion forces are moving very close to a surface, so the lubrication theory can be effectively applied in the study of cell adhesion. Of a particular importance is the drag force on the surface moving vertically near a flat, rigid and horizontal wall, which is derived here for a two-dimensional plate of length  $a$  and for a disk of radius  $a$ . These results can be directly coupled with the dissociating force and the elastic force in the bonds in the adhesive models, to derive the equation of motion for the moving surface.

#### Adhesion of a flat plate

The first application of lubrication theory computes the force resisting the motion between two parallel plane walls moving away from the other, and having liquid between, as shown in Fig. 2.4.

The thickness  $h(t)$  changes due to an unsteady flow, but we assume

$$\frac{\partial}{\partial t} \ll \nu \frac{\partial^2}{\partial z^2}, \quad (2.A.7)$$

so that the unsteadiness enters only through the change in the boundary condition. More details about the validity of this approximation can be found in [1].

Since the  $y$  coordinate is absent, we only need to solve the Reynolds lubrication equa-

tion

$$\frac{\partial}{\partial x} \left[ h^3 \frac{\partial p}{\partial x} \right] = 6\mu (-Uh_x + 2W), \quad (2.A.8)$$

for the boundary conditions

$$u = w = 0 \text{ on } z = 0; \quad u = 0, w = \frac{dh}{dt} \text{ on } z = h(t), \quad p(0, h) = p(a, h) = p_0.$$

where  $U = 0$  (no lateral move),  $W = \frac{dh}{dt}$ , and  $h$  independent of  $x$  (the mobile surface is flat). At the same time, the pressure is the same at the ends of the plate, and only depends on  $h$ . In this case, the above equation becomes

$$\frac{d}{dx} \left( h^3 \frac{dp}{dx} \right) = 12\mu \frac{dh}{dt},$$

and by integration we have

$$\frac{dp}{dx} = \frac{12\mu}{h^3} \frac{dh}{dt} + A(h).$$

Integrating again and applying the boundary conditions, we obtain

$$p(x, h) - p_0 = \frac{6\mu}{h^3} \frac{dh}{dt} x^2 + xA(h).$$

Since  $p(a, h) = p_0$ , we obtain

$$A(h) = -\frac{6\mu a}{h^3} \frac{dh}{dt},$$

and the pressure is finally

$$p(x, h) = p_0 + \frac{6\mu}{h^3} \frac{dh}{dt} x(x - a).$$

The force (per unit length) resisting the motion  $F$  is computed from the formula

$$F = \int_0^a (p - p_0) dx = \frac{6\mu}{h^3} \frac{dh}{dt} \int_0^a x(x - a) dx = -\frac{\mu a^3}{h^3} \frac{dh}{dt}. \quad (2.A.9)$$

This suggests that for the two-dimensional problem,  $F \sim O(h^{-3})$  as  $h \rightarrow 0$ .

### Adhesion of a flat plate with slip

It is often the case that in nanoscale flows a slip at the boundary occurs, which is expressed as

$$\frac{\lambda}{\mu} \tau = u,$$

at the boundaries, where  $\lambda > 0$  is determined from experiments and called *slip length*.

The equations for the problem described in Fig. 2.4, become

$$\begin{aligned} 0 &= -p_x + \mu u_{zz}, \\ 0 &= -p_z, \\ u_x + w_z &= 0, \end{aligned} \quad (2.A.10)$$

with boundary conditions

$$u = \lambda \frac{\partial u}{\partial y}, \quad w = 0 \text{ on } z = 0; \quad u = -\lambda \frac{\partial u}{\partial y}, \quad w = \frac{dh}{dt} \text{ on } z = h(x, t).$$

Integrating the first equation of (2.A.10) twice with respect to  $z$ , we obtain

$$u = \frac{1}{2\mu} p_x z^2 + Az + B.$$

Since  $dh/dx = 0$ , applying the boundary conditions we find

$$A = -\frac{1}{2\mu} p_x h, \quad B = -\lambda \frac{1}{2\mu} p_x h,$$

and obtain

$$u = \frac{1}{2\mu} p_x \left( z^2 - hz - \lambda h \right). \quad (2.A.11)$$

The third equation of (2.A.10) gives

$$w = - \int_0^y \frac{\partial u}{\partial x} dy,$$

so for  $y = h$  we have

$$-\frac{dh}{dt} = \frac{\partial}{\partial x} \int_0^h u dy = \frac{1}{2\mu} \frac{\partial}{\partial x} \left[ p_x \left( \frac{h^3}{3} - \frac{h^3}{2} - \lambda h^2 \right) \right],$$

which is integrated to give

$$p_x = \frac{12\mu}{h^2(h + 6\lambda)} \frac{dh}{dt} x.$$

Integrating in  $x$  and using that  $p(0, h) = p(a, h) = p_0$ , we finally obtain

$$p(x, h) = p_0 + \frac{6\mu}{h^2(h + 6\lambda)} \frac{dh}{dt} x(x - a).$$

The force per unit length resisting the motion  $F$ , is computed from the formula

$$F = \int_0^a (p - p_0) dx = \frac{6\mu}{h^2(h + 6\lambda)} \frac{dh}{dt} \int_0^a x(x - a) dx = -\frac{\mu a^3}{h^2(h + 6\lambda)} \frac{dh}{dt}. \quad (2.A.12)$$

This suggests that for the two-dimensional problem,  $F \sim O(h^{-3})$  as  $h \rightarrow 0$ . One can notice that the solutions as  $\lambda \rightarrow 0$ , are the ones obtained for the no-slip boundary. It is anticipated that the slip boundary solution for the disk is not very much different.

### Adhesion of a flat disk

Assume that a thin disk of radius  $a$  is immersed in a liquid of viscosity  $\mu$ . Writing the velocity in polar coordinates, we obtain

$$\mathbf{u} = u_r(r, z, t) \mathbf{e}_r + u_z(r, z, t) \mathbf{e}_z,$$

and using the new coordinates the thin film equation becomes

$$\frac{\partial p}{\partial r} = \mu \frac{\partial^2 u_r}{\partial z^2}, \quad p = p(r, t),$$

with the no slip boundary condition  $u_r = 0$  at  $z = 0$  and  $z = h(t)$ . Integrating twice with respect to  $z$  we obtain

$$u_r = \frac{1}{2\mu} \frac{\partial p}{\partial r} z(z - h).$$

From the incompressibility condition we have

$$\frac{1}{r} \frac{\partial}{\partial r}(ru_r) + \frac{\partial u_z}{\partial z} = 0,$$

from which we obtain (after replacing  $u_r$ , integration in  $z$  for the boundary condition  $u_z = 0$  on  $z = 0$ )

$$u_z = -\frac{1}{2\mu r} \frac{\partial}{\partial r} \left( r \frac{\partial p}{\partial r} \right) \left( \frac{z^3}{3} - \frac{hz^2}{2} \right).$$

Using the boundary condition  $u_z = dh/dt$  at  $z = h(t)$ , gives

$$\frac{\partial}{\partial r} \left( r \frac{\partial p}{\partial r} \right) = \frac{12\mu r}{h^3} \frac{dh}{dt},$$

which after integration in  $r$  becomes

$$\frac{\partial p}{\partial r} = \frac{6\mu r}{h^3} \frac{dh}{dt} + \frac{C(t)}{r}.$$

To prevent singularity at  $r = 0$ , we have  $C(t) = 0$ , and integrating once again we obtain

$$p = \frac{3\mu}{h^3} \frac{dh}{dt} r^2 + D(t). \quad (2.A.13)$$

Having  $p = p_0$  at  $r = a$ , this gives

$$p - p_0 = \frac{3\mu}{h^3} \frac{dh}{dt} (r^2 - a^2), \quad (2.A.14)$$

and the upward force exerted by the fluid on the disk is

$$F = \int_0^{2\pi} \int_0^a (p - p_0) r \, dr \, d\theta = -\frac{3\pi}{2} \frac{\mu a^4}{h^3} \frac{dh}{dt}. \quad (2.A.15)$$

Since the vertical velocity is of order  $dh/dt$ , from the continuity equation  $\nabla \cdot \mathbf{u} = 0$  we infer that the horizontal velocity is of order  $ah^{-1}dh/dt$ . The conditions  $h \ll L$ ,  $R_m \ll 1$  and (2.A.7) for this problem are written as

$$h \ll a, \quad h \frac{dh}{dt} \ll \nu.$$

The computations are based on [1].

## 2.B Stochastic hybrid systems: deterministic limits

In this section we adapt the theory of stochastic hybrid systems developed by Pakdaman *et al.* in [106], for analyzing the stochastic adhesion of clusters connecting a surface to a moving disk (Chapter 2). Compared to the renewal type algorithm used in Chapter 2 for the simulation of trajectories of the disk-bond system, the current formalism has the advantage of allowing a smooth passage to the global perspective over the system dynamics. This is particularly useful for showing that the solutions of the process converge in probability to the deterministic limit described in §2.2.3, while the speed of convergence is estimated as a function of the population of bonds in the cluster. The formulation of the disk-bond dynamics as a stochastic hybrid process for a cluster having  $n$  binding sites is detailed below.

Let  $u^{(k)}$  for  $1 \leq k \leq n$  be a collection of  $n$  independent jump Markov processes having the state space  $\{0, 1\}$ , representing the state (open or closed) of the  $k$ -th binding site in the cluster. The extension of the connected bonds in the cluster is the spacial variable  $H_n(t)$ . The transition between the closed and open states for individual binding has the rates  $\tilde{r}(H_n)$  and  $\tilde{g}(H_n)$  defined as

$$\tilde{r}(H_n) = \exp(\beta(H_n - 1)); \quad \tilde{g}(H_n) = \gamma \exp(\alpha(1 - H_n)), \quad (2.B.1)$$

corresponding to the rupture and rebinding rates for clusters of individual bonds defined in §2.1.3.

The stochastic hybrid model ( $S_n$ ) consists of two variables: an empirical measure of the population size  $e_n(t)$ , and the displacement of the plate  $H_n(t)$ , at time  $t$ . A convenient measure of the population size is

$$e_n(t) = \left( \frac{1}{n} \sum_{k=1}^n \delta_0(u^{(k)}(t)), \frac{1}{n} \sum_{k=1}^n \delta_1(u^{(k)}(t)) \right) \quad (2.B.2)$$

where  $\delta_i(k)$  represents the Kronecker delta function, which is 1 when  $k = i$  and 0 otherwise. By defining  $u_n(t) = 1/n \sum_{k=1}^n \delta_1(u^{(k)}(t))$ , (2.B.2) can be simplified to  $e_n(t) = (1 - u_n(t), u_n(t))$ . Between the jumps of  $e_n(t)$ , the disk's motion is deterministic.

To summarize, the hybrid model ( $S_n$ ) can be written as

$$\dot{H}_n(t) = v(H_n(t), e_n(t)), \quad e_n(t) = (1 - u_n(t), u_n(t)), \quad (2.B.3a)$$

$$H_n(0) = h_0, \quad e_n(0) = (u_0, 1 - u_0), \quad (2.B.3b)$$

where similarly to (2.1.9),  $v$  is defined by

$$v = \frac{dH_n}{dt} = -\frac{n}{c} H_n^3 \left[ u_n H_n - (\hat{f} + u_n) \right]. \quad (2.B.4)$$

The above general condition allows the cluster to start with any number of initial bonds, and the components of  $e_n$  are the proportions of processes in states 0 and 1.

The solution of the stochastic model  $(S_n)$  is given by  $X_n(t) = (H_n(t), u_n(t))$ . Each element of the sequence of jump Markov processes  $\{u_n\}_{n \geq 1}$  is characterized by

- its state space  $E_n = \{0, 1/n, 2/n, \dots, 1\}$ ;
- its intensity  $\lambda_n(H_n, u) = n[u\tilde{r}(H_n(t)) + (1-u)\tilde{g}(H_n(t))]$ ;
- its jump law

$$\mu_n(H_n, u, y) = \mu^+(H_n, u)\delta_y(u + 1/n) + \mu^-(H_n, u)\delta_y(u - 1/n),$$

where

$$\mu^+(H_n, u) = \frac{(1-u)\tilde{g}(H_n(t))}{u\tilde{r}(H_n(t)) + (1-u)\tilde{g}(H_n(t))}, \quad (2.B.5a)$$

$$\mu^-(H_n, u) = \frac{u\tilde{r}(H_n(t))}{u\tilde{r}(H_n(t)) + (1-u)\tilde{g}(H_n(t))}, \quad (2.B.5b)$$

are the probabilities deciding the nature of the next event (rupture or rebinding).

As one could easily see, both the intensity and jump law are time dependent through  $H_n(t)$ .

In [106] it is proven that the deterministic system  $(D)$  defined by

$$\dot{H}_d(t) = v(H_d(t), u_d(t)), \quad \dot{u}_d(t) = (1 - u_d(t))\tilde{g}(H_d(t)) - u_d(t)\tilde{r}(H_d(t)), \quad (2.B.6a)$$

$$H_d(0) = h_0, \quad u_d(0) = u_0, \quad (2.B.6b)$$

represents the asymptotic limit of the solution of  $(S_n)$  for sufficiently large  $n$ , under the *fluid limit assumption*. We explain below what this assumption means. Let  $(W_n)$  be a sequence of homogeneous Markov processes with states spaces  $E_n \subset \mathbb{R}^k$ , intensities  $\lambda_n(w)$ , and jump law  $\mu_n(w, dy)$ , with the flow defined as  $F_n(w) = \lambda_n(w) \int_{E_n} (z - w)\mu_n(w, dz)$ . The fluid limit occurs if the flow admits a limit and if the second-order moment of the jump size converges to zero when  $n \rightarrow \infty$ . As in our stochastic hybrid models  $(S_n)$  the jumps are of size  $1/n$  and the intensity is proportional with  $n$ , we are in the fluid limit assumption.

A more general version of this model, also developed in [106], allows a global formulation of the problem with multiple bond populations, attached to connected plates, and also allows the analysis of situations where the spatial coordinate  $H_n$  has more dimensions (lateral displacement of the plates). This may be potentially used for formulating a global treatment of the membrane-disk model presented in Chapter 5, and to justify the deterministic approximation for the system dynamics presented in §5.2.3.

## Limiting drag approximations

THE VERTICAL MOTION of the disk in the surrounding fluid is strongly dependent on hydrodynamic drag, which also modulates the force transmitted to the bonds (2.1.2). The properties of the disk, fluid and bonds have been incorporated in the dimensionless drag coefficient  $c \sim 10^{-2} - 10^4$  (2.1.10), which spans over several orders of magnitude and justifies a detailed treatment of the limiting cases of zero- and infinite-drag.

In the zero-drag limit, the disk's motion faces no resistance from the surrounding liquid, so the bonds support the whole dissociating force. When the disk starts moving from the initial displacement  $h_0 = 1$  (2.1.9), and the rates (2.1.12) and (2.1.13) are computed for  $\beta = 1$  and  $\alpha = 0$  respectively, we recover the models proposed by Erdmann & Schwartz, for constant [31], and linearly ramped force [33]. The state of the system is entirely described by the number of closed bonds, while the cluster dynamics are determined by only three parameters: the initial dimension of the cluster  $n$ , the rebinding coefficient  $\gamma$  and the force  $f$  (constant) or the loading rate  $\mu$  (linear force). On the other hand, for infinite drag the disk barely moves, and the unstretched bonds associate and dissociate under thermal fluctuations. The results obtained allow us to predict the range of cluster's lifetime and decay profile. As in many cases, the initial position of the disk is not fixed, we examine the effects induced by a normally distributed initial disk height, for the limiting-cases.

This Chapter is laid out as follows. In §3.1 we derive the trajectories of the disk for the zero- and infinite-drag limits, together with the relevant rupture and rebinding rates. In §3.2 we derive the master equation (ME) associated to the system [50, 138], and propose a solution based on the matrix exponential. We detail the numerical computation of the solution of the ME, and then sketch a simplified stochastic algorithm for simulating the system's individual trajectories. We end up with two deterministic approximations for the evolution of the mean number of closed bonds, one obtained from truncations of

the ME, and the other based on the Fokker-Planck equation (FPE) [117, 138]. The behaviour of clusters under constant force is analyzed in §3.3, for the vanishing rebinding (disk detachment), vanishing force and finally, for finite force and finite rebinding cases. Extending the work of Erdmann & Schwarz [31], we propose new probabilistic justifications for separating the various forcing regimes in  $(n, f/n)$  coordinates. We then compare a number of cluster statistics obtained by various methods. Particular attention is paid to the absorbing and reflecting boundaries at  $N = 0$ . Some results for the linearly ramped force are presented in §3.4. The deterministic approach relating the small, medium and large loading rates discussed in [33], is complemented with a probabilistic criterion to obtain a parameter map of the loading regimes in  $(n, \mu/n)$  coordinates. We also compare cluster statistics obtained from stochastic simulations with their deterministic approximations. The implications of the results for the general model are discussed in §3.5.

### 3.1 Disk motion in the limiting drag cases

---

In this section we present the disk trajectories under zero- and infinite-drag, together with the corresponding rupture and rebinding rates.

#### The zero-drag limit

In the zero-drag limit ( $c \ll 1$ ), we expand (2.1.9) as  $h = h_0 + ch_1 + \dots$ , and obtain (after the identification of coefficients of order zero in  $c$ ) that  $0 = (h_0)^3 \left[ h_0 - \left( \frac{f}{k} + 1 \right) \right]$ . Replacing  $h = \frac{f}{k} + 1$  in (2.1.12) and (2.1.13) together with  $\beta = 1$ ,  $\alpha = 0$ ,  $h_0 = 1$ , we obtain the rupture and rebinding rates  $ke^{f/k}$  and  $\gamma(n - k)$ , which show that the models proposed by Erdmann & Schwarz in [31], are recovered in the zero drag limit.

When  $k$  bonds are attached, the disk moves along solutions of (2.1.9), which in the zero-drag limit are

$$h(t) = 1 + f(t)/k. \quad (3.1.1)$$

This means that immediately after a rebinding/rupture event, the disk reaches a constant height under constant force (see Fig. 4.1,  $c = 0.1$ ), or moves along a certain line under ramped force (see Fig. 4.15,  $c = 0.1$ ), until the next event happens. When  $k$  bonds are closed, the rupture (backward) and rebinding (forward) rates are denoted by

$$r_k = ke^{f_b}, \quad g_k = \gamma(n - k), \quad (3.1.2)$$

where  $f_b = f(t)/k$  is the force per connected bond.

### The infinite-drag limit

In the large drag limit, ( $c \gg 1$ ), we expand (2.1.9) as  $h = h_0 + \frac{h_1}{c} + \dots$ ,  $h(0) = 1$  and identifying the coefficients of order zero and one in  $\frac{1}{c}$ , we obtain

$$\frac{dh_0}{dt} = 0 \quad (h_0(0) = 1), \quad \frac{dh_1}{dt} = -k(h_0)^4 + (k+f)(h_0)^3 \quad (h_1(0) = 0).$$

For  $h_0 = 1$ , the disk does not move significantly, since the dissociating force is balanced by drag, so the rupture and rebinding rates are

$$r_k = k, \quad g_k = \gamma(n - k), \quad (3.1.3)$$

which indicates that the infinite-drag limit can be recovered from (3.1.2) for  $f = 0$ .

This chapter is focused on the zero-drag problem and only mentions the infinite-drag limit results for cluster lifetimes or decay profiles, and in Appendix 3.A, where we discuss the impact of alternative distributions of the disk's initial height.

## 3.2 Methods

---

The main difference between the constant and linearly ramped force is that transition rates are time-independent for constant force, and time-dependent for ramped force. We give an overview of the available methods, with an emphasis on the constant force case, where a significant number of different approaches can be used and compared.

### 3.2.1 Master equation

The deterministic models employed in the analysis of clusters with large number of bonds fail to describe the stochastic fluctuations in small clusters, which can be described using the one-step master equation. Assuming a small time interval  $[t, t + \Delta t)$ , the cluster can leave the state  $N(t) = k \in \{1, \dots, n - 1\}$  to  $k - 1$  or  $k + 1$ , with probability  $(r_k + g_k)\Delta t$ . In the same time interval, the state  $k$  can only be reached from states  $k - 1$  and  $k + 1$  with probabilities  $g_{k-1}\Delta t$  and  $r_{k+1}\Delta t$ , respectively. Since the probability for two events to take place in the time interval  $(t, t + \Delta t)$  scales with  $(\Delta t)^2$ , we are actually dealing with a one-step process, also referred to as a “birth and death process” [138]. With zero drag, the disk moves directly to the position given by (3.1.1), the initial position of the disk is not relevant and the simplified notation  $P_k(t)$  is used instead of  $P_k(t; 0, h_0)$ , for the probabilities defined in (2.2.10). If the probabilities  $P_k(t) = \Pr \{N(t) = k\}$  are known, at time  $t + \Delta t$  they will satisfy the equation

$$P_k(t + \Delta t) = \left[ 1 - (r_k + g_k)\Delta t \right] P_k(t) + r_{k+1}\Delta t P_{k+1}(t) + g_{k-1}\Delta t P_{k-1}(t), \quad (3.2.1)$$

where the first term represents the probability that the cluster remains in the state with  $k$  bonds, while the second and third are the probabilities to enter state  $k$  from the states  $k + 1$  and  $k - 1$ , respectively. In the limit  $\Delta t \rightarrow 0$  we obtain the one-step ME

$$\frac{dP_k}{dt} = r_{k+1}P_{k+1} + g_{k-1}P_{k-1} - [r_k + g_k]P_k, \quad k = 0, \dots, n; \quad P_k(0) = \delta_{kn}, \quad (3.2.2)$$

where  $r_{n+1} = r_0 = g_n = g_{-1} = 0$ . More compact expressions can be obtained following the notations from the book of Van Kampen [138], who uses the “step operator”  $\mathbb{E}$  which is defined by its effect on an arbitrary function  $q(k)$  :

$$\mathbb{E}q(k) = q(k + 1), \quad \mathbb{E}^{-1}q(k) = q(k - 1). \quad (3.2.3)$$

With the aid of this symbol the ME (3.2.2) may be written

$$\frac{dP_k}{dt} = (\mathbb{E} - 1)r_kP_k + (\mathbb{E}^{-1} - 1)g_kP_k, \quad k = 0, \dots, n; \quad P_k(0) = \delta_{kn}, \quad (3.2.4)$$

where  $r_{n+1} = r_0 = g_n = g_{-1} = 0$ . These conditions are justified by the modelling assumptions. As  $n$  is the maximal number of available binding site, the state  $n + 1$  does not exist ( $r_{n+1} = 0$ ), while when all sites are occupied, no bond can be formed ( $g_n = 0$ ). At the same time, the state  $-1$  does not exist, which justifies  $r_0 = g_{-1} = 0$ .

Special attention is paid to the difference between the rebinding rates at  $k = 0$ , which are  $g_0 = n\gamma$  (reflecting boundary) and  $g_0 = 0$  (absorbing boundary). Each situation is analyzed separately. A full solution of (3.2.2) generally provides most relevant information about the cluster dynamics: mean number of bonds, dissociation rate, etc.

In matrix notation, the ME can be written from (3.2.2) as [138]

$$\frac{d\mathbf{P}}{dt} = \mathbf{A}(t)\mathbf{P}_0, \quad (3.2.5)$$

where  $\mathbf{P}(t) = (P_0(t), \dots, P_n(t))^T$  and  $\mathbf{A}(t)$  is a  $(n + 1) \times (n + 1)$  matrix defined as

$$\mathbf{A}(t) = \begin{pmatrix} -g_0 & r_1 & 0 & 0 & \cdots & 0 & 0 & 0 \\ g_0 & -r_1 - g_1 & r_2 & 0 & \cdots & 0 & 0 & 0 \\ 0 & g_1 & -r_2 - g_2 & r_3 & \cdots & 0 & 0 & 0 \\ \dots & \dots \\ 0 & 0 & 0 & 0 & \cdots & g_{n-2} & -g_{n-1} - r_{n-1} & r_n \\ 0 & 0 & 0 & 0 & \cdots & 0 & g_{n-1} & -r_n \end{pmatrix}, \quad (3.2.6)$$

which is time-dependent for ramped force, as (2.1.12) gives  $r_k = r_k(t) = k \exp(\mu t)$ . The system (3.2.5) is a first order linear ODE system, and can be solved by integration. When the matrices  $A(t)$  commute for any times  $t_1, t_2 > 0$  ( $\mathbf{A}(t_1)\mathbf{A}(t_2) = \mathbf{A}(t_2)\mathbf{A}(t_1)$ ), e.g. for constant force), the direct analytical formula

$$\mathbf{P}(t) = e^{\int_0^t \mathbf{A}(s) ds} \mathbf{P}_0, \quad (3.2.7)$$

is a solution for (3.2.5), where  $e^{\mathbf{A}}$  denotes the matrix exponential. For constant force (3.2.7) can be written as

$$\mathbf{P}(t) = e^{\mathbf{A}t} \mathbf{P}_0. \quad (3.2.8)$$

Even in the absence of a full analytical solution, the ME can be used to obtain the expectation and variance of  $N(t)$ , which in the compact notation  $\langle a_k \rangle = \sum_{k=0}^n a_k P_k$  [85], can be written as

$$\mu_N = \langle k \rangle = \sum_{k=0}^n k P_k, \quad (3.2.9a)$$

$$\sigma_N^2 = \sum_{k=0}^n k^2 P_k - \langle k \rangle^2. \quad (3.2.9b)$$

From (3.2.2), these satisfy the system [138]

$$\frac{d\mu_N}{dt} = \sum_{k=0}^n \frac{d(kP_k)}{dt} = - \sum_{k=0}^n r_k P_k + \sum_{k=0}^n g_k P_k = -\langle r_k \rangle + \langle g_k \rangle, \quad (3.2.10a)$$

$$\frac{d\sigma_N^2}{dt} = \langle g_k + r_k \rangle + 2\langle (k - \langle k \rangle)[g_k - r_k] \rangle. \quad (3.2.10b)$$

These results are exact, and their form is the same for constant ( $f$ ) and linearly ramped ( $\mu t$ ) force. Stochastic simulations can be used to estimate (3.2.10), as shown in §2.2.2.

### Numerical solution

As a first order ODE system, the ME can be easily solved numerically (for example using a `ode45` routine implemented in Matlab<sup>®</sup>). The difficulty is that the magnitude of the entries in matrix  $\mathbf{A}$  ranges from  $O(n)$  to  $O(e^f)$ , which makes the problem stiff for large values of  $f$  and  $n$ . The use of the analytical formula (3.2.7) extends considerably the dimension of the clusters for which we can solve the ME numerically. The matrix exponential is evaluated using either the `expm` Matlab<sup>®</sup> built-in routine (based on Padé approximation with scaling and squaring), or the formula

$$e^{\mathbf{X}} = \mathbf{V} \text{diag}(\exp(\text{diag}(\mathbf{D}))) \mathbf{V}^{-1},$$

where for a given matrix  $\mathbf{X}$ ,  $\mathbf{V}$  is the matrix whose columns are the eigenvectors of  $\mathbf{X}$ , while  $\mathbf{D}$  is the diagonal matrix having the eigenvalues of  $\mathbf{X}$  on the main diagonal. Results are presented in §3.3 below.

### 3.2.2 Deterministic approximation

When the ME itself is difficult to solve, one can obtain important information from a deterministic approximation for the evolution of  $\mu_N$  and  $\sigma_N^2$ . To this end, a continuous analogue of the transition rates  $r$  and  $g$  on the interval  $[0, n]$ , with the notation  $r_k = r(k)$  and  $g_k = g(k)$  is used, and several approximations for (3.2.10) can be obtained.

### Leading order

The deterministic approximation for the mean number of closed bonds evolves at a net rate given by the difference between rupture and rebinding, as in the equation

$$\frac{d\mu_N}{dt} = -\mu_N e^{f/\mu_N} + \gamma(n - \mu_N) = -r(\mu_N) + g(\mu_N), \quad (3.2.11)$$

first studied by Bell [10] for constant force, and later by Seifert [127] for ramped force. When the rates  $r$  and  $g$  are linear functions of  $k$ , we have

$$\langle r(k) \rangle = r(\langle k \rangle), \quad \langle g(k) \rangle = g(\langle k \rangle),$$

so equation (3.3.1) becomes (3.2.11). The range where the linearity assumption works, requires careful examination. While  $g_k$  (3.1.2) is linear,  $r_k$  may be considered linear only for  $f \ll 1$ , where  $r_k \approx k$ . As force increases,  $r_k \approx k \exp(f/k)$ , and (3.2.11) is no longer a good approximation.

### Higher order approximations

Assuming that  $r$  and  $g$  can be expanded in Taylor series around the average  $\mu_N$ , we write  $k = \mu_N + (k - \mu_N)$  and introduce the expansion in (3.2.10), to obtain [31]

$$\frac{d\mu_N}{dt} = -r(\mu_N) + g(\mu_N) + \sum_{i=2}^{\infty} \frac{g^{(i)}(\mu_N) - r^{(i)}(\mu_N)}{i!} \langle (k - \mu_N)^i \rangle, \quad (3.2.12a)$$

$$\frac{d\sigma_N^2}{dt} = r(\mu_N) + g(\mu_N) + \sum_{i=2}^{\infty} \left[ \frac{g^{(i)}(\mu_N) + r^{(i)}(\mu_N)}{i!} + 2 \frac{g^{(i-1)}(\mu_N) - r^{(i-1)}(\mu_N)}{(i-1)!} \right] \langle (k - \mu_N)^i \rangle, \quad (3.2.12b)$$

where the first order term vanishes because  $\langle (k - \mu_N) \rangle = 0$ . Truncating after second order term (error of magnitude  $\langle (k - \mu_N)^3 \rangle$ ), one obtains [31]

$$\frac{d\mu_N}{dt} = -\mu_N e^{f/\mu_N} + \gamma(n - \mu_N) - \frac{f^2}{2\mu_N^3} \sigma_N^2, \quad (3.2.13a)$$

$$\frac{d\sigma_N^2}{dt} = \mu_N e^{f/\mu_N} + \gamma(n - \mu_N) - \left[ e^{f/\mu_N} \left( 2 - \frac{2f}{\mu_N} - \frac{f^2}{2\mu_N^3} \right) + 2\gamma \right] \sigma_N^2, \quad (3.2.13b)$$

which is compared against solutions of (3.2.10), later in §3.3.1.

### Probabilistic justification

There is also a probabilistic basis for considering (3.2.11), which because  $r_k$  and  $g_k$  are functions of  $k/n$ , is precisely the large- $n$  limit of the solution of the ME (3.2.2). Denoting by  $X_n(t)$  the number of closed bonds at time  $t$ , in the terminology of Ethier and Kurtz [43, Chapter 11],  $\{X_n\}_{n \geq 1}$  is a density-dependent population process. Taking  $f = n\hat{f}$ , the following law of large numbers (see Theorem 2.1 on page 456 [43]) can be obtained.

**Theorem.** For any  $t > 0$ ,

$$\sup_{0 \leq s \leq t} \left| \frac{X_n(t)}{n} - \hat{N}(t) \right| \rightarrow 0 \quad \text{as } n \rightarrow +\infty \text{ almost surely,} \quad (3.2.14)$$

where  $\hat{N}(t)$  satisfies the ODE

$$\frac{d\hat{N}}{dt} = -\hat{N}e^{f/\hat{N}} + \gamma(1 - \hat{N}), \quad \hat{N}(0) = 1. \quad (3.2.15)$$

One can check easily that (3.2.15) is exactly (3.2.11) after the substitution  $\mu_N = n\hat{N}$ .

### 3.2.3 Gillespie Algorithm

For constant force, the rates are time-independent and a simplified version of the algorithm presented in §2.2.1, called the Gillespie algorithm [53] is available. The fact that makes it simple and efficient is that rather than discretizing time in small steps, the algorithm generates steps between subsequent reactions (assumed to happen one at a time). For our problem, the possible reactions are rebinding and rupture with corresponding rates  $g_k$  and  $r_k$ . The sojourn time in the state with  $k$  bonds is

$$S_k = \min \left( -\frac{\ln(\xi_{g_k})}{\gamma(n-k)}, -\frac{\ln(\xi_{r_k})}{ke^{f/k}} \right), \quad (3.2.16)$$

where  $\xi_{g_k}, \xi_{r_k} \sim U(0, 1)$  [31]. The next reaction is the one for which the minimum is attained. A single simulation generates a vector with the event times and one with the states of the system, allowing the computation of  $N(t)$ . The probabilities  $P_k(t)$ , are obtained as the frequency of  $k = 0, \dots, n$  in sufficiently many simulations ( $10^4 - 10^6$ ).

For ramped force  $f = \mu t$ , the rates are time-dependent and trajectories are simulated using the algorithm described in §2.2.1. However, as the disk's displacement is locally linear, the sojourn time  $S_{k,t_0}$  in the state with  $k$  bonds starting at time  $t_0$  (2.2.6), can be solved exactly giving the formula

$$S_{k,t_0} = \min \left[ -\frac{\ln(\xi_{g_k})}{\gamma(n-k)}, \frac{k}{\mu} \ln \left( 1 - \frac{\mu/k}{ke^{\mu t_0/k}} \ln \xi_{r_k} \right) \right], \quad (3.2.17)$$

where  $\xi_{g_k}, \xi_{r_k} \sim U(0, 1)$ .

### 3.2.4 Fokker-Planck Equation (FPE)

The FPE is a special type of ME, often used to replace the discrete solution  $\{P_k(t)\}_{0 \leq k \leq n}$  of the ME (3.2.2), with a continuous approximation  $P(X, t)$  which is the solution of a PDE (and hopefully easier to solve), where  $X$  is as a continuous variable interpolating  $\{0, 1, \dots, n\}$ . In §3.3 we examine parameter regions and time-windows where the FPE

approximation is valid, and then show that the FPE's first moments better approximate  $\mu_N$  and  $\sigma_N^2$  defined in (3.2.9), than the second order deterministic truncations (3.2.13).

In one dimension the FPE can be written as

$$\frac{\partial P(x, t)}{\partial t} = -\frac{\partial}{\partial x} \left[ A_{FPE}(x, t) P(x, t) \right] + \frac{1}{2} \frac{\partial^2}{\partial x^2} \left[ B_{FPE}(x, t) P(x, t) \right], \quad (3.2.18)$$

where the range of  $x$  is continuous and the coefficients  $A_{FPE}(x, t)$  and  $B_{FPE}(x, t)$  may be any positive differentiable functions [138, Chapter VIII]. The first term in the right-hand side of (3.2.18) is called convection or drift term, while the second is called diffusion or fluctuation term.

### Derivation of the FPE

The FPE is derived assuming a large cluster dimension  $n$ , and "smooth" rates  $r_k$  and  $g_k$  (i.e. small changes between  $k$  and  $k + 1$ ) [138, Chapter VIII]. Assuming that  $\phi(t)$  describes the macroscopic motion of the max of  $P_k(t)$ , one expects  $P_k$  to exhibit a sharp maximum at some position of order  $n\phi(t)$ , while its width to be of order  $n^{1/2}$  [138, Chapter X]. To capture this, we set

$$X = n\phi(t) + n^{1/2}x, \quad (3.2.19)$$

where the new variable  $x$  is of order 1. The continuous analogue  $P(X, t)$  is expected to verify

$$P(k, t) \approx P_k(t). \quad (3.2.20)$$

The initial condition of the ME (3.2.2) gives in the new variable

$$P(X, 0) = \delta(X - n). \quad (3.2.21)$$

Equation (3.2.19) is a time-dependent transformation from the variable  $X$  to the new variable  $x$ , involving the yet undetermined function  $\phi(t)$ . The function  $P(X, t)$  transforms into a function  $\Pi(x, t)$  of  $x$  according to

$$P(X, t) = P(n\phi(t) + n^{1/2}x, t) = \frac{1}{n^{1/2}} \Pi(x, t). \quad (3.2.22)$$

We shall find  $\Pi(x, t)$ , which will allow us to compute  $P(X, t)$  and then  $P_k(t)$ . The results are then compared against the solution of the ME (3.2.2). The sketch of the expected behaviour of  $P(X, t)$  is depicted in Fig. 3.1.

Consider the continuous and scaled versions of the rates  $r_k$  and  $g_k$  defined as

$$R(\phi) = \phi e^{\hat{f}/\phi}, \quad G(\phi) = \gamma(1 - \phi), \quad \phi \in [0, 1], \quad \hat{f} = f/n. \quad (3.2.23)$$

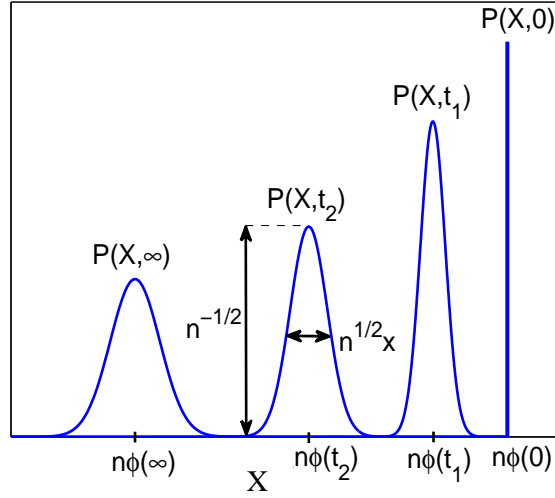


**Figure 3.1:** The evolution of the probability density  $P(X, t)$ , as  $N(t)$  decreases to an equilibrium.

The operator  $\mathbb{E}$  changes  $k$  into  $k + 1$  in (3.2.3), therefore  $x$  into  $x + n^{-1/2}$  in (3.2.22). Using (3.2.20) and (3.2.22), the terms of the ME (3.2.2) in the new variables are

$$\begin{aligned} r_k P_k &= nR(k/n) \frac{1}{n^{1/2}} \Pi(x, t) = n^{1/2} R\left(\phi + \frac{x}{n^{1/2}}\right) \Pi(x, t), \\ r_{k+1} P_{k+1} &= nR\left(\frac{k+1}{n}\right) \frac{1}{n^{1/2}} \Pi\left(x + \frac{1}{n^{1/2}}, t\right) = n^{1/2} R\left(\phi + \frac{x}{n^{1/2}} + \frac{1}{n}\right) \Pi\left(x + \frac{1}{n^{1/2}}, t\right), \\ g_k P_k &= nG(k/n) \frac{1}{n^{1/2}} \Pi(x, t) = n^{1/2} G\left(\phi + \frac{x}{n^{1/2}}\right) \Pi(x, t), \\ g_{k-1} P_{k-1} &= nG\left(\frac{k-1}{n}\right) \frac{1}{n^{1/2}} \Pi\left(x - \frac{1}{n^{1/2}}, t\right) = n^{1/2} G\left(\phi + \frac{x}{n^{1/2}} - \frac{1}{n}\right) \Pi\left(x - \frac{1}{n^{1/2}}, t\right). \end{aligned}$$

Using Taylor expansions of  $R$  and  $G$  about  $\phi$ , and of  $\Pi$  about  $x$ , we obtain

$$r_{k+1} P_{k+1} - r_k P_k = R \frac{\partial \Pi}{\partial x} + \frac{1}{n^{1/2}} \left( x R' \frac{\partial \Pi}{\partial x} + \frac{R}{2} \frac{\partial^2 \Pi}{\partial x^2} + R' \Pi \right) + O(1/n), \quad (3.2.24a)$$

$$g_{k-1} P_{k-1} - g_k P_k = -G \frac{\partial \Pi}{\partial x} + \frac{1}{n^{1/2}} \left( -x G' \frac{\partial \Pi}{\partial x} + \frac{G}{2} \frac{\partial^2 \Pi}{\partial x^2} - G' \Pi \right) + O(1/n), \quad (3.2.24b)$$

where  $R'$  and  $G'$  denote the differentials of the single-variable functions  $R$  and  $G$ . Using (3.2.19), the left-hand side of the ME (3.2.2) in the new variables is

$$\frac{dP_k}{dt} = \frac{1}{n^{1/2}} \left( \frac{\partial \Pi}{\partial t} - n^{1/2} \frac{d\phi}{dt} \frac{\partial \Pi}{\partial x} \right). \quad (3.2.25)$$

The ME can now be written as

$$\begin{aligned} \frac{1}{n^{1/2}} \left( \frac{\partial \Pi}{\partial t} - n^{1/2} \frac{d\phi}{dt} \frac{\partial \Pi}{\partial x} \right) &= (R - G) \frac{\partial \Pi}{\partial x} + \frac{1}{n^{1/2}} \left[ x(R' - G') \frac{\partial \Pi}{\partial x} \right. \\ &\quad \left. + (R' - G') \Pi + \frac{1}{2} (R + G) \frac{\partial^2 \Pi}{\partial x^2} \right] + O(1/n). \end{aligned} \quad (3.2.26)$$

Identifying the terms of orders  $O(1)$  and  $O(n^{-1/2})$  in (3.2.26) we obtain

$$O(1) : \quad \frac{d\phi}{dt} = A(\phi) \quad (3.2.27)$$

$$O(1/n^{1/2}) : \quad \frac{\partial \Pi(x, t)}{\partial t} = -A'(\phi) \frac{\partial}{\partial x} x \Pi + \frac{1}{2} B(\phi) \frac{\partial^2 \Pi}{\partial x^2}, \quad (3.2.28)$$

with the coefficients

$$A(\phi) = G(\phi) - R(\phi) = \gamma(1 - \phi) - \phi e^{\hat{f}/\phi}, \quad \phi(0) = 1, \quad (3.2.29a)$$

$$-A'(\phi) = -G'(\phi) + R'(\phi) = \gamma + e^{\hat{f}/\phi} \left(1 - \hat{f}/\phi\right), \quad (3.2.29b)$$

$$B(\phi) = R(\phi) + G(\phi) = \phi e^{\hat{f}/\phi} + \gamma(1 - \phi). \quad (3.2.29c)$$

Function  $\phi$  describes the macroscopic evolution of the cluster and is similar to the leading order deterministic equation (3.2.11). The terms of smaller orders represent fluctuations below the molecule level  $O(1/n)$ , and are therefore neglected. Equation (3.2.28) is a linear Fokker-Planck equation, also called the “linear noise approximation” [138, Chapter X.4], whose coefficients depend on time through  $\phi$ .

### Solution of the FPE

As shown in [138, Chapter VIII.6], the FPE (3.2.28) for a homogeneous boundary condition at  $\pm\infty$  is solved by a Gaussian, therefore it suffices to find the first and second moments of  $x$ . On multiplying (3.2.28) by  $x$  and  $x^2$  one obtains the first two moments of  $x$  and the variance

$$\langle x \rangle_t = A(\phi) \langle x \rangle, \quad (3.2.30a)$$

$$\langle x^2 \rangle_t = 2A'(\phi) \langle x^2 \rangle + B(\phi) \quad (3.2.30b)$$

$$\langle \langle x^2 \rangle \rangle_t = 2A'(\phi) \langle \langle x^2 \rangle \rangle + B(\phi), \quad (3.2.30c)$$

where the more compact notation

$$\langle \langle x^2 \rangle \rangle = \langle x^2 \rangle - \langle x \rangle^2 \quad (3.2.31)$$

for the variance was used. As our aim is to solve the ME with initial delta distribution (3.2.21) and with  $\phi(0) = 1$  for the microscopic part. It follows that the initial fluctuations vanish,

$$\langle x \rangle_{t=0} = \langle x^2 \rangle_{t=0} = \langle \langle x^2 \rangle \rangle_{t=0} = 0. \quad (3.2.32)$$

As shown in [138, Chapter X.4, Chapter VIII.6]), (3.2.28) is solved by the Gaussian

$$\Pi(x, t) = \left(2\pi \langle \langle x^2 \rangle \rangle\right)^{-1/2} \exp \left[ -\frac{(x - \langle x \rangle)^2}{2 \langle \langle x^2 \rangle \rangle} \right]. \quad (3.2.33)$$

One can see that (3.2.33) is the solution (3.2.28) for a homogeneous boundary at  $\pm\infty$ , and extends beyond the interval  $[0, n]$ . From (3.2.22),  $P(X, t)$  is also solved by a Gaussian, for which we find the mean and variance.

Inserting the solution of  $\phi(t)$  in (3.2.30a) with the initial conditions (3.2.32) one obtains the mean and variance of  $x$ . These are used to obtain the mean and variance of the original variable  $X$ , as

$$\langle X \rangle = n\phi(t) + n^{1/2}\langle x \rangle, \quad (3.2.34a)$$

$$\langle\langle X^2 \rangle\rangle = n\langle\langle x^2 \rangle\rangle. \quad (3.2.34b)$$

Differentiating (3.2.34a), the equations for the mean and variance are

$$\begin{aligned} \frac{d\langle X \rangle}{dt} &= n \frac{d\phi}{dt} + n^{1/2} \frac{d\langle x \rangle}{dt} = n \left( G - R \right) (\phi) + n^{1/2} (G' - R') \langle x \rangle \\ &= n \left( G(\phi) - R(\phi) \right) + \left( G'(\phi) - R'(\phi) \right) (\langle X \rangle - n\phi), \end{aligned} \quad (3.2.35a)$$

$$\frac{d\langle\langle X^2 \rangle\rangle}{dt} = 2 \left( G'(\phi) - R'(\phi) \right) \langle\langle X^2 \rangle\rangle + n \left( R(\phi) + G(\phi) \right), \quad (3.2.35b)$$

with the initial conditions  $\langle X \rangle_{t=0} = n$  and  $\langle\langle X^2 \rangle\rangle_{t=0} = 0$ . One can note that  $\phi(t)$  is not a trivial scaling of  $\langle X \rangle$  with  $n$ , as the two are related by

$$\frac{d(\langle X \rangle - n\phi)}{dt} = \left( G'(\phi) - R'(\phi) \right) (\langle X \rangle - n\phi), \quad (3.2.36)$$

which suggests that  $\langle X \rangle$  is a higher approximation for the first moment of the ME than (3.2.11). Simple computations show that it is not equivalent to (3.2.13a), and generally approximates  $\mu_N$  better, as we shall confirm in §3.3.

From (3.2.19), (3.2.22) we obtain

$$P(X, t) = \frac{1}{n^{1/2}} \Pi \left( \frac{1}{n^{1/2}} (X - n\phi), t \right). \quad (3.2.37)$$

As the mean and variance of  $\frac{1}{n^{1/2}}(X - n\phi)$  are  $n^{-1/2}\langle X \rangle - n^{1/2}\phi$  and  $\langle\langle x \rangle\rangle/n$  respectively, one can use (3.2.33) to write

$$P(X, t) = \frac{1}{n^{1/2}} \left( 2\pi \frac{1}{n} \langle\langle X^2 \rangle\rangle \right)^{-1/2} \exp \left( - \frac{\left[ \frac{1}{n^{1/2}} (X - n\phi) - \frac{1}{n^{1/2}} (\langle X \rangle - n\phi) \right]^2}{2 \frac{1}{n} \langle\langle X^2 \rangle\rangle} \right), \quad (3.2.38)$$

which after simplification proves that  $P(X, t)$  is indeed the Gaussian

$$P(X, t) = \left( 2\pi \langle\langle X^2 \rangle\rangle \right)^{-1/2} \exp \left[ - \frac{(X - \langle X \rangle)^2}{2 \langle\langle X^2 \rangle\rangle} \right]. \quad (3.2.39)$$

As the Gaussian distribution (3.2.39) extends beyond the interval  $[0, n]$ , the values  $P(k, t)$  computed from the FPE are expected to be a good match for the discrete probabilities  $P_k(t)$  just over a limited interval inside  $[0, n]$  which is far from the boundaries, and over a limited time-window. A significant improvement over the current solution can be made by considering no-flux boundaries at  $X = 0$  and  $X = n$ , to preserve the probability inside the interval  $[0, n]$ .

In summary, the ME (3.2.2) is approximated by a FPE with homogeneous boundary conditions at  $\pm\infty$ , which is solved by a Gaussian. The comparison between the solutions of the FPE and the ME, as well as estimates for the time-windows over which the FPE is a good approximation for the ME are presented in §3.3.1 and §3.3.2 below.

### 3.3 Results for constant force

---

When force is sufficiently large, the effects of rebinding are negligible. In this section we overview some relevant results regarding the cluster behaviour in  $n, f$  and  $\gamma$  parameter space, for zero rebinding §3.3.1, zero force with rebinding §3.3.2, and non-zero force with rebinding §3.3.3.

#### 3.3.1 Vanishing rebinding

First, an analytical solution for the ME (3.2.2) is discussed, and used to confirm the existence of three distinct forcing regimes. Then, the FPE approach is validated against deterministic approximations (3.2.13), and exact solutions of the ME computed from (3.2.8). We then analyze the cluster's decay and finally, prescribe upper and lower bound for cluster lifetime, using results obtained for zero- and infinite-drag.

#### Probabilities and force regimes

In the absence of rebinding, the cluster decay is a pure death process, with time-independent rates  $r_k$ . A direct formula for the state probabilities  $P_k(t)$  is available [75]

$$P_k(t) = \left( \prod_{j=k+1}^n r_j \right) \sum_{j=k}^n \left( e^{-r_j t} \prod_{i=k, i \neq j}^n \frac{1}{r_i - r_j} \right), \quad (3.3.1)$$

valid for  $r_i \neq r_j$ . In case  $f$  is such that  $r_i = r_j$ , (3.3.1) is replaced by

$$P_k(t) = \left( \prod_{j=k+1}^n r_j \right) \sum_{j=k}^n \left( e^{-r_j t} \prod_{i=k, r_i \neq r_j}^n \frac{1}{r_i - r_j} \prod_{i=k, r_i = r_j, i \neq j}^n \frac{t}{2} \right), \quad (3.3.2)$$

using that

$$\lim_{\Delta \rightarrow 0} (1 - e^{-t\Delta}) / \Delta = t, \quad \Delta = r_i - r_j.$$

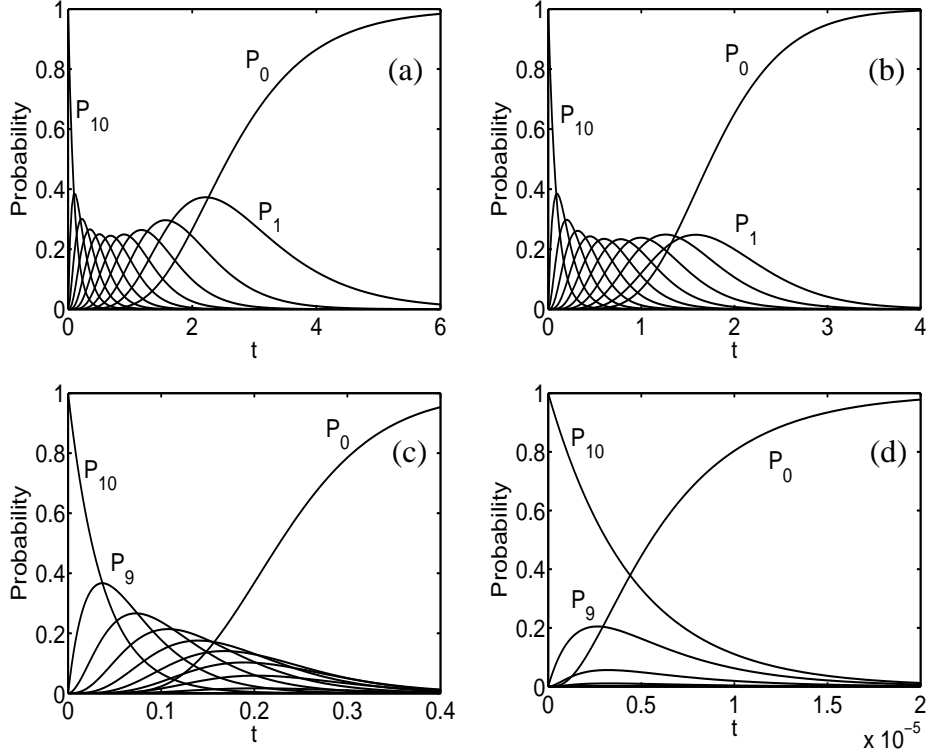


**Figure 3.2:** Probabilities  $P_k(t)$  obtained from the exact formula (3.3.1) for cluster size  $n = 10$ , rebinding coefficient  $\gamma = 0$  and (a)  $f = 0.1$ ; (b)  $f = 1$ ; (c)  $f = 10$ ; (d)  $f = 100$ .

For  $f = 0$ , (3.3.1) represents the stochastic version of the radioactive decay with the binomial distribution  $P_k(t) = \binom{n}{k}(1 - e^{-t})^{n-k}e^{-kt}$ . The full solution of the ME represented by the state probabilities  $P_k(t)$  is depicted in Fig. 3.2, suggesting the existence of three forcing regimes.

In what follows, we shall refer to a state  $k \in 0, \dots, n$  as being “visited” by the cluster at time  $t \geq 0$ , if

$$P_k(t) > P_i(t), \quad k \in \{0, \dots, n\}, \quad i \neq k \quad (3.3.3)$$

Under small force, there exists a time interval when the cluster visits each of the states  $k = 0, \dots, n$  (the probability  $P_k$  verifies (3.3.3)), as depicted in Fig. 3.2 (a). Because in the absence of rebinding the cluster dissociates,  $P_0$  approaches unity in the long run, while all other  $P_k$ 's vanish. As force increases, some of the states with lower number of bonds  $k$  are not visited, as illustrated in Fig. 3.2 (b) (state  $k = 1$  not visited) and (c) (states  $k = 5, 4, 3, 2, 1$  not visited), so the medium force regime can be considered to begin with the minimal force required for the cluster not to visit all states. Finally, from a certain value of  $f$ , the cluster only visits the states  $n$  and  $0$ , as plotted in Fig. 3.2 (d). The cluster decay in this regime is called “catastrophical”, the dissociation of the whole cluster immediately following the rupture of the first bond.

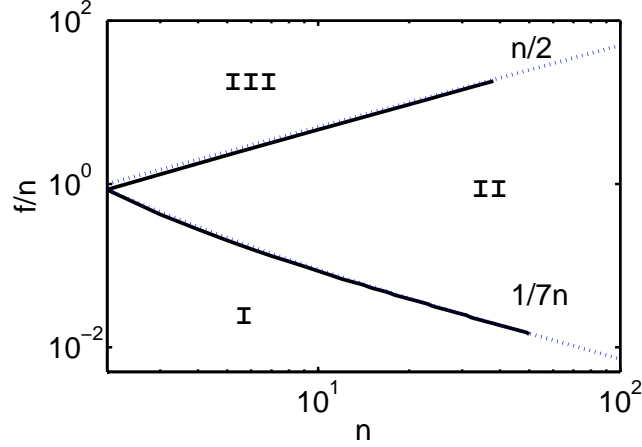


**Figure 3.3:** Force regimes in the  $(n, f/n)$  coordinates, generated from the analysis of probabilities  $P_k(t)$  obtained from (3.2.8) (solid lines). Solid lines represent boundaries computed from the numerical solution of the ME (3.2.8) for various values of  $n$ , while dotted lines represent results obtained by extrapolating the simulated data, using spline cubic functions. Plot obtained for  $n = 2, \dots, 100, \gamma = 0$  reveal the existence of small force (I), medium force (II) and large force (III) regimes.

### Force regimes obtained from the probability functions

The number of visited states defined in (3.3.3) is used to characterize the three force regimes as a function of cluster size, depicted in Fig. 3.3. Solid lines are determined by solutions (3.2.8) of the ME (3.2.2) (for values of up to  $n \sim 50$ ), while dotted asymptotes represent cubic spline extrapolations of the simulated data. For each value of  $n$ , the solutions (3.2.8) were computed for increasing values of  $f$ , and the small-intermediate and intermediate-large force boundaries, were identified using the function

$$D(f, t) = \max_{k=0, \dots, n} P_k(t).$$

The force regions are (I) for  $\#\{D(f, t) | t \geq 0\} = n + 1$ , (II) for  $2 < \#\{D(f, t) | t \geq 0\} < n + 1$  and (III) for  $\#\{D(f, t) | t \geq 0\} = 2$ , where  $\#\{D\}$  denotes the cardinal of set  $D$ .

The results predict that a small constant force is required to destabilize the smooth cluster decay ( $f \simeq 1/7$ ), while the force required for the cluster's catastrophic failure scales quadratically with  $n$  ( $f \simeq n^2/2$ ).

### Comparison ME vs. FPE

Despite the small cluster dimension  $n = 10$ , the solutions  $P(k, t)$  of the FPE (3.2.38), approximate reasonably well the solutions  $P_k(t)$  of the ME (3.2.2), especially for small force over a limited time-window, as sketched in Fig. 3.4 (a). As anticipated, the approximation is poor at the boundaries of  $[0, n]$ , as seen in Fig. 3.4 (a), where  $P_0(t)$  may

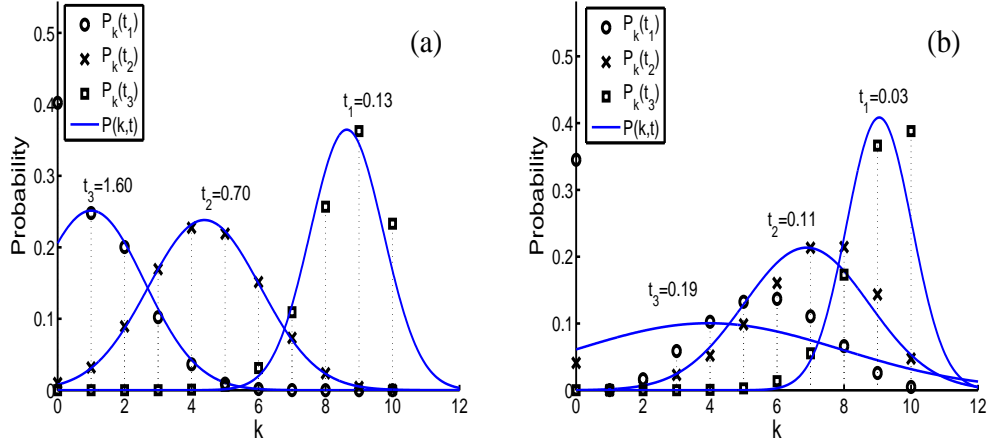


**Figure 3.4:** Solutions  $P_k(t)$  of the ME obtained from (3.2.8), are compared against the FPE approximations  $P(k, t)$  (3.2.38), for  $n = 10$ ,  $\gamma = 0$  and (a)  $f = 1$ ; (b)  $f = 10$ .

be severely underestimated by  $P(X, t)$ . The situation gets even worse with the increase in force, as depicted in Fig. 3.4 (b). This is expected, as the rupture rates increase exponentially with force, and the small number of bonds in the final phase ensure a big difference between the rates  $r_k$  and  $r_{k+1}$ . We expect then the FPE method to be totally irrelevant for approximating the catastrophic failure solution shown in Fig.3.2 (d) for  $f = 100$ , where cluster dynamics are dominated by the probabilities  $P_0$  and  $P_n$ .

### Cluster decay profiles

In the absence of the rebinding, the number of closed bonds in the cluster decays with time, until the cluster finally dissociates. The profile of this decay is analyzed from stochastic simulations of the system and deterministic approximations of  $\mu_N$ . The deterministic equation (3.2.11) can be transformed using the substitutions  $f = n\hat{f}$  and  $\mu_N = \hat{N}n$ , into

$$\frac{d\hat{N}}{dt} = -\hat{N}e^{\hat{f}/\hat{N}} + \gamma(1 - \hat{N}), \quad \hat{N}(0) = 1. \quad (3.3.4)$$

which only depends on  $\gamma$  and  $\hat{f}$ , the two key parameters of the deterministic model.

As discussed in Sec. §3.2, due to the nonlinear form of  $r_k$  (and continuous analogues  $r(x) = xe^{f/x}$ , where these are defined), the first moment  $\mu_N(t)$  of the stochastic solution for the mean number of closed bonds (3.3.1) is not identical with the solution of the deterministic equation (3.2.11). In Fig. 3.5, results for  $\mu_N(t)$  derived from stochastic simulations, the exact solution of the ME (3.2.2), the second-order deterministic approximation (3.2.13a), and solutions of the FPE (3.2.35a) are compared to each other.

For small force, the non-linearity is small and all methods agree in the initial phase of decay, as depicted in Fig. 3.5 (a).

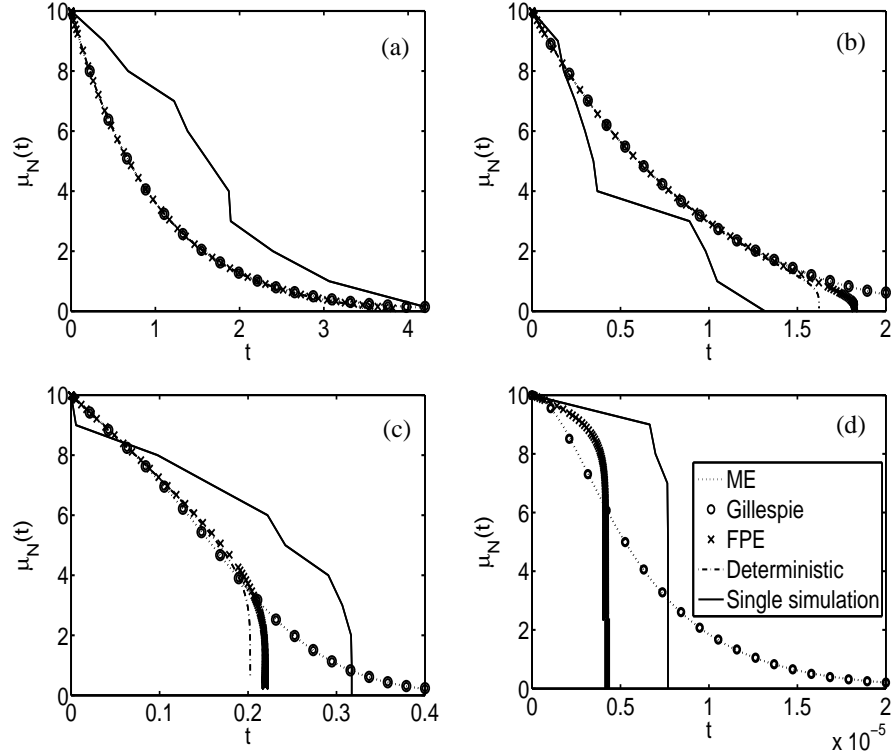


**Figure 3.5:** Comparison between single simulation trajectory (thin solid line) and  $\mu_N(t)$  obtained from the FPE (3.2.35a), DE (3.2.13a) (generally shadowed by FPE), ME (3.2.2) and average of  $10^4$  trajectories (perfectly match ME) for  $n = 10$ ,  $\gamma = 0$  and (a)  $f = 0.1$ ; (b)  $f = 1$ ; (c)  $f = 10$ ; (d)  $f = 100$ .

As shown in Fig. 3.5 (b) and (c), with the increase in force, the deterministic approximations deviate sooner and more significantly from results generated from the ME, with the FPE mean (3.2.35a) performing better than the deterministic mean (3.3.1). All deterministic results exhibit a steep breakdown since  $r(\mu_N)$  and  $d\mu_N/dt$  diverge as  $\mu_N \rightarrow 0$ . In the large force regime depicted in Fig. 3.5 (d) both deterministic approximations completely fail in describing the final decay phase, and the only reliable results are obtained from stochastic simulations. The stochastic results for  $\mu_N(t)$  show no scaling with  $f/n$  alone, because the ME includes all moments of the probability distribution  $\{P_k(t)\}_{k=0}^n$ .

In Fig. 3.6 we compare the variance  $\sigma_N^2(t)$  obtained from averages of stochastic simulations with results obtained from the exact solution (3.2.8) of the ME (3.2.2), the second order deterministic approximation of the variance (3.2.10b) obtained from (3.2.13b) and the solution of (3.2.35b), obtained from the FPE. The solutions agree even worse than the means, as the deterministic variances blow in finite time. As previously, the deterministic results are only relevant for the incipient phase of the decay, especially

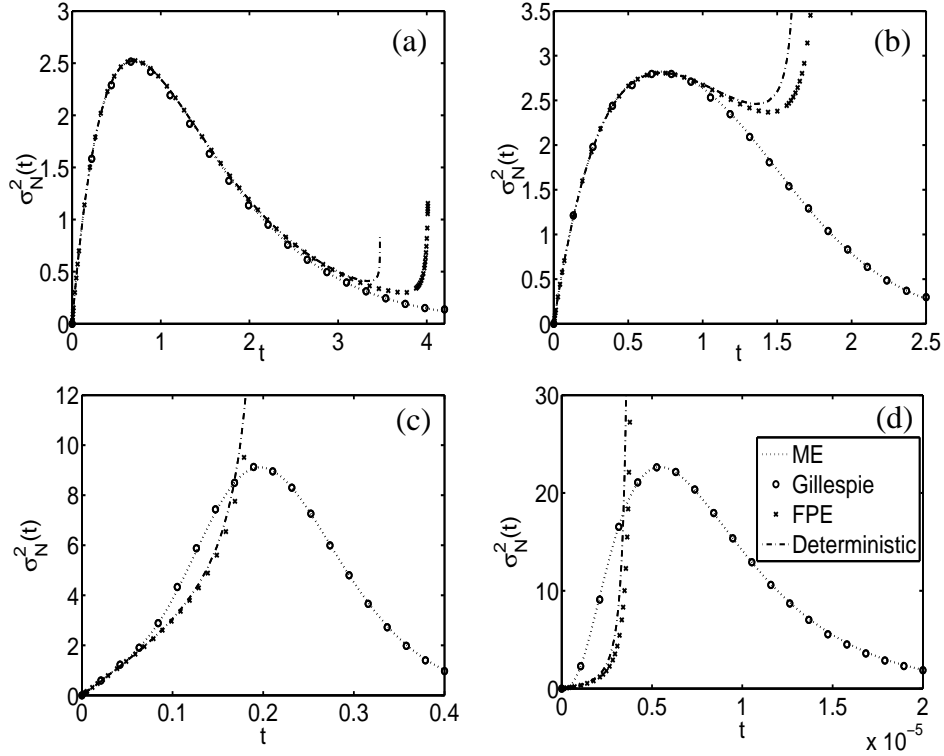


**Figure 3.6:** Variance  $\sigma_N^2(t)$  obtained from the FPE (3.2.35a), DE (3.2.13b), ME (3.2.2), and the average of  $10^4$  trajectories (perfectly match ME) for  $n = 10$ ,  $\gamma = 0$  and (a)  $f = 0.1$ ; (b)  $f = 1$ ; (c)  $f = 10$ ; (d)  $f = 100$ .

for small force, as depicted in Fig. 3.6 (a). As shown in Fig. 3.6 (b), (c) and (d), both deterministic approximations fail. The larger the force, the faster and worse the prediction. The conclusion is that one can only rely on stochastic simulations and the exact solution of the ME for describing the fluctuations in the terminal phase of the decay.

### Cluster decay and the ratio $f/n$

The dependence of the normalized decay  $\mu_N/n$  on the initial loading per bond  $f/n$  is depicted in Fig. 3.7, where we compare the solution of (3.3.4) against results from stochastic simulations. The difference between the two solutions increases with  $f$ , while for the same  $f/n$ , a large cluster decays faster than a small one. This is because for a large cluster the decay is slower in the initial phase, while after some ruptures the large force is shared by fewer bonds, so the decay becomes much faster. The deterministic approximation (3.3.4) does not reveal this behaviour, as the solution is completely determined by the ratio  $f/n$ .

For certain pure death processes, the relation between the deterministic decay and the mean number of closed bonds can be analyzed using a result of Ball & Donnelly [6,

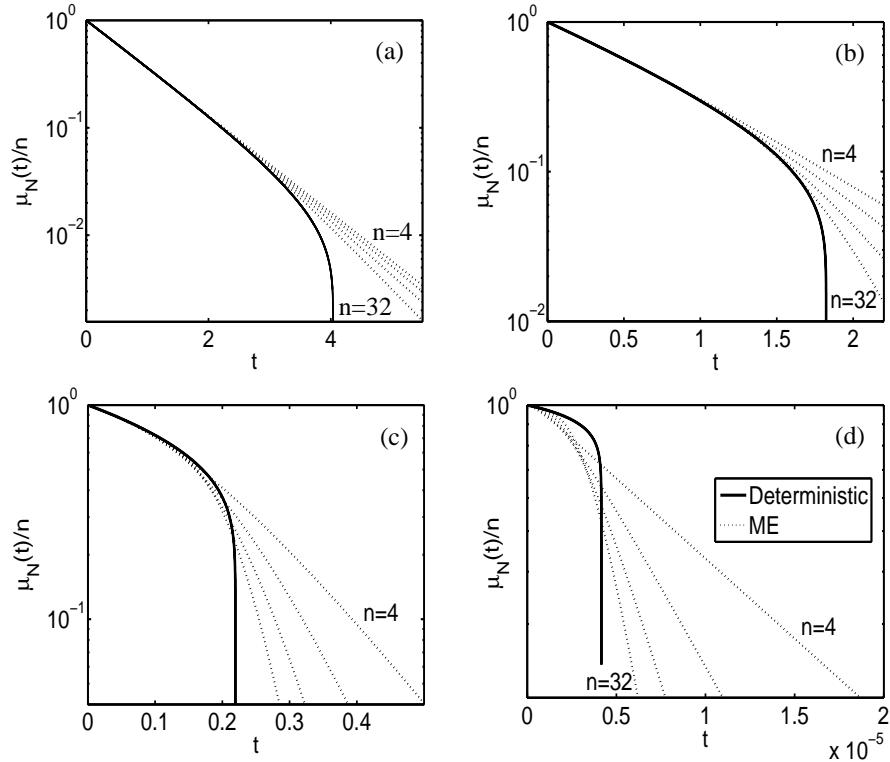


**Figure 3.7:** Plot of  $\mu_N(t)/n$  obtained from the DE (3.2.11) (solid lines), and the exact solution of the ME (3.2.8) realized for  $\gamma = 0$ ,  $n = 4, 8, 16, 32$  and (a)  $f/n = 0.01$ ; (b)  $f/n = 0.1$ ; (c)  $f/n = 1$ ; (d)  $f/n = 10$ .

Theorem 3.2]. When the rates  $r_0 = 0, r_1, \dots, r_n$  form a convex (concave) sequence, let  $r(x)$ ,  $x \in [0, n]$  be any extension of  $r$  from the integers  $0, 1, \dots, n$  to the closed real interval  $[0, n]$  which retains the property of convexity. The differential equation

$$\frac{dx}{dt} = -r(x), \quad x(0) = n,$$

provides a deterministic approximation for a certain death process  $N(t)$ ,  $t \geq 0$  (defined in [122, Chapter 6]). Then,

$$\mu_N(t) \geq (\leq) x(t), \quad (t \geq 0)$$

if  $r_0, r_1, \dots, r_n$  form a concave (convex) sequence. Further, the inequalities are strict for all  $t > 0$  if the sequence  $r_0, r_1, \dots, r_n$  is strictly concave or strictly convex.

Unfortunately, as shown in Fig. 3.8, the result above can only be applied for  $f = 0$ , where the rates are linear, the sequence is both concave and convex, hence the deterministic and stochastic means are the same. In all other cases, the sequence is only convex on the interval  $[1, n]$ . However, the result indicates that the deterministic mean initially overestimates, and terminally underestimates the stochastic mean, as shown in Figs. 3.5 and 3.7.

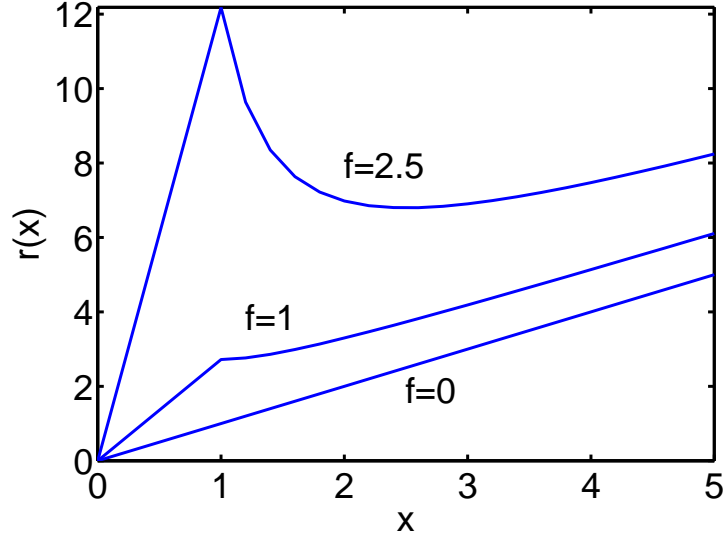


**Figure 3.8:** Continuous extension of the discrete rates  $r_k = ke^{f/k}$ , for  $n = 5$  and  $k = 0, \dots, 5$  to the interval  $\in [0, 5]$ . Line connecting  $r_0 = 0, r_1 = e^f$  for  $x \in [0, 1]$  and  $r(x) = xe^{f/x}$  for  $x \in [1, 5]$ .

### Mean cluster dissociation time

As explained in §1.2.3, most DFS experiments measure the dissociation time  $T_D$  defined in §2.2.2 (2.2.18) as a stochastic variable. We examine the dependence of its mean  $\mu_{T_D}$  (“cluster lifetime”) and variance  $\sigma_{T_D}^2$  on cluster size and applied force, and confirm the three force regimes identified before in cluster dynamics.

Since the stochastic decay of the cluster represents a succession of Poisson processes with time-independent rates  $r_k$ , and as shown in [75], the expected lifetime of the cluster is the sum of the inverses of the rates

$$\mu_{T_D} = \sum_{k=1}^n \frac{1}{r_k} = \sum_{k=1}^n \frac{1}{ke^{f/k}}. \quad (3.3.5)$$

For *small force* ( $\hat{f} \ll 1/n$ ), the lifetime (3.3.5) is well approximated by

$$\mu_{T_D} \approx \sum_{k=1}^n \frac{1}{k} \approx \ln n + \frac{1}{2n} + \Gamma, \quad (3.3.6)$$

in agreement with previous findings [31, 134].

For *intermediate force* ( $1/n \ll \hat{f} \ll 1$ ), the cluster decays slowly for  $k > f$  where we can approximate  $r_k \approx k$ . The decay becomes much faster for  $f/k > 1$ , and the cluster passes rapidly through the states  $k, \dots, 1$ . The lifetime can then be estimated from

$$\mu_{T_D} \approx \sum_{k=f}^n \frac{1}{k} \approx \ln(n/f). \quad (3.3.7)$$

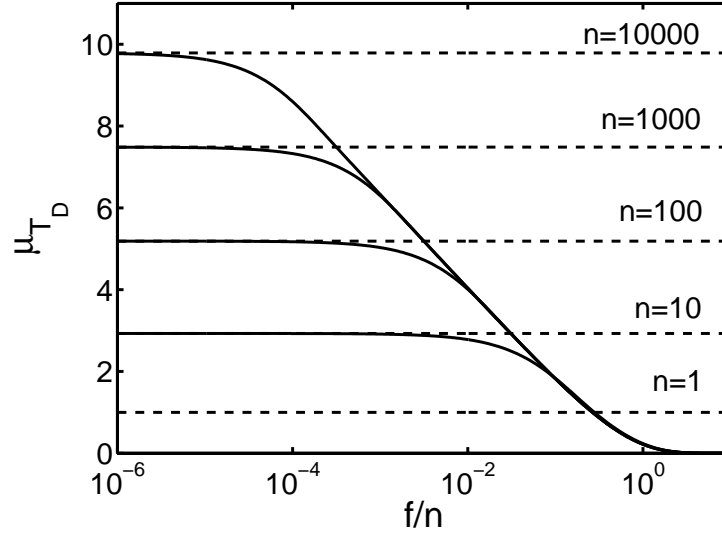


**Figure 3.9:** Cluster lifetime computed from (3.3.5) for the zero- (solid line) and infinite-drag (dashed lines) limits, and for  $h_0 = 1$ ,  $\beta = 1$ ,  $\gamma = 0$ , with  $n = 1, 10, 100, 1000$  and  $10000$ .

For *large force*, the dominant term in (3.3.5) is the one corresponding to the rupture of the first bond so the average lifetime is

$$\mu_{T_D} \approx e^{-f/n} / n, \quad (3.3.8)$$

because after the first bond breaks, all the other ones follow almost instantly.

The variance of the lifetime of the cluster bounded from above

$$\sigma_{T_D}^2 = \sum_{k=1}^n \frac{1}{r_k^2} \leq \sum_{k=1}^n \frac{1}{k^2} \leq \sum_{k=1}^{\infty} \frac{1}{k^2} = \frac{\pi^2}{6}. \quad (3.3.9)$$

This result is particularly useful for clusters with long life, where fluctuations are small compared to the lifetime.

In Appendix 3.B we present estimates for the cluster lifetime obtained from the analysis of the deterministic equation (3.2.11) as done by [31], and we also compare them with the results obtained from the analysis above.

### Limiting values for the mean cluster lifetime

The limiting drag cases provide upper and lower bounds for the mean cluster lifetime  $\mu_{T_D}$ , which are illustrated in Fig. 3.9 as functions of  $f/n$  for clusters having  $n = 1, 10, 100, 1000$  and  $10000$  bonds, respectively. The horizontal dashed lines represent the mean cluster lifetime in the infinite-drag limit, which is force-independent. In the zero-drag limit,  $\mu_{T_D}$  severely diminishes with the increase in force. For finite drag (Chapter 4) and given values of  $f$  and  $n$ , the stochastic mean dissociation time  $\mu_{T_D}$  is located between the values corresponding to the coordinates  $(f/n, n)$  in Fig. 3.9.

### 3.3.2 Vanishing force: role of rebinding

Rebinding can stabilize the decay of the cluster, and for sufficiently small force the bond population may fluctuate about an equilibrium value. In the absence of force, the disk is stationary and system's dynamics are dictated by only cluster dimension and rebinding. In this case the ME (3.2.2) can be solved explicitly for a reflective boundary at  $k = 0$ , and the validity of the FPE approximation (3.2.39) can be examined. The dependence of the cluster's lifetime on  $n$  and  $\gamma$  is also examined.

#### Exact probabilities and cluster dynamics for $f=0$

The deterministic equation (3.3.4) reads

$$\frac{d\mu_N}{dt} = \gamma(n - \mu_N) - \mu_N, \quad \mu_N(0) = n, \quad (3.3.10)$$

which has the solution

$$\mu_N(t) = n \frac{\gamma + e^{-(1+\gamma)t}}{1 + \gamma}. \quad (3.3.11)$$

The solution relaxes exponentially fast to the equilibrium configuration

$$N_{eq} = \lim_{t \rightarrow \infty} \mu_N(t) = \gamma n / (1 + \gamma),$$

predicting an infinite deterministic cluster lifetime.

The analysis of the stochastic birth and death process reveals the key role played by the boundary condition in the cluster's dynamics. For a reflecting boundary at  $k = 0$ ,  $N(t)$  can be viewed as a sum of  $n$  independent and identically distributed random variables, corresponding to single bond clusters. At time  $t$ , a single bond can be either open or closed, with probabilities  $P'_0(t)$  and  $P'_1(t)$ , which satisfy  $P'_0 + P'_1 = 1$  at all times. The corresponding ME for clusters with a single bond is

$$\frac{dP'_1}{dt} = -r_1 P'_1 + g_0 P'_0, \quad P'_1(0) = 1, \quad (3.3.12a)$$

$$\frac{dP'_0}{dt} = -g_0 P'_0, \quad P'_0(0) = 0, \quad (3.3.12b)$$

with  $r_1 = 1$  and  $g_0 = \gamma$ . One can show that (3.3.12) is solved by

$$P'_1(t) = \frac{\gamma + e^{-(1+\gamma)t}}{1 + \gamma}, \quad P'_0(t) = \frac{1 - e^{-(1+\gamma)t}}{1 + \gamma}. \quad (3.3.13)$$

Denoting by

$$q = \frac{\gamma + e^{-(1+\gamma)t}}{1 + \gamma}, \quad (3.3.14)$$

the number of bonds in the single bond cluster is distributed as a Binomial random variable  $B(1, q)$  [122, Chapter 2].

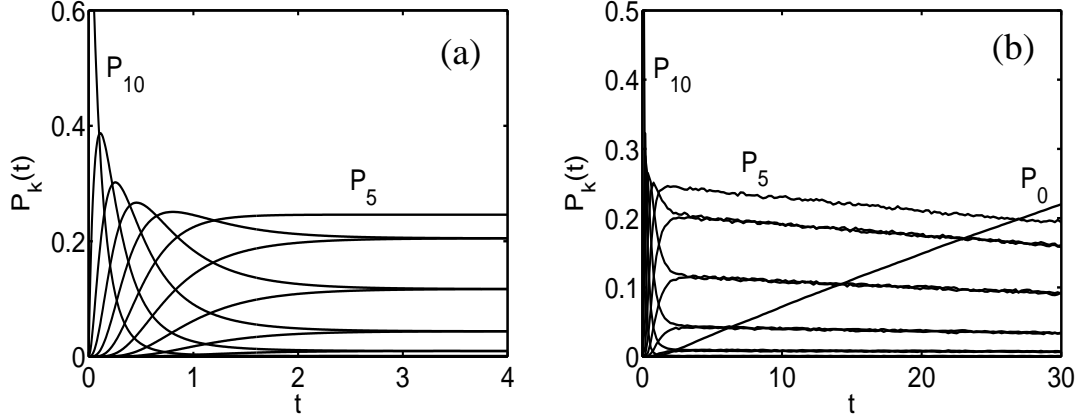


**Figure 3.10:** Probabilities  $P_k(t)$ ,  $k = 0, \dots, n$  where  $n = 10$ ,  $f = 0$ ,  $\gamma = 1$ , realized for (a) reflecting boundary at  $k = 0$  computed from (3.3.15) and (b) absorbing boundary at  $k = 0$  ( $10^5$  simulated trajectories).

Since  $N(t)$  is a sum of  $n$  such processes, it is distributed as  $B(n, q)$  so the ME (3.2.2) is solved by

$$P_k(t) = \binom{n}{k} q^k (1 - q)^{n-k} = \binom{n}{k} \frac{(\gamma + e^{-(1+\gamma)t})^k (1 - e^{-(1+\gamma)t})^{n-k}}{(1 + \gamma)^n}. \quad (3.3.15)$$

The probabilities verify  $\lim_{t \rightarrow \infty} P_k(t) = \binom{n}{k} \frac{\gamma^k}{(1+\gamma)^n}$ , so in the long run the distribution of the bonds in the cluster stabilizes to an equilibrium, as shown in Fig. 3.10 (a). However, as foreseen by Bell, the cluster might dissociate even in the absence of force, if we wait for long enough. This scenario corresponds to an absorbing boundary at  $k = 0$ , where  $P_k(t)$  can no longer be obtained in a closed analytical form. As depicted in Fig. 3.10 (b), all probabilities  $P_k(t)$  for  $k \geq 1$  reach a peak value, after which they vanish in the long run. The only increasing probability is  $P_0(t)$ , as the cluster finally dissociates.

From (3.3.14), the mean and variance of  $N(t)$  are

$$\mu_N(t) = nq, \quad \sigma_N^2(t) = nq(1 - q). \quad (3.3.16)$$

The relative standard deviation  $\sigma_N/\mu_N$  scales as  $\mu_N^{-1/2}$  for all times, thus fluctuation effects decrease with increasing bond number, converging to the stationary state value

$$\lim_{t \rightarrow \infty} \sigma_N/\mu_N = \sqrt{(1 + \gamma)N_{eq}} = \sqrt{\gamma n}.$$

This indicates that larger rebinding not only increases the equilibrium number of bonds, but also decreases the size of the fluctuations around the equilibrium value  $N_{eq}$ .

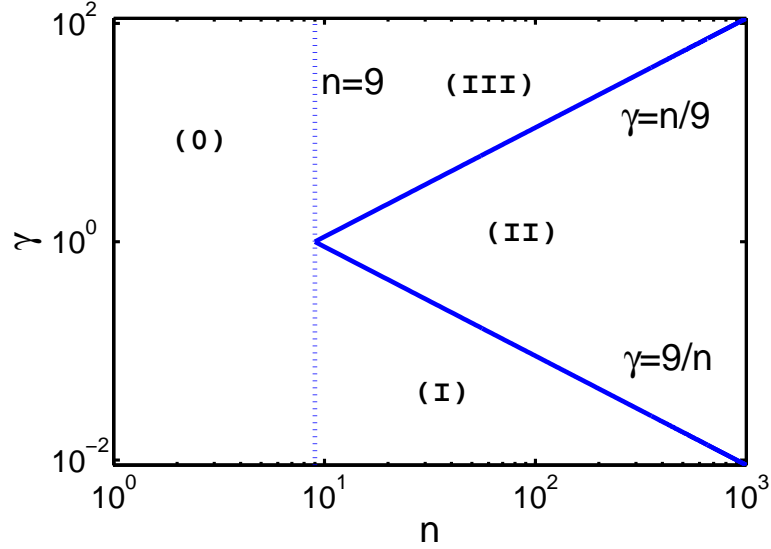


**Figure 3.11:** Domain of validity of the FPE (3.C.2) in the  $(n, \gamma)$  parameter space, computed for values suggested by the criterion (3.C.5). The criterion does not apply in region (0) (left of the dashed line). The FPE is not valid in (I), is valid in  $[t_{min}, \infty)$  in (II) and is valid in the time interval  $[t_{min}, t_{max}]$  in (III), where  $t_{min}$  and  $t_{max}$  can be determined (when real), from (3.C.7).

### Domain of validity of the FPE

It was shown in Fig. 3.4 that the FPE can accurately approximate the solutions  $P_k(t)$  of the (3.2.2), for certain values of force and cluster size, in a limited time-window. For zero-force, one can obtain explicit estimates of the parameter values  $\gamma$  and  $n$  when the FPE is a valid approximation for the FPE, together with the corresponding time-windows. As the argument is rather technical, we just present the parameter map, while the details can be found in Appendix 3.C.

The parameter regions where the FPE approximation is valid are sketched in Fig. 3.11. The criterion does not apply in region (0) (left of the dashed line). The FPE is not valid in (I), is valid in  $[t_{min}, \infty)$  in (II) and is valid in the time interval  $[t_{min}, t_{max}]$  in (III), where  $t_{min}$  and  $t_{max}$  can be determined (when real), from (3.C.7).

### Cluster lifetime

From [138], the mean cluster lifetime absorbing boundary is given by

$$\mu_{T_D} = \frac{1}{\gamma + 1} \left( \sum_{k=1}^n \frac{1}{k} + \sum_{k=1}^n \binom{n}{k} \frac{\gamma^k}{k} \right). \quad (3.3.17)$$

This equation is a polynomial of order  $n - 1$  in  $\gamma$ , and for  $f = 0$  we recover the result from (3.3.5). The dependence of  $\mu_{T_D}$  on  $\gamma$  and  $n$  is depicted in Fig. 3.12 (a) and (b). For

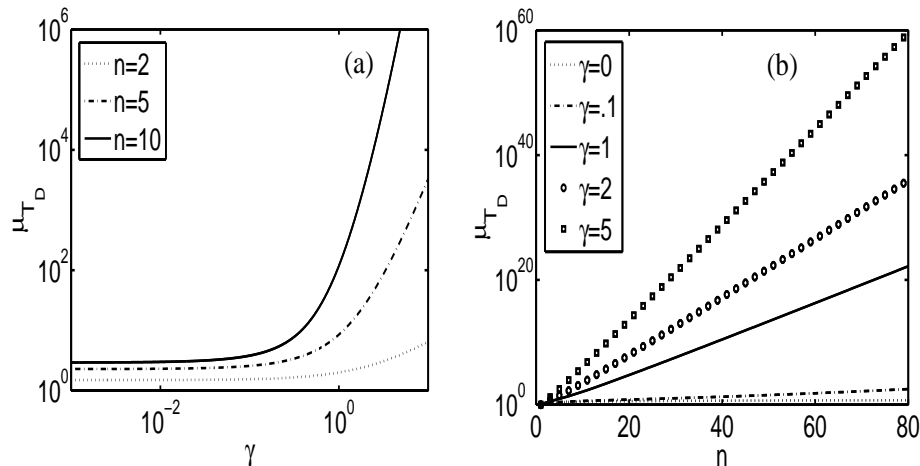


**Figure 3.12:** Cluster lifetime  $\mu_{T_D}$  from (3.3.17), plotted as a (a) function of  $\gamma$ ; (b) function of  $n$ .

$\gamma < 1$  the cluster lifetime grows logarithmically with cluster size, for moderate values of  $n$ . The increase of  $\mu_{T_D}$  with the cluster size is much faster (exponential) for  $\gamma > 1$ .

### 3.3.3 Finite force, finite rebinding

Force destabilizes the cluster, while rebinding stabilizes it again. In the context of adhesion clusters it was shown by Bell [10], that a cluster of bonds remains stable up to a critical force denoted by  $f_c$ , which can be determined theoretically or from experiment. In general, the probabilities  $P_k(t)$  can be obtained from stochastic simulations or from the direct solution (3.2.8) which involves the matrix exponential. Explicit solutions can be obtained for  $n = 2, 3$  [31], but these become complicated for larger values of  $n$ .

#### Critical force

The critical force that destabilizes a cluster of size  $n$  can be estimated from the deterministic equation (3.2.11). Denoting by  $N_{eq}$  the value of  $\mu_N$  at equilibrium (when  $d\mu_N/dt = 0$ ), we can write (3.2.11) as

$$N_{eq}e^{f/N_{eq}} = -\gamma(n - N_{eq}). \quad (3.3.18)$$

At small force  $f$ , (3.3.18) has two roots, the larger one corresponding to a stable equilibrium, as shown in Fig. 3.13 (a). As force increases, a saddle-node bifurcation occurs. Above the critical force no roots exist and the cluster becomes unstable. Exactly at critical loading, the two roots collapse, the slopes of the right- and left-hand side of (3.3.18)

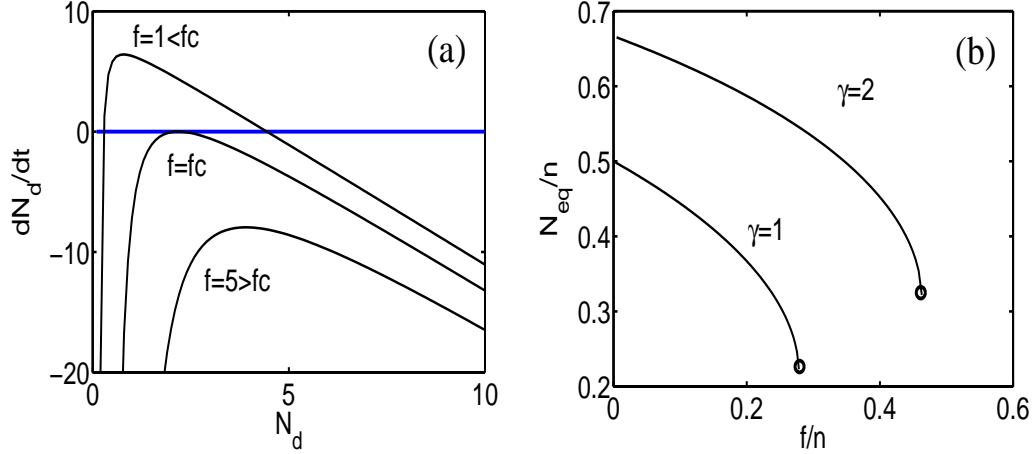


**Figure 3.13:** (a)  $dN_d/dt$  as a function of  $N_d$ , computed from (3.2.11). For forces  $f < f_c$  two steady states exist, which merge at  $f = f_c$  and vanish for  $f > f_c$ . Plot realized for  $n = 10$ ,  $\gamma = 1$ , and  $f_c \simeq 2.7846$  obtained from (3.3.20). (b) Number of closed bonds at equilibrium as a function of  $f/n$ , obtained from (3.3.18) for  $n = 10$ . For  $f \leq f_c$  there is a unique real solution, while for  $f > f_c$  there is no real solution (cluster disintegrates). Circles represent critical force and cluster size, respectively.

become equal, so by differentiating (3.3.18) we obtain

$$e^{f_{eq}/N_{eq}} \left( 1 - \frac{f_{eq}}{N_{eq}} \right) = -\gamma. \quad (3.3.19)$$

Solving the system (3.3.18) and (3.3.19), the critical values for force and number of closed bonds are obtained as

$$f_c = n \text{pln} \left( \frac{\gamma}{e} \right), \quad N_c = n \frac{\text{pln} \left( \frac{\gamma}{e} \right)}{1 + \text{pln} \left( \frac{\gamma}{e} \right)}, \quad (3.3.20)$$

where  $\text{pln}(a)$  is defined as the solution  $x$  of  $xe^x = a$ .

From the deterministic point of view, the cluster behaviour can be summarized as follows: for  $f \leq f_c$  we have  $N(t) \rightarrow N_c$ , while for  $f > f_c$  the cluster dissociates in finite time. We shall see below, that the stochastic behaviour of the cluster is strongly influenced by the boundary condition at  $N = 0$ , which is reflective if  $g_0 = \gamma n$ , or absorbing if  $g_0 = 0$  (rebinding no longer possible once the state  $N = 0$  is reached).

### Reflecting and absorbing boundaries

The mean number of bonds  $\mu_N(t)$  is illustrated in Figs. 3.14 and 3.15, for a reflecting and an absorbing boundary at  $N = 0$ , respectively. In both figures, the means computed from the FPE (3.2.35a) and the deterministic equation (3.2.11) are superposed.

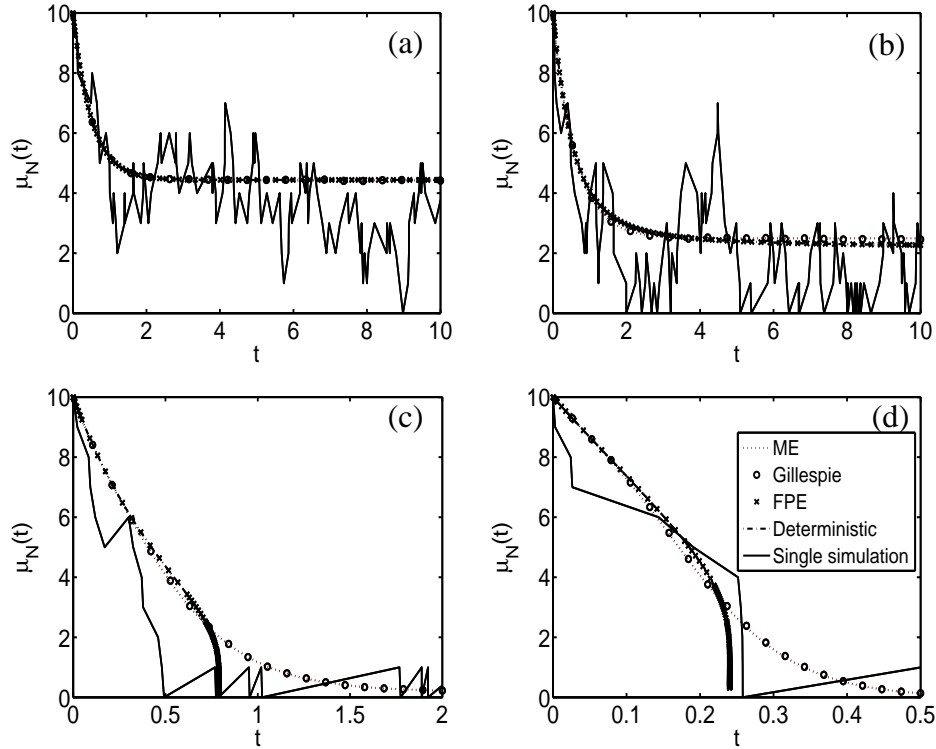


**Figure 3.14:** Comparison of single simulation trajectory with  $\mu_N(t)$  obtained from the FPE (3.2.35a), DE -  $N_{eq}$  (3.2.11), ME (3.2.2) and average of  $10^4$  trajectories for  $n = 10$ ,  $\gamma = 1$  and (a)  $f = 1$ ; (b)  $f = f_c \simeq 2.78$ ; (c)  $f = 5$ ; (d)  $f = 10$ , for a reflecting boundary at  $k = 0$ .

The reflecting boundary is the natural boundary for the deterministic equations (3.2.11) and (3.2.35a), as one can see in Fig. 3.14. For subcritical force  $f < f_c$  (Fig. 3.14 (a)) all methods agree, and the single trajectory fluctuates about the predicted equilibrium. Starting from the critical force  $f = f_c$  depicted in Fig. 3.14 (b), deterministic results deviate from the stochastic solutions, and for supercritical force  $f > f_c$  they predict an increasingly abrupt collapse with the increase in  $f$ , as seen in Figs. 3.14 (c) and (d).

The absorbing boundary case is plotted in Fig. 3.15. The deterministic equations are formulated for a reflecting boundary, so significant deviations from the stochastic mean (which predicts dissociation) arise even for subcritical force, as seen in Fig. 3.15 (a). Starting from  $f = f_c$ , the deterministic mean also predicts cluster dissociation (Fig. 3.15 (b)), but initially overestimates the stochastic results, and then predicts a sudden decay (Figs. 3.14 (c) and (d)). Compared to Fig. 3.5, the difference between the deterministic and stochastic results is enhanced by rebinding.

In summary, the deterministic approximations correctly estimate the number of closed bonds at equilibrium for a reflecting boundary, but fail to predict the cluster disintegration time for  $f > f_c$ . In the large-force limit, the effect of rebinding is negligible.

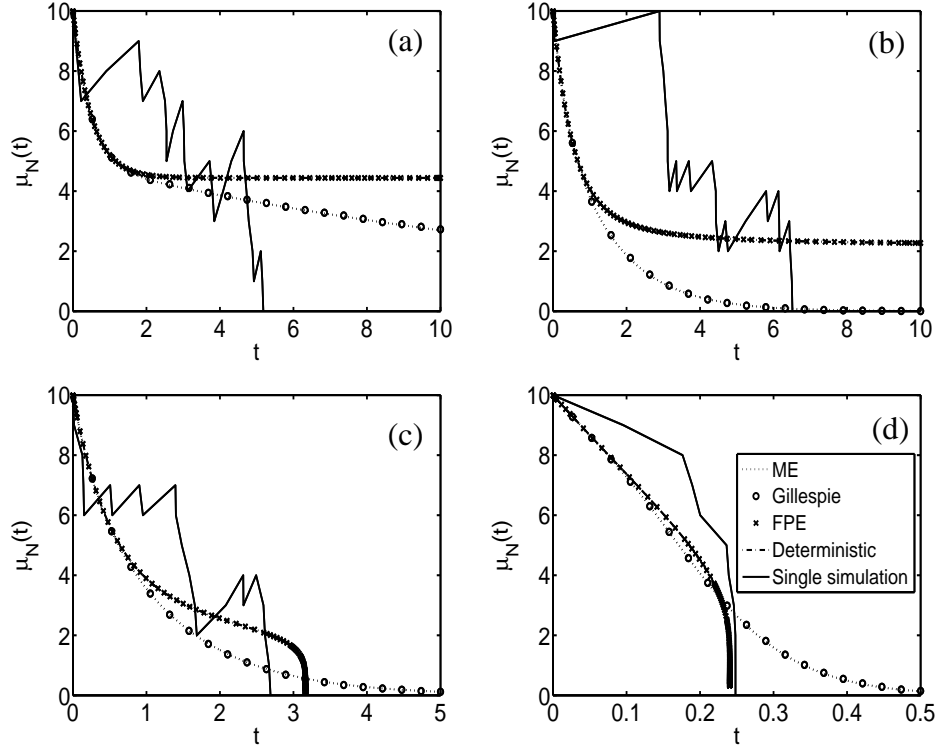


**Figure 3.15:** Comparison between single simulation trajectory and  $\mu_N(t)$  obtained from the FPE (3.2.35a), DE -  $N_{eq}$  (3.2.11), ME (3.2.2) and average of  $10^4$  trajectories for  $n = 10$ ,  $\gamma = 1$  and (a)  $f = 1$ ; (b)  $f = f_c \simeq 2.78$ ; (c)  $f = 5$ ; (d)  $f = 10$ , for an absorbing boundary at  $k = 0$ .

### Cluster lifetime

For an absorbing boundary, the cluster dissociates no matter how large the rebinding is. The average cluster lifetime can even be obtained in a closed form, using the formula of the mean extinction time for a Markov process [138],

$$\mu_{T_D} = \sum_{k=1}^n \frac{1}{r_k} + \sum_{k=1}^{n-1} \sum_{j=k+1}^n \frac{\prod_{i=j-k}^{j-1} g(i)}{\prod_{i=j-k}^j r(i)}. \quad (3.3.21)$$

For  $n = 2$ , (3.3.21) yields

$$\mu_{T_D} = e^{-f} + \frac{e^{-f/2}}{2} + \gamma \frac{e^{-3f/2}}{2}, \quad (3.3.22)$$

In general, one can prove that the average lifetime is a polynomial of order  $n - 1$  in  $\gamma$ , whose leading coefficient is  $\exp(-f/(1 + 1/2 + \dots + 1/n)) / n$ .

In the large number of bonds limit we have  $1 + 1/2 + \dots + 1/n \simeq \ln n$ , so the leading term of the polynomial is  $n^{-(f+1)}$ . For  $\gamma > 1$  and large  $n$ , the lifetime verifies

$$\mu_{T_D} \simeq O\left(\frac{\gamma^{n-1}}{n^{f+1}}\right).$$

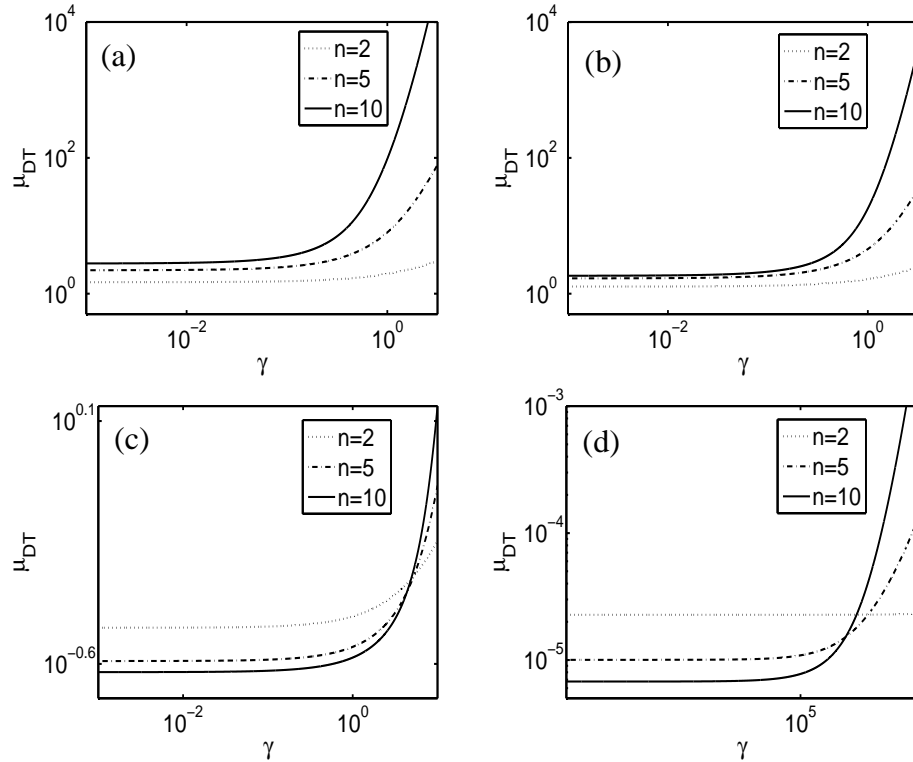


**Figure 3.16:** Cluster lifetime  $\mu_{TD}$  as a function of  $\gamma$  obtained from (3.3.21), for  $n = 2, 5, 10$  and (a)  $f/n=0.01$ ; (b)  $f/n=0.1$ ; (c)  $f/n=1$ ; (d)  $f/n=10$ .

In general, force always affects most strongly those terms of highest order in  $\gamma$ , thus for  $\gamma > 1$ , application of force is therefore an efficient way to reduce average lifetime  $\mu_{TD}$ . For  $\gamma < 1$ ,  $\mu_{TD}$  is dominated by those terms of lowest order in  $\gamma$ , thus here the reduction of lifetime with increasing force is only weakly modulated by rebinding.

In Fig. 3.16 we examine the lifetime of the cluster obtained from (3.3.21), as a function of  $\gamma$ , for constant values of  $f/n$  and various values of  $n$ . For small  $f/n$ , the lifetime of the cluster increases rapidly with  $\gamma$ , and the larger clusters survive for longer, as depicted in Figs. 3.16 (a) and (b). With the increase in force, for small values of  $\gamma$  a switch occurs, and as discussed for vanishing rebinding, larger clusters can dissociate faster than the smaller ones, being the case even for  $f/n = 1$ . However, as depicted in Fig. 3.16 (c), the large clusters can again survive longer than the smaller ones, as rebinding increases. In Fig. 3.16 (d) it is also shown that the value of  $\gamma$  from where this switch back takes place is also not  $f/n$  dependent.

### 3.4 Results for ramped force

The ramped force profile is very common in the DFS experiments [38] earlier discussed in §1.2.3, one of the reasons being that no steady state is possible. The slope  $\mu$  of the linear force  $\mu t$  is usually called *loading rate*. As the coefficients of the ME (3.2.2) are time-dependent, analytical solutions cannot be obtained explicitly, therefore we shall mostly rely on stochastic simulations. In this section we focus on the vanishing rebinding case, and first examine the three loading regimes suggested by the probability profiles as discussed in §3.3.1, and then by the deterministic equation (3.2.11). Decay profiles obtained from averages of stochastic simulations are compared against solutions of the deterministic equation (3.2.13a). In the end we present the evolution of force in single simulations and the rupture force distribution for single and multiple bond clusters.

#### 3.4.1 Loading regimes

As for constant force, the cluster's dynamics under ramped force are also characterized by three-loading rate regimes that we determine below.

##### Probability functions

The analysis of the probabilities  $P_k(t)$  help us describe more clearly the different loading regimes predicted by the analysis of the deterministic equation (3.2.11). The qualitative difference between the probability profiles depicted in Fig. 3.17 suggests considering three loading regimes, defined by the same argument used for Fig. 3.2.

The number of visited states (3.3.3) is used to characterize the three loading regimes, depicted in Fig. 3.18. Solid lines are numerical solutions of the ME (3.2.5), while dotted asymptotes are obtained by cubic spline extrapolation of computed data. For each value of  $n$ , the ME was solved for increasing values of  $\mu$ , and the small-intermediate and intermediate-large force boundaries, were identified using the function

$$D(\mu, t) = \max_{k=0, \dots, n} P_k(t).$$

The loading regions are (I) for  $\#\{D(\mu, t) | t \geq 0\} = n + 1$ , (II) for  $2 < \#\{D(\mu, t) | t \geq 0\} < n + 1$  and (III) for  $\#\{D(\mu, t) | t \geq 0\} = 2$ , where  $\#\{D\}$  denotes the cardinal of set  $D$ .

The scales are not as obvious as for constant force case, depicted in Fig. 3.3. The transition between regions (I) and (II) is made at a small loading rate, which now increases with  $n$  (opposed to the constant force value  $f \sim 1/7$  in Fig. 3.3). On the other hand, the transition between regions (II) and (III) takes place at much higher loading rates, which increase much faster than the constant forces in Fig. 3.3.

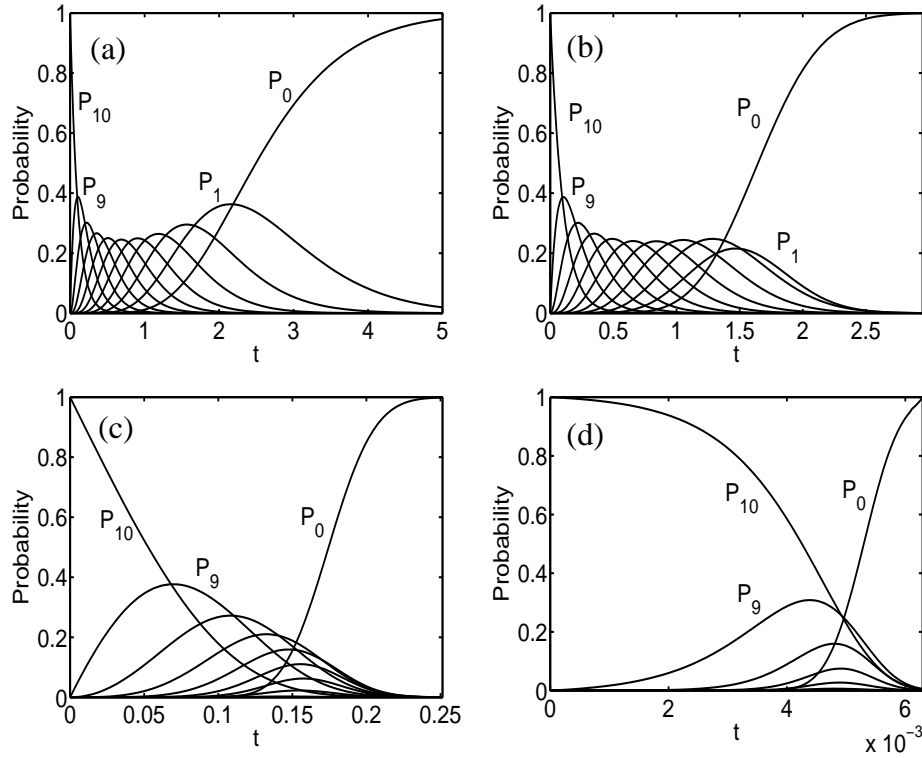


**Figure 3.17:** Probabilities  $P_k(t)$  obtained from the numerical solution of the ME (3.2.2), for  $n = 10$ ,  $\gamma = 0$  and loading rates (a)  $\mu = 0.1$ ; (b)  $\mu = 1$ ; (c)  $\mu = 100$ ; (d)  $\mu = 10000$  (cf Fig. 3.2).

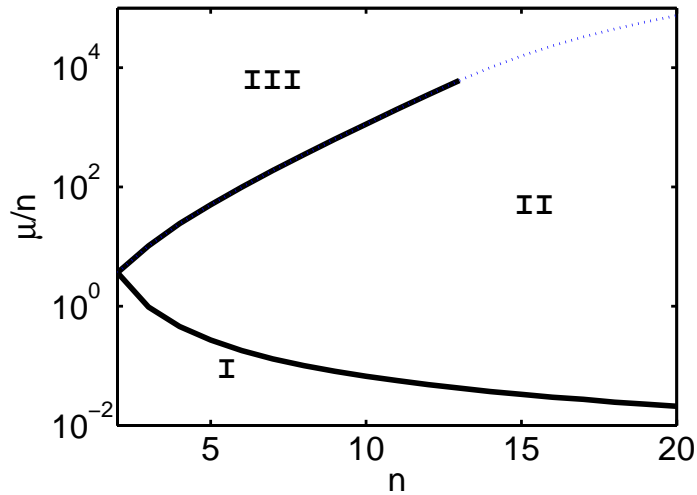


**Figure 3.18:** Loading regimes in the  $(n, \mu/n)$  coordinates, generated by the probabilities  $P_k(t)$  obtained from the numerical solution of the ME (3.2.2) (solid lines). Solid lines represent boundaries computed from the numerical solution of the ME (3.2.5) for various values of  $n$ , while dotted lines are obtained by cubic spline extrapolation of the data. Plot obtained for  $n = 2, \dots, 50$ ,  $\gamma = 0$  reveal the existence of small (I), medium (II), and large loading rate (III) regimes.

### Analysis of the deterministic equation

The analysis of (3.2.11) for linearly ramped force  $f = \mu t$  was first done by Seifert [127]. We present it below to support the empirical findings based on the properties of the probabilities  $P_k(t)$ . For  $\gamma = 0$  the equation reduces to

$$\frac{d\mu_N}{dt} = -\mu_N e^{\mu t / \mu_N}, \quad \mu_N(0) = n. \quad (3.4.1)$$

Considering the auxiliary variable  $u(t) = t / \mu_N(t)$ , (3.4.1) becomes

$$\frac{du}{dt} = \frac{u}{\mu} + u^{\mu t} = u \left( 1 + \frac{1}{t} \right) + u(e^{\mu u} - 1). \quad (3.4.2)$$

The magnitude of the terms of (3.4.2) at different times, reveals the existence of three loading regimes [33], summarized below.

For *slow loading* ( $\mu \ll 1$ ) the cluster behaves similarly to the small constant force case, so we have  $\mu_N(t) = ne^{-t}$ , and since  $T_d$  verifies  $\mu_N(T_d) = 1$ , we have  $T_d \sim \ln n$ .

For *intermediate loading* ( $1 < \mu \ll n$ ) the initial phase is similar to slow loading, and the crossover to fast decay takes place at  $T_d \sim \ln(n/\mu)$ .

For *fast loading* ( $\mu \gg n$ ) the lifetime of the adhesion cluster scales with  $T_d \sim (n/\mu) \ln(\mu/n)$ .

### Cluster decay comparison

The mean number of closed bonds  $\mu_N$  obtained from stochastic simulations, deterministic approximations and the numerical solution of the ME (3.2.2) provide a clear image of the decay profiles of the cluster under various loading regimes. As depicted in Fig. 3.19 (a), the results agree very well for small loading rate, where the cluster decays exponentially. The mean computed from the deterministic equation (3.4.1), starts deviating from the stochastic results even starting from  $\mu = 1$ , as shown in Fig. 3.19 (b), where deterministic results predict a faster decay. As illustrated in Fig. 3.19 (c) and (d), the differences become more pronounced with the increase in  $\mu$ . As expected, the difference between the deterministic and stochastic results is greatest for the largest values of  $\mu$ , but considerably the deterministic equation for  $\mu = 10000$  performs much better than for constant force  $f = 100$ , plotted in Fig. 3.5 (one should also note that the rupture force is about  $\mu t \sim 50$ ).

A specific feature of the cluster's dynamics under ramped force is that even for large loading rates, there is a plateau where the decay is not very significant, followed by a region of rapid decay. The conclusion is that for large loading rates, the longer the clusters survive, the more rapid their final decay phase is.

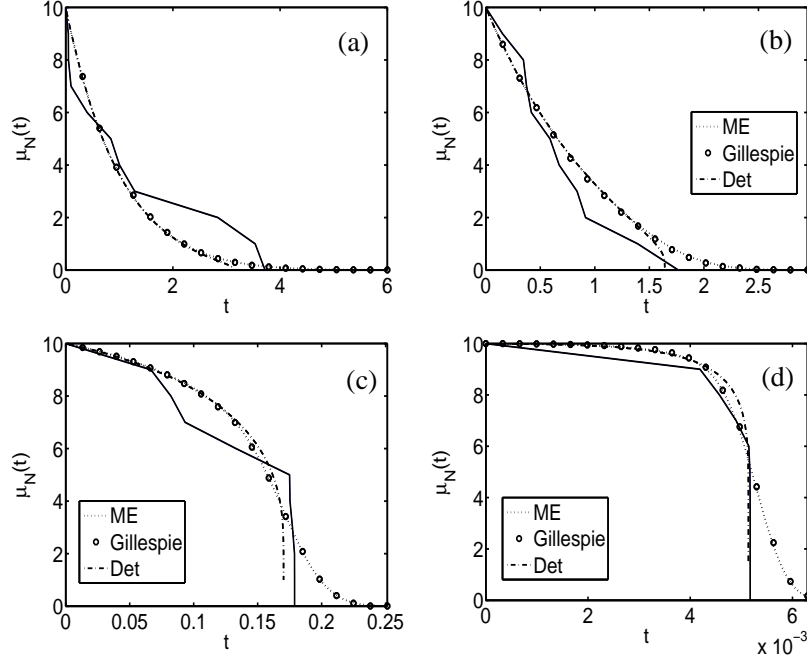


**Figure 3.19:** Comparison between single simulation trajectory and  $\mu_N(t)$  obtained from the DE (3.4.1), ME (3.2.2) and average of  $10^4$  trajectories for  $n = 10$ ,  $\gamma = 0$  and loading rates (a)  $\mu = 0.1$ ; (b)  $\mu = 1$ ; (c)  $\mu = 100$ ; (d)  $\mu = 10000$ .

### 3.4.2 Mimicking DFS experiments

Our model can be easily adapted for mimicking DFS experiments, not only for single bonds, but also for finding the unbinding pathway of the cluster. As discussed in §1.2.3 for single bonds, the notion of rupture force can be extended to clusters, as the force measured when the last bond dissociates.

In accordance with the findings of Merkel *et al.* [95] presented in §1.2.3, bond strength is not only a property of the bond, but is influenced by the loading rate  $\mu$ , as one can see from the evolution of force  $\mu t$  in the rupture of a single bond depicted in Fig. 3.20 (a), for  $\mu = 10$ ,  $\mu = 100$  and  $\mu = 1000$ . Because in the zero-drag limit the relation between force and disk displacement is linear (3.1.1), the disk's trajectory for single bonds can be read directly from the graph. The rupture force histogram illustrated in Fig. 3.20 (b) shows that the spread of rupture forces increases with  $\mu$ .

Our model can also be used to predict unbinding pathways for clusters having multiple bonds. In the zero-drag limit, the disk's displacement is piecewise linear, having slope  $\mu/k$  when  $k$  bonds are connected, as suggested by (3.1.1). This indicates that for multiple bond clusters much larger forces  $\mu t$  are attained, as plotted in Fig. 3.20(a), for  $\mu = 10$ ,  $\mu = 100$  and  $\mu = 1000$ . Despite the added complexity, the rupture force

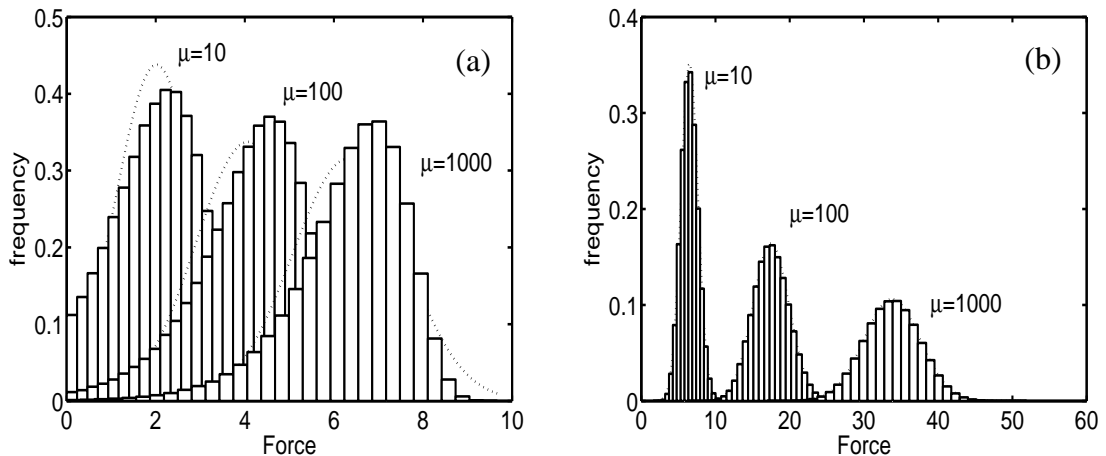


**Figure 3.20:** Cluster rupture force histograms for (a)  $n = 1$ ; (b)  $n = 10$ , computed from  $10^4$  simulated trajectories for loading rates  $\mu = 10, 10^2, 10^3$ . Dotted lines represent a fitted normal density, with the same mean and variance as the simulated data.

histogram illustrated in Fig. 3.20 (b) predicts that the rupture forces are normally distributed.

For comparing the simulated results against experimental data, one should restore the dimensions of time and force, and to use physiological data for the bond properties  $\kappa^*$ ,  $L^*$  and  $k_0^*$ . The role of drag is examined in Chapter 4.

### 3.5 Summary

The drag coefficient  $c$  (2.1.10) spanning several orders of magnitude lead us examine the zero- and infinite-drag limiting cases. It was first established in §3.1 that the disk's movement is solved by  $h(t) = 1 + f(t)/k$  (3.1.1), which is either locally constant for a force  $f$  that is constant, or piecewise linear for linearly ramped force  $f = \mu t$ . The infinite-drag limit was also identified as equivalent to the zero-force subcase of the zero-drag problem. The computation of the transition rates showed that the models proposed by Erdmann & Schwarz [31, 33] can be recovered as the zero-drag limit of our model.

Several methods have been developed specifically for this problem, of which we stress the Fokker-Plank equation (FPE) and the solution of the ME using the matrix exponential. We have established that the FPE (3.2.35a) generally gives better results for the mean and variance of the bond population, than the second order truncation of the deterministic equation (3.2.13), as depicted in Figs. 3.5 and 3.6. The FPE was found to be a good approximation for the solution of the ME (3.2.2) far enough from the boundaries,

over a limited time-window (Fig. 3.4), which depends on the parameter values (Fig. 3.11). Also, the matrix exponential was much more efficient than the brute force solutions of the ME (stiff for large clusters), considerably extending the cluster dimension where useful results can be obtained numerically.

Using the solutions  $P_k(t)$  of the ME (3.2.2) we have confirmed the existence of three forcing (small, intermediate, large) and three loading rate (slow, intermediate, fast) regimes, illustrated in Figs. 3.3 and 3.18, respectively. Our results also provide quantitative estimates for the corresponding boundaries, completing the qualitative descriptions discussed in [31] and [33].

The decay profile of clusters was extensively analyzed for the parameters  $n, f, \gamma, \mu$ . The deterministic decay (3.2.13) overestimates the initial phase, and underestimates the late phase of the decay, computed from stochastic simulations or from the numerical solution of the ME (3.2.2) (Fig. 3.5). The ratio  $f/n$  which completely characterizes the deterministic decay, does not influence the stochastic decay as much, the latter predicting that larger clusters decay faster for same value of  $f/n$  (Fig. 3.7). Larger clusters may again decay slower, for sufficiently large rebinding (Fig. 3.16). The decay of clusters is also strongly influenced by the choice of the boundary condition at  $N(t) = 0$ , as illustrated in Figs. 3.15 and 3.14, for an absorbing and reflecting boundary.

Cluster lifetime strongly depends on force and cluster dimension (Fig. 3.9), or rebinding (Fig. 3.16). Using the stochastic estimations for the mean cluster lifetime, we have established upper and lower bounds for cluster lifetime under drag, which are depicted in Fig. 3.9.

For the constant loading rate problem we have mimicked a DFS experiment, showing that the model is able to predict the rupture force as a function of the loading rate. Also, distributions of the rupture force computed for single and multiple bond clusters have shown an increasing spread with the increase in  $\mu$ , but also, that rupture forces for clusters are normally distributed (see Fig. 3.20). The analysis is completed in Chapter 4, where we examine the dependence of the results on finite drag.

As suggested by the experiments of Merkel *et al.* [95], Brownian effects play an important role especially for slow loading (see Fig. 1.4), so the addition of Brownian noise in the disk-bond system is expected to offer a closer resemblance with the experimental setup. After calibration with data from single bond experiments, our model can be used for a better understanding of the experiments for cluster unbinding.

# Appendix

## 3.A Normally distributed initial condition

---

Different assumptions about the experimental setup require the consideration of several types of initial condition, generated by the position of the disk relative to an equilibrium. In the ideal case when in all experiments the disk starts from the same height, the initial height is sampled from a Dirac distribution centered about the equilibrium position. Since all experiments are subject to error, the initial height is likely sampled from a normal distribution  $\mathcal{N}(h_0, \sigma^2)$ , where  $\sigma > 0$  is estimated from measurements. The role played by the distribution of the initial height is found to be significantly drag-dependent, with an importance ranging from no effect in the absence of drag (rapid jumps of the disk between equilibria), towards the preservation of many features of the initial configuration, in the infinite-drag limit (the disk does not move).

For a given type of initial condition we define the distributions

$$F_k(t, h) = \Pr\{N(t) = k \mid H(t) < h\}, \quad (3.A.1)$$

and the corresponding densities  $p_k(t, h)$ . Following the previous discussions, the densities  $p_k(t, h)$  provide most of the useful information regarding the cluster.

### 3.A.1 The zero-drag limit

In the zero-drag limit, the disk with  $k$  bonds attached to it rapidly moves to the equilibrium height  $h_{k,eq} = 1 + f/k$ , and only after this moment bond's rupture takes place. The time-dependent probability functions can be converted straightaway into (time, height) coordinates, as

$$p_k(t, h) = \delta(h - h_{k,eq})P_k(t), \quad (3.A.2)$$

so the initial condition does not affect the cluster's dynamics.

### 3.A.2 The infinite-drag limit

In the infinite-drag limit, the initial condition plays a key role, as the applied force is totally annihilated by the drag (the disk motion is negligible). The parameters involved in this limit are  $n$ ,  $\beta$  and the distribution  $N$ . Despite its simplicity, this case is an interesting limit case for the general problem. As shown previously, the rupture rates are time-independent (but height-dependent instead). Not surprisingly, they are also force-independent, since in this case the bonds do not 'feel' the force. An analytical formula for the probability functions can be obtained in this case, in both time and height coordinates.

#### Densities $p_k(h, t)$

Starting from a fixed initial height, the population of closed bonds keeps an unchanged length, with height dependent rates. In the absence of rebinding, the cluster is subject to a *linear death process*, with the rates

$$r_k(h) = ke^{\beta(h-1)}, \quad k = 0, \dots, n, \quad h > 0, \quad (3.A.3)$$

representing the decay rate of the cluster of  $k$  bonds at height  $h$ . For convenience we shall denote by  $\beta_h = e^{\beta(h-1)}$  the decay rate of an individual bond at height  $h$ . The general solution for a linear death process of individual death rate  $\beta_h$ , is computed as shown in [75, Chapter 6], to obtain

$$\Pr\{N(t) = k, H(t) = h\} = \binom{n}{k} e^{-k\beta_h t} \left(1 - e^{-\beta_h t}\right)^{n-k}. \quad (3.A.4)$$

When the initial condition is sampled from a normal distribution  $\mathcal{N}(h_0, \sigma)$ , the initial values of the joint densities are

$$p_k(0, h) = \begin{cases} \frac{1}{\sigma\sqrt{2\pi}} e^{-\frac{(h-h_0)^2}{2\sigma^2}}, & \text{if } k = n; \\ 0 & \text{if } k \leq n - 1. \end{cases} \quad (3.A.5)$$

Assuming the bonds start evolving from an un-stretched position, the situation  $h_0 = 1$  is considered.

The probability densities are given by

$$p_k(t, h) = p_n(0, h) \binom{n}{k} e^{-k\beta_h t} \left(1 - e^{-\beta_h t}\right)^{n-k}, \quad (3.A.6)$$

where  $p_n(0, h)$  comes from the initial density at height  $h$ ,  $\binom{n}{k}$  from the way we choose the  $k$  closed bonds out of the initial  $n$ ,  $e^{-k\beta_h t}$  is the decay rate of the cluster with  $k$  closed bonds, and  $\left(1 - e^{-\beta_h t}\right)^{n-k}$  from the evolution of the  $(n - k)$  bonds left open.

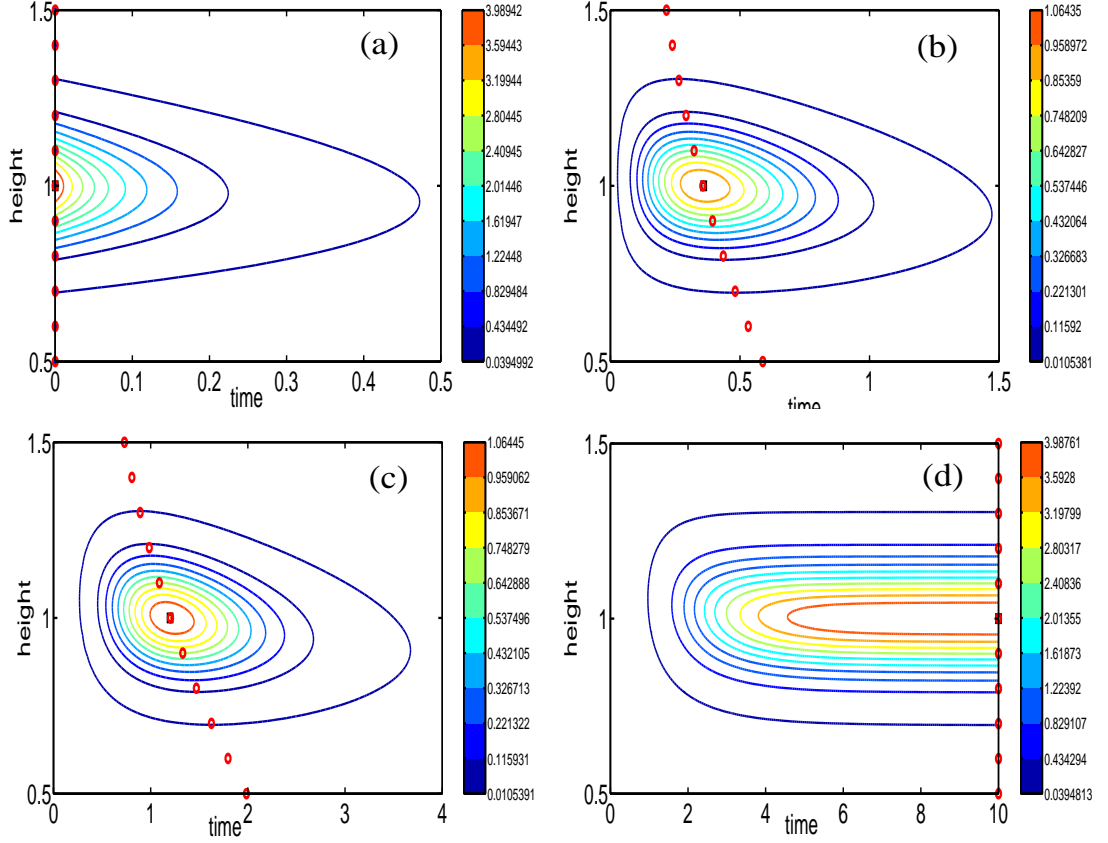


**Figure 3.21:** Probability densities  $p_k(t, h)$  obtained from the exact formula (3.A.6), for  $n = 10$ ,  $\beta = 1$ ,  $h_0 = 1$ ,  $\sigma = 0.1$ , with the initial condition (3.A.5) and (a)  $k = 10$ ; (b)  $k = 7$ ; (c)  $k = 3$ ; (d)  $k = 0$ . The position in the  $(t, h)$ -space of the global maximum of  $p_k(t, h)$ , is marked with squares, while the position of the peak  $p_k(t, h)$  for given values of  $h$  is marked with circles.

Fig. 3.21 reveals the existence of several types of densities  $p_k(0, h)$  for  $k = 0, \dots, n$  with distinct geometric properties. First, an initial phase, in which the  $p_n(h, t)$  decays with time, with a velocity depending on  $h$  (Fig. 3.21 (a)). For  $1 \leq k \leq n - 1$ ,  $p_k(h, t)$  resembles a peak which moves to the right as  $k$  decreases (Figs. 3.21 (b) and (c)). Finally,  $p_0(h, t)$  increases back to the value  $p_n(h, 0)$ , as  $t \rightarrow \infty$ .

For each value of height  $h$ ,  $p_k(t, h)$  peaks at time

$$t_k(h) = \frac{-\ln(k/n)}{\beta_h}, \quad (3.A.7)$$

and has the magnitude

$$p_k(t_k(h), h) = p_n(0, h) \binom{n}{k} k^k (n-k)^{n-k}. \quad (3.A.8)$$

The densities  $p_k(t, h)$  attain a global maximum for the value of  $h$  maximizing  $p_n(0, h)$ , as observed in Fig. 3.21 (b) and (c).

### Cluster lifetime and decay

As seen before for the zero-drag limit (3.3.5), the expected cluster lifetime for a displacement of the disk  $h$ , can be computed from the formula

$$\mu_{T_{Dh}}(h) = \sum_{k=1}^n \frac{1}{r_k(h)} = \sum_{k=1}^n \frac{1}{ke^{\beta(h-1)}}. \quad (3.A.9)$$

Averaging over all heights the expected lifetime of the cluster can be obtained from formula

$$\begin{aligned} \mu_{T_D} &= \int_{-\infty}^{\infty} \mu_{T_{Dh}}(h)_{c=\infty} p_n(h, 0) dh = \int_{-\infty}^{\infty} \sum_{k=1}^n \frac{1}{ke^{\beta(h-1)}} \frac{1}{\sigma\sqrt{2\pi}} e^{-\frac{(h-1)^2}{2\sigma^2}} dh \\ &= \sum_{k=1}^n \frac{1}{k} e^{\beta^2\sigma^2} \int_{-\infty}^{\infty} \frac{1}{\sigma\sqrt{2\pi}} e^{-\frac{(h-1-\beta\sigma^2)^2}{2\sigma^2}} dh = \left( \sum_{k=1}^n \frac{1}{k} \right) e^{\beta^2\sigma^2}. \end{aligned} \quad (3.A.10)$$

The mean time until absorption scales once again with the harmonic number  $H_n = \sum_{k=1}^n \frac{1}{k}$ . The minimum value  $\mu_{T_D} = \sum_{k=1}^n \frac{1}{k}$ , is obtained when  $\sigma = 0$  (Dirac initial condition), and increases exponentially with the variance  $\sigma^2$ . Due to physical constraints (the lower bound of the initial height is positive, so the variance  $\sigma^2$  is small) we could predict the lifetime of the cluster to be bounded above by  $(\sum_{k=1}^n \frac{1}{k}) e^{\beta^2}$ . One should note that the lifetime of the cluster also increases exponentially with  $\beta^2$ .

The expected number of closed bonds  $E[N(t)]_{c=\infty}$  can be obtained by using the integral formula

$$\begin{aligned} E[N(t)]_{c=\infty} &= \sum_{k=1}^n k P_k(t) = \sum_{k=1}^n k \int_{-\infty}^{\infty} p_k(t, h) dh \\ &= \int_{-\infty}^{\infty} \sum_{k=1}^n k p_n(0, h) \binom{n}{k} e^{-k\beta h t} \left(1 - e^{-\beta h t}\right)^{n-k} dh. \end{aligned} \quad (3.A.11)$$

Following the same steps, the variance  $\text{Var}[N(t)]_{c=\infty}$  is obtained as

$$\text{Var}[N(t)]_{c=\infty} = \sum_{k=1}^n k^2 P_k(t) - \left( \sum_{k=1}^n k P_k(t) \right)^2 = n \int_{-\infty}^{\infty} p_n(0, h) e^{-\beta h t} \left(1 - e^{-\beta h t}\right) dh. \quad (3.A.12)$$

When  $\sigma = 0$  and  $h_0 = 1$ , the initial condition verifies  $p_n(0, h) = \delta(h - 1)$ , and we obtain the limiting cases

$$E[N(t)]_{c=\infty} = ne^{-t}, \quad \text{Var}[N(t)]_{c=\infty} = ne^{-t}(1 - e^{-t}). \quad (3.A.13)$$

### 3.B Deterministic and stochastic approximations of cluster lifetime

The estimates for the cluster lifetime obtained from the analysis of the deterministic equation for  $T_d$  (3.2.11) as done by [31], are compared against the results obtained for the mean dissociation time  $\mu_{T_D}$  of the stochastic process, computed from the exact formulas (3.3.5), presented in §3.3.1.

#### Cluster lifetime estimations from (3.2.11)

The cluster's lifetime defined in (2.2.18) can be estimated via a deterministic analysis of (3.3.4) for  $\gamma = 0$ , or via a stochastic analysis of the solution of (3.2.2). The three parameter regimes behaviour of the cluster discovered by Erdmann and Schwarz [31] is supported by a parameter map obtained via stochastic simulations, which helps us determine the region's boundaries.

As seen from (3.3.4), the deterministic decay is determined by  $f/n = \hat{f}$ , and we obtain

$$t(\hat{N}) = \text{Ei}(\hat{f}) - \text{Ei}\left(\frac{\hat{f}}{\hat{N}}\right), \quad (3.B.1)$$

where  $\text{Ei}(z)$  is the exponential integral, defined by  $\text{Ei}(z) \equiv \int_z^\infty e^{-x}/x \, dx$ .

Considering the deterministic cluster lifetime  $T_d$  as the time required to reach the state with one bond attached, this is given by

$$T_d = \text{Ei}(\hat{f}) - \text{Ei}(n\hat{f}), \quad (3.B.2)$$

Using the expansion of  $\text{Ei}(z)$  for different ranges of  $z$ , three forcing regimes relative to the initial number of bonds are identified.

For *small force* ( $\hat{f} \ll 1/n$ ) the small argument expansion of the exponential integral is  $\text{Ei}(z) \approx -\Gamma - \ln z$  (where  $\Gamma = 0.5772$  is Euler's constant) [59], so

$$T_d \approx -\ln \hat{f} + \ln(n\hat{f}) \approx \ln n. \quad (3.B.3)$$

For *intermediate force* ( $1/n \ll \hat{f} \ll 1$ ) we can write (3.B.2) as a sum of two integrals

$$T_d = \int_{\hat{f}}^1 \frac{e^{-x}}{x} \, dx + \int_1^{n\hat{f}} \frac{e^{-x}}{x} \, dx. \quad (3.B.4)$$

Since  $x > 1$ , the second integral is bounded from above by  $1/e$ , while in the first integral we can expand the integrand for small arguments to obtain

$$\int_{\hat{f}}^1 \frac{e^{-x}}{x} \, dx \approx \int_{\hat{f}}^1 \frac{1-x}{x} \, dx \approx \ln\left(\frac{1}{\hat{f}}\right).$$

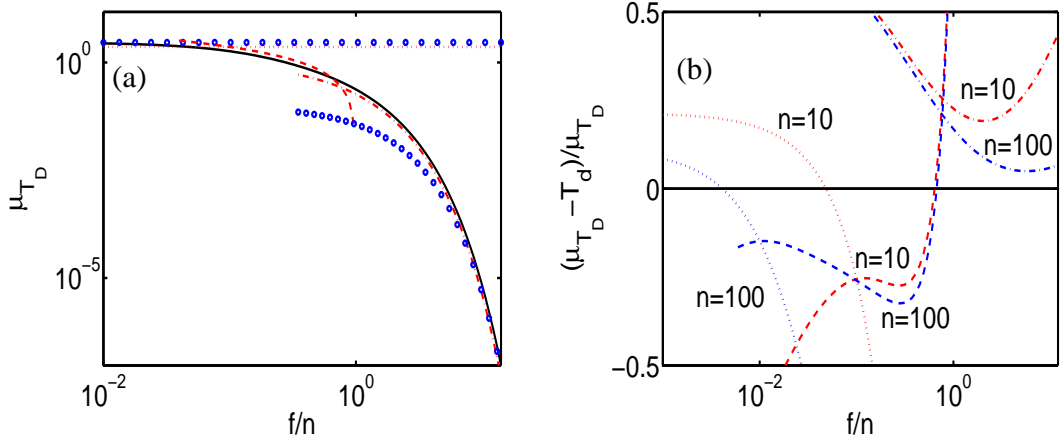


**Figure 3.22:** (a) Plot of  $\mu_{T_D}$  (3.3.5) (solid line), as a function of  $f/n$  for  $n = 10$ , compared against deterministic approximations for small (3.B.3) (dotted line), medium (3.B.5) (dashed line) and large force (3.B.6) (dash-dotted line). The horizontal circles represent the approximation for small force (3.3.6), while the circles in the lower part of the figure the large force approximation (3.3.8); (b) Relative error  $(\mu_{T_D} - T_d)/\mu_{T_D}$  as a function of  $f/n$ , for  $n = 10$  and  $n = 100$ .

Under the assumption that  $\hat{f} \ll 1$ , the second integral in (3.B.4) can be neglected and we obtain the scaling

$$T_d \approx -\ln(\hat{f}) = \ln(1/\hat{f}). \quad (3.B.5)$$

Because  $\hat{f} \ll 1$ , both exponential integrals in (3.B.1) can be replaced by the small argument approximation as long as  $\hat{f} \lesssim \hat{N}$ , so the cluster will decay exponentially in its initial phase until the force per bond reaches  $\hat{f} \lesssim \hat{N}$ . When  $\hat{f}/\hat{N} > 1$ , cluster dissociation will be faster and the overall cluster lifetime scales is a function of the scale  $\hat{f}$ , as opposed to zero-force situation given by (3.B.3).

For *large force* ( $\hat{f} \gg 1$ ) the second term in (3.B.2) can be neglected and the large argument approximation for the exponential integral,  $\text{Ei}(x) \approx e^{-x}/(1+x)$  [10], gives the approximation

$$T_d \approx \frac{e^{-f/n}}{1+f/n} \approx \frac{n}{f} e^{-f/n} = \frac{1}{\hat{f}} e^{-\hat{f}}. \quad (3.B.6)$$

The small argument expansion is not possible in any of the two terms of (3.B.1), and the cluster decays faster than exponential over the whole range of time. As in (3.B.5),  $\hat{f}$  is the key parameter and  $T_d$  decreases much faster than exponential with the increase of  $\hat{f}$ . The cluster decay in this parameter region is also called 'catastrophic', since the dissociation of the cluster and the rupture of the first bond take place almost simultaneously, as seen in Fig. 3.22 (a).

### Lifetime comparison: stochastic vs. deterministic

There is a fairly good agreement between the deterministic and stochastic predictions for cluster lifetime, with some notable differences. For small force, the deterministic approximation underestimates the expected lifetime with more than  $\Gamma = 0.57$  (significant for small clusters e.g. for  $n = 10$  and  $f \ll 1$ ,  $T_d = \ln(10) \sim 2.30$ ). For medium force, both approximations predict negative for  $f/n > 1$ . Of course, the  $f/n = O(1)$  range is expected to be the one where the deterministic approximations differ most from (3.3.5). Finally, in the large force regime, the stochastic result does not depend on the ratio  $f/n$ . The two approximations for large force match for  $f \simeq O(n^2)$ , which is important in finding the boundary between the medium and large force regimes.

The lifetime computed from formula (3.3.5) is compared against the deterministic approximations for small, medium and large force in Fig 3.22 (a), for ( $n = 10$ ) bonds. For large force, the stochastic estimate (3.3.7) of formula (3.3.5) is more accurate than the deterministic approximation (3.B.6), for  $f/n \geq n - 1$  (actually for quite large forces) while in the medium-large force ( $n < f < n^2$ ), the deterministic approximation can be used with better results. As depicted in Fig 3.22 (b), their performance improves with the increase in the cluster dimension.

### 3.C Validity domain of the FPE for zero force

---

For vanishing force, the FPE (3.2.39) can also be solved explicitly. It can be easily shown that the mean and variance verify

$$\langle X \rangle = \mu_N = nq, \quad \langle \langle X^2 \rangle \rangle = \sigma_N^2 = nq(1 - q), \quad (3.C.1)$$

so the solution is

$$P(X, t) = \left( 2\pi nq(1 - q) \right)^{-1/2} \exp \left[ -\frac{(X - nq)^2}{2nq(1 - q)} \right]. \quad (3.C.2)$$

Fig. 3.23 illustrates a good agreement between solutions of the FPE and the ME, especially 'far enough' from the boundaries. If  $n$  is large enough, the skew of the distribution is not too great. If a suitable continuity correction is used [44], a good approximation to the binomial distribution  $B(n, q)$  is given by the normal distribution

$$B(n, q) \sim \mathcal{N}(nq, nq(1 - q)). \quad (3.C.3)$$

The approximation generally improves as  $n$  increases, and we have to decide whether  $n$  is large enough, and  $q$  is far enough from the extremes of zero or one [17].

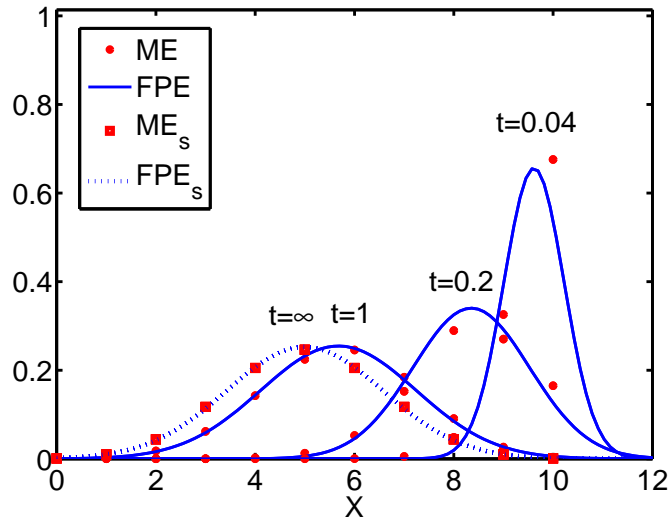


**Figure 3.23:** Solutions  $P_k(t)$  of the master equation (3.2.2) obtained from (3.2.8), are compared against the FPE approximations  $P(k, t)$  (3.2.38), for  $n = 10$  and  $\gamma = 1$ . The legend also contains  $ME_s$  and  $FPE_s$  which represent the stationary solutions (3.3.15) and (3.3.2).

The normal approximation in (3.C.3) is adequate only if

$$\mu_N \pm 3\sigma_N = nq \pm 3\sqrt{nq(1-q)} \in [0, n]. \quad (3.C.4)$$

This explains why the FPE approximation was working far enough from the boundaries. The approximation (3.C.4) is in fact a consequence of the central limit theorem [75]. Simple manipulations show that (3.C.4) is equivalent to

$$\frac{9}{n+9} \leq q(t) \leq \frac{n}{n+9}, \quad (3.C.5)$$

which also shows that it may only be applied for  $n \geq 9$ . As  $q(0) = 1$  does not verify (3.C.5), we expect the normal approximation not to work in the initial phase. It is worth then to check whether (3.C.5) is verified at least for the stationary distribution, where  $q(\infty) = \gamma/(1+\gamma)$ . With these notations, (3.C.4) is verified if

$$\frac{9}{n} \leq \gamma \leq \frac{n}{9}. \quad (3.C.6)$$

One could then ask which is the time window where the approximation is valid, which can be obtained from (3.C.5) as a function of  $n$  and  $\gamma$ . As  $q(t)$  is decreasing between 1 and  $\gamma/(1+\gamma)$ , we obtain the following situations

- If the r.h.s of (3.C.6) is false, then the r.h.s of (3.C.5) is false, which indicates that the FPE is not valid at all;

- If (3.C.6) is true, there is  $t_{\min} > 0$  verifying

$$q(t_{\min}) = \frac{n}{9},$$

and the FPE is valid on  $[t_{\min}, \infty)$ ;

- If the l.h.s of (3.C.6) is false, there are  $t_{\max} > t_{\min} > 0$  verifying

$$q(t_{\min}) = \frac{n}{9}, \quad q(t_{\max}) = \frac{9}{n},$$

and the FPE is valid on the time interval  $[t_{\min}, t_{\max})$ .

Using the definition(3.3.14), the times  $t_{\min}$  and  $t_{\max}$  can be obtained explicitly from

$$t = -\frac{\ln\left((1+\gamma)q - \gamma\right)}{1+\gamma}. \quad (3.C.7)$$

For the values  $n = 10$  and  $\gamma = 1$  plotted in Fig. 3.23, we are in the second situation, and the FPE is accurate in the time window  $t \in [1.47, \infty)$ .

## Cluster dynamics under finite drag

THE LIFETIME and decay profiles of the cluster vary significantly between the zero- and infinite-drag limits, when considering a cluster attached to a rigid disk in a fluid environment, as shown in Chapter 3. In this Chapter we examine the role of finite drag in the stochastic dynamics of the disk-bond system, under constant and linearly ramped force.

Constant loading in cell adhesion represents a good approximation for situations where the physical properties of the adhesion site do not change much during the lifetime of the adhesion cluster. This is the case with the adhesions of endothelial cells or the adhesion of white blood cells when they have been arrested in the bloodstream. In other cases of interest, the force exerted on adhesion clusters is not a constant but varies in time, as during the build-up of force at newly formed contacts in migrating cells, or during the rolling adhesion phase of the leukocyte cascade. Also, the most commonly used profile for the dissociating force in DFS experiments initiated by Evans & Ritchie is the ramped force [38], which has the advantage of shortening bond's lifetime to an appreciable degree.

We first sketch some trajectories of the disk for various values of drag and force, and then analyze distributions of the dissociation time and final extensions of the cluster. For the particular case of no rebinding, some analytical formulae obtained for various probability functions (e.g. the probability to have  $k$  closed bonds at time  $t$ ) are used to validate the stochastic simulations. For non-zero drag, we employ a phase plane analysis to obtain information about the critical force regimes, and identify the critical forces require to destabilize the cluster.

Bonds tend to survive longer in the presence of drag, but under constant loading rate, force also increases with time, generating a very abrupt decay in the terminal phase of cluster's dissociation. We examine how our model captures this feature, and analyze

the cluster's decay and lifetime as functions of loading rate and drag. We also simulate a DFS experiment for single and multiple bond clusters for non-zero drag in §4.2, and compare the results against the ones obtained in Chapter 3 and in [95].

A global description of the joint-time-height densities of having  $k$  bonds is examined in §4.3, in the framework of a differential Chapman Kolmogorov equation (dCKE) (4.3.1), as suggested by Lipniacki [91]. This PDE, which seeks to capture the nonlinear evolution of the piecewise deterministic Markov process, is solved using the method of characteristics, and is tested against stochastic simulations. The agreement of the two solutions for large drag indicate that the approach may be valid in some circumstances, but the disagreement for small values of drag suggests that either the Markov process cannot be formulated as a PDE, or our numerical method is not accurate for the given problem. To address this issue we derive an integro-differential equation for the evolution of the probability density (4.3.14), in §4.3.4.

The Chapter is laid out as follows. In §4.1 we examine the case of constant force in the presence of drag, and the force necessary to destabilize the cluster under rebinding. In §4.2 we illustrate the effects of ramped force on the evolution of the system, and simulate data suitable for the analysis of the DFS experiments. A global formulation of the cluster dynamics in terms of a dCKE is attempted in §4.3. The implications of our results are discussed in §4.4. This Chapter is followed by an Appendix.

## 4.1 Constant force

---

In this section we study the evolution of clusters of biological bonds under constant force and drag. We first examine trajectories of the disk under various values of force and drag and then analyze distributions of cluster lifetimes and extensions. Analytical formulae for probabilities are used to validate the results obtained by stochastic simulations, and then cluster decay profiles and lifetimes are analyzed, using both deterministic and stochastic methods. For the problem with rebinding, we derive the force necessary to destabilize the cluster, and compute the bond population and disk displacement at equilibrium.

The disk's motion between events is solved using Matlab<sup>®</sup> ode45s ode solver, to ensure the accuracy of the simulations. The integration of the deterministic approximation (2.2.23) is performed using Matlab<sup>®</sup> stiff ode solver ode15s with relative and absolute tolerances of  $10^{-7}$  and  $10^{-8}$ , respectively. These values ensure that the solver does not fail to converge in the final abrupt decay of  $N_d$ , in the absence of rebinding.

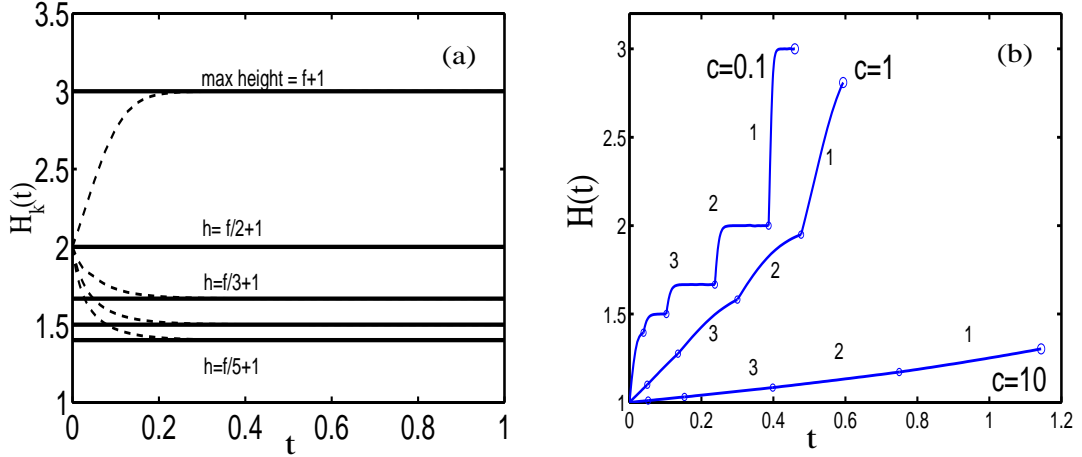


**Figure 4.1:** (a) Disk's displacement  $H_k(t)$  (dashed lines) with  $k = 1, \dots, 5$  bonds attached (2.1.9), towards the equilibrium heights (4.1.2) (solid lines), for  $f = 2$ ,  $h_0 = 2$ ,  $\beta = 1$ ,  $c = 1$ , in the absence of rupture. (b) Displacement of the disk in the  $(t, h)$ -plane, for  $n = 5$ ,  $f = 2$ ,  $h_0 = 1$ ,  $\beta = 1$ , and  $c = 0.1, 1, 10$ , as the bonds break. The circles represent the rupture coordinates.

#### 4.1.1 Preliminaries: local and global motion of the disk

Drag and force significantly affect disk's motion between events and individual trajectories, indicating the existence of distinct patterns in the system's dynamics.

##### Disk trajectories as function of drag

For a constant force  $f$  and number of bonds  $k \geq 1$ , the disk moves deterministically along the solution curves  $H_k(t)$  of (2.1.9)

$$\frac{dh}{dt} = -\frac{1}{c}h^3[kh - (f + k)], \quad h(0) = h_0, \quad (4.1.1)$$

where  $c$  is a drag coefficient (2.1.10), which converge asymptotically towards the value

$$h_{eq,k} = \frac{f}{k} + 1, \quad (4.1.2)$$

while for  $k = 0$  the disk moves freely under the influence of the dissociating force. The equilibrium curves satisfy  $h_{eq,n} \leq h_{eq,n-1} \leq \dots \leq h_{eq,1}$ , so the more bonds attached, the lower the equilibrium position is, as shown in Fig. 4.1 (a).

As suggested by (4.1.1), drag sets the time-scale for reaching the equilibria and the six orders of magnitude it spans generates significant variations between the profile of individual trajectories. For large drag, the disk barely moves (depending on force and number of bonds), and ruptures occur before the disk changes position significantly. For very small values of drag the disk motion has a staircase profile, and the bonds rupture when the disk is stationary at the equilibrium, as seen in Fig. 4.1 (b).

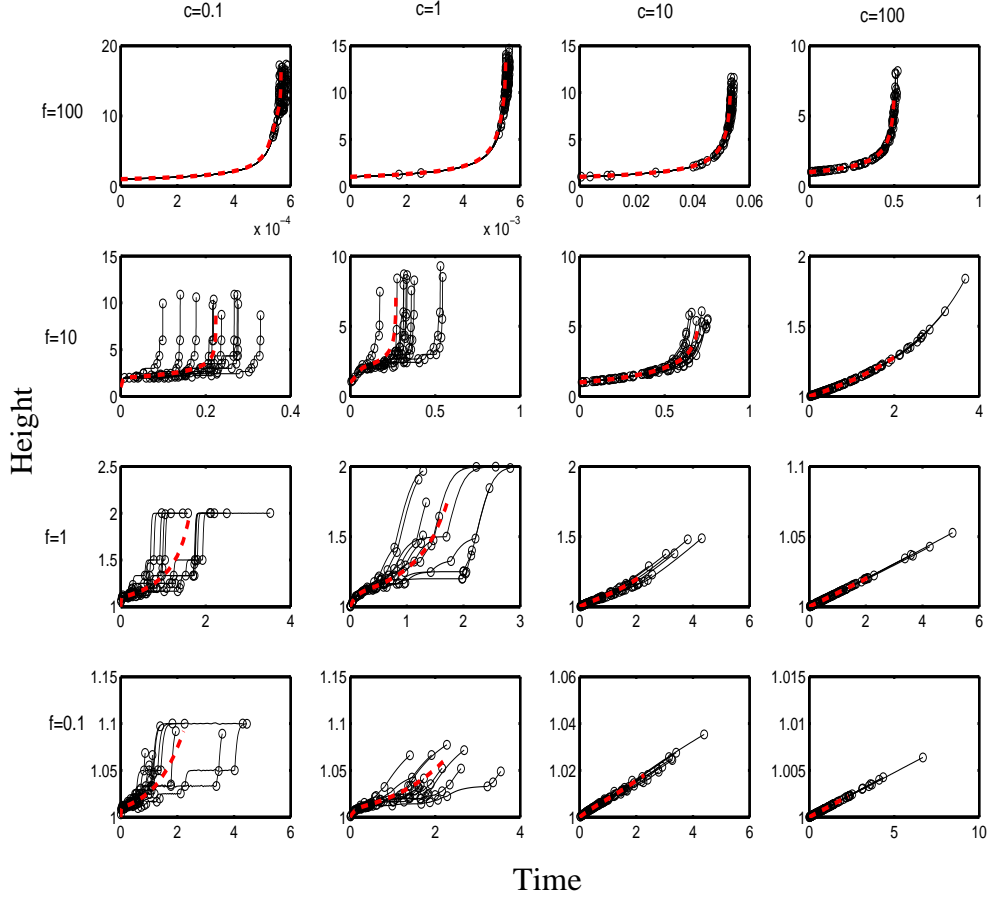


**Figure 4.2:** Plot of 10 individual trajectories of the disk (solid lines) in the (time, height)-plane, for  $n = 10$  bonds,  $f = 0.1, 1, 10, 100$  and  $c = 0.1, 1, 10, 100$ . The circles indicate the position of the rupture events, while the dashed line represents the deterministic approximation (2.2.23).

### Disk trajectories in the $(c, f)$ -plane

In Fig. 4.2 we plot individual trajectories of the disk in the (time, height)-space, realized for various values of  $f$  and  $c$ , against solutions of the deterministic approximation (2.2.23), integrated until  $N_d(T_d) = 1$ . The disk's displacement is negligible for small force/large drag, and can be significant for large forces. Fig. 4.2 suggests the existence of distinct regions in the  $(c, f)$  parameter space. In certain cases ( $f \gg c, c \gg f$  or  $f \simeq c \gg n$ ), simulated trajectories differ little from the deterministic approximation, sometimes being even able to estimate accurately cluster's dissociation time and height ( $c = 1, f = 100$ ). In other cases, individual trajectories show wide variation about the deterministic approximation, which is unable to capture the large variations of the stochastic breakup times ( $c = 0.1, f = 1$ ) or cluster extensions ( $c = 1, f = 1$ ).

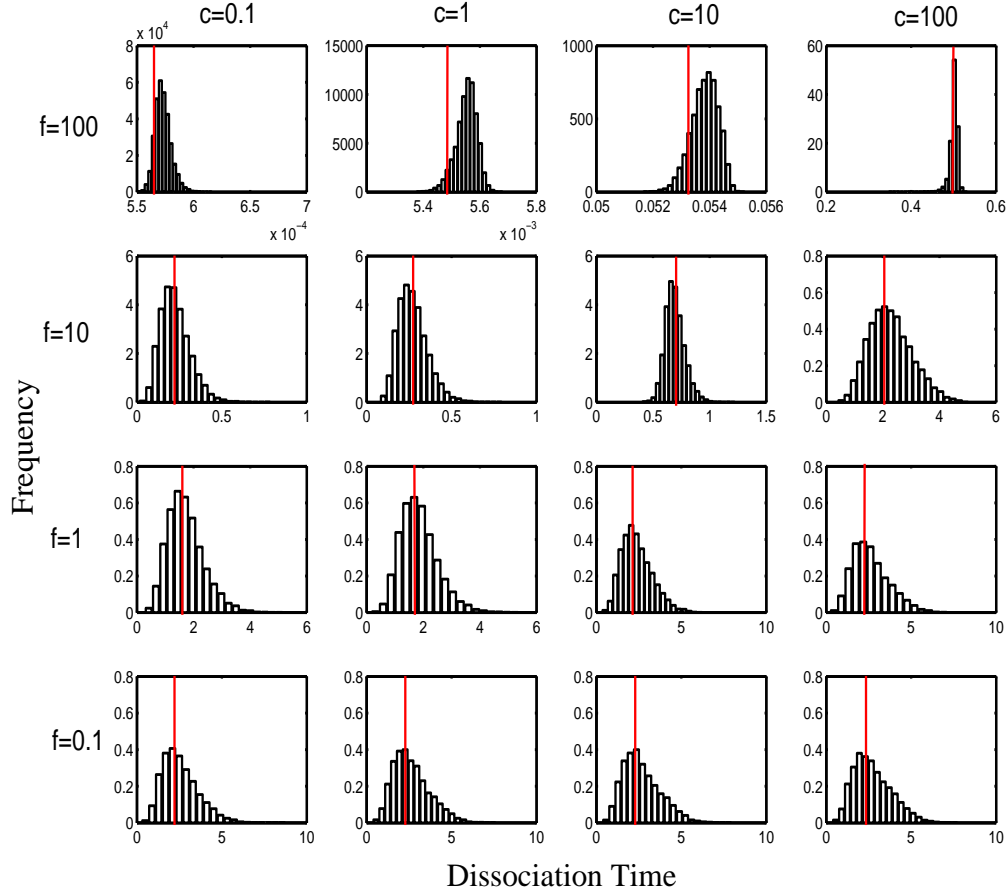


**Figure 4.3:** Histograms of simulated cluster dissociation times  $T_D(t)$  realized for  $n = 10, h_0 = 1, \beta = 1, f = 0.1, 1, 10, 100$  and  $c = 0.1, 1, 10, 100$ , obtained from  $10^4$  single trajectories. Horizontally, the red vertical lines represent the times  $T_d$  obtained from  $N_d(T_d) = 1$  in (2.2.23).

### Distribution of the dissociation times

The distribution of the corresponding dissociation times  $T_D$  obtained from stochastic simulations is plotted in Fig. 4.3, against solutions of the deterministic approximation (2.2.23). For small force ( $f = 0.1$ ) the distributions depend little on drag. At the same time, the dissociation of the cluster happens over a wide time interval, as in the case of vanishing force, where the bonds' rupture is entirely caused by thermal fluctuations. As force increases, the time interval where the cluster dissociates shifts to smaller values and becomes narrower. Increasing drag for large force ( $f = 100$ ), the distributions  $T_D$  dramatically shrink and shift to the left.

The deterministic lifetime  $T_d$  obtained by solving  $N_d(T_d) = 1$  in (2.2.23), is generally in good agreement with the the mean of  $T_D$ , with notable exceptions for  $f = 100, c = 1, 10$ .

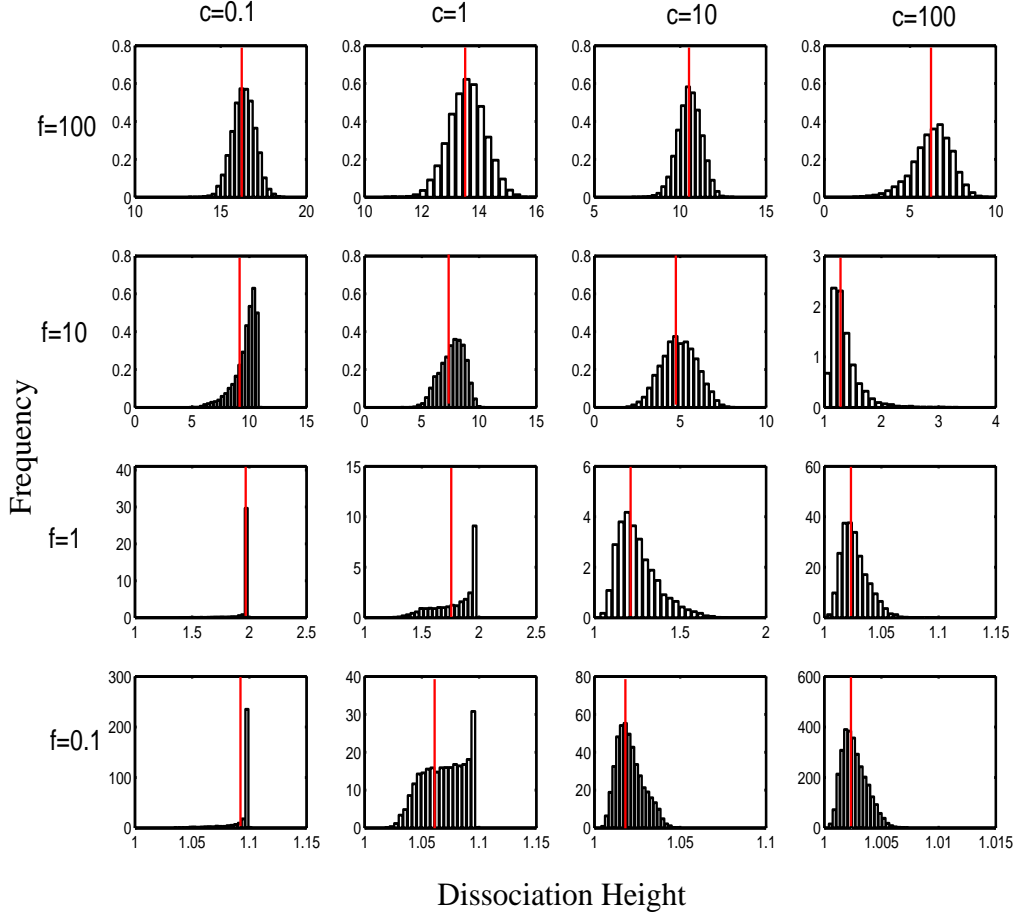


**Figure 4.4:** Histograms of simulated cluster dissociation height  $H_D(h)$  of a cluster realized for  $n = 10, h_0 = 1, \beta = 1, f = 0.1, 1, 10, 100$  and  $c = 0.1, 1, 10, 100$ , obtained from  $10^4$  single trajectories. Horizontally, the red vertical lines represent the deterministic height  $H_d(T_d)$ , solved from  $N_d(T_d) = 1$  in (2.2.23).

### Distribution of the dissociation height

The dissociation height  $H_D$  is plotted in Fig 4.4. For small values of force and drag, the disk jumps to the next equilibrium  $h_{eq,k}$  before the  $k$ -th bond breaks, so the dissociation height is approximately  $h = h_{eq,1}$  (Fig. 4.4,  $c = 0.1, f = 0.1, 1$ ). This suggests that for any  $f > 0$ ,  $H_D$  converges to  $\delta(h - 1 - f)$  in the zero-drag limit (this is not obvious in our figure, as for  $f = 10, 100$  a much smaller  $c$  is needed). As drag increases,  $H_D$  shifts towards 1 and shrinks as seen for  $f = 0.1$  Fig. 4.4, approaching  $\delta(h - h_0)$  in the infinite-drag limit.

The deterministic displacement  $H_d(T_d)$  obtained by solving  $N_d(T_d) = 1$  in (2.2.23), is generally in good agreement with the mean of  $H_D$ .

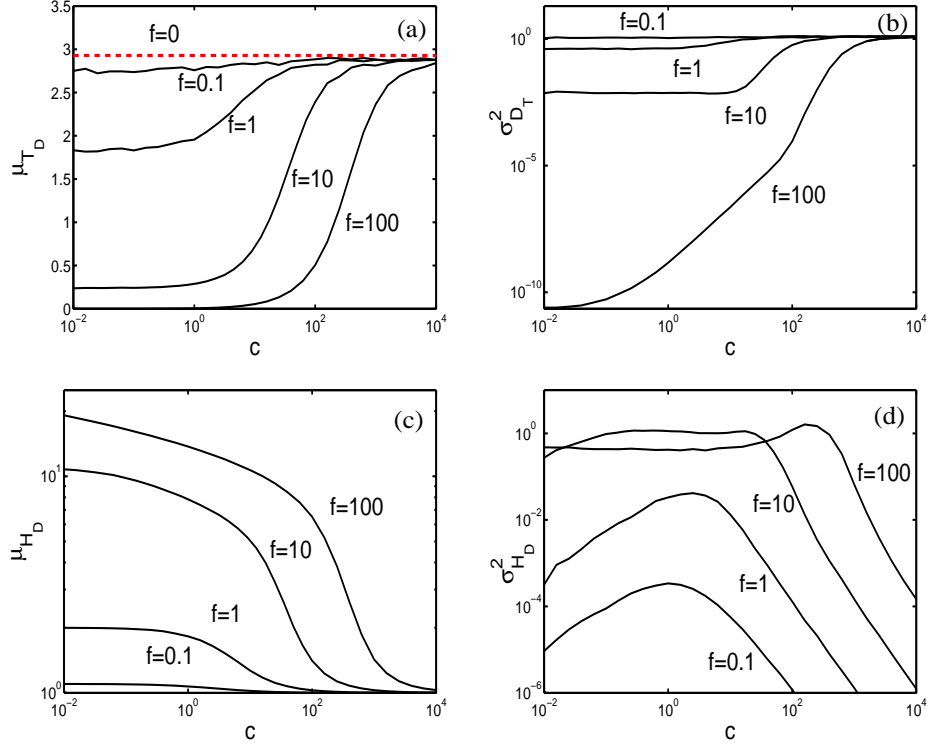


**Figure 4.5:** Statistics of the cluster's rupture for  $n = 10$  bonds, as functions of drag and force, realized from minimum 3000 simulations per  $(c, f)$  point (50 points used for each). (a)  $\mu_{T_D}$ ; (b)  $\sigma_{T_D}^2$ ; (c)  $\mu_{H_D}$ ; (d)  $\sigma_{H_D}^2$ . The dashed line represents results for  $f = 0$ .

### Means and variances of $T_D$ and $H_D$ from stochastic simulations

The means and variances of the random variables  $T_D$  and  $H_D$  defined in §2.2.2 are depicted in Fig. 4.5. For small force,  $\mu_{T_D}$  is drag independent, as in Fig. 4.5 (a). As expected,  $\mu_{T_D}$  is shortened by raising the force force, and increases with drag (for fixed force), being bounded by  $\sum_{k=1}^n \frac{1}{n}$ , as shown in (3.3.6). The variance  $\sigma_{T_D}^2$  indicates that the distribution does not change for small force (as predicted earlier by Fig. 4.3). As force increases, the distributions are initially completely force-dominated for small drag, with all the bonds breaking rapidly in a narrow time region. However, as drag increases, the motion of the disk is slower, and the cluster dynamics are similar to the case of  $f = 0$ , all curves converging to  $\sum_{k=1}^n \frac{1}{n^2}$  (3.3.9), as shown in Fig. 4.5 (b).

The analysis of  $H_D$  confirms that the larger the drag, the smaller the disk's displacement, as illustrated in Fig. 4.5 (c). As suggested by Fig. 4.4, the variance  $\sigma_{H_D}^2$  should vanish at zero drag for any positive force, raise to a maximal value as drag increases, and vanish again as drag approaches infinity, as depicted in Fig. 4.5 (d). The larger the force, the higher the corresponding peak is, and especially for large force, even a small amount of drag can provoke a significant variance in the final displacement.

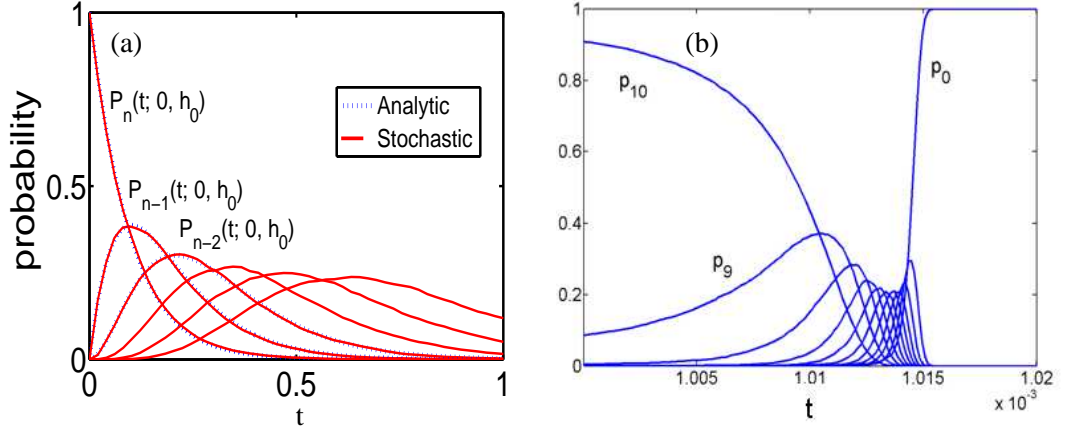


**Figure 4.6:** Probabilities  $P_k(t; 0, h_0)$  for  $n = 10$ ,  $c = 1$ ,  $\beta = 1$ ,  $\gamma = 0$  in the case of (a) low force ( $f/n = 0.1$ ). Analytical solutions (dotted lines) and stochastic simulations (solid lines) obtained for  $10^4$  trajectories; (b) large force  $f/n = 50$  (right) (results obtained from  $10^4$  trajectories).

#### 4.1.2 Testing stochastic simulations against other methods

The stochastic fluctuations in the system can be accurately described in terms of the various types of probability functions described in §2.2.2.

##### Validation of the stochastic simulations

For vanishing rebinding, the probabilities  $P_k(t; 0, h_0)$  (2.2.10) for  $k = 0, \dots, n$  can be obtained analytically (as  $n + 1 - k$ -dimensional integrals, see (4.A.14) in Appendix 4.A) and used to validate the stochastic simulations. For  $k = n, n - 1$  analytical formulae are obtained in Appendix 4.A for the distributions  $F_k(t, h; 0, h_0)$  and densities  $p_k(t, h; 0, h_0)$  of  $P_k(t; 0, h_0)$  over the height coordinate, defined by (2.2.14) and (2.2.16) respectively.

The probabilities  $P_n$ ,  $P_{n-1}$  and  $P_{n-2}$  are evaluated using the integral formulae (4.A.6, 4.A.11, 4.A.13), and compared against their stochastic counterparts in Fig. 4.6 (a).

##### Catastrophic failure of cluster under force and drag

An important result concerns the influence of drag on the behaviour of the probability functions  $P_k(t; 0, h_0)$ . For low force, the rupture events are expected to occur sequentially as in Fig. 4.6 (a), while for large force per bond, Erdmann & Schwarz [31] predict a catastrophic rupture regime sketched in Fig. 3.2 (d), where the only visited states (in the sense discussed in (3.3.3)) are the ones with 0 and  $n$  bonds. As shown in Fig. 4.6 (b), for small drag ( $c = 1$ ), the cluster does not exhibit the catastrophic behaviour anymore, even under large force, at least for the parameter values investigated. However, the length of the time-segment containing the rupture events significantly shrinks.

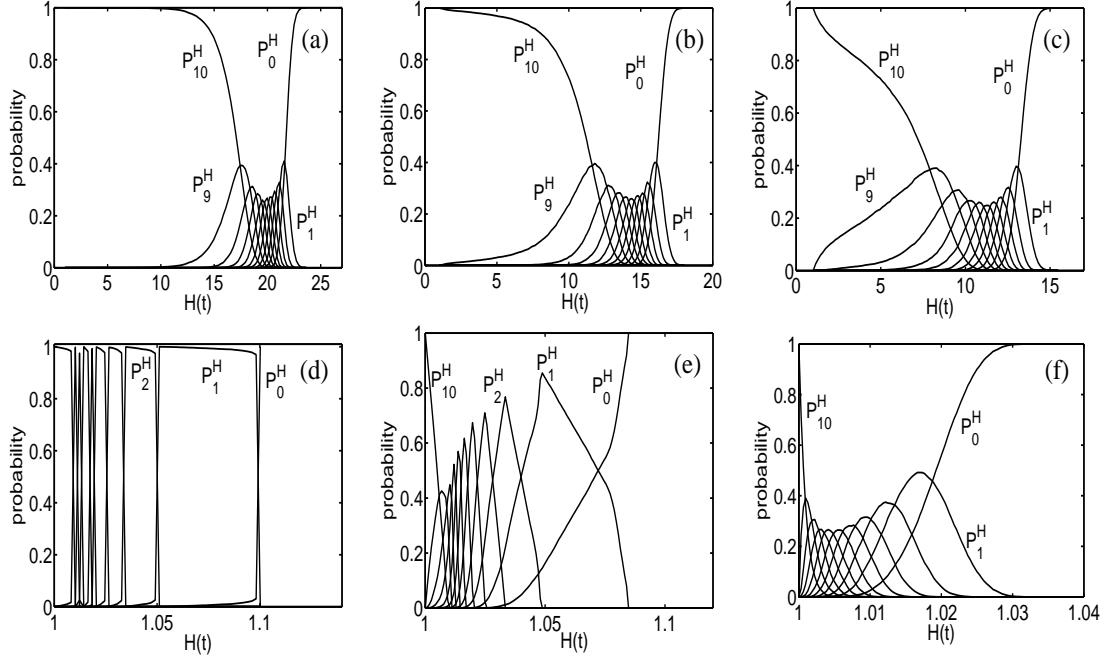


**Figure 4.7:** Probabilities  $P_k^H(h; 0, h_0)$  obtained from  $10^4$  trajectories, for  $n = 10$ ,  $h_0 = 1$ ,  $\beta = 1$ ,  $\gamma = 0$ , and (a)  $c = 0.1$ ,  $f = 500$ ; (b)  $c = 1$ ,  $f = 500$ ; (c)  $c = 10$ ,  $f = 500$ ; (d)  $c = 0.1$ ,  $f = 0.1$ ; (e)  $c = 1$ ,  $f = 0.1$ ; (f)  $c = 10$ ,  $f = 0.1$ .

### The probability of having $k$ bonds at height $h$ : influence of drag and force

We can use stochastic simulations to predict alternative descriptions of the evolving bond-disk system, for example with respect to disk height rather than time.

The probabilities  $P_k^H$  defined in (2.2.13) are illustrated in Fig. 4.7. For large force, the disk rapidly moves over a long range, with all the bonds attached. The rupture of a first bonds is immediately follow by the others, until the cluster disintegrates, as depicted in Fig. 4.7 (a), (b) and (c). As drag increases, the height region where the rupture events occur drifts to smaller values.

In the low-drag-low-force regime depicted in Fig. 4.7 (d), the disk jumps between the equilibrium heights  $h_{eq,k}$  (4.1.2), so each of the probabilities  $P_k^H$  is about 1 inside the segments  $[h_{eq,k+1}, h_{eq,k}]$  for  $k = 1, \dots, n - 1$ . The domains where  $k$  bonds are attached can be easily identified by measuring the length of these intervals. The profiles of the probabilities  $P_k^H$  is significantly altered by the increase in drag, the passage between subsequent states becoming smoother. As one can see in Fig. 4.7 (e), in the intermediate-drag regime the probabilities  $P_k^H$  intersect their neighbors when their value is about  $1/2$ . In the large-drag-low-force regime sketched in Fig. 4.7 (f), there are many overlapped states. In this case the disk barely moves and bonds break under thermal excitation.

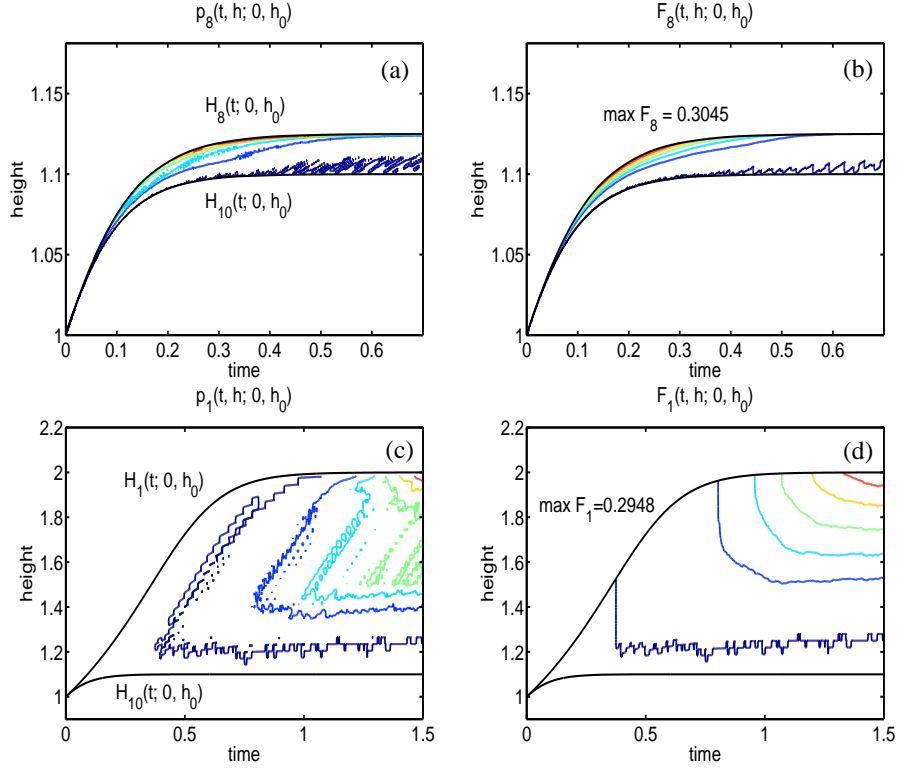


**Figure 4.8:** Densities and cumulative distributions defined in §3.2, obtained for  $n = 10$ ,  $c = 1$ ,  $\beta = 1$ ,  $h_0 = 1$ ,  $\gamma = 0$ , from  $10^4$  simulations. (a)  $p_8(t, h; 0, h_0)$ , (b)  $F_8(t, h; 0, h_0)$ , (c)  $p_1(t, h; 0, h_0)$ , (d)  $F_1(t, h; 0, h_0)$ . Trajectories  $H_k(t; 0, h)$  are solutions of (2.1.9).

### Probability density and cumulative distribution over $h$ of having $k$ bonds at time $t$

The corresponding distributions  $F_k(t, h; 0, h_0)$  and densities  $p_k(t, h; 0, h_0)$  defined in (2.2.14) and (2.2.16), provide a clear image of the way probabilities  $P_k(t; 0, h_0)$  are distributed over the height coordinate. This allows the simultaneous analysis of the most probable rupture times and extensions in the  $(N, H)$  space.

In Fig. 4.8 we examine the time-height probabilistic description of the decay of a cluster having initially 10 closed bonds. As suggested by (4.A.19), the curves  $H_k(t; 0, h_0)$  play a very important role in establishing the region where the distributions change significantly. The profiles of the densities  $p_k$  and distributions  $F_k$  change significantly as the bonds rupture. In the initial phase,  $p_k$  is positive only between  $H_{10}$  and  $H_k$ , and both the distribution  $F_k$  and density  $p_k$  have their peaks near the upper curve, as revealed by Fig. 4.8 (a) and (b). In the terminal phase, the densities expand to the whole area between  $H_{10}$  and  $H_k$  (now much wider), as shown in Fig. 4.8 (c) and (d) and the peaks moves to the right, while still being close to the upper curve  $H_k$ .

We can conclude that for a given cluster, at the moment when the highest probability of having  $k$  closed bonds is attained, the disk is probably situated near the curve  $H_k$ .

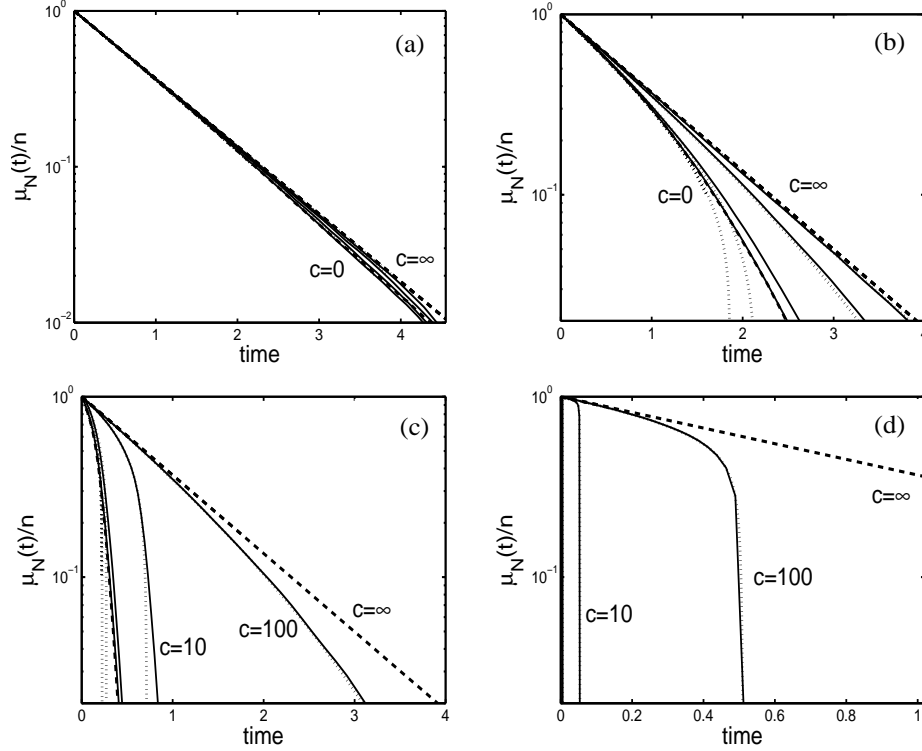


**Figure 4.9:** Normalized decay of the cluster for  $n = 10$  bonds, (a)  $f = 0.1$ ; (b)  $f = 1$ ; (c)  $f = 10$ ; (d)  $f = 100$ . Results from  $10^4$  stochastic trajectories realized for  $c = 0.1, 1, 10, 100$  (solid lines) and  $c = \infty$  (dashed lines), are compared against solutions of the deterministic equations (2.2.23) (dotted lines).

The motion of the disk is however largely force and drag dependent, so the conclusion is valid in this form only for the small force, small drag regime.

### Expected number of closed bonds and variances

Cluster decay, represented by the mean number of bonds  $\mu_N(t)$ , is depicted in Fig. 4.9. As shown in (3.A.13),  $\mu_N(t) = n \exp(-t)$  and  $\sigma_N^2(t) = n \exp(-t) (1 - \exp(-t))$ . Dynamics are similar in the infinite-drag limit, plotted with dashed lines in Fig. 4.9 (a). For intermediate force, the cluster decays faster under small drag, as depicted in Fig. 4.9 (b) and (c). For large force, there is a significant difference in the decay profiles, as illustrated in Fig. 4.9 (d). For small drag, the rupture of the first bond leads to the immediate disintegration of the cluster as a whole. The deterministic decay obtained from (2.2.23) accurately approximates the cluster decay just for small (exponential decay) and large force (either exponential decay, or abrupt rupture of bonds), as shown by Fig. 4.9 (a) and (d). As force increases from 1 to 10, the deterministic decay for  $c = 10$  deviates more from the stochastic value, as depicted in Fig. 4.9 (b) and (c).

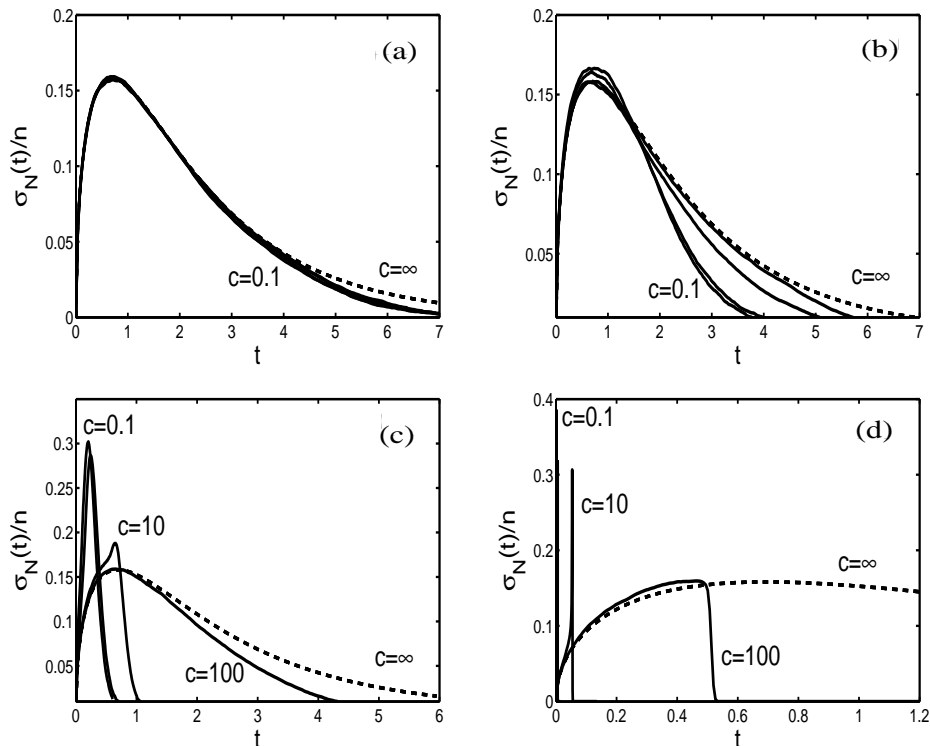


**Figure 4.10:** Evolution of the normalized standard deviation  $\sigma_N(t)/n$  for  $n = 10$  bonds, (a)  $f = 0.1$ ; (b)  $f = 1$ ; (c)  $f = 10$ ; (d)  $f = 100$ . Results from  $10^4$  stochastic trajectories realized for  $c = 0.1, 1, 10, 100$  (solid lines) and  $c = \infty$  (dashed lines) (3.A.13).

The normalized standard deviations for the number of closed bonds,  $\sigma_N(t)/n$ , identifies the times when the rupture of bonds is most intensive. In the small force regime ( $f \ll 1$ ) depicted in Fig. 4.10 (a), the situation is identical for all drag values, and the bonds rupture under thermal excitation. As force increases ( $f \simeq 1$ ), variance profiles begin to differentiate and the higher the drag, the slower the decay is, as sketched in Fig. 4.10 (b). For larger values of force ( $f \simeq 10 \simeq n$ ) we can identify three drag regimes, as shown in Fig. 4.10 (c). For small drag ( $c \ll n$ ), the disk moves reaches a near equilibrium position, when the bonds start breaking rapidly, generating a sharp peak of  $\sigma_N(t)/n$ . For intermediate drag ( $c \simeq n$ ), bonds start dissociating while the disk is still moving. After the disk reaching a critical position,  $\sigma_N(t)/n$  exhibits a sharp peak, suggesting a rapid cluster disintegration. The profile of  $\sigma_N(t)/n$  is now lower and wider, reflecting the dampening of the rupture events intensity, generated by drag on the moving disk. For large drag ( $c \gg n$ ), the bonds break before the disk moves significantly, and the bonds decay smoothly. Finally, for the large force case ( $f \ll n$ ) depicted in Fig. 4.10 (d), the bonds do not “feel” the force, being shielded by drag for a while. Soon after the disk’s displacement increases, the ruptures become very rapid and the cluster dissociates.

### 4.1.3 Non-zero rebinding: Critical force and equilibrium configurations

Force destabilizes the cluster, while rebinding stabilizes it again. In the context of adhesion clusters under constant force, it was shown by Bell that a cluster of bonds remains stable up to a critical force denoted by  $f_c$ , which is to be determined theoretically or from experiment [10]. Here we analyze the force required to destabilize a cluster, and estimate the number of bonds at equilibrium. The computations are largely similar to the ones in §3.3.3.

In this section a phase plane analysis of the deterministic system (2.2.23) is presented. This approach leads to the discovery of analytical formulae for the critical force to destabilize the cluster and the critical initial number of bonds to ensure that a non-zero equilibrium is attained. Also, a stability analysis for the equilibrium configurations is performed.

#### Phase plane analysis

The starting point of this analysis is the deterministic system is (2.2.23), where for convenience, the notations  $x = N_d$ ,  $y = H_d$  are used, along with the physical constraints  $0 \leq x \leq n$  and  $y > 0$ .

In the new notations (2.2.23) gives

$$\begin{aligned} \frac{dx}{dt} &= X(x, y) \equiv -x e^{\beta(y-1)} + \gamma(n-x) e^{\alpha(1-y)}, \\ \frac{dy}{dt} &= Y(x, y) \equiv -(xy^4 - (x+f)y^3)/c. \end{aligned} \quad (4.1.3)$$

The nullclines for (4.1.3) can be written in explicit form as

$$\begin{aligned} \frac{dx}{dt} = 0 : \quad y(x) &= 1 + \frac{1}{\beta + \alpha} \log \left( \frac{\gamma(n-x)}{x} \right), \\ \frac{dy}{dt} = 0 : \quad y(x) &= 1 + \frac{f}{x} \quad (0 < x \leq n). \end{aligned} \quad (4.1.4)$$

The equilibrium configurations  $(x_0, y_0)$  are the solutions of the system satisfy the relations

$$x_0 e^{\frac{f(\beta+\alpha)}{x_0}} = \gamma(n-x_0), \quad y_0 = \frac{f}{x_0} + 1. \quad (4.1.5)$$

The terms of the Jacobian matrix  $\mathbf{J}(x_0, y_0)$

$$\begin{pmatrix} \bar{x} \\ \bar{y} \end{pmatrix}, \quad \mathbf{J}(x_0, y_0) = \begin{pmatrix} X_x(x_0, y_0) & X_y(x_0, y_0) \\ Y_x(x_0, y_0) & Y_y(x_0, y_0) \end{pmatrix},$$

in our case are

$$\begin{aligned}
 X_x &= -e^{\beta(y-1)} - \gamma e^{\alpha(1-y)}, \\
 X_y &= -x \beta e^{\beta(y-1)} - \gamma(n-x) \alpha e^{\alpha(1-y)}, \\
 Y_x &= -\frac{y^4 - y^3}{c}, \\
 Y_y &= -\frac{4xy^3 - 3(x+f)y^2}{c}.
 \end{aligned} \tag{4.1.6}$$

To find the eigenvalues of  $\mathbf{J}(x_0, y_0)$  we solve the equation  $\det(\mathbf{J}(x_0, y_0) - \lambda I_2) = 0$ , which is the quadratic equation

$$\lambda^2 + B\lambda + C = 0, \tag{4.1.7}$$

with the coefficients

$$\begin{aligned}
 B &= e^{\beta(y-1)} + \gamma e^{\alpha(1-y)} + \frac{4xy^3 - 3(x+f)y^2}{c}, \\
 C &= \frac{\left(e^{\beta(y-1)} + \gamma e^{\alpha(1-y)}\right) \left(4xy^3 - 3(x+f)y^2\right)}{c} \\
 &\quad - \frac{\left(x\beta e^{\beta(y-1)} + \gamma(n-x)\alpha e^{\alpha(1-y)}\right) (y^4 - y^3)}{c} = \det \mathbf{J}(x, y).
 \end{aligned} \tag{4.1.8}$$

The discriminant  $\Delta = B^2 - 4C$  of (4.1.7) is defined for  $\{(x, y) \mid 0 \leq x \leq n, y \geq 1\}$  as

$$\begin{aligned}
 \Delta(x, y) &= \left(e^{\beta(y-1)} + \gamma e^{\alpha(1-y)} - \frac{4xy^3 - 3(x+f)y^2}{c}\right)^2 \\
 &\quad + \frac{4\left(x\beta e^{\beta(y-1)} + \gamma(n-x)\alpha e^{\alpha(1-y)}\right) (y^4 - y^3)}{c} > 0,
 \end{aligned}$$

and shows that both roots  $\lambda_1$  and  $\lambda_2$  of (4.1.7) are real for  $(x, y)$  in the specified region.

The coefficients  $B$  and  $C$  satisfy

$$\lambda_1 + \lambda_2 = -B/2, \quad \lambda_1 \lambda_2 = C.$$

Since  $\gamma > 0$ ,  $B$  is always positive, so least one of the eigenvalues values is negative.

For the analysis of  $C$  we also use the second part of (4.1.5) (only having in mind that now  $x = x_0, y = y_0$ ) to obtain (after some computational effort)

$$C = \frac{(x+f)^3 e^{-\frac{f\alpha}{x}}}{x^4 c} \left( (x-f)x e^{\frac{(\beta+\alpha)f}{x}} + x^2 \gamma - f \gamma \alpha n + f \gamma \alpha x \right). \tag{4.1.9}$$

Using the first part of (4.1.5) we have  $x e^{\frac{(\beta+\alpha)f}{x}} = \gamma(n-x)$ , so (4.1.9) is equivalent to

$$C = \frac{\gamma(x+f)^3 e^{-\frac{f\alpha}{x}}}{x^4 c} \left[ \left( n + (\beta + \alpha) f \right) x - f(\beta + \alpha) n \right]. \tag{4.1.10}$$

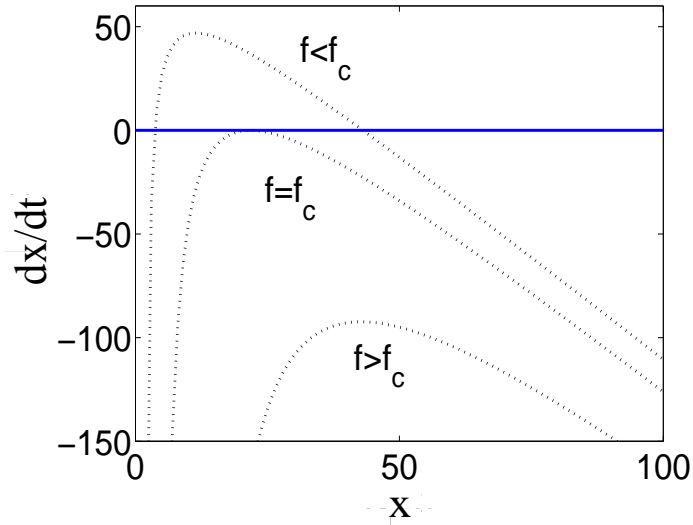


**Figure 4.11:** The derivative of the number of closed bonds  $dx/dt(x, y)$  along the nullcline  $dy/dt = 0 : y = f/x + 1$ , as a function of  $x$ . For forces  $f < f_c$  two steady states exist, which merge at  $f = f_c$  and vanish for  $f > f_c$ . In this figure  $n = 100$ ,  $\beta = 1$ ,  $\alpha = 0.2$ ,  $\gamma = 1$ , where as computed from (4.1.13),  $f_c \simeq 23.2054$ .

The sign of  $C$  (therefore the nature of the equilibrium point) depends on the position of  $x_0$  relative to a critical value denoted by

$$x_{BIF} = \frac{n f (\beta + \alpha)}{n + f (\beta + \alpha)}, \quad (4.1.11)$$

which only depends on  $f(\beta + \alpha)$  and  $n$ . There are three cases.

**Case 1.**  $x_0 > x_{BIF}$ . In this case  $C > 0$  and the roots of (4.1.7) satisfy  $0 > \lambda_1 > \lambda_2$ , so  $(x_0, y_0)$  is a stable node.

**Case 2.**  $x_0 = x_{BIF}$ . In this case  $C = 0$  and the roots of the equation (4.1.7) satisfy  $\lambda_1 = 0 > \lambda_2$ , so  $(x_0, y_0)$  is a degenerate saddle point.

**Case 3.**  $x_0 < x_{BIF}$ . In this case  $C < 0$  and the roots of the equation (4.1.7) satisfy  $\lambda_1 > 0 > \lambda_2$ , with  $|\lambda_2| > |\lambda_1| > 0$ , so  $(x_0, y_0)$  is a saddle point.

### Equilibrium solution - critical force regime

The focus here is to analyze the number of solutions for (4.1.5) in different forcing and drag regimes.

Force destabilizes the cluster, while rebinding stabilizes it again. In the context of adhesion clusters it was shown by Bell that a cluster of bonds remains stable up to a critical force denoted by  $f_c$ , which is to be determined theoretically or from experiment. For the stability analysis it is helpful to examine the equation (4.1.5).

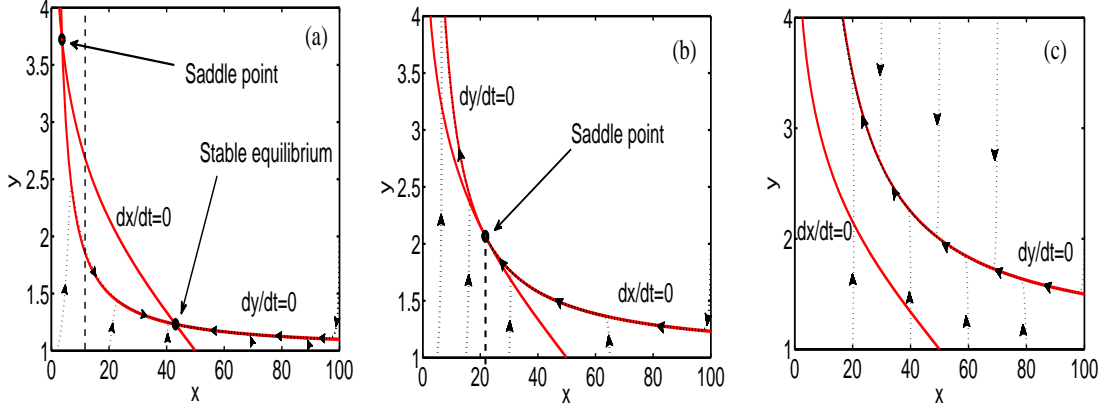


**Figure 4.12:** Phase plane of the system (4.1.5) realized for  $n = 100$ ,  $c = 1$ ,  $\beta = 1$ ,  $\alpha = 0.2$ ,  $\gamma = 1$  in the cases of (a) subcritical force  $f = 10$ , (b) critical force  $f = f_c = 23.2054$  and (c) supercritical force  $f = 50$  regimes.

The relation between the stability of the number of closed bonds in the cluster and force is sketched in Fig. 4.11. At small force, this equation has two roots, with the larger one corresponding to a stable equilibrium (since as shown in Fig. 4.12 a), the roots are separated by the line  $x = x_{BIF}$ ). As the force increases, a saddle-node bifurcation occurs, at the point where  $dy/dt = dx/dt = d^2x/dt^2 = 0$ . For forces above the critical limit, no roots exist therefore the cluster is unstable.

Precisely at the critical force, the two roots collapse and the slopes of the two terms of equation (4.1.5) become equal. The coordinates  $(f_c, x_c)$  where this happens in the force-displacement plane represent the solution of the system

$$\begin{cases} x_c e^{\frac{f(\beta+\alpha)}{x_c}} = \gamma(n - x_c), \\ e^{(\beta+\gamma)f_c/x_c} \left(1 - (\beta + \gamma)f_c/x_c\right) = -\gamma, \end{cases} \quad (4.1.12)$$

where  $f_c$  and  $x_c$  represent the critical force and the coordinate where the two roots collapse. The critical values for the cluster size and force can be obtained in an analytical form as

$$x_c = n \frac{\text{pln}\left(\frac{\gamma}{e}\right)}{1 + \text{pln}\left(\frac{\gamma}{e}\right)}, \quad (4.1.13)$$

$$f_c = \frac{n}{\beta + \alpha} \text{pln}\left(\frac{\gamma}{e}\right), \quad (4.1.14)$$

where the product logarithm function  $\text{pln}$  is the solution  $a$  of  $ae^a = b$ , as in §3.3.3.

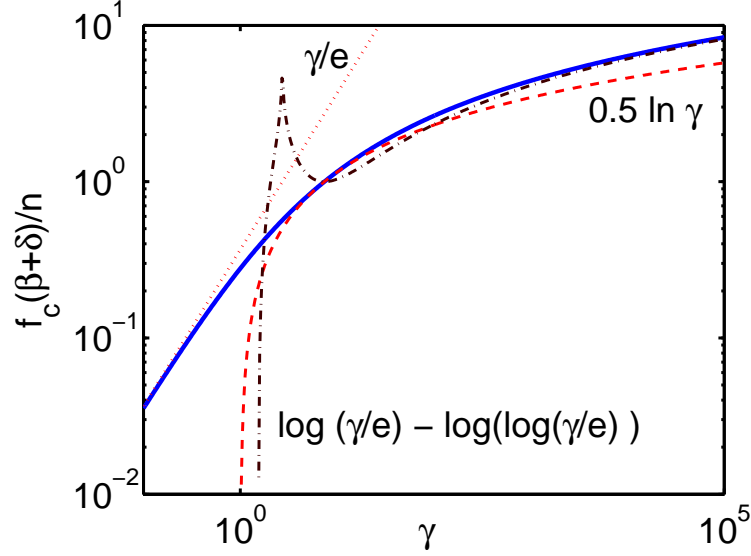


**Figure 4.13:** Critical force (4.1.13) in relation to the total cluster size and  $(\beta + \alpha)$ , as function of the rebinding constant  $\gamma$ . It scales linearly with (dotted line) at small, logarithmically (dashed line) for medium  $\gamma$ . In the large  $\gamma$  limit it approaches asymptotically  $\ln(\gamma/e) - \ln \ln(\gamma/e)$  (dash-dotted line).

Equation (4.1.5) can also be solved directly using the  $\text{pln}$  notation having the solution

$$x_0 = - \frac{n(\beta + \alpha)f}{\text{pln} \left( - \frac{(\beta + \alpha)f e^{\frac{(\beta + \alpha)f}{n}}}{\gamma n} \right) n - (\beta + \alpha)f}, \quad (4.1.15)$$

which highlights the importance of the scaling  $(\beta + \alpha)f$ .

The impact of the three forcing regimes on the phase plane descriptions of the system is sketched in Fig. 4.12. In the presented situation, the critical force is  $f_c = 23.2053$ , and the drag is small compared to the initial number of bonds ( $c/n \ll 1$ ). There are two timescales here. On a  $O(c/n)$  time scale there is a rapid relaxation onto the curve  $dy/dt = 0$ , and a slow bond breakage. Over  $O(1)$  times the system can be described then as a 1D equation along the  $dy/dt$  nullcline.

The subcritical force regime  $f = 10 < f_c$  is plotted in Fig. 4.12 (a) and it can be seen that the intersection of the nullclines generates two equilibrium points. The line  $(x_{BIF}, y)$  with  $x_{BIF}$  computed from (4.1.11), separates the two equilibrium points and using the earlier analysis, the point at the right of  $x_{BIF}$  is a stable node, while the other one is a saddle point. For critical force, the two previous equilibrium points collapse into a single equilibrium point, which in the case sketched in Fig. 4.12 (b) is a saddle point, since  $x_{BIF} = 21.7846 > 21.7812 = x_c$ . For supercritical force the cluster dissociates in all situations and no equilibrium is attained, as shown in Fig. 4.12 (c) for  $f = 50$ .

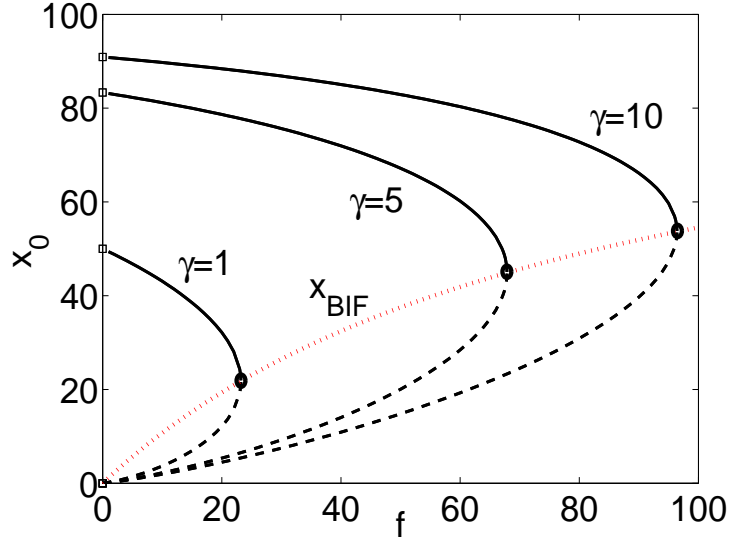


**Figure 4.14:** Dependence of  $x_0$  on force and rebinding. In this figure  $n = 100$ ,  $\beta = 1$ ,  $\alpha = 0.2$ . For each  $\gamma \in \{1, 5, 10\}$ , the squares represent the equilibrium for zero force which is  $\gamma n / (1 + \gamma)$ , while the circles represent the equilibrium number of bonds  $x_c$  at critical force  $f_c$ , computed from (4.1.13). Solid lines represent the stable nodes, while the dashed lines stand for the saddle points. The dotted line represents the value of  $x_{BIF} = \frac{nf(\beta+\alpha)}{n+f(\beta+\alpha)}$ .

Asymptotic approximations for the critical force  $f_c$  are illustrated in Fig. 4.13 for small, intermediate and large values of the rebinding coefficient  $\gamma$ .

The critical force scales in a trivial way with  $n$  and  $(\beta + \alpha)$ , and in a complicated way with  $\gamma$ . For  $\gamma < 1$  we obtain  $f_c \simeq \gamma n / [e(\beta + \alpha)]$ . Since the cluster dissociates even in the absence of force, the critical force is zero in the absence of rebinding. For  $\gamma > 1$  and up to the appreciable high value  $\gamma \simeq 100$  we have  $f_c \simeq 0.5n / (\beta + \alpha) \ln \gamma$ . This dependence shows that the single bond scale set by  $(\alpha + \beta)$  sets the force scale on which the cluster dissociates. The crossover of  $f_c$  from linear to logarithmic dependence on  $\gamma$  is shown in Fig. 4.13. In the large  $\gamma$  limit the critical force is well approximated by  $n / (\beta + \alpha) [\ln(\gamma) - \ln(e \ln(\gamma/e))]$ , where we can see a weak deviation from the logarithmic dependence as  $\gamma$  increases, as shown in Fig. 4.13. The asymptotic expansions of the  $\text{pln}$  function are based on [25].

In Fig. 4.14 is sketched the dependence of the number of closed bonds at equilibrium  $x_0$ , on force and rebinding. As one could easily notice, for all values of  $\gamma$ , the upper arch of  $x_0$  is situated entirely above the corresponding value of  $x_{BIF}$ , so the values on this branch represent stable nodes.

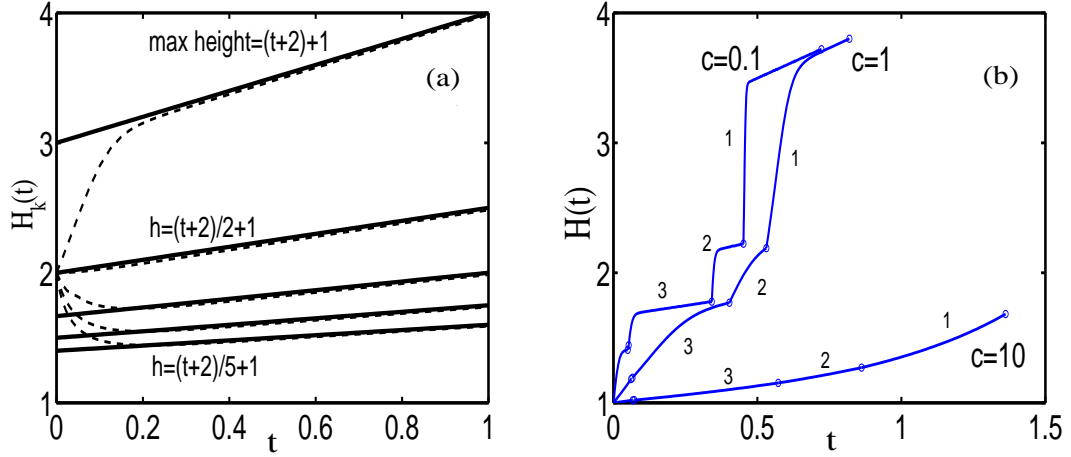


**Figure 4.15:** (a) Disk's displacement  $H_k(t)$  (dashed lines) with  $k = 1, \dots, 5$  bonds attached (2.1.9), towards the equilibrium heights (4.1.2) (solid lines), for ramped force  $f = t + 2$ ,  $h_0 = 2$ ,  $\beta = 1$ ,  $c = 1$ . (b) Disk's displacement in the  $(t, h)$ -plane, for  $n = 5$ ,  $f = t + 2$ ,  $h_0 = 1$ ,  $\beta = 1$ ,  $\gamma = 0$  and  $c = 0.1, 1, 10$ , as the bonds break. Circles indicate bond rupture coordinates.

## 4.2 Cluster dynamics under ramped force

The most commonly used profile for the dissociating force in DFS experiments is the ramped force [38], since it has the advantage of shortening the lifetime to an appreciable degree. We examine how our model captures this feature. Results of the stochastic description will be compared to deterministic results. As the force increases with time, rebinding is only relevant for the initial evolution of the system. To capture the effects of ramping the force, in this section we assume therefore, vanishing rebinding.

### 4.2.1 Preliminaries

Drag and loading rate significantly affect the disk's motion between events and individual trajectories, indicating the existence of distinct patterns in system's dynamics.

#### Disk trajectories

Since the motion of the disk depends on force (2.1.9), ramping the force will alter significantly the profile of the motion of the disk, as one can see in Fig. 4.15. As shown in Fig. 4.15 (a), in the absence of ruptures, the disk approaches asymptotically the curves

$$h_{eq,k} = \frac{\mu t}{k} + 2. \quad (4.2.1)$$

The disk's trajectories under different drag regimes are illustrated in 4.15 (b). Compared to Fig. 4.1 (b), the disk's displacement is permanently increasing.

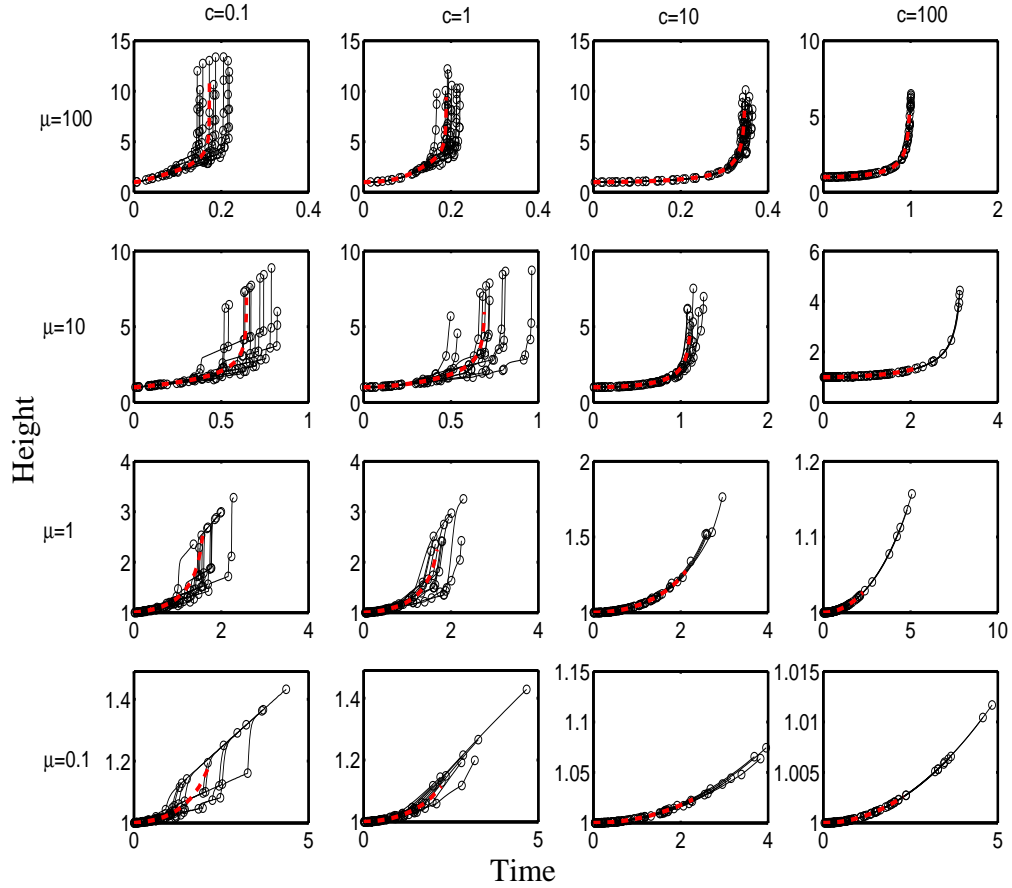


**Figure 4.16:** Plot of 10 individual disk trajectories (solid lines) in the (time, height)-plane, for  $n = 10$  bonds,  $\mu = 0.1, 1, 10, 100$  and  $c = 0.1, 1, 10, 100$ . The circles indicate the position of the rupture events, while red the dashed line represents the deterministic approximation (2.2.23).

### Disk trajectories in the $(c, \mu)$ -plane

As shown earlier, the trajectories of the disk exhibit a large variety of behaviour. In Fig. 4.16 we plot individual trajectories of the disk in (time, height)-space, realized for various values of  $\mu$  and  $c$ , against solutions of the deterministic approximation (2.2.23). Compared to Fig. 4.2, the deterministic trajectories of the disk approximate to a much greater extent their stochastic counterparts, and significant variations can only be seen for small drag ( $c = 0.1, 1$ ). The disk's displacement is negligible for small force/large drag, and can be significant for large loading rates. Fig. 4.16 suggests the existence of distinct regions in the  $(c, \mu)$  parameter space. At the same time, for large drag and loading rate ( $c, \mu \geq 10$ ), the profile of the disk's displacement in the final phase is almost a vertical climb following a plateau, suggesting a sudden dissociation of bonds.

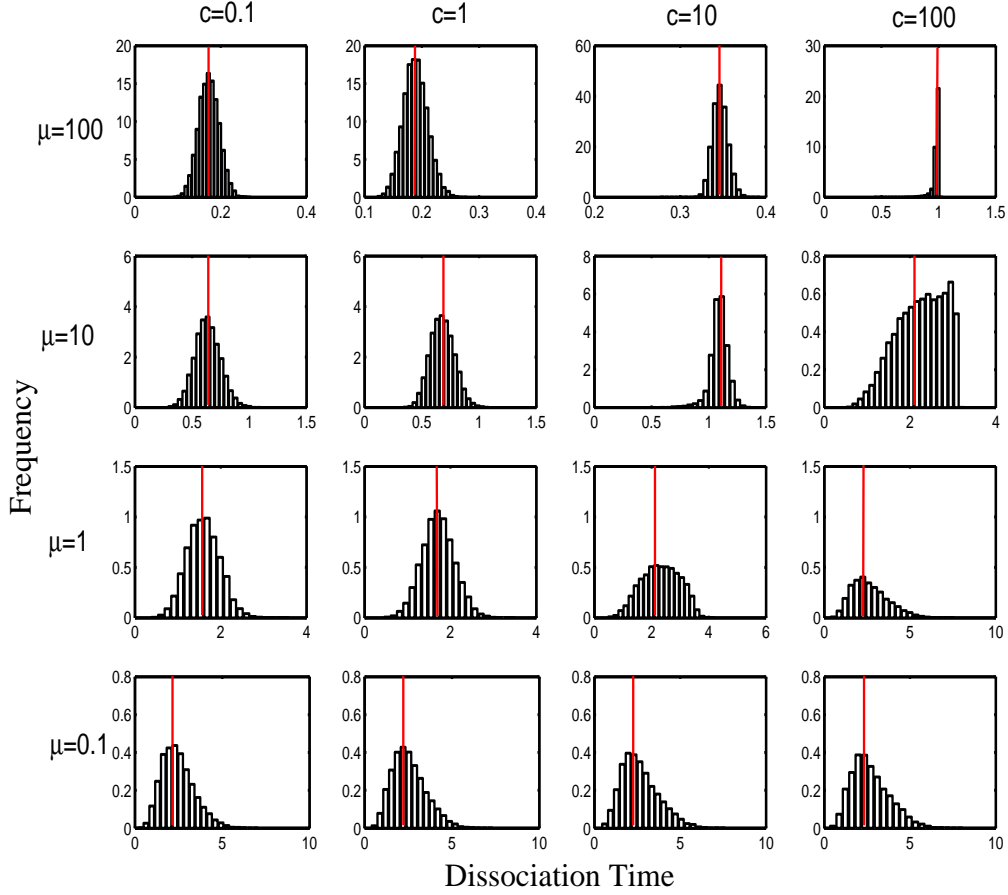


**Figure 4.17:** Dissociation time  $T_D(t)$  of a cluster for  $n = 10$ ,  $h_0 = 1$ ,  $\beta = 1$ ,  $\mu = 0.1, 1, 10, 100$  and  $c = 0.1, 1, 10, 100$ , obtained from  $10^4$  single trajectories. Horizontally, the red vertical lines represent the times  $T_d$  obtained from  $N_d(T_d) = 1$  in (2.2.23).

### Distribution of the dissociation times

The distribution of the dissociation time  $T_D$  obtained from stochastic simulations is plotted in Fig. 4.17, against solutions of the deterministic approximation (2.2.23). For small loading rate (bottom line), the results are similar to Fig. 4.3. Drag significantly extends cluster lifetime, especially for large loading rates (horizontal). Increasing the loading rate, rapidly shortens cluster lifetime, especially for large drag ( $c = 100$ ), where the bonds kept near the equilibrium by drag, suddenly rupture once force becomes large enough. At large loading rates, the force distribution is narrow, as seen for larger values of  $\mu$ , especially and large drag, as for  $\mu = 100$ ,  $c = 100$ . An important parameter in the loading rate experiments is the rupture force  $\mu T_D$ , whose relevance is discussed later in this section. The deterministic lifetime  $T_d$  obtained by solving  $N_d(T_d) = 1$  in (2.2.23), is generally in good agreement with the the mean of  $T_D$ .

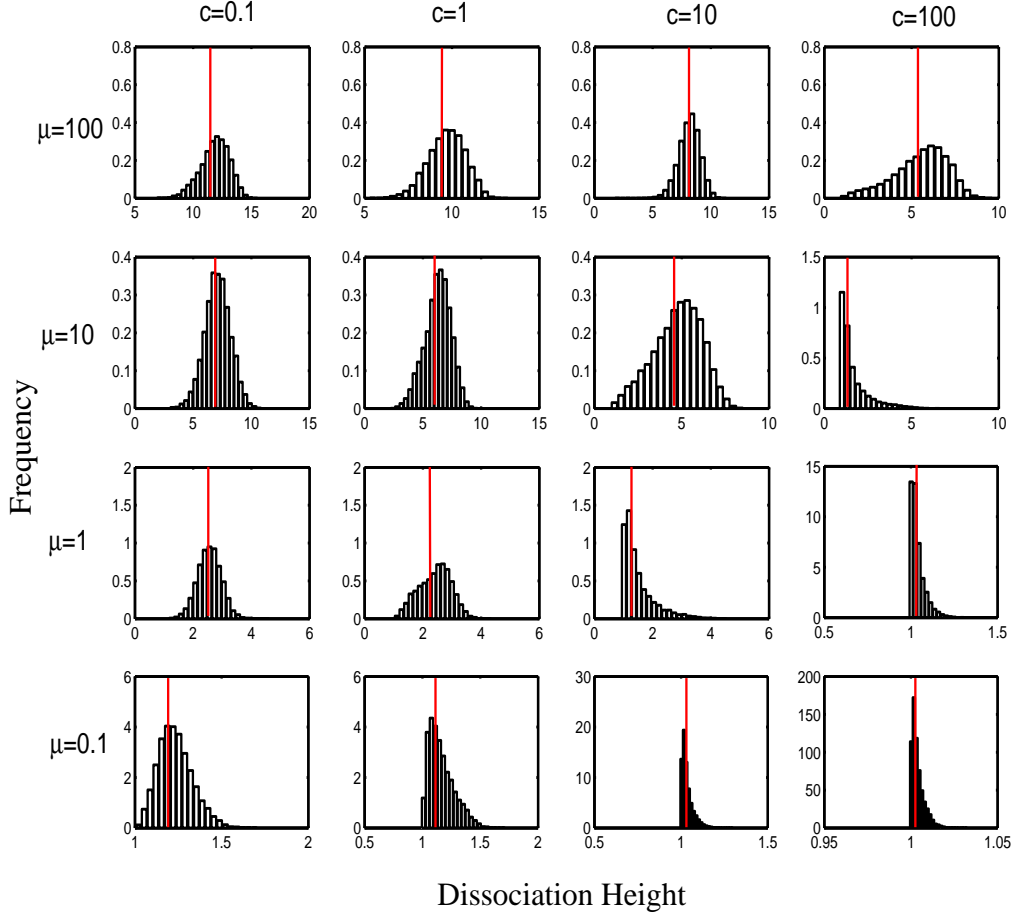


**Figure 4.18:** Dissociation height  $H_D(h)$  of a cluster for  $n = 10$ ,  $h_0 = 1$ ,  $\beta = 1$ ,  $\mu = 0.1, 1, 10, 100$  and  $c = 0.1, 1, 10, 100$ , obtained from  $10^4$  single trajectories. Horizontally, the red vertical lines represent the deterministic height  $H_d(T_d)$ , solved from  $N_d(T_d) = 1$  in (2.2.23).

### Distribution of the dissociation heights

The distribution of the dissociation height  $H_D$  is plotted in Fig 4.18. As the disk moves permanently, the profiles of  $H_D$  are very different from the ones shown in Fig. 4.4 for constant force. For small drag ( $c = 0.1$ ), the disk moves almost freely under force, and  $H_D$  rapidly shifts to larger values, while spreading over a wider region. Along the bottom line, the displacement is significant even for small loading rate and drag ( $\mu = c = 0.1$ ). Keeping  $\mu$  fixed and increasing drag,  $H_D$  approaches  $\delta(h - 1)$  in the infinite-drag limit. For large drag ( $c = 100$ ), the distribution  $H_D$  initially confined near 1, is spread to the right with the increase of  $\mu$ .

The deterministic displacement  $H_d(T_d)$  (represented in Fig 4.18 by red dots) obtained by solving  $N_d(T_d) = 1$  in (2.2.23), is generally in good agreement with the mean of  $H_D$  in the upper part of the antidiagonal of Fig. 4.18.

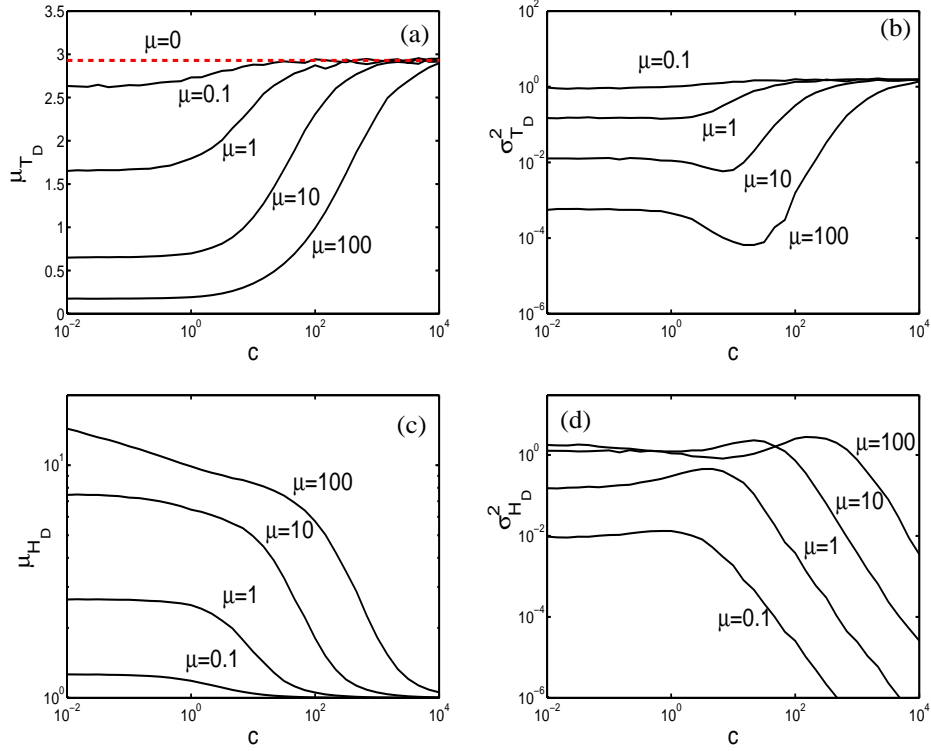


**Figure 4.19:** Statistics of the cluster's rupture for  $n = 10$  bonds, as functions of drag and force, realized from minimum 3000 simulations per  $(c, \mu)$  point (a)  $\mu_{T_D}$ ; (b)  $\sigma_{T_D}^2$ ; (c)  $\mu_{H_D}$ ; (d)  $\sigma_{H_D}^2$ . The dashed line represents results for  $\mu = 0$ . Both  $c$  and  $\mu$  domains are spanned by 50 logarithmically spaced points.

### Means and variances of $T_D$ and $H_D$ obtained from stochastic simulations

The mean values and variances of  $T_D$  and  $H_D$  defined in §2.2.2 as functions of loading rate and drag are depicted in Fig. 4.19. As anticipated,  $\mu_{T_D}$  increases with drag (for fixed loading rate), having the upper bound  $\sum_{k=1}^n \frac{1}{n}$  as predicted in Chapter 3 (see Fig. 4.5), and decreases with the loading rate. Also, in the small force regime  $\mu_{T_D}$  is largely drag independent, while for large force it increases with drag, as in Fig. 4.19 (a). The behaviour of  $\mu_{H_D}$  and  $\sigma_{H_D}$  depicted in Fig. 4.19 (c) and (d), can be interpreted in the same key as their correspondents for constant force, plotted in Fig. 4.5 (c) and (d).

The variance  $\sigma_{T_D}^2$  instead has a significantly different profile, as shown in Fig. 4.5 (b).. For small drag, the profile is drag-independent. Increasing drag at a constant  $\mu$ , the variance exhibits a minimum for a certain value of drag (which increases with  $\mu$ ), where the lifetimes also start to increase in  $\mu_{T_D}$ . This coordinate may potentially have experimental values, allowing us to choose the value of  $c$  that leads to the most precise measurement of  $\mu_{T_D}$ . Increasing drag even further,  $\sigma_{T_D}^2$  near the value  $\sum_{k=1}^n \frac{1}{n^2}$  (3.3.9).

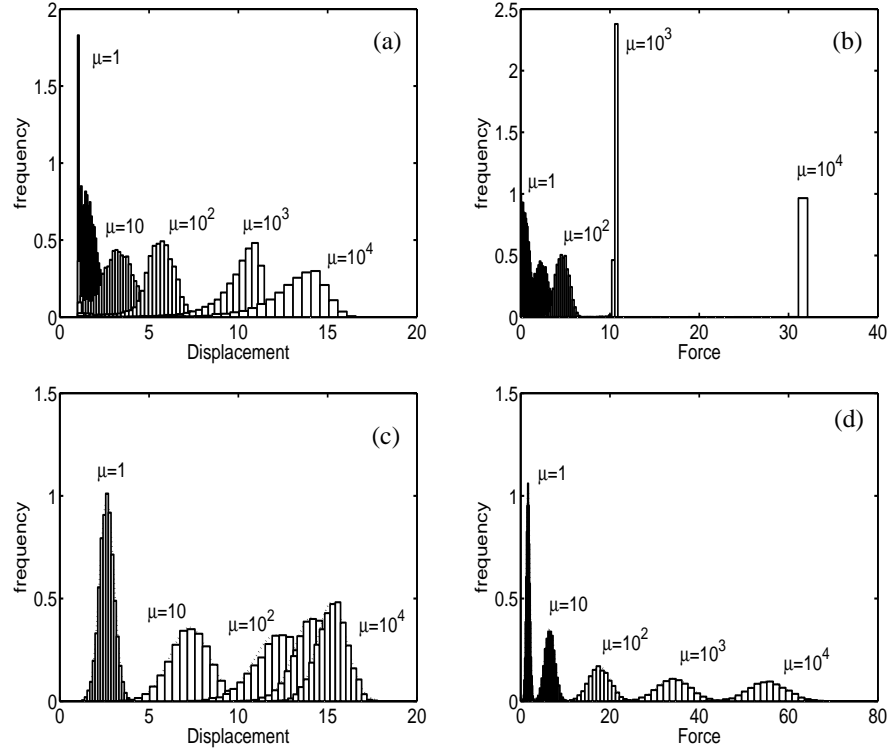


**Figure 4.20:** Small drag ( $c=0.1$ ) cluster dissociation histograms for (a) displacement,  $n = 1$  bond; (b) rupture force,  $n = 1$  bond; (c) displacement,  $n = 10$  bonds; (d) rupture force,  $n = 10$  bonds, computed from  $10^4$  simulated trajectories for loading rates  $\mu = 1, 10, 10^2, 10^3, 10^4$ . The dotted line represents a fitted normal density, with the same mean and variance as the simulated data.

## 4.2.2 Mimicking DFS experiments

Our model can be used to mimic the DFS experiments, not only for single bonds, but also for clusters with multiple bonds. As discussed in §1.2.3, in experiments we can measure the force when the last bond dissociates. In this section we show that drag can fundamentally change the distribution patterns of the rupture force, as a direct consequence of force buildup. In accordance with the findings of Merkel *et al.* [95] presented in §1.2.3, bond strength is not only a property of the bond, but is also influenced by the loading rate  $\mu$ , as one can see in Fig. 4.20 (b). Moreover, disk trajectories are considerably modified by drag (see Fig. 4.15), and so does the distribution of the individual bond rupture forces, illustrated in Figs. 4.21 (b) and 4.20 (b).

For small drag the profile of rupture forces shares the same properties with the zero-drag experiment, for both single bond, and multiple bond clusters in Fig. 3.20: the force distribution shifts to the right with the increase in loading rate, the effect being amplified for larger clusters, where the force profiles are normally distributed.

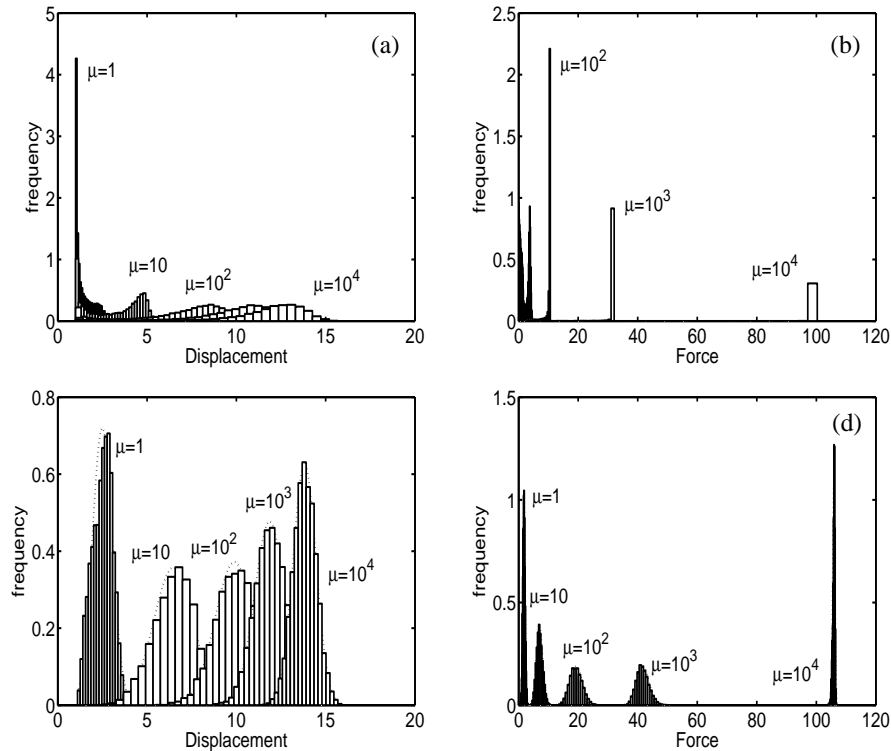


**Figure 4.21:** Intermediate drag ( $c=1$ ) cluster dissociation histograms for (a) displacement,  $n = 1$  bond; (b) rupture force,  $n = 1$  bond; (c) displacement,  $n = 10$  bonds; (d) rupture force,  $n = 10$  bonds, computed from  $10^4$  simulated trajectories for loading rates  $\mu = 1, 10, 10^2, 10^3, 10^4$ . The dotted line represents a fitted normal density, with the same mean and variance as the simulated data.

In Fig. 4.20 (a) and (c) we also plot for comparison the distribution of final displacement, showing that cluster displacement is significantly increased by loading rate. The difference in the position of the final displacement distributions is more evident for smaller values of loading rate. Nonetheless, even for relatively small clusters, the final displacement closely resembles a normal distribution.

Drag induced effects can already be observed for  $c = 1$ . The distribution of final force and displacement illustrated in Fig. 4.21 for both single and multiple bond clusters are strikingly different, compared to Fig. 4.20. First, as drag slows down the extension of individual bonds, the final displacement's distribution is much wider. At the same time, drag has induced a significant separation between the rupture force distributions as shown Fig. 4.21 (b), which is even more evident as the cluster dimension is increased.

Model predictions can be compared against experiments, if we restore the dimensions of time and force, and use physiological data for the bond properties  $\kappa^*$ ,  $L^*$  and  $k_0^*$ , and also for the parameters of the experimental setup  $R^*$  and  $\mu^*$ .

In summary, the bond/cluster rupture force is not only a bond or loading property, but also depends on drag. Drag enhances the separation between the bond rupture force distributions induced by increasing loading rate.

**Note:** The histograms in Figs. 4.20 and 4.21 are realized using 21 bins, between the minimum and maximum of the simulated data. The wider bins corresponding to  $\mu = 10^4$  in Figs. 4.20 (b) and 4.21 (b), appear because the data was not filtered for the very rare extreme events, which occurred.

### 4.3 A possible PDE formulation of cluster dynamics

---

In this section we analyze a differential Chapman-Kolmogorov Equation (dCKE) formulation, proposed to be suitable for the analysis of stochastic processes with joint continuous and discrete state space, inspired from the paper of Lipniacki *et al.* [91]. The starting point is the formulation of the problem as a piecewise-deterministic Markov process with the random variables  $N(t)$  and  $H(t)$ , representing the number of closed bonds and the displacement of the disk, respectively. We wish to determine if this process can be reformulated as a dCKE. We solve the relevant dCKE with the method of characteristics, and then compare the results against stochastic simulations. We find that the solution approximates well the stochastic simulations for large values of drag, but performs poorly for small values of drag, especially in the terminal phase of the cluster's decay. We explain the results, and derive forward and backward integro-differential equations for the bivariate Markov Processes  $(N, H)$ , in §4.3.4.

#### 4.3.1 The dCKE

The steps described in [91], are adapted to our problem in Appendix 4.B, leading to a forward equation describing the evolution of the cluster in the velocity field  $v(h, k)$  written as

$$\begin{aligned} \frac{\partial p_k(h, t)}{\partial t} + \frac{\partial}{\partial h} \left[ v(h, k) p_k(h, t) \right] &= \\ &= - [r_k(H(t)) + g_k(H(t))] p_k(h, t) + g_{k-1}(H(t)) p_{k-1}(h, t) + r_{k+1}(H(t)) p_{k+1}(h, t), \end{aligned} \quad (4.3.1)$$

where  $k = 0, 1, \dots, n$  and  $p_k(h, t)$  represents the probability density over  $h$ , of having  $k$  closed bonds at time  $t$  (2.2.16). For a fixed  $k = 0, \dots, n$ , the displacement  $H$  satisfies  $\frac{dH(t)}{dt} = v(H(t), k)$ , where

$$v(h, k) = -\frac{1}{c} h^3 [kh - (f + k)], \quad (4.3.2)$$

The rupture and rebinding rates

$$r_k(H) = \lambda_{k,k-1}(H) = ke^{\beta(H-1)}, \quad (4.3.3a)$$

$$g_k(H) = \lambda_{k,k+1}(H) = (n-k)e^{-\delta(H-1)}, \quad (4.3.3b)$$

are similar to the ones defined in §2.1.3.

The initial condition for this problem is a Gaussian

$$p_k(h,0) = \begin{cases} \frac{1}{\sigma\sqrt{2\pi}} e^{-\frac{(h-h_0)^2}{2\sigma^2}}, & \text{if } k = n; \\ 0 & \text{if } k \leq n-1, \end{cases} \quad (4.3.4)$$

with a small standard deviation  $\sigma > 0$ , to mimick what would happen in an experiment. We briefly describe the solution of (4.3.1-4.3.4) by the method of characteristics.

### 4.3.2 Solution along characteristics

The system of PDEs (4.3.1) is generally called a *linear advection or transport equation*, describing the evolution of the probability density  $p_k$  in a flow having the velocity field  $v(h,k)$ . In the absence of rebinding,  $p_k$  can be obtained recurrently from  $p_{k+1}, \dots, p_n$  for  $k = 0, \dots, n-1$ . The system of PDE's (4.3.1) becomes

$$\begin{cases} \frac{dh}{dt} = -(1/c) \left[ kh^4 - (k+f)h^3 \right], & h(0) = h^0, \\ \frac{dp_k}{dt} = - \left[ ke^{\beta(h-1)} + \frac{dv(h,k)}{dh} \right] p_k(h,t) + (k+1)e^{\beta(h-1)} p_{k+1}(h,t), \end{cases} \quad (4.3.5)$$

where  $p_{n+1} \equiv 0$  (as  $n$  is the maximum number of binding sites) and the initial condition  $p_k(h^0,0)$  satisfies (4.3.4). As seen in Fig. 4.22 and discussed in Appendix 4.B.3, the characteristic curves converge to a fixed line which depends on the number of bonds. For large values of drag, the convergence is very slow. The properties of the characteristic curves have a significant impact on the solution of (4.3.5), since they determine the direction along which the initial configuration is transported. For simplicity, the solution is tested for constant force.

#### Solution for the initial decay $p_n$

First we solve  $p_n$  along a numerous set of characteristic curves, from the equation

$$\begin{aligned} \frac{dh}{dt} &= -(1/c) \left[ nh^4 - (n+f)h^3 \right], & h(0) &= h^0 \\ \frac{dp_n}{dt} &= \left[ -ne^{\beta(h-1)} + (1/c) (4nh^3 - 3(n+f)h^2) \right] p_n(h,t), \end{aligned} \quad (4.3.6)$$

where  $p_n(h^0,0)$  satisfies (4.3.4). The previous equation is solved using the classical Runge-Kutta ode45 Matlab<sup>®</sup> routine.

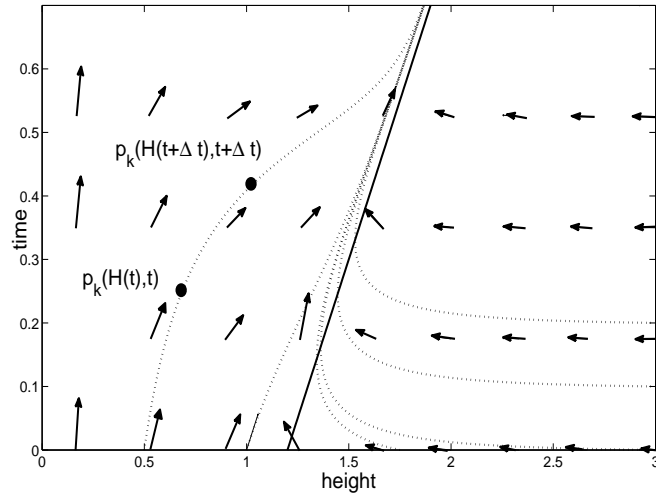


**Figure 4.22:** Transport of  $p_k(h, t)$  in the velocity field  $v(h, k, t)$  for  $k = 5$  and  $f = 5t + 1$ . Arrows show the direction of the flow field, while the solid line represents the asymptote of the characteristic curves (dotted lines).

**Solution for the steps  $k = 0, \dots, n - 1$ .**

To avoid confusions between the characteristic curves corresponding to different bond populations  $k$ , the solution of the equation

$$\begin{cases} \frac{dh}{dt} = v(h, k), \\ h(0) = h^0. \end{cases}$$

is denoted by  $h_k(t)$ . Suppose that for a given  $k \in n - 1, \dots, 0$  we already obtained the densities down to  $p_{k+1}$ , computed along a sufficiently large number of characteristic curves  $h_{k+1}$ . The algorithm used for the computation of the densities  $p_k$  along the characteristic curves  $h_k$  is described below.

- Obtain the curves  $h_{k-1}$  starting at the same initial heights  $h^0$ .

The characteristic curves (implicitly the densities) are only solved only below a relevant height  $h_{max}$ .

- For each value of time  $t$ , the values of  $p_{k+1}$  computed at  $(h_{k+1}(t), t)$ , are used to approximate  $p_{k+1}$  along the new characteristic curves  $(h_k(t), t)$ .

In Matlab<sup>®</sup> this is done using linear or cubic interpolation (`interp1`).

- The density  $p_k$  is obtained by solving (4.3.5) along each characteristic curve  $h_k$ , using the source term  $(k + 1) \exp(\beta(h_k - 1))p_{k+1}(h_k(t), t)$ . This is done in Matlab<sup>®</sup> using a time-dependent coefficient routine based on `ode45`.

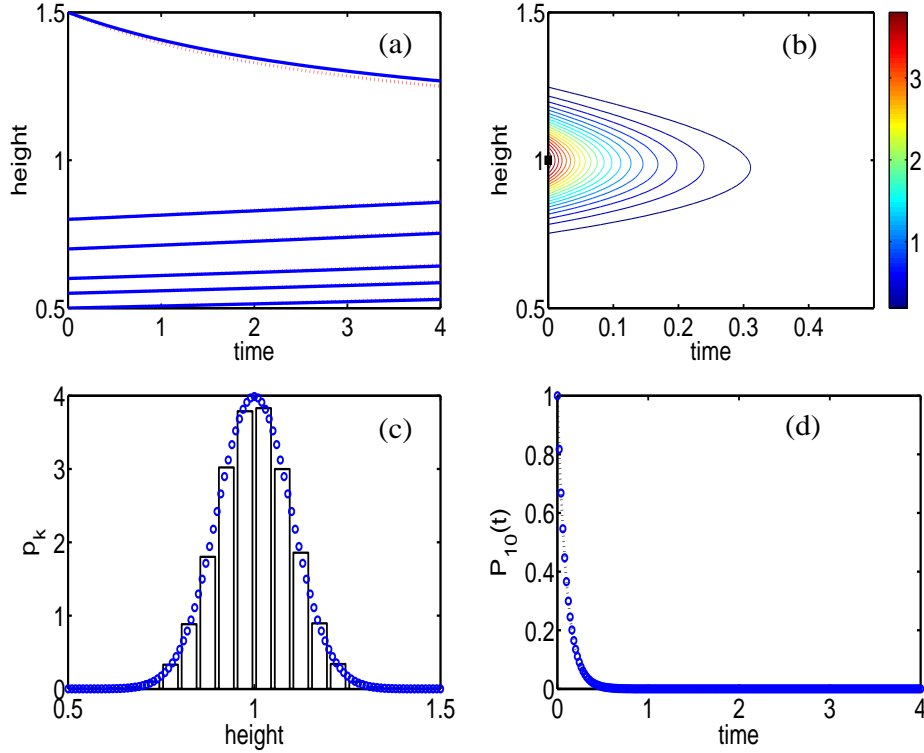


**Figure 4.23:** Solution comparison for  $k = 10$ . (a) characteristics (4.3.2) for  $k = 10$  (solid) and  $k = 9$  (dotted) bonds; (b) density  $p_{10}(h, t)$  (4.3.5); (c)  $p_{10}(h, t)$  at the time when attains its maximum (characteristics - solid line, simulations - histogram); (d) Estimate of  $P_{10}(t) = \Pr\{N(t) = k\} = \int_0^\infty p_k(h, t)dh$  from simulations (circles) and the method of characteristics (solid line). The parameters are  $n = 10$ ,  $f = 1$ ,  $\beta = 1$ ,  $h_0 \sim N(1, 10^{-2})$ , and  $c = 100$  (large drag).

### 4.3.3 Validation of the solution against stochastic simulations

Solutions of the dCKE obtained by the method of characteristics are compared against results obtained from stochastic simulations, for large and small values of drag.

#### Large drag

In the infinite-drag limit the characteristic curves are straight lines  $h_k(t) \equiv h$ , and the  $p'_k$ 's do not exhibit singularities. Since  $v_k = O(1/c)$ , the evolution of the probability densities  $p_k$  at height  $h$  is given at leading order by the equation

$$\frac{dp_k(h, t)}{dt} = -r_k(h)p_k(h, t) + r_{k+1}(h)p_{k+1}(h, t), \quad (4.3.7)$$

$$p_k(h, 0) = \begin{cases} \frac{1}{\sigma\sqrt{2\pi}} e^{-\frac{(h-h_0)^2}{2\sigma^2}}, & \text{if } k = n; \\ 0 & \text{if } k \leq n-1, \end{cases} \quad (4.3.8)$$

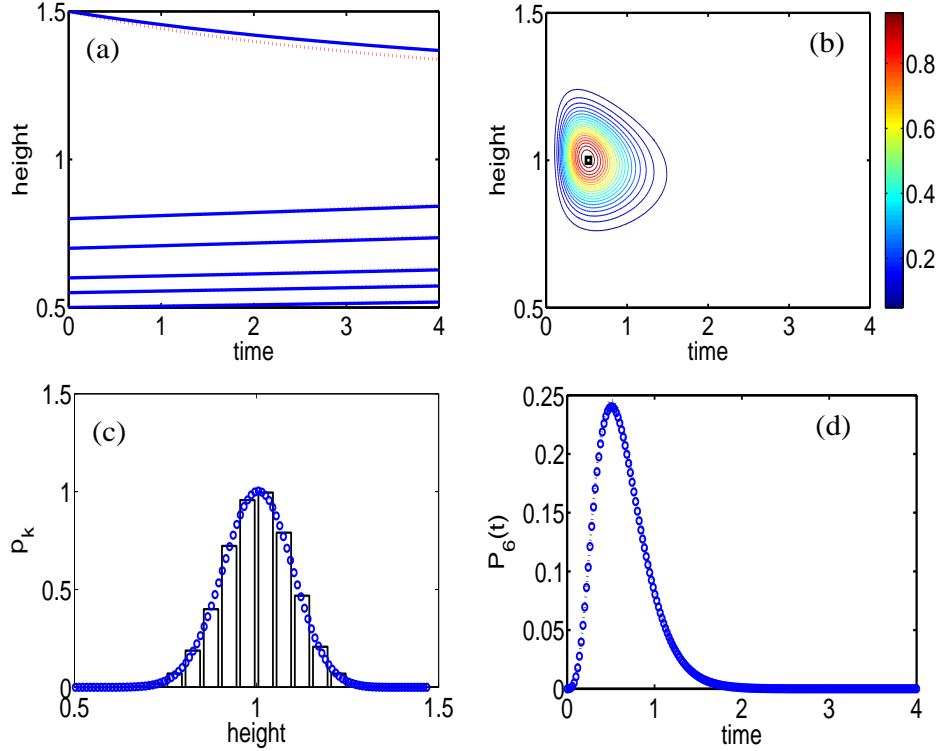


**Figure 4.24:** Solution comparison for  $k = 6$ . (a) characteristics (4.3.2) for  $k = 6$  (solid) and  $k = 5$  (dotted) bonds; (b) density  $p_6(h, t)$  (4.3.5); (c)  $p_6(h, t)$  at the time when attains its maximum (characteristics - solid line, simulations - histogram); (d) Estimate of  $P_6(t) = \Pr\{N(t) = k\} = \int_0^\infty p_k(h, t)dh$  from simulations (circles) and the method of characteristics (solid line). The parameters are  $n = 10$ ,  $f = 1$ ,  $\beta = 1$ ,  $h_0 \sim N(1, 10^{-2})$ , and  $c = 100$  (large drag).

where  $r_{n+1} \equiv r_0 \equiv 0$  (for the reasons discussed in §3.2.1 (3.2.4)). The solution of (4.3.7) is given by (3.A.6), which was analyzed earlier in Appendix 3.B.

For large but finite drag ( $c = 100$ ), the solutions obtained from the method of characteristics show a good agreement with the ones obtained from stochastic simulations. We compare solutions for  $n = 10$  bonds from the initial phase  $k = 10$  (initial decay of the cluster) and  $k = 6$  (intermediate phase).

In Figs. 4.23 and 4.24 (a), the characteristic curves corresponding to  $k$  (solid line) and  $k - 1$  (dotted line) bonds are shown to differ little for large drag. In Figs. 4.23 and 4.24 (b) a contour plot for  $p_k$  is presented, together with its maximum (square). The densities  $p_k(h, t)$  are depicted in Figs. 4.23 and 4.24 (c) at the fixed time  $t_{k, \max}$ , when the maximum of  $p_k$  is attained in the  $(h, t)$  space. A comparison of the probabilities  $P_k(t) = \Pr\{N(t) = k\} = \int_0^\infty p_k(h, t)dh$  (2.2.10) is plotted in Figs. 4.23 and 4.24 (d).

The results are motivated by the slow variation of the characteristics between consecutive states of the system.

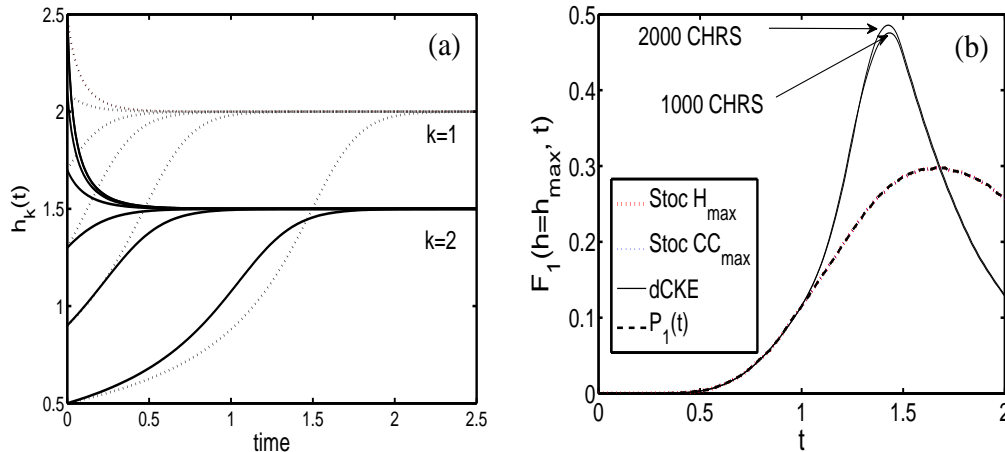


**Figure 4.25:** Comparison of solutions obtained from the method of characteristics and stochastic simulations in the terminal phase of cluster decay ( $k = 1$ ). The parameters are  $n = 10$ ,  $f = 1$ ,  $\beta = 1$ ,  $h_0 \sim N(1, 10^{-2})$ ,  $H_{max} = 2.5 > 1 + f$  and  $c = 1$  (small drag). (a) characteristics (4.3.2) for  $k = 2$  (solid) and  $k = 1$  (dotted) bonds; The characteristic  $h_k(t)$  for  $k = 1$  starting from  $h_k(0) = H_{max}$  is denoted by  $CC_{max}(t)$ . (b) Distributions  $F_1(CC_{max}(t), t)$  (3.A.1) from the dCKE solved along characteristics are compared against  $F_1(CC_{max}(t), t)$  (dotted, red line) and  $F_1(H_{max}, t)$  (dotted, blue line), as well as probabilities  $P_1(t)$  (dashed, black line) defined by (2.2.10) estimated from stochastic simulations.

### Small drag

For small drag, the characteristics corresponding to consecutive states quickly become different as depicted in Fig. 4.25 (a) for  $k = 1$ .

The comparison of between the characteristics and stochastic simulations solutions plotted in Fig. 4.25 (b) shows a strong disagreement, especially in the final cluster decay phase ( $k=1$ ). The solution  $p_k(h, t)$  obtained from the dCKE (4.3.2) along 1000 or 2000 characteristics starting from equally spaced points in the interval  $[0.5, H_{max}]$  is used to estimate the distribution

$$F_k(\mathcal{H}(t), t) = \Pr\{N(t) = k \mid H(t) < \mathcal{H}(t)\}, \quad (4.3.9)$$

along different curves  $\mathcal{H}(t)$ .

Denoting by  $CC_{max}(t)$  the characteristic  $h_1(t)$  starting from  $h_1(0) = H_{max} = 2.5 > 1 + f$ , we compute the distribution  $F_1(CC_{max}(t), t)$  (solid lines), which differs little with the increase in the number of characteristics.

The distribution  $F_1$  is also estimated from stochastic simulations along different curves. As shown in Fig. 4.25 (b), lines obtained from simulations along  $\mathcal{H}(t) = 2.5$  (Stoc  $H_{max}$  - red dotted line) and  $\mathcal{H}(t) = CC_{max}(t)$  (Stoc  $CC$  - blue dotted line), as well as

the probabilities  $P_1(t)$  (dashed, black line) are superposed, indicating that the region between the chosen characteristic curves contains all the probability to have one bond.

The difference between the solutions obtained from the dCKE and stochastic simulations seems to be sensitive neither to the height grid choice, nor to the number of characteristic curves.

In summary, the solution of the dCKE computed using the method of characteristics was shown to be significantly different from the results obtained from stochastic simulations, particularly for smaller values of the drag coefficient  $c$ . This indicates that a PDE formulation is not appropriate for our model. The solution is to derive new forward/backward equations for the evolution of the probability densities  $p_k(t, h)$ , which is presented below.

#### 4.3.4 Bivariate stochastic processes

In this section we examine a bivariate stochastic process  $\{(X(t), H(t)) : t \geq 0\}$  with state space  $E \times \mathbb{R}$ , where  $E = \{0, 1, 2, \dots, n\}$ . For  $i = 1, 2, \dots, n$ , when  $X(t) = i$ ,  $H(t)$  follows the deterministic path described by the ODE

$$\frac{dH}{dt} = v_i(H).$$

For  $i = 1, 2, \dots, n$ , whilst  $X(t)$  is in state  $i$ , it jumps to state  $j$  ( $j \neq i$ ) at rate  $q_{ij}(H(t))$ . The process  $\{(X(t), H(t))\}$  is Markov. For convenience we shall use these notations below.

##### Sojourn time in a state

For  $i = 1, 2, \dots, n$ , let

$$q_i(h) = \sum_{j \in E, j \neq i} q_{ij}(h),$$

be the rate at which  $\{X(t)\}$  leaves state  $i$  if  $H(t) = h$ .

Suppose that  $(X(0), H(0)) = (i, h_0)$  and let  $T = \inf\{t \geq 0 : X(t) \neq i\}$  be the time when  $\{X(t)\}$  first leaves the state  $i$ . Then,

$$\Pr\{T > t\} = \exp\left(-\int_0^t q_i(h_i(u; h_0)) du\right),$$

where  $h_i(u; h_0)$  is the solution of

$$\frac{dh}{dt} = v_i(h), \quad h(0) = h_0.$$

As shown previously,  $T$  has the pdf

$$f_i(t; h_0) = q_i(h_i(t; h_0)) \exp\left(-\int_0^t q_i(h_i(u; h_0)) du\right), \quad (t > 0). \quad (4.3.10)$$

**Forward equation**

Suppose that  $X(0) = i$  and  $H(0)$  has density  $\pi_i(h)$  ( $h \in \mathbb{R}$ ). For  $t \geq 0$ , let

$$F_j(t, h) = \Pr \{X(t) = j, H(t) \leq h\}, \quad (j = 1, \dots, n; h \in \mathbb{R}), \quad (4.3.11)$$

and

$$p_j(t, h) = \frac{\partial}{\partial h} F_j(t, h). \quad (4.3.12)$$

Our aim is to find an equation satisfied by the densities  $p_j(t, h)$  ( $j = 1, \dots, n; h, t \geq 0$ ). Fix  $t, j$  and  $h$  with  $i \neq j$ . To determine an equation for  $p_j(t, h)$ , let  $U = \sup\{U < t : X(t) \neq j\}$  be the time of the last jump of  $\{X(t)\}$  in  $(0, t)$ .

For  $u \in [0, t]$ , let  $\tilde{h}_j(u; t, h)$  be the solution of the ODE

$$\frac{d\tilde{h}}{dt} = v_j(h), \quad \tilde{h}(t) = h.$$

Hence, assuming for simplicity that  $\tilde{h}_j(u; t, h)$  is increasing in  $h$ , given  $X(t) = j$  and  $U = u$  we have the relation

$$H(t) \in (h, h + \Delta h) \iff H(u) \in \left( \tilde{h}_j(u; t, h), \tilde{h}_j(u; t, h) + \frac{\partial \tilde{h}_j(u; t, h)}{\partial h} \Delta h + o(\Delta h) \right). \quad (4.3.13)$$

Thus we obtain

$$\Pr \{X(t) = j, H(t) \in (h, h + \Delta h)\} = \int_0^t \sum_{k \neq j} \Pr \left\{ X(u-) = k, H(u) \in \left( \tilde{h}_j(u; t, h), \tilde{h}_j(u; t, h) + \frac{\partial \tilde{h}_j(u; t, h)}{\partial h} \Delta h + o(\Delta h) \right) \right\} q_{kj}(\tilde{h}_j(u; t, h)) \exp \left( - \int_u^t q_j(\tilde{h}_j(s; t, h)) ds \right) du.$$

It follows that for  $j \neq i$ ,  $p_j(t, h)$  satisfies the integral equation

$$p_j(t, h) = \int_0^t \sum_{k \neq j} p_j(u, \tilde{h}_j(u; t, h)) \frac{\partial \tilde{h}_j(u; t, h)}{\partial h} q_{kj}(\tilde{h}_j(u; t, h)) \exp \left( - \int_u^t q_j(\tilde{h}_j(s; t, h)) ds \right) du.$$

When  $j = i$ , there is an extra term corresponding to  $\{X(t)\}$  not jumping in  $(0, t)$ . Specifically,

$$\begin{aligned} p_i(t, h) &= \int_0^t \sum_{k \neq i} p_i(u, \tilde{h}_i(u; t, h)) \frac{\partial \tilde{h}_i(u; t, h)}{\partial h} q_{ki}(\tilde{h}_i(u; t, h)) \exp \left( - \int_u^t q_i(\tilde{h}_i(s; t, h)) ds \right) du \\ &\quad + \pi_i(\tilde{h}_i(0; t, h)) \frac{\partial \tilde{h}_i(0; t, h)}{\partial h} \exp \left( - \int_0^t q_i(\tilde{h}_i(s; t, h)) ds \right). \end{aligned} \quad (4.3.14)$$

### Backward equation

For  $i, j \in E, y, z \in \mathbb{R}$  and  $t \geq 0$ , let

$$F_{ij}(t, y, z) = \Pr \{X(t) = j, H(t) \geq z \mid X(0) = i, H(0) = y\}.$$

Fix  $i \in E$  and  $y \in \mathbb{R}$ . Suppose that  $(X(0), H(0)) = (i, y)$  and let

$$V = \inf\{t > 0 : X(t) \neq i\},$$

be the time of the first jump of  $\{X(t)\}$ . Then, for  $j \neq i$  and  $z \in \mathbb{R}$

$$F_{ij}(t, y, z) = \int_0^t \sum_{k \neq i} \exp\left(-\int_0^u q_i(h_i(s; y)) ds\right) q_{ik}(h_i(u; y)) F_{kj}(t - u, h_i(u; y), z) du,$$

and for  $j = i$  there is an extra term corresponding to  $\{X(t)\}$  not jumping in  $(0, t)$

$$\begin{aligned} F_{ii}(t, y, z) &= \int_0^t \sum_{k \neq i} \exp\left(-\int_0^u q_i(h_i(s; y)) ds\right) q_{ik}(h_i(u; y)) F_{ki}(t - u, h_i(u; y), z) du \\ &\quad + \exp\left(-\int_0^t q_i(h_i(u; y)) du\right) 1_{\{h_i(t; y) \leq z\}}. \end{aligned} \quad (4.3.15)$$

The conditioning argument is classical. We have used [74, p.183] for the forward and [121, p.67] for the backward arguments, respectively.

## 4.4 Summary

---

The addition of drag allowed a more detailed physical understanding of the system mechanics. Drag was shown to strongly influence the disk's motion under force, which resulted in significant changes in bond dynamics, under the two force profiles considered in this study. For constant force it was shown that the disk moves towards equilibria depending on the force magnitude and the number of bonds. When rebinding is considered, this was shown to generate stable equilibria, for forces below a critical force. Forces larger than this critical value were found to destabilize the cluster. It was also shown that a large force considerably reduces cluster lifetime, but the catastrophic failure of bonds (instantaneous jump between probabilities  $P_{10}(t)$  and  $P_0(t)$ ) predicted in [31], was not spotted, even for very large values of force. The interplay between force and drag was examined using cluster dissociation time and displacements, as well as averages and standard deviations of the bond population. For large drag, the disk barely moves and the cluster's evolution is largely dictated by bond kinetics, while for small drag bond dynamics are enslaved to the motion of the disk. In between, there is a transient regime, where the bonds break as the disk moves.

Drag has an even more profound impact when the disk is under ramped force. It was shown that large values of drag allow the bonds to extend at a slower rate, hence to survive for longer. At the same time, force has the time to build up, resulting in a very abrupt terminal decay. We also simulated cluster statistics aimed at mimicking dynamic force spectroscopy experiments. Adding drag significantly changes the profile of the rupture force distributions. If in the absence of drag the distributions were overlapping to an appreciable degree, adding drag induces an increasingly pronounced separation. The behaviour of clusters is even more distinct, as the cluster dimension increases and the bonds are gradually exposed to larger forces, until they eventually break. The expected sudden cluster dissociation for large values of drag and loading rate, is evident in Fig. 4.21.

A possible PDE formulation for the time-evolution of the probability density of the stochastic process  $(N, H)$  was examined, following the work of [91]. A solution based on the method of characteristics was developed, and compared against stochastic simulations, showing a good agreement for large values of drag, but a poor agreement for the late phase of the cluster decay. We have identified two potential reasons for this outcome. One is associated with the difficulty of solving the PDE system using a characteristic-based method. The complicated nature of the solution geometry is largely generated by the characteristics converging curve. This generates solutions resembling a Dirac distribution of decreasing magnitude, for certain values of the parameters. Moreover, the density  $p_k$  represents a source term used to compute  $p_{k-1}$ , which significantly complicates the problem. However, we were able to obtain reliable numerical solutions in some parts of the parameter space. A different possibility is that the problem may not even admit a PDE formulation, at all. This is suggested by the complicated nature of the marginal probabilities  $P_k(t; 0, h_0)$ , solved explicitly for the initial condition (4.3.4). As the solution was a multi-dimensional integral with time-dependent limits, it is expected that the formula for the density  $p_k(h, t)$  is even more complicated. To address this issue, we have developed in §4.3.4 forward (4.3.14) integro-differential formula, for the evolution of the probability densities corresponding to the bivariate stochastic process  $(N, H)$ .

In Chapter 5 we shall also address spatial effects induced by the differential stretching of bonds located beneath a flexible membrane.

# Appendix

## 4.A Exact analytical solutions for $P_k(t; 0, h_0)$

---

In certain cases, analytical formulae for the probability functions characterizing the cluster dynamics can be obtained. The theory of simple death processes with time-dependent rates is used to obtain the probabilities  $P_k(t; 0, h_0)$  (2.2.10) defined in §2.2.2. The first rupture occurring in a cluster having  $k$  out of  $n$  closed bonds left is referred to as “the rupture of the  $k$ -th bond”, for  $k = 1, \dots, n$ .

Consider that  $k = 1, \dots, n$  bonds are attached at time  $t$ , let  $u$  be the time of the last rupture and  $h_u \equiv H(u)$ . The transition rate at this moment (from (2.1.12)) is denoted by

$$\lambda_k(t; u, h_u) = ke^{\beta(H_k(t; u, h_u) - 1)}, \quad t \geq u. \quad (4.A.1)$$

Let  $T_k(u, h_u)$  be the time when one of the  $k$  remaining closed bonds ruptures, provided that last rupture occurred at time  $u$  and height  $h_u$ .

Denote by  $P_k^+(t; u, h_u) = \Pr\{T_k \geq t \mid H(u) = h_u\}$ , the probability that the rupture of the  $k$ -th bond occurs after time  $t$ , when we start from the initial condition  $(u, h_u)$ .

The distribution of  $T_k(u, h_u)$  is given by

$$P_k^-(t; u, h_u) = \Pr\{T_k < t \mid H(u) = h_u\} = 1 - P_k^+(t; u, h_u), \quad (4.A.2)$$

while the density of  $T_k(u, h_u)$  is given by the formula

$$f_k(t; u, h_u)\Delta t = \Pr\{t \leq T_k < t + \Delta t \mid H(u) = h_u\}, \quad \Delta t > 0, \quad (4.A.3)$$

which as  $\Delta t \rightarrow 0$  becomes

$$f_k(t; u, h_u) = \frac{\partial P_k^-(t; u, h_u)}{\partial t} = -\frac{\partial P_k^+(t; u, h_u)}{\partial t}. \quad (4.A.4)$$

**Solution for  $P_n$** 

We first compute  $P_n(t; 0, h_0)$ . Since the probability to have  $n$  bonds at time  $t$  is the same as the probability that the first rupture occurs after time  $t$ , we have

$$P_n(t; h_0, 0) = P_n^+(t; 0, h_0) = \Pr\{T_n \geq t \mid H(0) = h_0\}.$$

The transition rate from the state with  $n$  closed bonds and initial height  $h_0$  is  $\lambda_n(t; 0, h_0) = ne^{\beta(H_n(t; 0, h_0) - 1)}$ . For a small  $\Delta t > 0$ , the change in  $P_n$  in the time interval  $[t, t + \Delta t]$  is given by

$$P_n(t + \Delta t; 0, h_0) = P_n(t; 0, h_0)(1 - \lambda_n(t; 0, h_0))\Delta t,$$

so as  $\Delta t \rightarrow 0$  we obtain

$$\frac{dP_n(t; 0, h_0)}{dt} = -\lambda_n(t; 0, h_0)P_n(t; 0, h_0), \quad (4.A.5)$$

with the initial condition  $P_n(0; 0, h_0) = 1$ .

The solution of (4.A.5) is obtained by direct integration

$$P_n(t; 0, h_0) = e^{-\int_0^t du \lambda_n(u; 0, h_0)}. \quad (4.A.6)$$

From (4.A.2) we obtain  $P_n^-(t; 0, h_0) = 1 - e^{-\int_0^t du \lambda_n(u; 0, h_0)}$ , while (4.A.4) yields

$$f_n(t; 0, h_0) = \lambda_n(t; 0, h_0)e^{-\int_0^t du \lambda_n(u; 0, h_0)}. \quad (4.A.7)$$

Before proceeding with the other cases, we derive some useful relations. First, the probability of having no rupture in the time interval  $[u, t]$  when the disk starts at time  $u$  and height  $h_u$  with  $k = 1, \dots, n$  bonds attached is computed as above

$$P_k^+(t; u, h_u) = e^{-\int_u^t ds \lambda_k(s; u, h_u)}, \quad (4.A.8)$$

where  $\lambda_k$  is given by (4.A.1). The densities  $f_k$  are obtained as

$$f_k(t; u, h_u) = \lambda_k(t; u, h_u)e^{-\int_u^t ds \lambda_k(s; u, h_u)}. \quad (4.A.9)$$

**Solution for  $P_{n-1}$** 

The next step is to find  $P_{n-1}(t; 0, h_0)$ . Since we only have  $(n - 1)$  closed bonds at time  $t$ , we analyze all single trajectories in the  $(t, h)$ -space which could contribute to this probability. A single path contributes  $P_{n-1}$  at time  $t$  if the rupture of the  $n$ -th bond takes place at a time  $u$  with  $0 \leq u \leq t$ , and then nothing happens until  $t$ . This can be expressed as

$$P_{n-1}(t; 0, h_0) = \int_0^t du f_n(u; 0, h_0) P_{n-1}^+(t; u, H_n(u; 0, h_0)), \quad (4.A.10)$$

and (4.A.10) becomes

$$P_{n-1}(t; 0, h_0) = \int_0^t du f_n(u; 0, h_0) e^{-\int_u^t ds \lambda_{n-1}(s; u, H_n(u; 0, h_0))}. \quad (4.A.11)$$

Replacing  $f_n$  from (4.A.7) we obtain

$$P_{n-1}(t; 0, h_0) = \int_0^t du \lambda_n(u; 0, h_0) e^{-\int_0^u ds \lambda_n(s; 0, h_0)} e^{-\int_u^t ds \lambda_{n-1}(s; u, H_n(u; 0, h_0))}. \quad (4.A.12)$$

**Solution for  $P_k$ ,  $k = 0, \dots, n - 2$**

Obtaining explicit formulae for  $P_k$ , where  $k = 0, \dots, n - 2$ , needs the use of more appropriate notation. Denote by  $u_k$  the time when one of the remaining  $k$  closed bonds ruptures where clearly  $0 \leq u_n \leq u_{n-1} \leq \dots \leq u_1$ .

Define  $h_n = H_n(u_n; 0, h_0)$  to be the height of the disk at the moment of the first rupture. For  $k = 1, \dots, n$  we obtain recursively

$$h_k = H_k(u_k; u_{k+1}, h_{k+1}) = H_k(u_k; u_{k+1}, H_{k+1}(u_{k+1}; u_{k+2}, h_{k+2})) = \dots$$

Clearly,  $h_1$  is a function of  $u_1, u_2, \dots, u_n$ . When  $f$  is constant one obtains

$$h_{n-1} = H_{n-1}(u_{n-1}; u_n, h_n) = H_{n-1}(u_{n-1} - u_n; 0, h_n) = H_{n-1}(u_{n-1} - u_n; 0, H_n(u_n; 0, h_0)),$$

...

$$h_1 = H_1(u_1 - u_2; 0, h_2) = H_1(u_1 - u_2; 0, H_2(u_2 - u_3; 0, H_3(\dots H_n(u_n; 0, h_0) \dots))).$$

Analyzing all the paths which could contribute, the probability  $P_{n-2}$  is obtained as

$$P_{n-2}(t; 0, h_0) = \int_0^t du_n f_n(u_n; 0, h_0) \int_{u_n}^t du_{n-1} f_{n-1}(u_{n-1}; u_n, h_n) P_{n-2}^+(t; u_{n-1}, h_{n-1}). \quad (4.A.13)$$

This relation is easily generalized to

$$P_k(t; 0, h_0) = \int_0^t du_n f_n(u_n; 0, h_0) \int_{u_n}^t du_{n-1} f_{n-1}(u_{n-1}; u_n, h_n) \dots \int_{u_{k+2}}^t du_{k+1} f_{k+1}(u_{k+1}; u_{k+2}, h_{k+2}) P_k^+(t; u_{k+1}, h_{k+1}), \quad (4.A.14)$$

where  $P_k^+$  and  $f_k(u_k; u_{k+1}, h_{k+1})$  are given by (4.A.8) and (4.A.9) respectively.

To compute  $P_k(t; 0, h_0)$  an  $n - k + 1$  dimensional integral for  $u_{k+1}, \dots, u_n$  and  $P_k^+$  has to be estimated, which is only practical for small clusters.

### Probability density and cumulative distribution over $h$ of having $k$ bonds at time $t$

The next thing to do would be to obtain some analytical formulae for the distribution of the probabilities  $P_k(t; 0, h_0)$  defined in (2.2.10) over  $h$ , using the cumulative distributions and densities  $F_k(t, h; 0, h_0)$  and  $p_k(t, h; 0, h_0)$ , defined by (2.2.14) and (2.2.16).

**Probabilities for  $k = n$** 

In this case the distribution of  $P_n(t; 0, h_0)$  is easy to track in  $(t, h)$ -space, since the only paths contributing to the probability  $P_n(t; 0, h_0)$  (hence to  $F_n(t, h; 0, h_0)$  and  $p_n(t, h; 0, h_0)$ ) are the ones moving along  $H_n(s; 0, h_0)$  for the time  $s \geq t$ . We clearly obtain

$$F_n(t, h; 0, h_0) = \begin{cases} 0, & h < H_n(t; 0, h_0), \\ P_n(t; 0, h_0), & h \geq H_n(t; 0, h_0), \end{cases} \quad (4.A.15)$$

which means essentially that at time  $t$  we have a step function with the jump at height  $H_n(t; 0, h_0)$  and magnitude  $P_n(t; 0, h_0)$ .

The density  $p_n(t, h; 0, h_0)$  be expressed as follows

$$p_n(t, h; 0, h_0) = \frac{\partial F_n(t, h; 0, h_0)}{\partial h} = P_n(t; 0, h_0) \delta(h - H_n(t; 0, h_0)), \quad (4.A.16)$$

where  $\delta(h - H_n(t; 0, h_0))$  stands for the Dirac  $\delta$  function, and  $P_n$  is given by (4.A.6).

**Probabilities for  $k = n - 1$** 

The paths contributing to the probability  $P_{n-1}(t; 0, h_0)$  have only a rupture in the time interval  $[0, t]$ , which determines  $H(t)$  uniquely in the interval  $[H_n(t; 0, h_0), H_{n-1}(t; 0, h_0)]$ .

For a fixed value of  $t > 0$  define the bijective function (only without rebinding)  $\mathcal{H}_t : [0, t] \rightarrow [H_n(t; 0, h_0), H_{n-1}(t; 0, h_0)]$ , given by the formula

$$\mathcal{H}_t(u) = H_{n-1}(t; u, H_n(u; 0, h_0)),$$

and by  $\mathcal{H}_t^{-1} : [H_n(t; 0, h_0), H_{n-1}(t; 0, h_0)] \rightarrow [0, t]$  its inverse. For a fixed  $h$  consider  $u = \mathcal{H}_t^{-1}(h)$ . Since the segments starting at the same times and heights are steeper as the number of closed bonds decreases, the paths satisfying  $H(t) \leq h$  are exactly the ones for which  $u_n \geq u$ , so

$$F_{n-1}(t, h; 0, h_0) = \int_{\mathcal{H}_t^{-1}(h)}^t du_n f_n(u_n; 0, h_0) P_{n-1}(t; u_n, h_n), \quad (4.A.17)$$

where  $u_n, h_n$  and  $f_n$  are those defined as in the previous section. The densities are obtained as follows

$$\begin{aligned} p_{n-1}(t, h; 0, h_0) &= \frac{\partial F_{n-1}(t, h; 0, h_0)}{\partial h} = - \frac{d\mathcal{H}_t^{-1}(h)}{dh} f_n(u; 0, h_0) P_{n-1}^+(t; u, H_n(u; 0, h_0)) \\ &= - \frac{1}{d\mathcal{H}_t(u)} dt f_n(u; 0, h_0) P_{n-1}^+(t; u, H_n(u; 0, h_0)). \end{aligned} \quad (4.A.18)$$

It is known from the literature [21, 83, 111] that in the presence of rebinding, or for  $k \leq n - 2$ , only numerical approximations are usually possible and the most common

approach is to use Monte-Carlo simulations developed in Chapter 2. It can be easily shown that in the zero-drag limit we obtain the formulas predicted in [31], for constant force and vanishing rebinding.

In the general case, we can still say that due to geometrical constraints, the paths contributing to  $F_k$  can not reach the region below  $H_n(t; 0, h_0)$  or the region above  $H_k(t; 0, h_0)$ , for  $k = 0, \dots, n$  so the distributions are locally constant outside the region between the curves  $H_n(t; 0, h_0)$  and  $H_k(t; 0, h_0)$ , that is

$$F_k(t, h; 0, h_0) = \begin{cases} 0, & h < H_n(t; 0, h_0), \\ P_k(t; 0, h_0), & h \geq H_k(t; 0, h_0). \end{cases} \quad (4.A.19)$$

## 4.B The differential Chapman-Kolmogorov Equation (dCKE)

---

In this appendix we discuss a PDE formulation suitable for the analysis of stochastic processes with joint continuous and discrete state space, based on [91].

### 4.B.1 The dCKE for the disk-bonds model

Following the steps used by Lipniacki *et al.* in [91], we derive the dCKE corresponding to a Markov process which consists of a piecewise deterministic motion described by the continuous r. v.  $H(t)$ , which depends on the stochastic jumps of the discrete r. v.  $N(t)$ , which takes values  $\{0, 1, \dots, n\}$ . The boundary  $N(t) = 0$  is assumed to be absorbing (rebinding is no longer possible once complete dissociation is attained), while the boundary  $N(t) = n$  is assumed to be reflecting (once we have  $n$  bonds, the following event is a rupture). In the case when the Brownian fluctuations of the disk are significant, we can use a global description of our problem, as a system of SDEs. For the moment, since the motion of the disk is piecewise deterministic, we will describe the evolution of the height in terms of single realizations of the r.v.  $N(t)$ .

#### Derivation

For the moment assume that  $N = N(t)$  is a right-continuous function having the domain and codomain defined as

$$N : [0, \infty) \rightarrow \{0, 1, \dots, n\}. \quad (4.B.1)$$

The displacement can be represented by a family of autonomous ODEs of the form

$$\begin{aligned} \frac{dH}{dt}(t; h_0, 0) &= v(H, N), \quad t \geq 0, \\ H(0; h_0, 0) &= h_0, \end{aligned} \quad (4.B.2)$$

where  $h_0 \in \mathbb{R}$ , and  $H = H(t; h_0, 0)$ ,  $v$  are real valued functions.

The functions  $v$  are assumed to be continuous and bounded, having the domain and codomain given by

$$v : D \times \{0, 1, \dots, n\} \rightarrow \mathbb{R}. \quad (4.B.3)$$

The domain  $D = [0, d]$  is considered to be invariant for the system i.e., for initial conditions  $h_0 \in D$  and any  $N(t)$ , we have  $H(t) \in D$ . This is indeed the case for  $N = 1, \dots, n$  for constant force  $f$ , while for  $N = 0$  we could use a different equation for  $v(H, 0)$ , since the disk escapes from the region where the thin-film approximation applies (see Chapter 3).

For a given  $N(t)$ , the solution of the system (4.B.2) extended from value  $H_s$  at time  $s$  is denoted by simply

$$H(t) = H(t; H_s, s), \quad t \geq s, \quad (4.B.4)$$

and defines a mapping  $H^*(\cdot; s, t) = H(t; \cdot, s) : \mathbb{R} \rightarrow \mathbb{R}$ , which represents a translation from  $s$  to  $t$ , along the solution of the ODE (4.B.2) (see [91]).

We can now go back to our problem, where the function  $N(t)$  is itself a continuous-time finite Markov chain with finite state space. Provided that at time  $t \geq 0$  we have  $N(t) = k \in 0, 1, \dots, n$  and a small  $\Delta t > 0$  is chosen, there is at most one event (rupture or rebinding) which could happen in the time interval  $[t, t + \Delta t]$ . In this case, at time  $t + \Delta t$  we could only have  $N(t + \Delta t) \in \{k - 1, k, k + 1\}$ . In terms of probabilities this writes as

$$\Pr\{N(t + \Delta t) = k - 1 \mid N(t) = k\} = \lambda_{k, k-1}(H(t)) \Delta t + o(\Delta t), \quad (4.B.5)$$

$$\Pr\{N(t + \Delta t) = k + 1 \mid N(t) = k\} = \lambda_{k, k+1}(H(t)) \Delta t + o(\Delta t),$$

$$\Pr\{N(t + \Delta t) = k \mid N(t) = k\} = \left[ 1 - \lambda_{k, k-1}(H(t)) - \lambda_{k, k+1}(H(t)) \right] \Delta t + o(\Delta t),$$

where  $\lambda_{k, k-1}(H)$  and  $\lambda_{k, k+1}(H)$  represent the rupture and rebinding rates defined by (2.2.1a), in §2.2.1. Since number of closed bonds only varies in the range  $\{0, 1, \dots, n\}$ , we use the convention  $\lambda_{0, -1} = \lambda_{n, n+1} = 0$ . Since the boundary  $N(t) = 0$  is absorbing, the transition rate  $\lambda_{0, 1}$  also vanishes. These rates are bounded and continuous on  $D$ . As one could see, the transition intensities of the process  $N$  are coupled to the solution of the ODE system (4.B.2).

We shall derive the evolution equation for the joint distributions of the random variables  $H(t)$  (continuous) and  $N(t)$  (discrete), at a given time  $t$ . Consider  $k \in 0, \dots, n$ ,  $h \in D$  and denote by  $p_k(h, t)$  the joint function of probability density (in  $H(t)$ ) and probability (in  $N(t)$ ). It is assumed that the initial condition  $p_n(h, 0)$  is known for any

value of  $h$ . We can define the probability function

$$P_k^*(h, \Delta h, t) = \Pr\{H(t) \in (h, h + \Delta h), N(t) = k\} \quad (4.B.6)$$

$$= p_k(h, t)\Delta h + o(\Delta h). \quad (4.B.7)$$

For  $t \geq 0$ , we also define  $P_k(h, \Delta h, t, \Delta t)$  as

$$P_k(h, \Delta h, t, \Delta t) = \Pr\{H_t, H(t + \Delta t; H_t, t) \in (h, h + \Delta h), N(t + \Delta t) = k\}, \quad (4.B.8)$$

representing the probability that  $H_{t+\Delta t}$  falls into the region  $(h, h + \Delta h)$  containing solutions of system (4.B.2), provided that at time  $t$  we also had  $H_t \in (h, h + \Delta h)$  and the number of bonds satisfies  $N(t + \Delta t) = k$ .

The major difference between  $P_k^*$  and  $P_k$  is that the first one considers the situation when  $N(t) = k$ , while the latter takes  $N(t + \Delta t) = k$ . In the case when  $N(t) = k$  no jump occurs in the time interval  $(t, t + \Delta t]$ , (so  $N(t + \Delta t) = 0$  as well), we have

$$P_k(h, \Delta h, t, \Delta t) = P_k(h, \Delta h, t, 0) = P_k^*(h, \Delta h, t). \quad (4.B.9)$$

Assuming small  $\Delta t$  and  $N(t + \Delta t) = k$ , then at time  $t$  we could only have  $N(t) \in \{k - 1, k, k + 1\}$ .

Balancing the inputs and outputs in the time interval  $[t, t + \Delta t]$ , we find that  $P_k$  satisfies

$$\begin{aligned} P_k(h, \Delta h, t, \Delta t) &= P_k^*(h, \Delta h, t) \left[ 1 - \sum_{l \in \{k-1, k+1\}} \lambda_{k,l}(H(t))\Delta t - o(\Delta t) \right] \\ &+ \sum_{l \in \{k-1, k+1\}} P_l^*(h, \Delta h, t) \left[ \lambda_{l,k}(H(t))\Delta t - o(\Delta t) \right]. \end{aligned} \quad (4.B.10)$$

Using the notation  $\lambda_{kk} = -(\lambda_{k,k-1} + \lambda_{k,k+1})$  and the relations (4.B.9) and (4.B.10), as  $\Delta \rightarrow 0$  we obtain

$$\begin{aligned} \left. \frac{\partial P_k(h, \Delta h, t, \Delta t)}{\partial \Delta t} \right|_{\Delta t=0} &= \lim_{\Delta \rightarrow 0} \frac{P_k(h, \Delta h, t, \Delta t) - P_k(h, \Delta h, t, 0)}{\Delta t} \\ &= P_k^*(h, \Delta h, t)\lambda_{kk}(H(t)) + P_{k-1}^*(h, \Delta h, t)\lambda_{k-1,k}(H(t)) + P_{k+1}^*(h, \Delta h, t)\lambda_{k+1,k}(H(t)), \end{aligned} \quad (4.B.11)$$

As which is in fact the partial derivative at  $\Delta t = 0$ .

An integral formula for  $P_k(h, \Delta h, t, \Delta t)$  is derived using Fig. 4.26. Note that the solutions of (4.B.2) starting within the interval  $(h, h + \Delta h)$ , end in the range

$$\tilde{H} = H^* \left( (h, h + \Delta h); t, t + \Delta t \right).$$

Since we want to obtain all the paths having  $N(t + \Delta t) = k$ , we obtain

$$P_k(h, \Delta h, t, \Delta t) = \int_{\tilde{H}} p_k(\xi, t + \Delta t) d\xi, \quad k = 0, \dots, n. \quad (4.B.12)$$

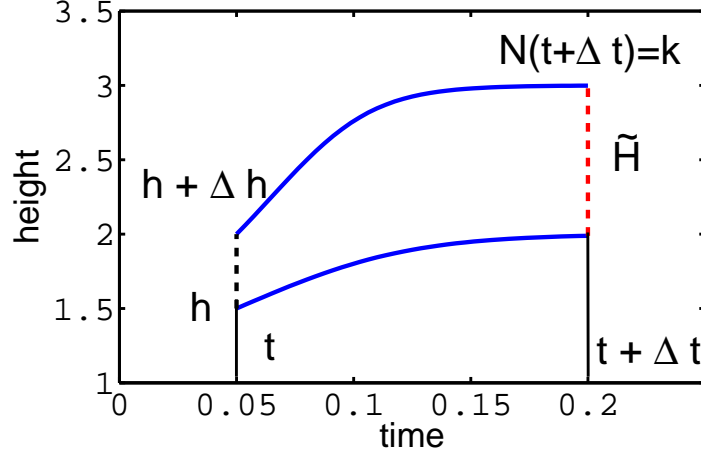


**Figure 4.26:** Scheme used for the derivation of the probability function  $P_k(h, h + \Delta h, t, t + \Delta t)$ .

Since  $\tilde{H}$  is not easily representable, we use a change of variable  $\zeta = H^*(u; t, t + \Delta t)$  to obtain

$$P_k(h, \Delta h, t, \Delta t) = \int_h^{h+\Delta h} \left| \frac{dH^*(u; t, t + \Delta t)}{du} \right| p_k \left( H^*(u; t, t + \Delta t), t + \Delta t \right) du, \quad (4.B.13)$$

which holds for  $k = 0, \dots, n$ .

We also have

$$P_k(h, \Delta h, t, 0) = P_k^*(h, \Delta h, t) = \int_h^{h+\Delta h} p_k(u, t) du, \quad k = 0, \dots, n. \quad (4.B.14)$$

Following the computations of Lipniacki [91] which involve the sensitivity matrix defined in [124, Chapter 11], we find that

$$\left| \frac{dH^*(u; t, t)}{du} \right| = 1, \quad (4.B.15)$$

and

$$\frac{d}{d\Delta t} \left\{ \left| \frac{dH^*(u; t, t + \Delta t)}{du} \right| \right\}_{\Delta t=0} = \frac{\partial v(u, N(t))}{\partial u}. \quad (4.B.16)$$

Replacing (4.B.14) into (4.B.11), differentiating under the integral sign in (4.B.13) and using (4.B.15), (4.B.16), we finally obtain

$$\frac{\partial P_k(h, \Delta h, t, \Delta t)}{\partial \Delta t} \Big|_{\Delta t=0} = \int_h^{h+\Delta h} \left\{ \frac{\partial p_k(u, t)}{\partial t} + \frac{\partial v(u, k)}{\partial u} p_k(u, t) + v(u, k) \frac{\partial p_k(u, t)}{\partial u} \right\} du. \quad (4.B.17)$$

Comparing (4.B.11), (4.B.17) and using (4.B.14), the evolution equation for  $p_k$  is ob-

tained as a system of first-order linear PDEs:

$$\begin{aligned} \frac{\partial p_k(h, t)}{\partial t} + \frac{\partial v(h, k)}{\partial h} p_k(h, t) + v(h, k) \frac{\partial p_k(h, t)}{\partial h} = \\ p_k(h, t) \lambda_{kk}(H(t)) + \sum_{l \in \{k-1, k+1\}} p_l(h, t) \lambda_{l, k}(H(t)), \quad k = 0, 1, \dots, n. \end{aligned} \quad (4.B.18)$$

In a compact form the above system can be written as

$$\frac{\partial p_k(h, t)}{\partial t} + \frac{\partial}{\partial h} \left[ v(h, k) p_k(h, t) \right] = p_k(h, t) \lambda_{kk}(H(t)) + \sum_{l \in \{k-1, k+1\}} p_l(h, t) \lambda_{l, k}(H(t)), \quad (4.B.19)$$

for  $k = 0, 1, \dots, n$ .

### Preservation of probability property

It can be proven that at each time  $t$  the joint densities  $p_k$  have the preservation of probability property. Adding equations (4.B.19) for  $k = 0, \dots, n$  one obtains

$$\sum_{k=0}^n \frac{\partial p_k(h, t)}{\partial t} + \frac{\partial}{\partial h} \left[ v(h, k) p_k(h, t) \right] = 0, \quad (4.B.20)$$

where we used the relation for the total leaving rate from state  $N(t) = k$  given by

$$\lambda_{kk} = - \sum_{l \in \{k-1, k+1\}} \lambda_{k, l}.$$

Since we assumed the existence of the invariant domain  $D$  for system (4.B.2), for all  $k$  and  $t$  we have  $\text{supp } p_k(\cdot, t) \subseteq D$ . We show that the integral of the marginal distribution  $\rho(h, t)$  defined as

$$\rho(h, t) = \sum_{k=0}^n p_k(h, t), \quad (4.B.21)$$

is preserved in time, using equation (4.B.20).

Let  $[a, b]$  be a real interval such that  $\text{cl } D \subset (a, b)$ . For this interval we have the boundary conditions

$$p_k(a, t) = p_k(b, t) = 0, \quad k = 0, \dots, n. \quad (4.B.22)$$

Applying the Newton-Leibnitz formula to the marginal distribution  $\rho$  and the values of  $p_k$  on the boundaries given by (4.B.22), we obtain

$$\frac{\partial}{\partial t} \int_a^b \rho(h, t) dh = - \sum_{k=0}^n \int_a^b \frac{\partial}{\partial h} \left[ v(h, k) p_k(h, t) \right] dh \quad (4.B.23)$$

$$\begin{aligned} &= - \sum_{k=0}^n \left[ v(b, k) p_k(b, t) - v(a, k) p_k(a, t) \right] \\ &= 0. \end{aligned} \quad (4.B.24)$$

This proves that the marginal distribution is time invariant. The value of the marginal distributions norming  $\int_a^b \rho(h, t) dh$  is not determined by the system (4.B.19) itself, so we can impose

$$\int_a^b \rho(h, t) dh = 1.$$

This feature can be explained as follows. Since the system (4.B.2) describes the motion of a particle in the  $\mathbb{R} \times \{0, 1, \dots, n\}$  space, the conservation of marginal probability norming is a natural consequence of the fact that the particle remains in the  $D \times \{0, 1, \dots, n\}$  subdomain.

### 4.B.2 Initial conditions

Different assumptions about the experimental setup require the consideration of several types of initial condition, generated by the position of the disk relative to an equilibrium. In the ideal case when in all experiments the disk starts from the same height, the initial height is sampled from a *Dirac distribution* centered about the equilibrium position. Since all experiments are subject to error we could also assume that the initial height is sampled from a *normal distribution*  $N(h_0, \sigma^2)$ , where the standard deviation  $\sigma > 0$  is a parameter to be estimated from measurements.

In the one dimensional case, the forward equation describing the evolution of the cluster in the velocity field  $v(h, k)$  is

$$\begin{aligned} \frac{\partial p_k(h, t)}{\partial t} + \frac{\partial}{\partial h} [v(h, k)p_k(h, t)] = & \quad (4.B.25) \\ = - [r_k(H(t)) + g_k(H(t))] p_k(h, t) + g_{k-1}(H(t))p_{k-1}(h, t) + r_{k+1}(H(t))p_{k+1}(h, t), \end{aligned}$$

where for a fixed  $k = 0, \dots, n$ , the displacement  $H$  satisfies  $\frac{dH(t)}{dt} = v(H(t), k)$ . The rupture and rebinding rates

$$\begin{aligned} r_k(H) &= \lambda_{k, k-1}(H) = ke^{\beta(H-1)}, \\ g_k(H) &= \lambda_{k, k+1}(H) = \gamma(n-k)e^{-\alpha(H-1)}, \end{aligned}$$

defined in §2.1.3 or §4.3.1.

#### Impulse initial condition.

Assuming the initial displacement of the disk  $h_0$  is constant over different experiments, the initial condition for the system (4.B.25) is

$$p_k(h, 0) = \begin{cases} \delta(h - h_0), & \text{if } k = n; \\ 0 & \text{if } k \leq n - 1, \end{cases} \quad (4.B.26)$$

where  $\delta$  is the Dirac delta function. We shall call this the *impulse initial condition*.

### Initial height sampled from a normal distribution.

Repeating the experiment with the detachment of the disk several times it is unlikely to start each time from the same initial position. It is then reasonable to assume that the initial height is sampled from a normal distribution  $N(h_0, \sigma^2)$ . This initial condition for (4.B.25) writes as

$$p_k(h, 0) = \begin{cases} \frac{1}{\sigma\sqrt{2\pi}} e^{-\frac{(h-h_0)^2}{2\sigma^2}}, & \text{if } k = n; \\ 0 & \text{if } k \leq n - 1. \end{cases} \quad (4.B.27)$$

and will be called the *normal initial condition*.

### 4.B.3 Solution of the dCKE using the method of characteristics

The most effective and popular method for the numerical solution of hyperbolic equations is via the method of characteristics. If the initial data is smooth, this method is the most reliable companion to the stochastic simulations.

The system of PDEs (4.B.25) is generally called a *linear advection* or *transport equation*, describing the evolution of the probability density  $p_k$  in a flow having the velocity field  $v(h, k)$ . Although possibly of the simplest PDE, this simplicity is deceptive in the sense that it can be very difficult to integrate numerically since it propagates discontinuities, a distinctive feature of first order hyperbolic PDEs [110]. The difficulty is enhanced by the nonlinearity of the velocity field.

The idea of this method is to transform the system of PDEs into a system of ODEs which can be solved along some curves called characteristics. Stepping in  $t$  is then replaced with stepping along a characteristic line.

In the absence of rebinding,  $p_k$  only depends on  $p_{k+1}, \dots, p_n$  for  $k = 0, \dots, n$ . The system of PDE's (4.B.25) to be solved recurrently becomes

$$\begin{cases} \frac{dh}{dt} = -(1/c) \left[ kh^4 - (k+f)h^3 \right], & h(0) = h^0, \\ \frac{dp_k}{dt} = - \left[ ke^{\beta(h-1)} + \frac{dv(h,k)}{dh} \right] p_k(h, t) + (k+1)e^{\beta(h-1)} p_{k+1}(h, t), \end{cases} \quad (4.B.28)$$

where  $p_{n+1} \equiv 0$ , and the initial condition  $p_k(h^0, 0)$  satisfies (4.B.27).

#### Characteristic curves

The properties of the characteristic curves have a significant impact on the solution of (4.B.28), since they determine the direction along which the initial configuration is

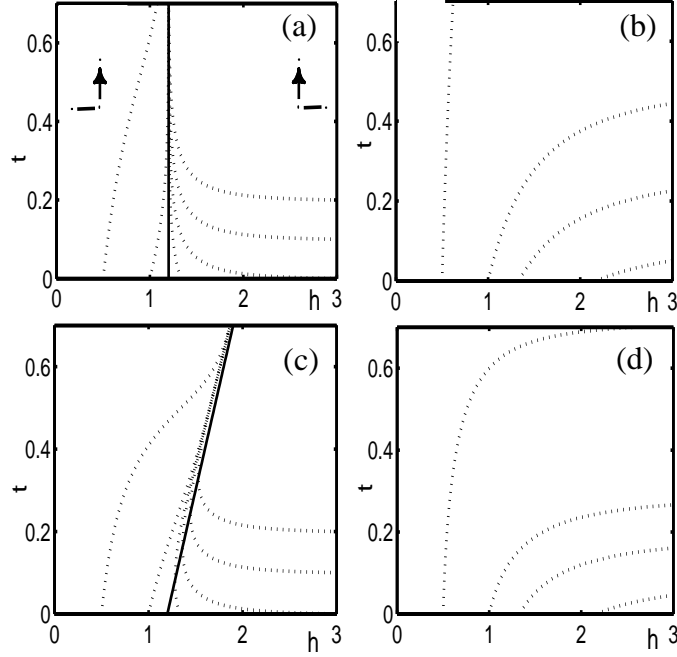


**Figure 4.27:** Characteristic curves for  $c = 1$ . *a)*  $k = 5, f = 1$ ; *b)*  $k = 0, f = 1$ ; *c)*  $k = 5, f = 5t + 1$ ; *d)*  $k = 0, f = 5t + 1$ . The stencils suggest the scheme used in a FD difference algorithm. If the disk moves upwards we use a downwind scheme, while in the other case an upwind scheme.

transported. In the general case of time-dependent force, the characteristic curve corresponding to  $k = 0, \dots, n$  closed bonds which starts from the initial height  $h^0$  satisfies

$$\frac{dh}{dt} = v(h, k, t) = -(1/c) \left[ kh^4 - (k + f(t)) h^3 \right], \quad h(0) = h^0. \quad (4.B.29)$$

The solution of the non-linear equation (4.B.29) is denoted by  $h(t)$ . Even for a constant force  $f$  (when  $v(h, k, t) = v(h, k)$ ), the characteristic curve  $h_k(t)$  can only be obtained as a function of  $t$  in implicit form, as

$$\frac{1}{\alpha_2^3} \left[ \ln \left( \left| \frac{h_k - \alpha_2}{h_k} \right| \right) + \frac{\alpha_2}{h_k} + \frac{1}{2} \left( \frac{\alpha_2}{h_k} \right)^2 \right] = \alpha_1 t + C,$$

where we have denoted

$$C = \frac{1}{\alpha_2^3} \left[ \ln \left( \left| \frac{t - \alpha_2}{t} \right| \right) + \frac{\alpha_2}{t} + \frac{1}{2} \left( \frac{\alpha_2}{t} \right)^2 \right],$$

and  $\alpha_1 = -k/c, \alpha_2 = f/k + 1$ .

The characteristic curves for constant and linearly ramped forces are sketched in Fig. 4.27. Note that for  $k = 1, \dots, n$  the characteristic curves approach the equilibrium curves  $h_{k,eq}(t) = \frac{f(t)}{k} + 1$ . For constant force these curves represent a constant height

$$\lim_{t \rightarrow \infty} h_k(t) = \frac{f}{k} + 1,$$

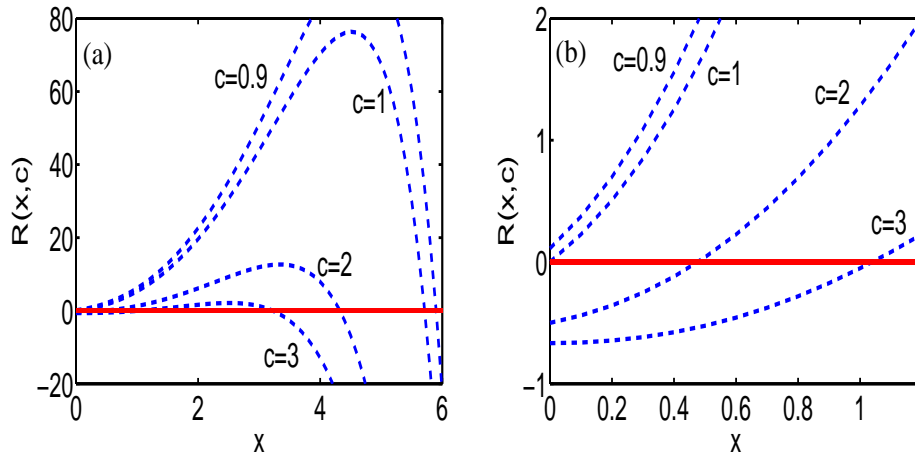


**Figure 4.28:** Plot of  $-e^{\beta x} + (1/c)(1+x)^3$  for  $\beta = 1$ , and  $c=0.9, 1, 2, 3$  a) All intersections with the horizontal axis; b) caption with the region near the origin.

provided that  $h_k(0) > 0$ .

For  $k = 0$  the disk moves upwards with a high velocity  $\left(\frac{dh}{dt} = \frac{f}{c}h^3\right)$ . The latter situation has to be amended since the disk soon escapes from the thin-film approximation region.

Since we don't have the characteristic curves in explicit analytic form, finding closed explicit formulas for the  $p_k$  along these curves is very unlikely (as it was the case for the analytical solution in the full  $(h, t)$  space). The evolution of  $p_k$  along these curves is depicted in Fig. 4.22.

#### 4.B.4 Qualitative behaviour of the dCKE solution: infinite-time limit

In this section the qualitative analysis of the dCKE solutions in the infinite-time limit is done. The performance of the dCKE is assessed for various drag regimes, by comparing the solutions obtained from the method of characteristic curves with the ones obtained from stochastic simulations.

The method of characteristics is particularly helpful in the analysis of the qualitative behaviour of the probability densities. We prove that the profile of  $p_k$  is driven in the long term by the behaviour of  $p_k$  along the characteristic curve  $h(t) = h_{k,eq}$ , and by the forcing regimes.

In the low force regime,  $p_k$  approaches a spike centered at  $h = h_{k,eq}$ , whose integral along the height coordinate vanishes for  $k = 1, \dots, n$ , while for large force the  $p_k$  only exhibits a decay of the initial probability in the long run.

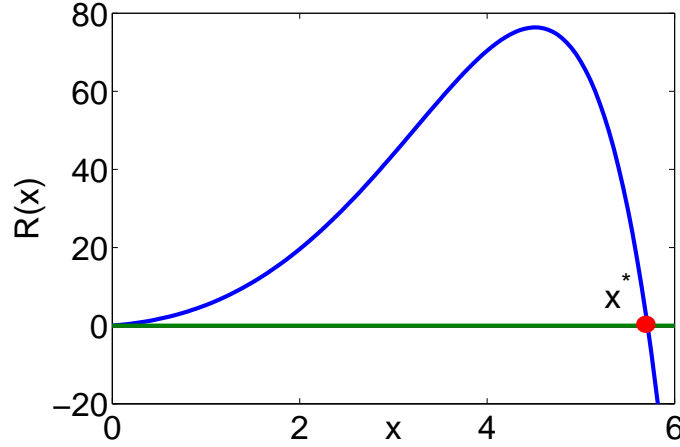


Figure 4.29: Plot of  $-e^{\beta x} + (1/c)(1+x)^3$  for  $c = \beta = 1$ .

### Evolution of $p_n$ along the equilibrium characteristic curve

As shown in Chapter 3, the characteristic curves describing the motion of the disk with  $n$  bonds attached in the absence of a rupture event, approach the equilibrium height  $h_{eq,n} = 1 + f/n$ . Along the constant height characteristic curve  $h(t) = 1 + f/n$ ,  $p_n$  satisfies

$$\frac{dp_n}{dt} \left( 1 + f/n, t \right) = n \left[ -e^{\beta(f/n)} + \frac{1}{c}(1 + f/n)^3 \right] p_n(1 + f/n, t). \quad (4.B.30)$$

For a fixed value of  $\beta$ , define the function  $R : [0, \infty) \rightarrow \mathbb{R}$

$$R(x) = -e^{\beta x} + \frac{1}{c}(1+x)^3, \quad (4.B.31)$$

representing the coefficient of  $p_n$  in (4.B.30), as a function of  $x$ , and also define the function  $R^* : [0, \infty) \rightarrow \mathbb{R}$

$$R^*(x) = (1+x)^3 e^{-\beta x}.$$

The maximum of  $R^*$  is  $R^*(x_0) = \left( 3/\beta \right)^3 \exp(\beta - 3)$ , attained for  $x_0 = 3/\beta - 1$ . Since  $\beta \simeq 1$ , we only focus on the case  $\beta = 1$ , for which maximal value is  $27/e^2$ . The profiles of  $R(x)$  for different values of  $c$  are sketched in Fig. 4.28.

It is shown that the profile of the  $p'_k$ s is determined by their position relative to the solutions of  $R(x) = 0$ . Depending on the drag coefficient  $c$ , the equation  $R(x) = 0$ , has

1. No solution for  $c > 27/e^2 \approx 3.6541$ .
2. Two (distinct) positive solutions for  $1 < c < 3.6541$ .
3. One negative and one positive solution for  $0 < c < 1$ .

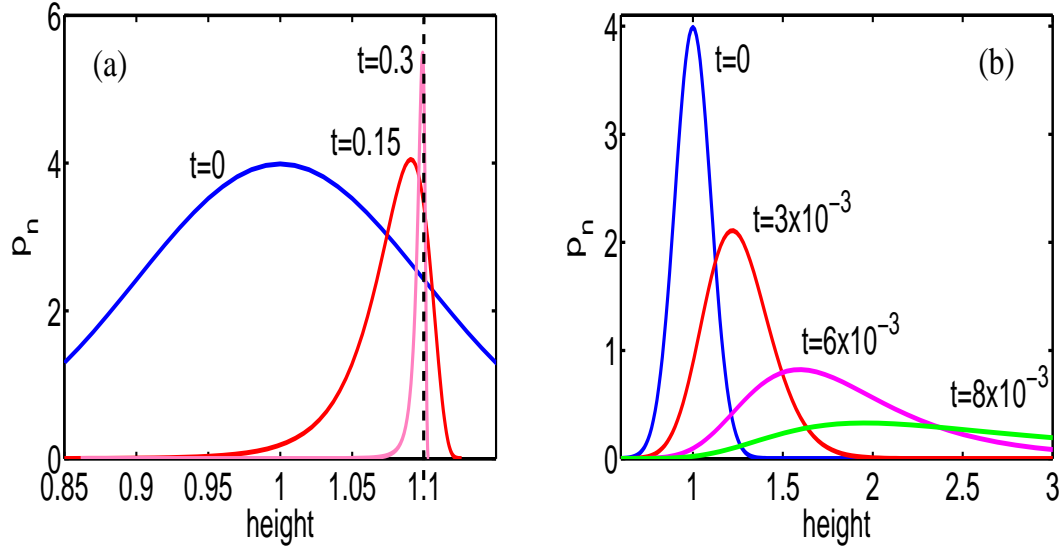


**Figure 4.30:** Force driven patterns for  $p_n$ , realized for  $n = 10$ ,  $c = 1$  and  $\beta = 1$ . a) Infinite spike  $f/n = 0.1 < x^*$  for  $f = 1$ ; b) Damped spike  $f/n = 6 > x^*$ , for  $f = 60$ .

The special cases are

4. A single positive solution (superposed solutions) for  $c = 3.6541$ .
5. Two distinct solutions:  $x^* = 0$  and  $x^* = 5.7114$  for  $c = 1$ .

Equation (4.B.30) is solved by

$$p_n(1 + f/n, t) = p_n(1 + f/n, 0)e^{nR(f/n)t}, \quad p_n(1 + f/n, 0) \geq 0, \quad (4.B.32)$$

If  $p_n(1 + f/n, 0) = 0$ , the trivial solution  $p_n(1 + f/n, t) = 0$ ,  $t > 0$  is obtained.

For  $p_n(1 + f/n, 0) > 0$ , the solution  $p_n(1 + f/n, t)$  is a decreasing (to 0 if  $R(f/n) < 0$ ) or increasing (to  $\infty$  if  $R(f/n) > 0$ ) exponential.

In the particular case  $c = 1$ , the different profile of  $p_n$  can be examined using Fig. 4.29. The solution  $x^*$  of  $R(x) = 0$  divides the force space into three regions. For a force verifying  $f/n < x^*$  (small force), one has  $R(f/n) > 0$ , so  $p_n(1 + f/n, t)$  increases to  $\infty$ . However,  $p_n$  shrinks with time as sketched in Fig. 4.30 (a), so the marginal distribution

$$P_n(t) = \int_0^\infty p_n(h, t)dh,$$

is expected to decrease to 0 as  $t \rightarrow \infty$ .

For a force verifying  $f/n > x^*$  (large force), one has  $R(f/n) < 0$  and  $p_n(1 + f/n, t)$  decays to 0 as in Fig. 4.30 (b).

For  $f/n = x^*$ , the solution is a constant function,  $p_n(1 + f/n, t) = p_n(1 + f/n, 0)$ .

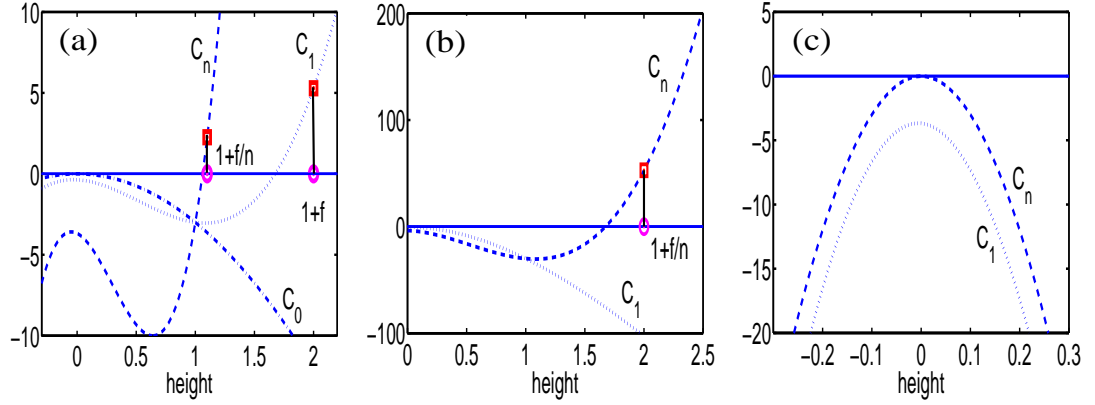


**Figure 4.31:** Coefficients  $C_k(h)$ ,  $k = 0, \dots, n$  obtained for  $n = 10$ ,  $c = 1$ , and  $\beta = 1$ , in three distinct force regimes (a) small force  $f/n < f = 1 < x^* = 5.7$ ; (b) medium force  $f/n < x^* < f = 10$ ; (c) large force  $x^* < f/n < f = 100$ .

### Evolution of $p_n$ along a general characteristic curve

The evolution of  $p_n$  along a characteristic curve starting at the initial height  $h^0 \neq 1 + f/n$ , follows in the same manner. Initially  $p_n$  evolves according with the sign of  $R(h^0)$ , while after the characteristic curve approaches the equilibrium, the profile is dominated by the sign of  $R(f/n)$ , and can be examined in Fig. 4.31.

### Profile of $p_k$ for $k = n - 1, \dots, 0$

A similar approach can be considered for the other cases, using the evolution of  $p_k$ 's along the corresponding characteristic curves. The system (4.B.28) can be written as

$$\begin{cases} \frac{dh}{dt} = -(1/c) \left[ kh^4 - (k+f)h^3 \right], & h(0) = h^0, \\ \frac{dp_k}{dt} = C_k(h)p_k(h,t) + S_k(h,t), \end{cases} \quad (4.B.33)$$

where the initial condition  $p_k(h^0, 0)$  satisfies (4.B.27), while

$$C_k(h) = - \left[ ke^{\beta(h-1)} + \frac{dv(h,k)}{dt} \right], \quad (4.B.34)$$

$$S_k(h,t) = (k+1)e^{\beta(h-1)}p_{k+1}(h,t). \quad (4.B.35)$$

Consider a characteristic curve  $h_{n-1}(t)$  along which examine the behaviour of  $p_{n-1}$ . Since  $h_{n-1}$  collapses onto the equilibrium  $h_{n-1,eq} = 1 + f/(n-1)$ , the long run behaviour of  $p_{n-1}(h_{n-1}(t), t)$  is dictated by the coefficients  $C_{n-1}$  and  $S_{n-1}$  at  $h = h_{n-1,eq}$  and  $t > 0$ .

Since in the long run  $p_n$  is significantly positive along near the characteristic curve  $h(t) = 1 + f/n$ , one has  $\lim_{t \rightarrow 0} S_{n-1}(1 + f/(n-1), t) = 0$ , so  $S_{n-1}$  vanishes along this curve. The conclusion is that the coefficient  $C_k(1 + f/(n-1))$  alone dictates the behaviour of  $p_{n-1}$ .

For any  $k = 1, \dots, n-1$ , the characteristic curves  $h_k$  collapse in finite time onto the equilibrium  $h_{k,eq}$ . Since the source terms decay rapidly for large times away from the curve  $h(t) = 1 + f/k$ , it can be assumed that  $p_k$  after some time  $t_0$ , satisfies approximately the equation

$$\frac{dp_k}{dt} \left(1 + f/k, t\right) \simeq k \left[ -e^{\beta(f/k)} + \frac{1}{c}(1 + f/k)^3 \right] p_k(1 + f/k, t), \quad (4.B.36)$$

with the approximate solution

$$p_k(1 + f/k, t) \simeq p_k(1 + f/k, t_0) e^{kR(f/k)t},$$

where the function  $R(x)$  depicted in Fig. 4.29 was defined in (4.B.31) and the initial condition at  $t = t_0$  verifies  $p_k(1 + f/k, t_0) \geq 0$ .

#### 4.B.5 Force and drag regimes

The different profiles of the  $p'_k$ s can be used to identify various regions in the force and drag parameter space.

##### General force regimes

As established earlier, the profiles of the densities  $p_k$  depend on the position of  $f/k$ ,  $k = 1, \dots, n$  relative to the solutions of the equation  $R(x) = 0$ , where  $R$  is given by (4.B.31).

**Case 1.** *Large drag:*  $c > 27/e^2$ . Equation  $R(x) = 0$  has no real solution.

In this case irrespective of force, all the densities  $p_k$  vanish in the infinite time limit.

**Case 2.** *Medium drag:*  $1 < c \leq 27/e^2$ . Equation  $R(x) = 0$  has two positive solutions,  $0 < x_1 < x_2$ .

For various values the force  $f$ , the behaviour of the densities  $p_k$  can be very different. To summarize,  $p_k$  is an infinite width-infinite tall spike for each value of  $f$  and  $k$  for which we have  $x_1 \leq f/k \leq x_2$ .

There are several types of behaviour:

1. Very small force:  $f/n < \dots < f < x_1$ .
2. Very large force:  $f/n > x_2$ .

3. Intermediate force:  $f/n < x_1 < f/k < x_2 < f$ ,  $f/n < \dots < f/k < x_1 < f/k - 1 < \dots < f < x_2$ , and  $x_1 < f/n < \dots < f/k < x_2 < f/k - 1 < \dots < f$ .

If  $c = 27/e^2$ , the solution of the equation  $R(x) = 0$  is  $x = 2$  and we can even have only a single infinitely-tall spike, if  $f/k = 2$  for some values of  $f$  and  $k$ .

**Case 3.** *Small drag* :  $0 < c \leq 1$ . Equation  $R(x) = 0$  has one positive and one negative root  $x_1 < 0 < x_2$ .

The discussion for this case is similar to the one already done for  $c = 1$ , with the only difference that  $x^* = x_2$ .

### Force regimes for $c = 1$

For  $c = 1$ , the analysis of Fig. 4.29 highlights the existence of three forcing regimes.

- *Small force*:  $f < x^*$ . In this case, the profile of  $p_k$  in the large time limit for  $k = 1, \dots, n$  is a spike which gets narrower and higher as the time goes.
- *Intermediate force*: There exists  $k^* \in 2, \dots, n$  such that

$$\frac{f}{k^*} < x^* < \frac{f}{k^* - 1}.$$

In this case the densities  $p_k$  exhibit a spike behaviour for  $k = k^*, k^* + 1, \dots, n$ , and they are damped to 0 if  $k = 1, \dots, k^* - 1$ .

- *Large force*:  $f/n > x^*$ . In this case all  $p'_k$ s are damped to 0.

# Adhesive molecular bond clusters between a membrane and a surface

IN THIS CHAPTER we extend the results obtained for the vertical motion of a disk with bonds attached underneath, to the vertical motion of a thin, flexible membrane connected to a flat planar surface via adhesion clusters, in the presence of hydrodynamic effects and vertical forces acting at the membrane boundaries.

The variable gap between the two surfaces differentially stretches the bonds, assumed to behave as elastic springs under force. The bonds are allowed to form and break at discrete binding sites spread over the membrane, as in the adhesive dynamics models extensively analyzed by Hammer [61, 66], or by Ward *et al.* [141], for rigid cells. The dynamics of the membrane-clusters system are addressed in the framework of piecewise deterministic Markov processes, and an exact stochastic algorithm is developed for the simulation of individual trajectories. As an approximation for the coupled evolution of adhesion clusters and the membrane's displacement, we also formulate a differential equation whose solution is compared against results obtained from averages of the stochastic simulations.

This Chapter is laid out as follows. In §5.1 we develop a model for the binding kinetics of clusters attached to a moving membrane, in the limit of negligible sliding and small membrane slope. In §5.2 we introduce a stochastic simulation algorithm, a deterministic limit and present the wavelet-based semblance method. Numerical and deterministic results are given in §5.3 for the problem of liquid spreading beneath the membrane, and in §5.4 for the problem of fluid spreading in the presence of upwards and downwards forcing at the membrane's left-end. In §5.5 the individual simulations are analyzed by comparing several statistics using the wavelet-based semblance method, and the comparison against the deterministic limit. Also in this section, we

discuss some measures for the stochastic peeling of discrete adhesion clusters. In §5.6 the results are summarized, and suggestions for further study are outlined.

## 5.1 A stochastic model for clusters between a surface and a membrane

---

In this section we present a detailed statement of the physical model. The balance of forces in the system is used to derive the equations characterizing the motion of the membrane with bonds attached to it. The dimensionless problem is then formulated, followed by an analysis of relevant initial and boundary conditions.

### 5.1.1 The dimensional model

The membrane model consists of a thin, long and wide rectangular surface, attached to a rigid planar substrate through clusters of biological bonds. We use the notation  $x^*, y^*$  for horizontal coordinates,  $t^*$  for time,  $h^*(x^*, y^*, t^*)$  for membrane displacement and  $X^*, Y^*$  for the horizontal lengthscales. Between the two surfaces there is a narrow gap filled with a liquid of viscosity  $\mu^*$ , which exerts a pressure  $p^*$  on the membrane's surface. In each section perpendicular to the axis  $0y^*$ , the membrane is subject to a tension  $T^*$ . The membrane's shape and behaviour are assumed uniform along the  $0y^*$  axis, so the system may be reduced to a 2D problem in the coordinates  $(x^*, h^*(x^*, t^*))$  (as  $h^*(x^*, y^*, t^*) = h^*(x^*, t^*)$ ). The lengthscales involved in our model satisfy the thin-film conditions

$$X^*, Y^* \gg h^*(x^*, y^*, t^*), \quad (5.1.1)$$

so the vertical motion of the membrane is subject to significant viscous forces and is derived using lubrication theory [1].

It is assumed that the bonds are identical, parallel to the vertical axis, differentially share the load when connected (depending on their extension), and behave as elastic springs of rest length  $L^*$  and elastic modulus  $\kappa^*$ . The formation and termination of bonds is naturally caused by thermal fluctuations, while the rupture of bonds increases exponentially with the mechanical loading, as suggested by Bell [10]. Adapted to our problem, it is natural to assume that the association and dissociation rates depend exponentially on the membrane's displacement, as discussed in Chapter 2.

The receptor-ligand bonds sharing the same coordinate  $x^*$  are grouped in a cluster and are located at the fixed coordinates  $X_1^*, \dots, X_M^*$  along the  $0x^*$  axis. The clusters have  $N_1(t^*), \dots, N_M(t^*) \geq 0$  bonds and extension  $H_1^*(t^*), \dots, H_M^*(t^*)$  at time  $t^*$ . It is also realistic to assume that the binding sites support a finite number of bonds  $n_1, \dots, n_M$ .

As individual bonds are allowed to break and rebind, the variables  $N_1(t^*), \dots, N_M(t^*)$  are discrete, and  $H_1^*(t^*), \dots, H_M^*(t^*)$  are continuous random variables, respectively.

To investigate the dynamics of the membrane/bond system, we consider a model problem in which initially, a liquid drop of considerable height ( $\sim 3 - 10L^*$ ) is squeezed under the membrane's left-end, while the connected bonds are in equilibrium, and located near the right end of the membrane. Assuming the liquid's total mass is conserved in the contact region, the release of the membrane allows the blob to spread to the right, widening the vertical gap between the surfaces, and stretching the bonds in the process.

Between the stochastic jumps in the number of bonds, the membrane moves deterministically, so the model is a piecewise deterministic Markov process. The individual trajectories of the system can be simulated using an adapted version of the algorithm presented in §2.2.1, which consists of several steps. First, one has to solve the deterministic motion of the membrane for a fixed configuration of bonds  $K_1, \dots, K_M$ . The following step is simulating the time of the next event. This is followed by finding the location (index  $i = 1, \dots, M$  of the cluster involved), and finally the nature of the event (rupture or rebinding).

In a tight adhesion scenario, sliding of bonds is expected to have a negligible impact on the cell-substrate interaction, so for the moment the lateral motion of the membrane is assumed negligible (nonetheless, a model accounting for the membrane's lateral displacement is formulated in Appendix 5.B).

### Discrete membrane notations

The membrane is assumed to be composed of flat connected plates, having the horizontal coordinates of their edges given by the partition

$$x_1^* = 0, x_2^* = \Delta^*, \dots, x_m^* = (m-1)\Delta^* = LX^*, \quad m \in \mathbb{N}, \quad m \geq 2, \quad (5.1.2)$$

where  $L$  is a non-dimensional scaling for the domain length, the deterministic motion of the membrane for a given configuration of clusters located at  $X_1^*, \dots, X_M^*$  can be obtained in the  $\Delta^* \rightarrow 0$  limit.

Assuming the partition is fine enough to include the clusters' horizontal coordinates

$$\{X_1^*, \dots, X_M^*\} \subseteq \{x_1^*, \dots, x_m^*\}, \quad (5.1.3)$$

we denote by  $k_1, \dots, k_m$  the number of closed bonds at coordinates  $x_1^*, \dots, x_m^*$ . This is defined by  $k_i = N_j$  for any pair  $(i, j) \in \{1, \dots, m\} \times \{1, \dots, M\}$  satisfying  $x_i^* = X_j^*$ , and zero otherwise.

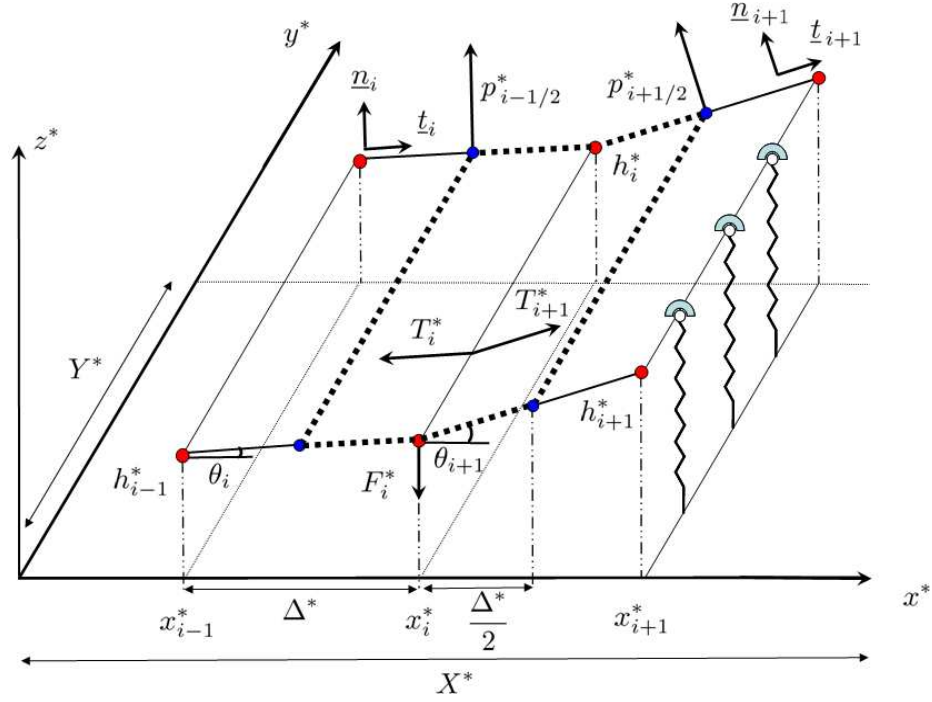


Figure 5.1: Force balance on the membrane region near the  $i$ -th node.

A diagram of the forces present in our model is sketched in Fig. 5.1. The coordinates of the  $i$ -th node along the membrane are  $x_i^*$  and  $h_i^*(t^*) = h(x_i^*, t^*)$ , while the two plates it connects are called the  $i$ -th (to the left, having vertices  $(x_{i-1}^*, 0, h_{i-1}^*)$ ,  $(x_{i-1}^*, Y^*, h_{i-1}^*)$ ,  $(x_i^*, 0, h_i^*)$  and  $(x_i^*, Y^*, h_i^*)$ ) and  $(i+1)$ -th (to the right).

The angles made by the two plates with the  $0x^*$  axis are  $\theta_i$  and  $\theta_{i+1}$ , so the tangent and normal directions of the  $i$ -th plate are

$$\underline{t}_i = (\cos \theta_i, \sin \theta_i) \approx (1, \theta_i), \quad \theta_i \ll 1, \quad (5.1.4a)$$

$$\underline{n}_i = (-\sin \theta_i, \cos \theta_i) \approx (-\theta_i, 1), \quad \theta_i \ll 1. \quad (5.1.4b)$$

Beneath each of the plates  $i$  and  $(i+1)$ , the constant pressures denoted by  $p_{i-1/2}^*$  and  $p_{i+1/2}^*$  exert force in the directions of the normals  $\underline{n}_i$  and  $\underline{n}_{i+1}$ , as sketched in Fig. 5.1.

In each section parallel to  $x^*0z^*$ , the membrane's tension which acts in the directions of the plates  $i$  and  $(i+1)$ , pointing outwards from the edge  $(x_i^*, y^*, h_i^*)$ , is denoted by  $T_i^*$  and  $T_{i+1}^*$ .

Finally, the  $k_i$  bonds located along the coordinates  $(x_i^*, y^*)$  generate a vertical elastic force at the  $i$ -th membrane node, having magnitude

$$F_i^* = k_i \kappa^* (h_i^* - L^*). \quad (5.1.5)$$

### Force balance and deterministic membrane motion

In the absence of horizontal displacement, the overall motion of the membrane is given by the evolution of the nodes  $h_1^*(t^*), \dots, h_m^*(t^*)$ . The motion of the  $i$ -th node of the membrane can be derived from the force balance on the region situated below the dotted domain depicted in Fig. 5.1.

Summing up the forces generated by the membrane tension, pressures and bonds' stiffness described earlier, we have

$$[T_{i+1}^* \underline{t}_{i+1} - T_i^* \underline{t}_i] Y^* + k_i \kappa^* (h_i^* - L^*) (-\underline{z}) + [p_{i-1/2}^* \underline{n}_i + p_{i+1/2}^* \underline{n}_{i+1}] Y^* \frac{\Delta^*}{2} = 0. \quad (5.1.6)$$

Defining the average of the pressures below the dotted domain by

$$p_i^* = \frac{p_{i-1/2}^* + p_{i+1/2}^*}{2}, \quad (5.1.7)$$

and assuming uniform tensions in the membrane, as well as small angles  $\theta_i, \theta_{i+1} \ll 1$ , we use (5.1.4) to write the vertical component of (5.1.6) as

$$T^* (\theta_{i+1} - \theta_i) Y^* - k_i \kappa^* (h_i^* - L^*) + p_i^* \Delta^* Y^* = 0, \quad (5.1.8)$$

which by using  $\theta_i = (h_i^* - h_{i-1}^*) / \Delta^*$ , becomes

$$\frac{T^*}{\Delta^*} (h_{i+1}^* - 2h_i^* + h_{i-1}^*) Y^* - k_i \kappa^* (h_i^* - L^*) + p_i^* \Delta^* Y^* = 0. \quad (5.1.9)$$

Dividing (5.1.9) by  $\Delta^* Y^*$  we obtain

$$p_i^* = -\frac{T^*}{(\Delta^*)^2} (h_{i+1}^* - 2h_i^* + h_{i-1}^*) + (F_i^* / Y^*) / \Delta^*, \quad (5.1.10)$$

where

$$F_i^* / Y^* = k_i / Y^* \kappa^* (h_i^* - L^*) \quad (5.1.11)$$

represents the elastic force density at node  $i$  ( $k_i / Y^*$  is the linear density of bonds in the transverse direction). The units of the quantities in (5.1.10) are  $[p_i^*] = \text{N/m}^2$  (pressure),  $[T^*] = \text{N/m}$  (membrane tension). The components of the elasticity coefficient  $\kappa^* (k_i / Y^*)$  have the units  $[k_i / Y^*]$  bonds/m (linear density of bonds) and  $[\kappa^*] = \text{N/m}$  (stiffness of an individual bond), showing that (5.1.10) is dimensionally consistent.

The meaning of (5.1.10) is that for a given partition  $x_1^*, \dots, x_m^*$ , the force  $F_i^* / Y^*$  is distributed over an interval of length  $\Delta^*$ , which as  $\Delta^* \rightarrow 0$  acts as a Dirac mass function of magnitude  $F_i^* / Y^*$ , localized at  $x^* = x_i^*$ . Counting all the clusters situated at the coordinates  $X_1^*, \dots, X_M^*$ , the downwards force acting at  $x^*$  in the section perpendicular to  $0y^*$  is given by

$$F^*(x^*, t^*) = \sum_{i=1}^M N_i(t^*) / Y^* \kappa^* [h^*(x^*, t^*) - L^*] \delta(x^* - X_i^*). \quad (5.1.12)$$

Finally, in the  $\Delta^* \rightarrow 0$  limit, the pressure and the smooth function  $h^*$  that interpolates coordinates  $(x_i^*, h_i^*)$  satisfy

$$p^* = -T^* h_{x^* x^*}^* + F^*. \quad (5.1.13)$$

The vertical motion of the membrane under tension  $T^*$  and force  $F^*$  can be obtained by introducing the pressure term from (5.1.13) in the mass and flux conservation equations

$$h_{t^*}^* + q_{x^*}^* = 0, \quad (5.1.14a)$$

$$q^* = -\frac{1}{12\mu^*} (h^*)^3 p_{x^*}^*, \quad (5.1.14b)$$

derived using lubrication theory [1] (see also Appendix 2.A), to obtain

$$h_{t^*}^* = \frac{1}{12\mu^*} \left[ (h^*)^3 p_{x^*}^* \right]_{x^*} = \frac{1}{12\mu^*} \left[ (h^*)^3 \left( -T^* h_{x^* x^*}^* + F^* \right) \right]_{x^*}. \quad (5.1.15)$$

### Association and dissociation of bonds

The deterministic motion of the membrane is perturbed by the stochastic formation and breakage of bonds. The rates for the rupture and rebinding of individual bonds are the same as given in §2.1.2, while the transition rates for clusters are discussed in the section dedicated to the dimensionless model.

### 5.1.2 Dimensionless model

Relation (5.1.10) can be explicitly written as

$$p_i^* = -\frac{T^*}{(\Delta^*)^2} (h_{i+1}^* - 2h_i^* + h_{i-1}^*) + k_i \frac{\kappa^* L^*}{Y^* \Delta^*} \left( \frac{h_i^*}{L^*} - 1 \right), \quad (5.1.16)$$

which suggests defining the non-dimensional variables

$$t = k_0^* t^*, \quad (5.1.17a)$$

$$h = (L^*)^{-1} h^*, \quad h_i = (L^*)^{-1} h_i^*, \quad H_i = (L^*)^{-1} H_i^*, \quad (5.1.17b)$$

$$x = (X^*)^{-1} x^*, \quad x_i = (X^*)^{-1} x_i^*, \quad X_i = (X^*)^{-1} X_i^*, \quad (5.1.17c)$$

$$\Delta = \Delta^* / X^*, \quad (5.1.17d)$$

$$p = p^* \frac{X^* Y^*}{\kappa^* L^*}, \quad (5.1.17e)$$

$$T = T^* \frac{Y^*}{X^* \kappa^*}, \quad (5.1.17f)$$

where  $k_0^*$  is the individual unstretched bond off-rate, introduced in §2.1.2. In the new notations, (5.1.16) can be written in dimensionless form as

$$p_i = -\frac{T}{\Delta^2} (h_{i+1} - 2h_i + h_{i-1}) + \frac{f_i}{\Delta}, \quad (5.1.18)$$

where  $f_i = k_i(h_i - 1)$ . Using the same argument as for the dimensional problem, the general equation of the pressure as  $\Delta \rightarrow 0$  is shown to be

$$p = -Th_{xx} + f, \quad (5.1.19)$$

where the force  $f$  pointing downwards is given by the function

$$f(x, t) = \sum_{i=1}^M N_i(t) [h(x, t) - 1] \delta(x - X_i). \quad (5.1.20)$$

In the new variables, (5.1.15) becomes

$$h_t = \frac{1}{c} \left[ h^3 \left( -Th_{xx} + f \right) \right]_{x,x}, \quad (5.1.21)$$

where the dimensionless parameter  $c$ , defined by

$$c = \frac{12\mu^* k_0^* (X^*)^3 Y^*}{\kappa^* (L^*)^3}, \quad (5.1.22)$$

has a similar role to the drag coefficient (2.1.10) introduced in §2.2.1 for the plate model.

As specified in Table 2.1, the dimensional variables are in the ranges  $\kappa^* \simeq 0.01 - 5$  dyn/cm =  $10^{-5} - 5 \cdot 10^{-3}$  N/m,  $\mu^* \sim 10^{-3}$  Pa · s =  $10^{-3}$  N/m<sup>2</sup>,  $L^* \sim 10 - 100$  nm and  $k_0^* \sim 2.8$  s<sup>-1</sup>. For a membrane patch of dimensions  $X^* \sim Y^* \sim 1$  μm [141], and a typical bond elastic force range  $\kappa^* L^* \sim 1 - 50$  (2.1.7), we obtain  $c \in [10^{-3}, 10^2]$ .

Defining the dimensionless flux

$$q = q^* \frac{1}{k_0^* L^* X^*}, \quad (5.1.23)$$

the lubrication equations (5.1.14) can be written in dimensionless form as

$$h_t + q_x = 0, \quad (5.1.24a)$$

$$q = -\frac{1}{c} h^3 p_x. \quad (5.1.24b)$$

**Remark.** The force  $f(x, t)$  defined in (5.1.20) only accounts at present for the vertical force in the elastic bonds. The formulation of the model allows considering much more complex forcing regimes ( $x$ - and  $t$ - dependent). In this thesis we shall only consider vertical forces acting at the membrane boundaries, starting from §5.1.3.

### Boundary conditions

As the evolution of  $h$  depends on  $h_{xxxx}$ , a double boundary condition is imposed at each end of the membrane. Considering solutions which are symmetric near  $x = 0$  and  $x = L$ , and the conservation of fluid below the membrane, a set of convenient boundary conditions for this problem is

$$h_x(0, t) = h_x(L, t) = 0, \quad h_{xxx}(0, t) = h_{xxx}(L, t) = 0. \quad (5.1.25)$$

As long as no rupture or rebinding happens, the membrane relaxes towards an equilibrium position, which the absence of bonds is a line parallel to the horizontal axis  $0x^*$ , whose height depends on the amount of liquid below the membrane.

### Initial condition

As we want to examine the motion of the liquid drop under the left part of the membrane depicted in Figs. 5.1 or 5.2, we would ideally like the support (the set of points where the function is not zero) of the membrane's initial position to include this drop.

Denoting the density of the normal distribution of mean  $\mu$  and standard deviation  $\sigma$  by

$$N_{\mu,\sigma}(x) = \frac{1}{\sqrt{2\pi}\sigma} e^{-\frac{(x-\mu)^2}{2\sigma^2}}, \quad x \in [0, L], \quad (5.1.26)$$

and its scaled version by  $\bar{N}_{\mu,\sigma}(x) = N_{0,\sigma}(x) / \int_0^L N_{0,\sigma}(x) dx$ ,  $x \in [0, L]$ , we obtain the initial condition

$$h(x, 0) = 1 + \Lambda \bar{N}_{0,\sigma}(x), \quad (5.1.27)$$

where  $\Lambda > 0$  is a scaling factor and the bonds are assumed to be initially at equilibrium  $H_i(0) = 1$ . This function clearly satisfies the boundary condition at  $x = 0$ , and also the boundary condition at  $x = L$  (with an exponentially small error), for small enough values of  $\sigma$ , for example  $\sigma \leq L/6$ .

A more rigorous approach is to consider the family of smooth functions

$$f_{a,b}(x) = \begin{cases} \exp\left(-\frac{b}{(1-x^2)^a}\right), & |x| < 1 \\ 0, & |x| \geq 1, \end{cases} \quad (5.1.28)$$

often called mollifiers [123], having the support included in the compact interval  $[-1, 1]$ .

As seen in Fig. 5.2 (a), varying the parameters  $a$  and  $b$ , a wide variety of profiles can be obtained. These functions can be modified to have unit integral over the interval  $[0, \infty]$  and their support included in any interval  $[-e, e]$ ,  $e > 0$ , by the transformation

$$f_{a,b,e}(x) = \frac{1}{e} f_{a,b}\left(\frac{x}{e}\right) \frac{1}{\int_{x=0}^{\infty} f_{a,b}(x) dx}. \quad (5.1.29)$$

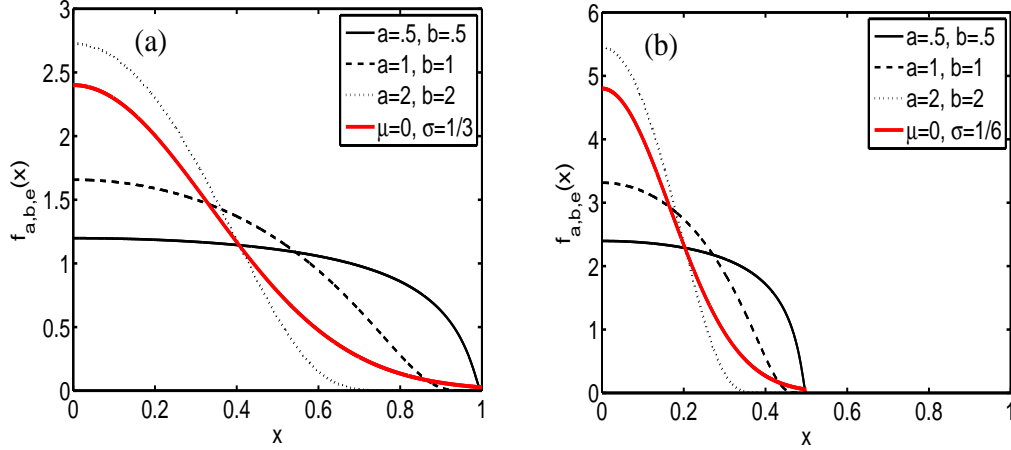


**Figure 5.2:** Positive part of the mollifiers obtained from (5.1.29) for  $(a, b) = (0.5, 0.5), (1, 1), (2, 2)$  and  $L = 1$ , compared against  $\bar{N}_{0,\sigma}$  defined in (??) for (a)  $e = 1, \sigma = L/3$ ; (a)  $e = 0.5, \sigma = L/6$ .

This is particularly useful for our problem, when we want the liquid drop to be confined in a subinterval  $[0, e]$  of  $[0, L]$ . A couple of candidates for the shape of the membrane's initial position are depicted in Fig. 5.2 (b), suggesting a large variety of profiles. The initial membrane position could be

$$h(x, 0) = 1 + \Lambda f_{a,b,e}(x), \quad (5.1.30)$$

where  $\Lambda > 0$  is a scaling factor, and  $0 < e \leq L$ .

### Conservation of fluid volume

Denoting by  $V$  the fluid volume below the membrane, the mass conservation is

$$\int_0^L h(x, t) dx = L + \Lambda = V,$$

valid for all the initial conditions generated by (5.1.27) and (5.1.30).

### Dissociation and association rates

Using the same argument as in Chapter 2, if at time  $t$  the state of the system is  $H(t) = (H_1(t), \dots, H_M(t))$  and  $N(t) = (K_1, \dots, K_M)$ , with  $K_i \in \{0, \dots, n_i\}$ ,  $i = 1, \dots, M$ , the rupture and rebinding rates corresponding to the local transitions to  $K_i - 1$  and  $K_i + 1$  bonds in cluster  $i$ , are:

$$r_{i,K_i}(H_i(t)) = K_i \exp(\beta(H_i(t) - 1)), \quad (5.1.31a)$$

$$g_{i,K_i}(H_i(t)) = \gamma(n_i - K_i) \exp(-\alpha(H_i(t) - 1)), \quad (5.1.31b)$$

where  $\alpha, \beta$  and  $\gamma$  have the same meaning as established in §2.1.3.

### 5.1.3 Membrane motion under vertical force at boundaries

The spreading membrane model can be adapted for the study of adhesive peeling and rolling of cells, when the membrane's boundaries are subject to the vertical forces  $f_L$  (left) and  $f_R$  (right). The new overall profile of the downwards force will then be

$$f(x, t) = -f_L \delta(x) - f_R \delta(x - L) + \sum_{i=1}^M N_i(t) [h(x, t) - 1] \delta(x - X_i). \quad (5.1.32)$$

Due to these point forces, the boundary conditions also change.

#### Boundary conditions

As discussed for the membrane spreading, a double boundary condition is imposed at each end of the membrane. Considering solutions symmetric near the ends, the boundary conditions are shown (see Appendix 5.A.2) to be

$$h_x^+(0, t) = -\frac{f_L}{2T}, \quad h_x^-(L, t) = \frac{f_R}{2T}, \quad h_{xxx}^+(0, t) = h_{xxx}^-(L, t) = 0. \quad (5.1.33)$$

## 5.2 Solution of the model

The dynamics of the membrane-clusters system are addressed in the framework of piecewise deterministic Markov processes, and an exact stochastic algorithm is developed for the simulation of individual trajectories. The deterministic motion of the membrane is solved using a finite difference approach, while the stochastic jumps are simulated using an adapted version of the algorithm developed in §2.2.1. As an approximate treatment for the coupled evolution of the adhesion clusters and the membrane's displacement, we also formulate a differential equation, whose solution is compared against averages of stochastic simulations. In the end we present a wavelet-based semblance analysis approach, based on the work of Cooper & Cowan [23], which is later used for the comparison of simulated time series.

### 5.2.1 Numerical scheme for the deterministic motion of the membrane

The differential equation (5.1.21) characterizing the vertical motion of the membrane with bonds attached, can be transformed into a system of  $m$  coupled ODEs, corresponding to each node of the partition  $x_1 = 0, x_2 = \Delta, \dots, x_m = (m - 1)\Delta = L$  using a finite difference method [99]. From (5.1.24), the mass conservation at node  $i$  can be written as

$$\frac{dh_i}{dt} + \frac{(q_{i+1/2} - q_{i-1/2})}{\Delta} = 0, \quad (h_t + q_x = 0), \quad (5.2.1)$$

while the pressure gradient beneath plate  $i$  is  $(p_i - p_{i-1}) / \Delta$ , so the mean flux can be approximated by

$$q_{i-1/2} = \frac{1}{c} (h_{i-1/2})^3 \frac{(p_i - p_{i-1})}{\Delta}, \quad (q = -\frac{1}{c} h^3 p_x), \quad (5.2.2)$$

where  $h_{i-1/2} = (h_i + h_{i-1}) / 2$ . Finally, the average pressure  $p_i$  can be obtained from (5.1.18) as

$$p_i = -T \frac{(h_{i+1} - 2h_i + h_{i-1})}{\Delta^2} + \frac{f_i}{\Delta}, \quad f_i = f_i(h_i, N_i), \quad (p = -Th_{xx} + f). \quad (5.2.3)$$

As seen in (5.1.21),  $h_t$  is a function of  $h_{xxxx}$ , so the time evolution of  $h_i$  is expected to depend on at least four neighbours.

Combining (5.2.1), (5.2.2) and (5.2.3), we obtain

$$\begin{aligned} \frac{dh_i}{dt} &= -\frac{1}{\Delta} (q_{i+1/2} - q_{i-1/2}), \\ &= -\frac{1}{\Delta} \left( -\frac{1}{c} (h_{i+1/2})^3 (p_{i+1} - p_i) / \Delta + \frac{1}{c} (h_{i-1/2})^3 (p_i - p_{i-1}) / \Delta \right), \\ &= \frac{1}{c\Delta^2} \left( \frac{(h_{i+1} + h_i)^3}{8} \left[ -\frac{T}{\Delta^2} \left( (h_{i+2} - 2h_{i+1} + h_i) - (h_{i+1} - 2h_i + h_{i-1}) \right) + \frac{f_{i+1} - f_i}{\Delta} \right] \right. \\ &\quad \left. - \frac{(h_i + h_{i-1})^3}{8} \left[ -\frac{T}{\Delta^2} \left( (h_{i+1} - 2h_i + h_{i-1}) - (h_i - 2h_{i-1} + h_{i-2}) \right) + \frac{f_i - f_{i-1}}{\Delta} \right] \right) \\ &= \frac{1}{8c\Delta^4} \left( (h_{i+1} + h_i)^3 \left[ -T (h_{i+2} - 3h_{i+1} + 3h_i - h_{i-1}) + \Delta (f_{i+1} - f_i) \right] \right. \\ &\quad \left. - (h_i + h_{i-1})^3 \left[ -T (h_{i+1} - 3h_i + 3h_{i-1} - h_{i-2}) + \Delta (f_i - f_{i-1}) \right] \right), \end{aligned} \quad (5.2.4)$$

where  $f_i = k_i (h_i(t) - 1)$ , valid for  $i = 3, \dots, m - 2$ .

For symmetrical solutions near the boundaries  $x = 0$  and  $x = L$ , (5.2.4) can still be used for  $i = 1, 2$  and  $i = m - 1, m$  if we define  $h_0 = h_2$ ,  $h_{-1} = h_3$  and  $h_{m+1} = h_{m-1}$ ,  $h_{m+2} = h_{m-2}$ .

When vertical forces  $f_L$  and  $f_R$  are applied at  $x = 0$  and  $x = L$ , the equations (5.2.4) are still valid, if we define  $f_1 = -f_L + k_1[h_1 - 1]$  and  $f_m = -f_R + k_m[h_m - 1]$ .

## 5.2.2 Exact stochastic simulation of the next rupture or rebinding

As the membrane moves deterministically for a fixed cluster configuration, the individual trajectories of the membrane-clusters system are uniquely defined by the time, location and nature of the stochastic jumps (also called ‘‘events’’) in the number of bonds corresponding to each cluster. An adapted version of the algorithm detailed in §2.2.1, which allows the simulation of all the three steps is presented below.

### Step 1: Next event time

The total transition rates at node  $i$  and at state  $(H(t), N(t))$  respectively, are

$$\lambda_{i,K_i} = r_{i,K_i}(H_i(t)) + g_{i,K_i}(H_i(t)), \quad (5.2.5a)$$

$$\lambda_K(t) = \sum_{i=1}^M \lambda_{i,K_i}(t). \quad (5.2.5b)$$

As seen in §2.2.1, the time until the next event  $S$  is simulated from the formula

$$-\log(\xi_1) = \int_0^S \lambda_K(u) du, \quad (5.2.6)$$

where  $\xi_1 \sim U(0, 1)$ , so the next event happens at time  $T_{ev} = t + S$ .

### Step 2: Next event location

Once we know the time of the next event  $T_{ev}$ , the cluster involved in the event can be identified by partitioning the interval  $[0, 1]$  in  $M$  time-intervals proportional to the rates  $\lambda_{i,K_i}(T_{ev})$ , as

$$\left[ 0, \frac{\lambda_{1,K_1}(T_{ev})}{\lambda_K(T_{ev})}, \frac{\sum_{j=1}^2 \lambda_{j,K_j}(T_{ev})}{\lambda_K(T_{ev})}, \dots, \frac{\sum_{j=1}^{M-1} \lambda_{j,K_j}(T_{ev})}{\lambda_K(T_{ev})}, \frac{\sum_{j=1}^M \lambda_{j,K_j}(T_{ev})}{\lambda_K(T_{ev})} = 1 \right]. \quad (5.2.7)$$

For a given  $\xi_2 \sim U(0, 1)$ , the event is located at cluster  $i \in \{1, \dots, M\}$  if

$$\xi_2 \in \left[ \frac{\sum_{j=1}^{i-1} \lambda_{j,K_j}(T_{ev})}{\lambda_K(T_{ev})}, \frac{\sum_{j=1}^i \lambda_{j,K_j}(T_{ev})}{\lambda_K(T_{ev})} \right), \quad (5.2.8)$$

where the convention  $\sum_{j=1}^0 = 0$  was used.

### Step 3: Next event nature

The decision upon the nature (rupture or rebinding) of the event follows the same idea. Having identified the location  $i$  of the event, the interval  $[0, 1]$  is partitioned in two segments proportional with  $r_{i,K_i}(H_i(T_{ev}))$  and  $g_{i,K_i}(H_i(T_{ev}))$ , as for instance

$$\left[ 0, \frac{r_{i,K_i}(H_i(T_{ev}))}{\lambda_{i,K_i}(T_{ev})}, \frac{r_{i,K_i}(H_i(T_{ev})) + g_{i,K_i}(H_i(T_{ev}))}{\lambda_{i,K_i}(T_{ev})} = 1 \right]. \quad (5.2.9)$$

A bond ruptures if

$$\xi_3 \in \left[ 0, \frac{r_{i,K_i}(H_i(T_{ev}))}{\lambda_{i,K_i}(T_{ev})} \right), \quad (5.2.10)$$

and a new bond is formed otherwise, where  $\xi_3 \sim U(0, 1)$ . In the absence of rebinding this step is not required.

The above algorithm is exact in principle, in the sense that the sources of inaccuracy lie in the choice of the random number generator and the precision used for solving  $S$  in (5.2.6). When estimating probability distributions, a source of error is also the finite number of trajectories. One should note that  $\xi_1$ ,  $\xi_2$  and  $\xi_3$  are independent.

### 5.2.3 A deterministic approach

When the total number of bonds in the clusters is large enough, the rupture and re-binding of individual bonds has a small effect on the behaviour of the system as a whole, and the number of closed bonds can be assumed to vary continuously. We shall propose both a discrete and a continuous version of the deterministic limit.

The deterministic analogues of  $h(x, t)$ ,  $h_i$  and  $N_i(t)$  are denoted by  $h_d(x, t)$ ,  $H_{d,i}(t) = h_d(X_i, t)$  and  $N_{d,i}(t)$  for  $i = 1, \dots, M$ . With these notations, the deterministic rupture and rebinding rates for cluster  $i = 1, \dots, M$  at time  $t$  can be defined as

$$r_{d,i}(t) = N_{d,i}(t) \exp [\beta(H_{d,i}(t) - 1)], \quad (5.2.11a)$$

$$g_{d,i}(t) = \gamma (n_i - N_{d,i}(t)) \exp [-\alpha(H_{d,i}(t) - 1)], \quad (5.2.11b)$$

obtained by replacing  $K_i$  and  $H_i$  in (5.1.31) with their deterministic analogues. The deterministic system dynamics are then given by

$$\frac{dN_{d,i}}{dt}(t) = -r_{d,i}(t) + g_{d,i}(t), \quad (5.2.12a)$$

$$\frac{\partial h_d}{\partial t}(x, t) = \frac{1}{c} \left[ h_d^3 \left( -T \frac{\partial^2 h_d}{\partial x^2} + f_d \right) \right]_{x,x}, \quad (5.2.12b)$$

where the deterministic force  $f_d$  is

$$f_d(x, t) = \sum_{i=1}^M N_{d,i}(t) [h_d(x, t) - 1] \delta(x - X_i). \quad (5.2.13)$$

This problem can be solved very similarly to the membrane's motion discussed earlier, and results are compared against stochastic simulations in §5.3, §5.4 and §5.5.

One could further proceed to the continuum limit in which  $f_d$  is replaced by a smooth function  $F_d$  that interpolates  $f_d$  at  $x = X_i$ . In the same way are defined the smooth displacement  $H_d$  interpolating  $H_{d,i}$ , and the smooth bond density  $N_d$  interpolating  $N_{d,i}$  at  $x = X_i$ . The continuous and deterministic rupture and rebinding rates denoted by  $R_d(x, t)$  and  $G_d(x, t)$  are defined as

$$R_d(x, t) = N_d(x, t) \exp [\beta(H_d(x, t) - 1)], \quad (5.2.14a)$$

$$G_d(x, t) = \gamma (n_i - N_d(x, t)) \exp [-\alpha(H_d(x, t) - 1)]. \quad (5.2.14b)$$

The dynamics of the continuous deterministic system are given by

$$\frac{\partial N_d}{\partial t}(x, t) = -G_d(x, t) + G_d(x, t), \quad (5.2.15a)$$

$$\frac{\partial H_d}{\partial t} = \frac{1}{c} \left[ H_d^3 \left( -T \frac{\partial^2 H_d}{\partial x^2} + F_d \right) \right]_{x,x}, \quad (5.2.15b)$$

where the continuous deterministic force  $F_d$  is

$$F_d(x, t) = N_d(x, t) [H_d(x, t) - 1]. \quad (5.2.16)$$

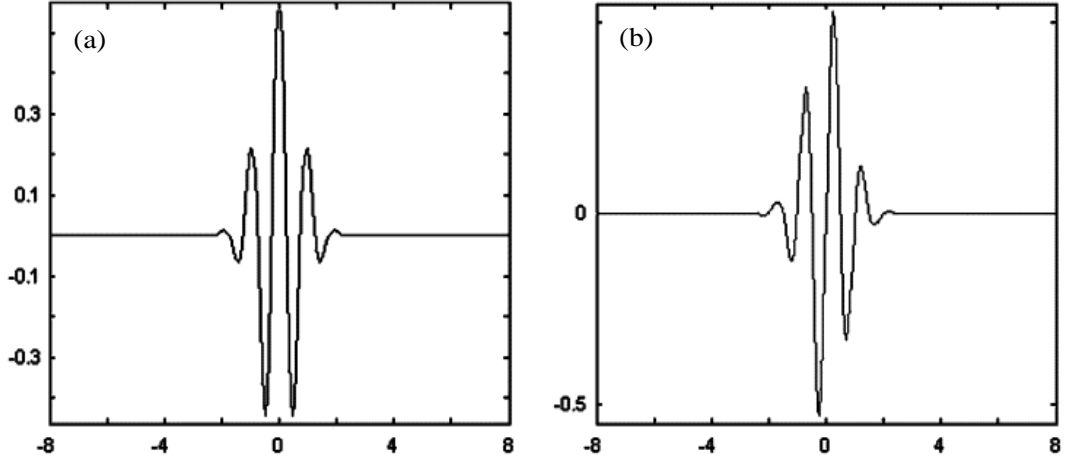


Figure 5.3: (a) Real part of the complex Morlet wavelet. (b) Imaginary part of the complex Morlet wavelet [23].

#### 5.2.4 Time series comparison using wavelet-based semblance analysis

The continuous wavelet transform (CWT) can be used in the semblance analysis of time and spatial data series to display their correlations as a function of both scale (wavelength) and time (or position). The method was introduced by Cooper & Cowan [23], and used for the study of Earth gravity and pseudogravity profiles. Among the advantages are the straightforward computations accompanied by an effective visual aid in their interpretation, as well as the wider generality of the method, compared to the Fourier-based semblance analysis.

We briefly describe the basic formulas, while detailed summaries of wavelet analysis are contained in [92] or [105]. The continuous wavelet transform (CWT) of a dataset  $w(t)$  is given by [92, p.5]:

$$\text{CWT}_w(u, s) = \int_{-\infty}^{\infty} w(t) \frac{1}{|s|^{0.5}} \Psi^* \left( \frac{t-u}{s} \right) dt, \quad (5.2.17)$$

where  $s$  is scale,  $u$  is displacement,  $\Psi$  is the mother wavelet used, and  $*$  means complex conjugate. The CWT is therefore a convolution of the data with scaled version of the mother wavelet. As in [23], we use the complex Morlet wavelet shown in Fig. 5.3:

$$\Psi(x) = \frac{1}{\pi f_b} e^{2\pi i f_c x} e^{-x^2 / f_b}, \quad (5.2.18)$$

where  $f_b$  controls the wavelet bandwidth and  $f_c$  is the wavelet centre frequency.

A great advantage of the method over the Fourier transform-based approach, is that it does not require the assumption that the frequency content of a data set is constant with time (or position), hence providing much better temporal or spatial resolution.

The use of different values of  $s$  in (5.2.17) gives information about the behaviour of the dataset at different scales.

One method of comparing two time series  $w_1$  and  $w_2$  using wavelets is the cross-wavelet transform [22], defined as

$$\text{CWT}_{w_1, w_2} = \text{CWT}_{w_1} \times \text{CWT}_{w_2}^*, \quad (5.2.19)$$

which is a complex quantity having an amplitude given by

$$A_{w_1, w_2} = | \text{CWT}_{w_1, w_2} |, \quad (5.2.20)$$

and local phase

$$\theta_{w_1, w_2} = \tan^{-1} \left( \frac{\Im(\text{CWT}_{w_1, w_2})}{\Re(\text{CWT}_{w_1, w_2})} \right). \quad (5.2.21)$$

Finally, the semblance is defined as

$$S_{w_1, w_2} = \cos(\theta_{w_1, w_2}), \quad (5.2.22)$$

which ranges from  $-1$  (inversely correlated) through zero (uncorrelated) to  $+1$  (correlated). Because  $\theta_{w_1, w_2}$  and  $S_{w_1, w_2}$  (when no confusion is possible, we use  $S$ , for simplicity) compare phase angles rather than amplitude information, they have the advantage that the two datasets being compared do not have to have the same units. The disadvantage of the lack of amplitude information is the sensitivity to the noise, so the authors in [23] also defined

$$D_{w_1, w_2} = \cos^n(\theta_{w_1, w_2}) | \text{CWT}_{w_1} \times \text{CWT}_{w_2}^* |, \quad (5.2.23)$$

which is particularly useful when one is interested in the phase correlations between dataset regions having larger amplitudes.

For our model, the method represents a powerful tool for visualizing the correlations between the evolution of the bond populations and the membrane's positions, when the system is subject to motion, rupture and rebinding near the equilibrium.

### 5.3 Results: Membrane spreading

---

In this section steady states and validate codes, then analyze the behaviour of the bond population below the membrane, as the fluid confined near the left-end boundary spreads freely from it's initial position (see Fig. 5.2). We then analyze the membrane's detachment, and finally discuss the influence of rebinding. The dependence of system's dynamics on most of the model parameters is examined from the analysis of relevant statistics.

### 5.3.1 Code validation using equilibria

Following the membrane's release, the liquid blob starts spreading to the right (as depicted in Fig. 5.5), pushing the membrane upwards and stretching the connected bonds underneath. For a fixed configuration of clusters, the membrane relaxes towards a steady state, which is solved explicitly and employed to validate the codes used for solving the deterministic motion of the membrane, between the rupture and rebind-ing events. As shown in §3.1 for the disk-bonds model, the steady states represent the discrete positions occupied by the membrane in the zero-drag limit. The main steps of the algorithm solving the steady states and an example are detailed below, while the details can be found in Appendix 5.A.1.

#### Steady state solution

From (5.1.21), for a given cluster configuration, the membrane is in equilibrium if

$$c \frac{dh}{dt} = 0 = \left[ h^3 (-Th_{xx} + f)_x \right]_x, \quad (5.3.1)$$

with the boundary conditions  $h_x = h_{xxx} = 0$  at  $x = 0, L$ .

Denoting the equilibrium position by  $h = h_{eq}(x)$ , we integrate (5.3.1) in  $x$  to obtain  $h^3 (-Th_{xx} + f)_x = B$ , which satisfies the boundary conditions only for  $B = 0$ , so

$$-Th_{xx} + f = C, \quad (5.3.2)$$

where  $C$  is a constant to be determined. When the membrane is attached to the surface through  $M$  clusters located at  $X_1, \dots, X_M$  each having  $K_1, \dots, K_M$  bonds, (5.3.2) can be written explicitly as

$$-Th_{xx} + \sum_{i=1}^M K_i [h(x) - 1] \delta(x - X_i) = C. \quad (5.3.3)$$

Integrating (5.3.3) for  $\epsilon > 0$  over the interval  $[X_i - \epsilon, X_i + \epsilon]$  and letting  $\epsilon \rightarrow 0$  one obtains

$$-\left[ Th' \right]_{X_i^-}^{X_i^+} + K_i (h - 1) \Big|_{x=X_i} = 0. \quad (5.3.4)$$

This suggests that the Dirac just imposes a jump in  $h'$  at  $X_i$ , which is directly proportional to  $K_i$  and inversely proportional to  $T$ . For  $x \in (X_i, X_{i+1})$ , the solution satisfies  $h_{xx} = -C/(2T)$ , so it is locally solved by a parabola. When no clusters are attached the steady state is  $h(x) = \frac{V}{L}$ . A full algorithm for solving the steady state for  $M$  clusters located at  $X_1, \dots, X_M$  and having  $K_1, \dots, K_M$  bonds is detailed in Appendix 5.A.1.

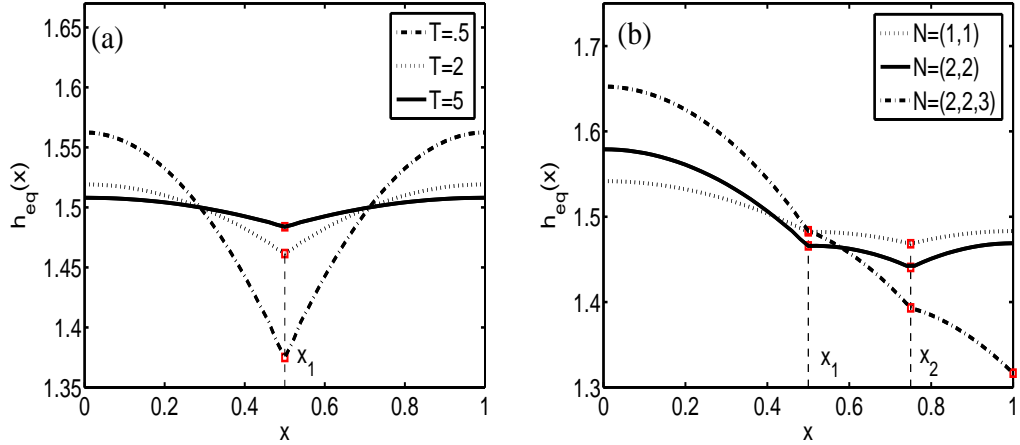


**Figure 5.4:** Membrane steady state obtained for  $L = 1$ ,  $V = 1.5$  in the situations (a)  $X_1 = .5$ ,  $N_1(t) = 2$  for  $T = .5, 2, 5$ ; (b)  $T = 2$ ,  $X_1 = .5$ ,  $X_2 = .75$ ,  $X_3 = 1$ , and  $(N_1, N_2, N_3) = \{(1, 1, 0), (2, 2, 0), (2, 2, 3)\}$  bonds. Squares represent the clusters's ends.

### Dependence on parameters

The steady state membrane position is strongly influenced by the parameters of the problem, as seen in Fig. 5.4. As suggested by (5.3.4) and depicted in Fig. 5.4 (a), a small (dimensionless) tension  $T$  may induce sharp cusps at the cluster's coordinates. This indicates that in our problem  $T$  should be reasonably large, as otherwise our thin film assumptions may no longer be valid near the cusps.

The variation in the number of clusters/bonds as well, significantly changes the membrane's equilibrium position, as sketched in Fig. 5.4 (b). The more clusters/bonds we have, the larger elastic forces make the membrane take a lower equilibrium position, as well as to bend more at the cluster's coordinates. The presence of a large cluster at the membrane's right end, may also induce an equilibrium position which decreases with the increase in  $x$ .

### Numerical methods

The integration of the system (5.2.4) which solves the deterministic motion of the membrane between events, is performed using Matlab<sup>®</sup> stiff ODE solver `ode15s` with relative and absolute tolerances of  $10^{-7}$  and  $10^{-8}$ , respectively. These values ensure that the solver does not fail to converge even when solving the abrupt decay of  $N_{d,i}$  (5.2.12), in the absence of rebinding. The Matlab<sup>®</sup> Runge-Kutta ODE solver `ode45` could not solve the problem in reasonable time, as the time-scale for the liquid relaxation is very small compared to the timescale of the bond rupture.

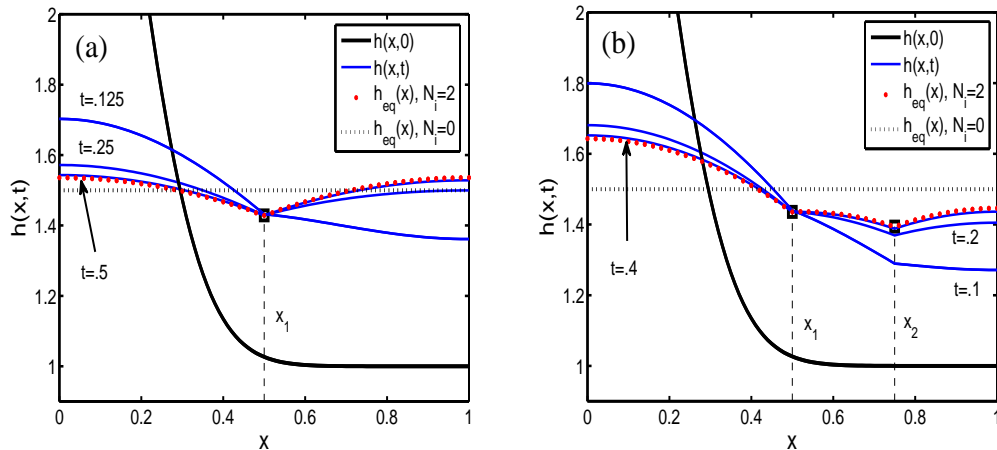


**Figure 5.5:** Motion of the membrane from the initial position given by (5.1.27), towards the steady state in the absence of rupture/rebinding. The results are obtained for  $T = 1$ ,  $c = 1$ ,  $\sigma = 1/6$ ,  $L = 1$ ,  $V = 1.5$  and (a) one cluster having  $X_1 = .5$ ,  $N_1(t) = 2$ ; (b) two clusters having  $X_1 = .5$ ,  $X_2 = .75$  and  $N = (N_1(t), N_2(t)) = 2$ . Squares represent the clusters's ends.

### Validation of membrane trajectories

The numerical code solving the deterministic motion of the membrane is validated by showing that for sufficiently large times the membrane approaches the steady state as depicted in Fig. 5.5, assuming a fixed number of bonds.

From (5.1.21) we infer that the drag coefficient  $c$  determines the timescale of the convergence  $h(x,t) \rightarrow h_{eq}(x)$ , but plays no role in the position of the steady state. The steady states are particularly relevant in the zero-drag limit, where following a change in the cluster structure (rupture or rebinding), the membrane reaches the corresponding steady state long before the next event happens.

Having solved the membrane motion between events, the next step is to simulate individual trajectories of the system, and compare their average against deterministic approximations.

### 5.3.2 Membrane detachment in the absence of rebinding

In the absence of rebinding the bonds can only dissociate and the clusters decay and stretch with the rates (5.1.31), depending on their extension. The overall cluster's dissociation time can be defined, as the moment when the last bond ruptures and the membrane starts moving freely. The system's dynamics can be explored from individual simulated trajectories, but also from averages of stochastic simulations compared against deterministic approximations.

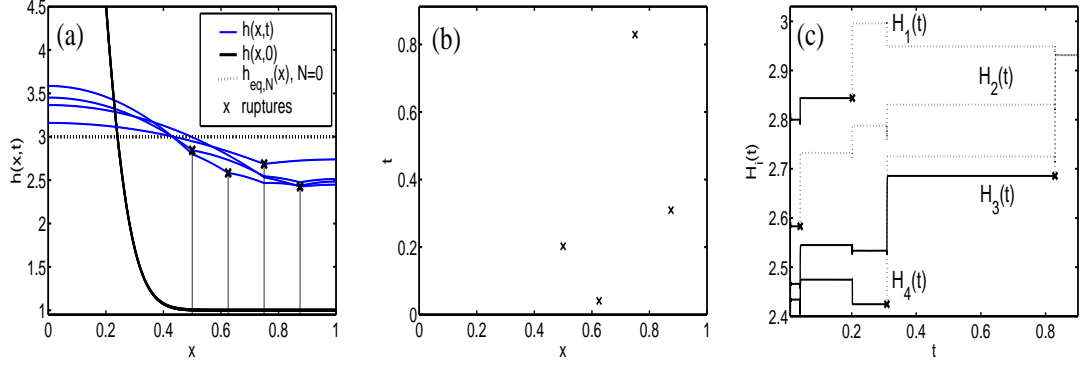


**Figure 5.6:** Motion of the membrane from the initial position  $h(x,0)$  (5.1.27), towards the equilibrium  $h_{eq}(x) = V$ , as the bonds dissociate. Results are obtained for  $T = 1$ ,  $c = 1$ ,  $L = 1$ ,  $\beta = 1$ ,  $\sigma = 1/8$ ,  $V = 3$  and four clusters having  $X_i = 1/2 + (i - 1)/8$ ,  $N_i(0) = 1$ , for  $i = 1, \dots, 4$ . (a) Membrane position at the dissociation times; (b) Events' time and location; (c) Cluster trajectories  $H_i(t)$ ,  $i = 1, \dots, 4$ . We have used solid lines for as long as the bonds are connected, and dotted lines after dissociation. Crosses represent the location of the rupture events.

### Single trajectory analysis

Immediately after the membrane attached to the surface through clusters of bonds is released from the initial position, the liquid drop moves to the right, pushing the membrane upwards and extending the bonds, as depicted in Fig. 5.6 (a). As the bonds start to rupture, following an event, the membrane moves along a different path, depending on the current number of bonds and membrane's position. A single trajectory of the system is then a sequence of time segments  $[T_{ev}, T_{ev+1})$ , along which the number of bonds is constant, while the membrane's motion is deterministic and can be solved from (5.1.21). The dissociation rates (5.1.31a) predict that individual bonds dissociate even at equilibrium, due to thermal fluctuation. When extended, the bonds break in a much more rapid succession. The time and location of the rupture events diagram presented in Fig. 5.6 (b) shows that the first bond to break is not necessarily the one stretched first. The clusters' extensions  $H_i(t)$  in single simulations are also not-monotonic, as one can see in the trajectory of  $H_4(t)$  in Fig. 5.6 (c).

Finally, in Fig. 5.6 the membrane is rather stationary between the events and the clusters are then suddenly extended to new equilibria following a rupture. This behaviour is similar to the one of the disk-bond system in the zero-drag limit discussed in Chapter 3, and indicates that  $c = 1$  belongs to a low drag regime for the membrane model.

Fig. 5.6 also shows that event in the absence of rebinding, the cluster extensions are not necessarily increasing, as it was the case with the bonds attached to a disk problem, discussed in Chapter 4 (see Fig. 4.1 (b)).

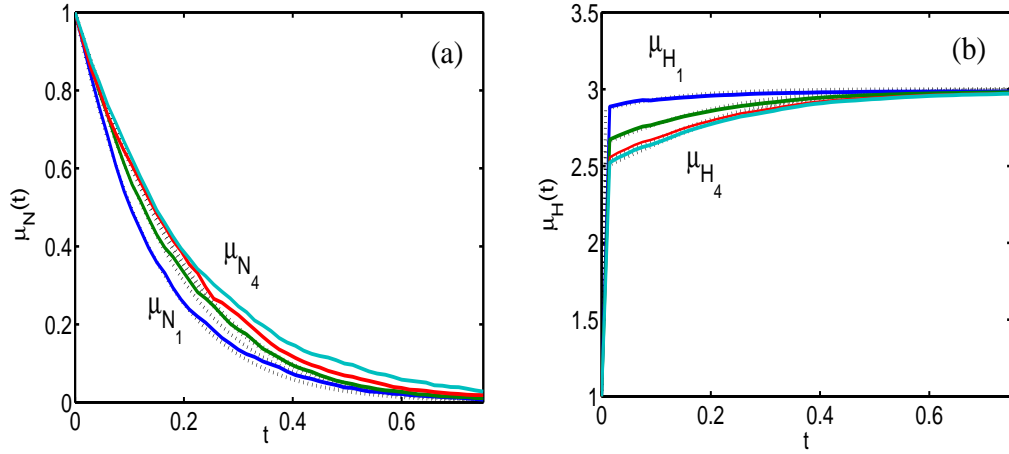


**Figure 5.7:** (a) Stochastic average decay  $\mu_{N_i}$  (solid lines) vs. deterministic  $N_{d,i}$  decay (dotted lines),  $i = 1, \dots, 4$ ; (b) Stochastic average extension  $\mu_{H_i}$  (solid lines) vs. deterministic extension  $H_{d,i}$  (dotted lines),  $i = 1, \dots, 4$ . Stochastic averages are computed from 1600 trajectories. Results obtained for  $T = 1$ ,  $c = 1$ ,  $L = 1$ ,  $\beta = 1$ ,  $\sigma = 1/8$ ,  $V = 3$  and four clusters having  $X_i = 1/2 + (i - 1)/8$ , and  $N_i(0) = 1$ , for  $i = 1, \dots, 4$ .

### Mean bond population and extension of clusters

Of particular interest are the mean bond populations in each cluster  $\mu_{N_1}, \dots, \mu_{N_M}$  and the average cluster extensions  $\mu_{H_1}, \dots, \mu_{H_M}$ , obtained from stochastic simulations or by solving the discrete deterministic equation (5.2.12). Although not a property of individual simulations, the clusters situated closer to the left-end decay faster on average, as depicted in Fig. 5.7 (a). This is clearly because the liquid drop spreads to the right, extending the bonds near the left-end faster and higher than the ones near the right-end, as seen in Fig. 5.7 (b). The solution of the deterministic approximation (5.2.12-5.2.13) is a good match for the average of stochastic trajectories, despite the small number of simulations (1600), assumed to be enough to guarantee an error of about 2.5% (using the central limit theorem [75]).

The cluster's decay can also be examined from the profile of standard deviations of the cluster's dimension  $\sigma_{N_1}, \dots, \sigma_{N_M}$  and cluster extensions  $\sigma_{H_1}, \dots, \sigma_{H_M}$ , obtained from a large number of simulations. As suggested by the means, Fig. 5.8 (a) shows that on average, the clusters break successively from the left to the right, indicating the existence of a 'peeling on average' process. The peeling of the membrane is going to be examined in a special section later on. As seen in Fig. 5.8 (b), the standard deviations  $\sigma_{H_1}, \dots, \sigma_{H_M}$  display peaks proportional to the rates at which the clusters are extended, and then vanish as the bonds dissociate and the membrane relaxes to the equilibrium  $h_{eq}(x) = V$ .

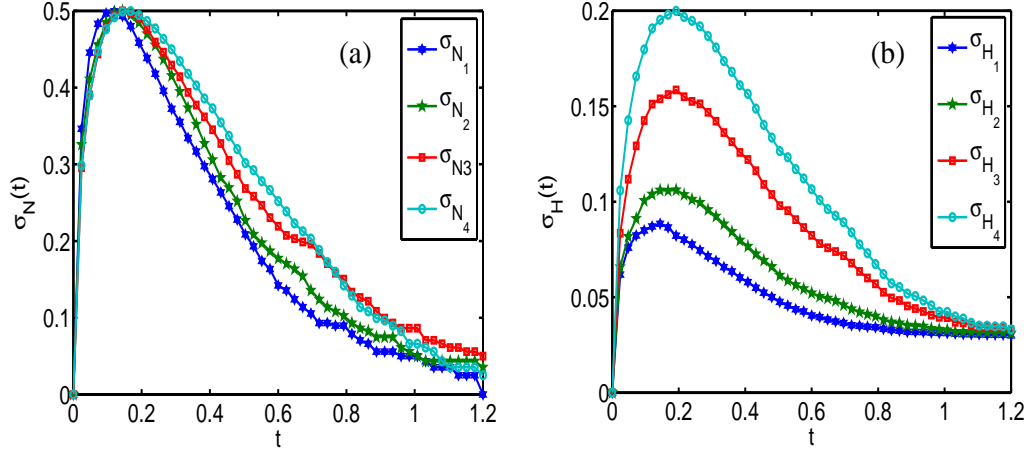


**Figure 5.8:** Standard deviation of the number of (a) closed bonds  $\sigma_{N_i}$ ,  $i = 1, \dots, 4$  and (b) extension of each cluster  $\sigma_{H_i}$ ,  $i = 1, \dots, 4$  computed from 1600 simulations. Results obtained for  $T = 1$ ,  $c = 1$ ,  $L = 1$ ,  $\beta = 1$ ,  $\sigma = 1/8$ ,  $V = 3$  and four clusters having  $X_i = 1/2 + (i - 1)/8$ ,  $N_i(0) = 1$ , for  $i = 1, \dots, 4$ .

The overall cluster decay can also be examined via the stochastic average decay and deterministic decay normalized by the total number of bonds

$$\mu_N(t) = \frac{\sum_{i=1}^M \mu_{N_i}(t)}{\sum_{i=1}^M n_i}, \quad (5.3.5a)$$

$$\mu_{N_d}(t) = \frac{\sum_{i=1}^M \mu_{N_{d,i}}(t)}{\sum_{i=1}^M n_i}. \quad (5.3.5b)$$

At the time when  $\sum_{i=1}^M N_i(t) = 0$ , the membrane is no longer attached to the surface. The first time when this happens represents the membrane's detachment time, denoted by  $T_D$ . The density of  $T_D$  and relevant statistics can be estimated from stochastic simulations. In the absence of rebinding, the mean lifetime can be defined as  $\mu_{T_D}$ .

### Effect of increasing fluid volume

For larger volumes of liquid, the membrane is pushed faster and higher, so the cluster decays more rapidly, as illustrated in Fig. 5.9 (a). The same effect can be identified in Fig. 5.9 (b), where the histograms of the detachment time  $T_D$  become narrower and  $\mu_{T_D}$  is a decreasing function of  $V$ .

We can also make some quantitative estimates on the range of  $\mu_{T_D}$ . Given that for most of the time we have  $1 \leq h \leq V$ , the rupture rates are bounded by

$$K_i \leq r_{i,K_i} = K_i \exp[\beta(H_i - 1)] \leq K_i \exp[\beta(H_i - 1)], \quad i = 1, \dots, M. \quad (5.3.6)$$

The left-hand equality is attained in the  $c \rightarrow \infty$  limit, while the other in the  $c \rightarrow 0$  limit.

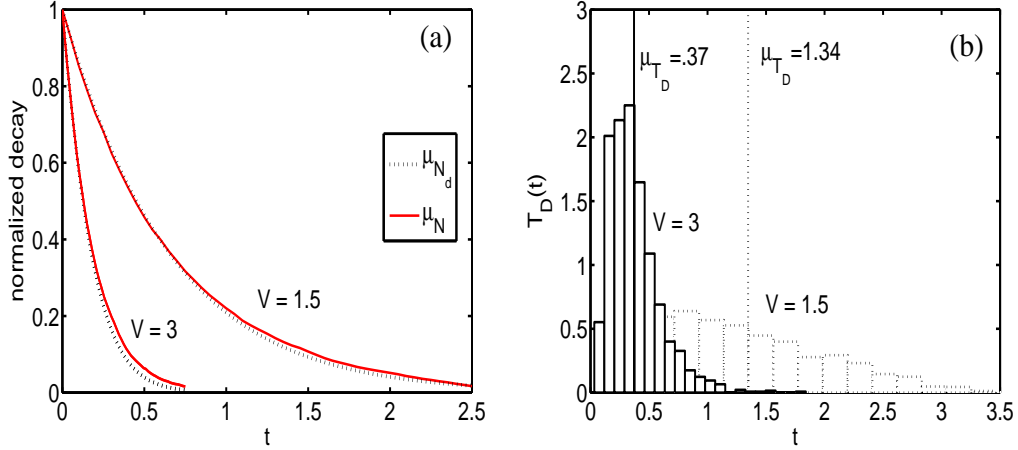


**Figure 5.9:** (a) Stochastic vs. deterministic overall decay profiles (5.3.5), for  $V = 1.5$  and  $V = 3$ ; (b) Histogram of the membrane detachment time  $T_D(t)$ , from 1600 trajectories when  $V = 1.5$  (dotted line) and  $V = 3$  (solid line). Results obtained for  $T = 1$ ,  $c = 1$ ,  $L = 1$ ,  $\beta = 1$ ,  $\sigma = 1/8$ , and four clusters having  $X_i = 1/2 + (i - 1)/8$ ,  $N_i(0) = 1$ , for  $i = 1, \dots, 4$ .

In the two limits, the transition rates (5.1.31a) are time-independent and cluster's decay is sequence of Poisson processes, as discussed when we derived (3.3.5) in §3.2.1. When the intensity of the process is  $r$ , the mean lifetime is  $1/r$  and the variance is  $1/r^2$ . For single bond clusters we obtain the following intervals for the mean and variance of  $T_D$

$$\sum_{i=1}^M \frac{1}{i} \exp[-\beta(V-1)] \leq \mu_{T_D} \leq \sum_{i=1}^M \frac{1}{i}, \quad (5.3.7a)$$

$$\sum_{i=1}^M \frac{1}{i^2} \exp[-2\beta(V-1)] \leq \sigma_{T_D}^2 \leq \sum_{i=1}^M \frac{1}{i^2} \leq \frac{\pi^2}{6}. \quad (5.3.7b)$$

In the example depicted in Fig. 5.9 (b) we have  $1.26 < \mu_{T_D} = 1.34 < 2.08$  for  $V = 1.5$  and  $0.28 < \mu_{T_D} = 0.37 < 2.08$  for  $V = 3$ .

Lower and upper bounds for  $N_i(t)$  can also be obtained from (5.3.6) as

$$n_i \frac{\exp[-\exp[\beta(V-1)]t]}{\exp[-\beta(V-1)]} \leq N_i(t) \leq n_i \exp(-t), \quad i = 1, \dots, M,$$

from where we obtain

$$\frac{\exp[-\exp[\beta(V-1)]t]}{\exp[-\beta(V-1)]} \leq \mu_N(t) \leq \exp(-t). \quad (5.3.8)$$

In the presence of rebinding, new bonds will form again after the system hits the boundary  $\sum_{i=1}^M N_i(t) = 0$ , so the detachment time is no longer defined.

In summary, the clusters decay and stretch differentially depending on their location and the membrane's detachment time is decreased by increasing the fluid's volume.

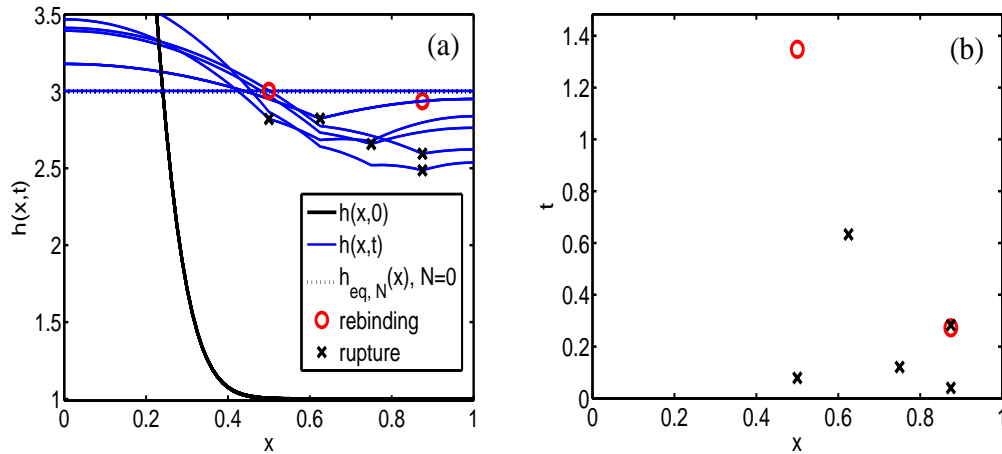


**Figure 5.10:** Motion of the membrane from the initial position (5.1.27), towards the equilibrium  $h_{eq}(x) = V$ , as the bonds form and break. Results are obtained for  $T = 1$ ,  $c = 10$ ,  $L = 1$ ,  $\beta = 1$ ,  $\sigma = 1/8$ ,  $V = 3$ ,  $\alpha = 1$ ,  $\gamma = 1$  and four clusters having  $X_i = 1/2 + (i - 1)/8$ ,  $N_i(0) = 1$ , for  $i = 1, \dots, 4$ . (a) Membrane position at various times (region above 3.5 not shown, to allow the distinction between the membrane's positions). (b) Event time, location and nature. Rebinding represented by circles and rupture by crosses.

### 5.3.3 Membrane dynamics under rupture and rebinding of bonds

When rebinding is present, the boundary  $\sum_{i=1}^M N_i(t) = 0$ , is reflective, so new bonds are allowed to form. As suggested by the analysis of steady states in §5.3.1, the more bonds we have in a cluster, the lower the position of the membrane is likely to be, so if after a rupture event the membrane generally moves upwards towards  $h_{eq} = V$ , following a rebinding event the membrane moves towards a lower position, farther from the equilibrium.

#### Single trajectories under rebinding

Immediately after the membrane attached to the surface through clusters of bonds is released from the initial position, the liquid drop moves to the right, pushing the membrane upwards and extending the bonds which rupture sequentially, as depicted in Fig. 5.10 (a). From time to time, some of the rupture bonds reform, as illustrated in Fig. 5.10 (b) (red circles), the newly formed bonds rapidly pulling the membrane downwards, as seen in 5.10 (a) (the upper curves containing circles).

As illustrated in Fig. 5.11, for drag  $c = 10$  the membrane's motion is slower, and the trajectories of the membrane are smoother. At the same time, one can spot three time-regions with distinct behaviour in the evolution of the membrane-cluster system. In region (I), the fluid spreads rapidly beneath the bonds, so the system is dominated

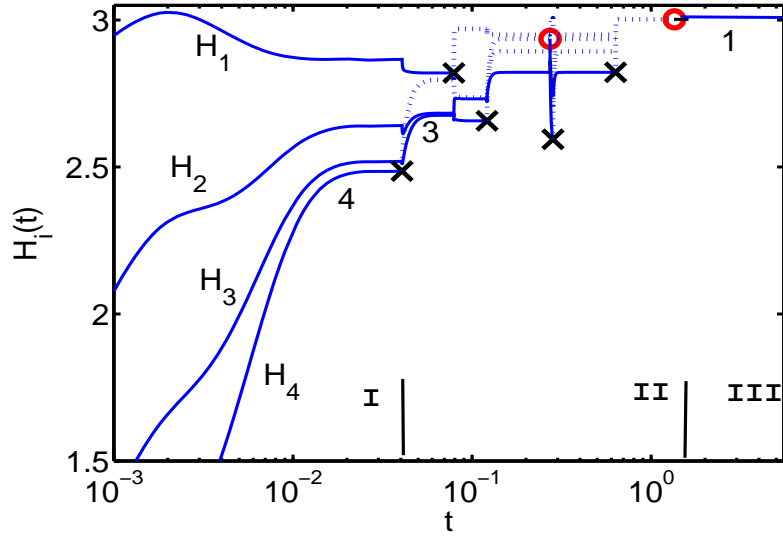


**Figure 5.11:** Cluster trajectories  $H_i(t)$ ,  $i = 1, \dots, 4$  represented together with the rebinding (circles) and rupture (crosses) times. Connected bonds are represented by solid lines, while dissociated bonds by dashed lines. Results obtained for  $T = 1$ ,  $c = 10$ ,  $L = 1$ ,  $\beta = 1$ ,  $\sigma = 1/8$ ,  $V = 3$ ,  $\alpha = 1$ ,  $\gamma = 1$  and four clusters located at  $X_i = 1/2 + (i - 1)/8$ , and having  $N_i(0) = 1$  bonds,  $i = 1, \dots, 4$ . System dynamics dominated by (I) flow; (II) bond kinetics; (III) fluctuations near an equilibrium.

by the fluid flow. It is only after some time when the bonds start to break and rebind. The system enters in the second phase (II) dominated by bond kinetics, where the rapid variation in the number of bonds produces significant local variations in the trajectories  $H_i(t)$ . Eventually, the membrane approaches an equilibrium position where  $H_i(t) \sim V$ . In this region (III), there is small, but non-zero probability for new bonds to form. Occasionally, a new bond forms, followed by small oscillations of the membrane near the equilibrium, and finally, by the rapid dissociation of the stretched bond. At equilibrium, the average waiting time for the formation of a new bond is exponentially increasing with  $V$  as  $1/\sum_{i=1}^M g_{i,0} \sim \exp[\alpha(V - 1)]/4$ . Once a new bond is formed in cluster  $i$ , the probability for the same bond to rupture is

$$\frac{r_i}{r_i + \sum_{j \neq i, j=1}^M g_{j,0}} \sim \frac{1}{1 + (M - 1)\gamma \exp[-(\alpha + \beta)(V - 1)]}. \quad (5.3.9)$$

For  $\alpha = 1$ ,  $\beta = 1$ ,  $M = 3$ ,  $\gamma = 1$ ,  $V = 3$  the probability that the following event is another rebinding is about 5%. However, this probability greatly improves by increasing  $\gamma$  and  $M$ , or by decreasing  $\alpha$ ,  $\beta$  and  $V$ . For  $V = 1.5$  the probability of rebinding is already close to 52%, and 75% for  $V = 1$ .

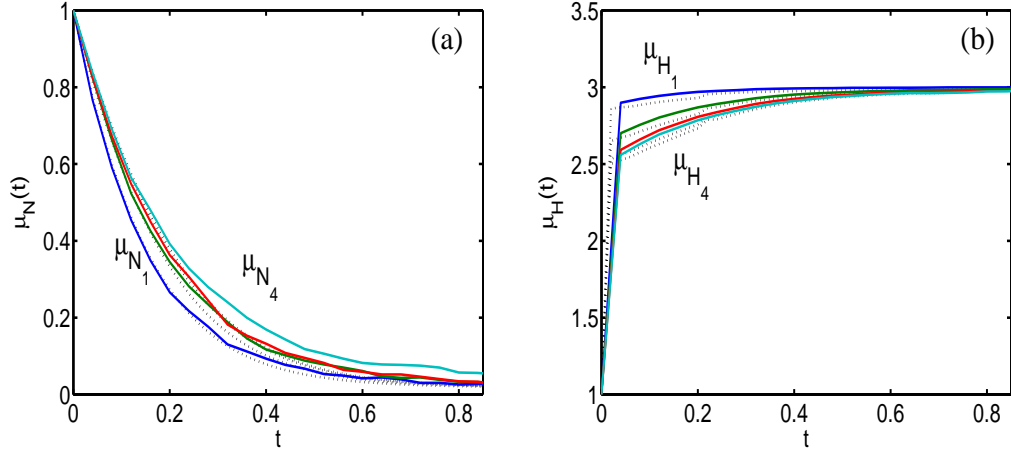


**Figure 5.12:** (a) Stochastic average decay  $\mu_{N_i}$  (solid line) vs. deterministic  $N_{d,i}$  decay (dotted line); (b) Stochastic average extension  $\mu_{H_i}$  (solid line) vs. deterministic extension  $H_{d,i}$  (dotted line),  $i = 1, \dots, 4$ . Results obtained for  $T = 1, c = 1, L = 1, \beta = 1, \sigma = 1/8, V = 3, \alpha = 1, \gamma = 1$ . The clusters are located at  $X_i = 1/2 + (i - 1)/8$ , and have  $N_i(0) = 1$  bonds for  $i = 1, \dots, 4$ . Stochastic average computed from 1600 simulations.

### Mean bond population and extension of clusters

For large rebinding, the membrane may even not detach from the substrate, so the average decay of individual clusters  $\mu_{N_i}$ ,  $i = 1, \dots, 4$  is expected to stabilize to a non-zero equilibrium  $N_{eq,i}$ . At the same time, the clusters' average extensions  $\mu_{H_i}$  are also expected to approach an equilibrium, as illustrated in Fig. 5.12. Compared to Fig. 5.7, the clusters' decay is slowed down by rebinding.

Because the trajectories permanently fluctuate even near the equilibrium, the standard deviations  $\sigma_{N_i}$  and  $\sigma_{H_i}$  of the bond populations  $N_i(t)$  and cluster extensions  $H_i(t)$  do not vanish any more. Moreover, they exhibit significant fluctuations as depicted in Fig. 5.13, and a much larger number of simulations is required to obtain a certain accuracy. At the same time, compared to Fig. 5.8, it takes longer for the clusters to reach the final equilibrium position.

### Impact of the rebinding parameters and bond population size

The role played by the rebinding parameters  $\alpha$  and  $\gamma$  in the system dynamics is examined in Fig. 5.14. Being an average of  $\mu_{N_1}, \dots, \mu_{N_M}$ , the overall decay  $\mu_N(t)$  converges to a non-zero equilibrium, for any values of the parameters. For a given configuration of bonds  $M = 4$ , the smaller  $\alpha$ , the higher the equilibrium position is, as one can see from the comparison of the results obtained for  $\alpha = 0, \gamma = 1$  and  $\alpha = 1, \gamma = 1$ . This is expected, because the rebinding rates are decreasing with  $\alpha$ . From the comparison

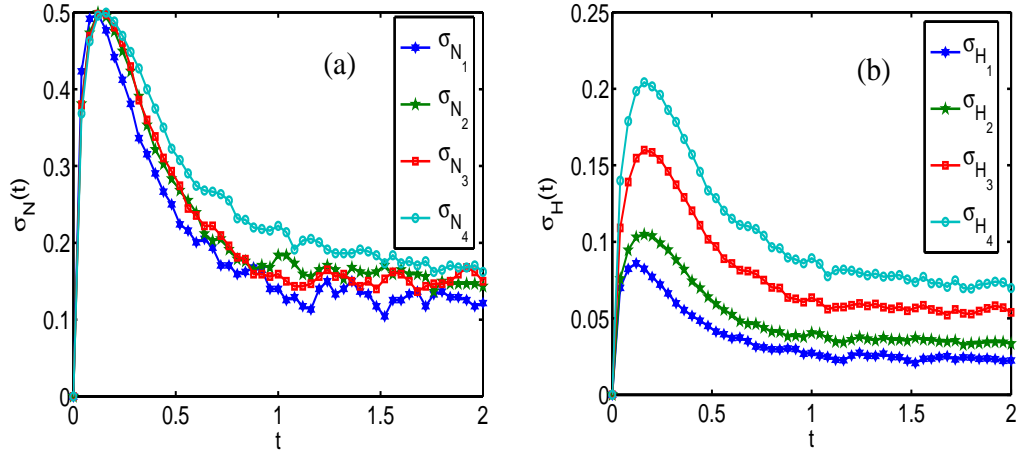


**Figure 5.13:** Standard deviation of the (a) bond population  $\sigma_{N_i}$ ,  $i = 1, \dots, 4$  and (b) cluster extension  $\sigma_{H_i}$ ,  $i = 1, \dots, 4$  computed from 1600 simulations. Results obtained for  $T = 1$ ,  $c = 1$ ,  $L = 1$ ,  $\beta = 1$ ,  $\sigma = 1/8$ ,  $V = 3$ , and rebinding parameters  $\alpha = 1$ ,  $\gamma = 1$ . The clusters are located at  $X_i = 1/2 + (i - 1)/8$ , and have  $N_i(0) = 1$  bonds for  $i = 1, \dots, 4$ .

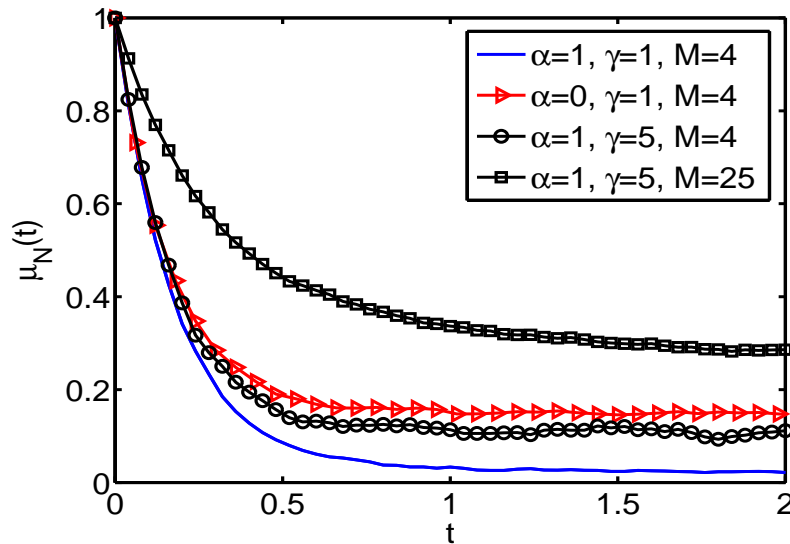


**Figure 5.14:** Influence of the rebinding parameters  $\gamma$  and  $\alpha$  on the overall cluster decay  $\mu_N(t)$  (5.3.5a) obtained from the average of 500 simulations. Plot realized for  $T = 1$ ,  $c = 1$ ,  $L = 1$ ,  $\beta = 1$ ,  $\sigma = 1/8$ ,  $V = 3$  and  $M = 4$  or  $M = 25$  clusters are located at  $X_i = 1/2 + (i - 1)/(2M)$ , for  $i = 1, \dots, M$  having  $N_i(0) = 1$  bonds for  $i = 1, \dots, M$ .

$\alpha = 1$ ,  $\gamma = 1$  and  $\alpha = 1$ ,  $\gamma = 5$ , one can see that the equilibrium position is higher when  $\gamma$  increases. Finally, for the same parameters  $\alpha$  and  $\gamma$  but for different cluster configurations  $M = 4$  and  $M = 25$ , the cluster with more bonds has a larger proportion of connected bonds at equilibrium.

### 5.3.4 Membrane vs. disk model dynamics under rebinding

Using the rates (5.1.31) and the algorithm presented in §6.2.2, we show that the dynamics of the bond-disk model were fully determined by  $\alpha + \beta$  and  $\gamma$ , while in the membrane model  $\alpha$ ,  $\beta$  and  $\gamma$  act independently.

For a given configuration of bonds  $K_1, \dots, K_M$  of length  $H_1, \dots, H_M$  at time  $t$ , the probability of the next event to be located in cluster  $i$ , is proportional to

$$\frac{\lambda_{i,K_i}}{\sum_{j=1}^M \lambda_{j,K_j}} = \frac{K_i e^{\beta(H_i-1)} + \gamma(n_i - K_i) e^{-\alpha(H_i-1)}}{\sum_{j=1}^M K_j e^{\beta(H_j-1)} + \gamma(n_j - K_j) e^{-\alpha(H_j-1)}}. \quad (5.3.10)$$

On the other hand, when the location  $i$  is known, the probability that the next event is a rupture is proportional to

$$\frac{r_{i,K_i}}{\lambda_{i,K_i}} = \frac{K_i e^{\beta(H_i-1)}}{K_i e^{\beta(H_i-1)} + \gamma(n_i - K_i) e^{-\alpha(H_i-1)}} = \exp[(\alpha + \beta)(H_i - 1)] \frac{K_i}{K_i + \gamma(n_i - K_i)}. \quad (5.3.11)$$

In the disk model the bonds share the same extension  $H$ , so the rate (5.3.10) is

$$\frac{\lambda_{i,K_i}}{\sum_{j=1}^M \lambda_{j,K_j}} = \frac{K_i e^{(\alpha+\beta)(H-1)} + \gamma(n_i - K_i)}{\sum_{j=1}^M K_j e^{(\alpha+\beta)(H-1)} + \gamma(n_j - K_j)}, \quad (5.3.12)$$

which is a function of  $\alpha + \beta$  and  $\gamma$  only. As the probability deciding the nature of the next event (5.3.11) is also a function of  $\alpha + \beta$ , the trajectory of the disk-bond system is determined by only  $\alpha + \beta$  and  $\gamma$ .

On the other hand, for the membrane model we generally have  $H_i \neq H_j$ , in which case (5.3.10) depends on each of the variables  $\alpha$ ,  $\beta$ , and  $\gamma$ .

## 5.4 Results: Membrane dynamics under vertical force

---

In many adhesive interactions between cells and substrates, the membranes are also subject to various forces at the boundaries of the contact region, as it is the case for peeling or rolling of leukocytes along the blood vessels [28, 70, 115]. A step closer towards modelling more complex adhesive scenarios is to consider that the spreading of the liquid blob is stimulated by applying vertical forces at the boundaries. We begin with the identification of steady states for fixed cluster configurations, used to make predictions about system's evolution and to validate the codes. The effects of positive and negative vertical force on the membrane's ends are examined in parallel, using individual trajectories and averages of stochastic simulations. The membrane's detachment in the absence of rebinding and the membrane's fluctuation near an equilibrium in the presence of rebinding are also dealt with separately.

### 5.4.1 Code validation using equilibria

In the absence of rupture and rebinding events, the membrane moves towards an equilibrium position depending on the number/position of clusters, and now also on the applied forces  $f_L$  and  $f_R$ . The main steps of the algorithm used for solving the steady states and an example are presented below, while the technical details can be found in Appendix 5.A.2. The solution for the deterministic motion of the membrane under force is shown to converge towards the steady state. Finally, the general behaviour of the system is assessed from the shape of limiting steady states.

#### Steady states

Following the steps used for the membrane spreading problem presented in §6.3.1, the steady state for the membrane attached to the surface through  $M$  clusters having  $K_1, \dots, K_M$  bonds located at the coordinates  $X_1, \dots, X_M$ , satisfies

$$-Th_{xx} - f_L\delta(x) - f_R\delta(x - L) + \sum_{i=1}^M K_i(h(x) - 1)\delta(x - X_i) = C, \quad (5.4.1)$$

which can be solved in a very similar way to (5.3.3), the main difference being the boundary conditions. As the solution is again expected to consist of parabola arches, we still have  $h_{xxx}^+(0) = h_{xxx}^-(L)$ , and we just have to find the directional derivatives  $h_x^+(0)$  and  $h_x^-(L)$ . To do this, (5.4.1) is integrated over the intervals  $[\epsilon, \epsilon]$  and  $[L - \epsilon, L + \epsilon]$ , and as  $\epsilon \rightarrow 0$  we obtain

$$-\left[Th'\right]_{0^-}^{0^+} - f_L = 0, \quad -\left[Th'\right]_{L^-}^{L^+} - f_R = 0, \quad (5.4.2)$$

which suggests the existence of jumps in  $h'$  at  $x = 0$  and  $x = L$ , directly proportional to  $f_L$  and  $f_R$ , and inversely proportional to  $T$ . For symmetry reasons, we should have the same slope with different signs at the right and left of zero (and the same near  $L$ ) so the boundary conditions are

$$h_x^+(0) = -\frac{f_L}{2T}, \quad h_x^-(L) = \frac{f_R}{2T}. \quad (5.4.3)$$

When no clusters are attached, we have  $h_{xx} = -C/(2T)$  for  $0 < x < L$ , so the steady state is solved by the quadratic  $h(x) = -\frac{C}{2T}x^2 + Ax + B$ , subject to the boundary conditions (5.4.3) and the volume conservation property  $\int_0^L h(x, t)dx = V$ . Simple computations reveal that

$$h(x) = \frac{f_L + f_R}{4LT}x^2 - \frac{f_L}{2T}x + \frac{2f_L - f_R}{12T}L + \frac{V}{L}, \quad (5.4.4)$$

which is a line for  $f_L = f_R = 0$ . The algorithm for solving the steady state position of the membrane under upwards forces  $f_L$  and  $f_R$  at  $x = 0$  and  $x = L$  respectively, when

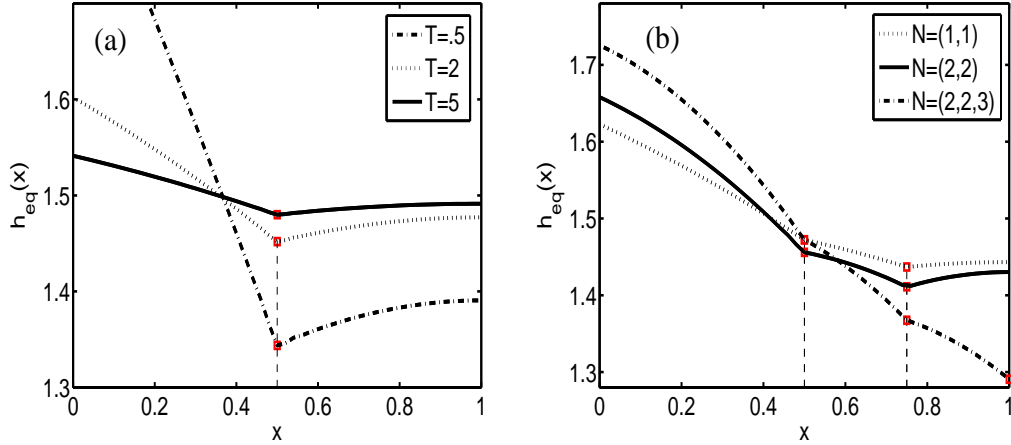


**Figure 5.15:** Membrane steady state obtained for  $L = 1$ ,  $V = 1.5$  and force  $f_L = 1$  in the situations (a)  $X_1 = .5$ ,  $N(t) = 2$  for  $T = .5, 2, 5$ ; (b)  $T = 2$ ,  $X_1 = .5$ ,  $X_2 = .75$ ,  $X_3 = 1$ ,  $(N_1, N_2, N_3) = (1, 1, 0)$ ,  $(2, 2, 0)$ ,  $(2, 2, 3)$ . Squares represent the clusters's ends.

$K_1, \dots, K_M$  bonds are located at the coordinates  $X_1, \dots, X_M$  is described in Appendix 5.A.2. For the rest of the chapter we shall focus on the case  $f_L \neq 0 = f_R$ .

### Dependence on tension and number of clusters

The steady state membrane position is strongly influenced by the parameters of the problem, as seen in Fig. 5.15. As suggested by (5.4.2) and depicted in Fig. 5.15 (a), a small tension  $T$  may induce sharp cusps at the cluster's coordinates. The lateral force significantly changes the membrane's overall position, abruptly raising the left end when  $f_L > 0$ . It is expected that moving towards such a steady state, the clusters situated near the left end will experience a larger force than the ones situated at the right. The variation in the number of clusters/bonds as well, also significantly changes the membrane's equilibrium position, as sketched in Fig. 5.4 (b). The more clusters/bonds we have, the larger elastic forces make the membrane take a lower equilibrium position. The presence of a large cluster at the membrane's right end, may tilt the membrane even more, as shown by the dash-dotted line.

The behaviour of the steady states under force is depicted in Fig. 5.16 and provides a useful insight in the dynamics of the membrane-clusters system. This study is especially relevant for vanishing rebinding, or even in the presence of small rebinding, when the membrane fluctuates near the steady state. Because in general the fluid drop spreads much faster than the bond's breakage time, the membrane stabilizes near an equilibrium position, with all the bonds still connected  $N_i = n_i$  (dotted lines),  $i = 1 \dots, M$  (bond's ends attached to the membrane are represented by squares). After

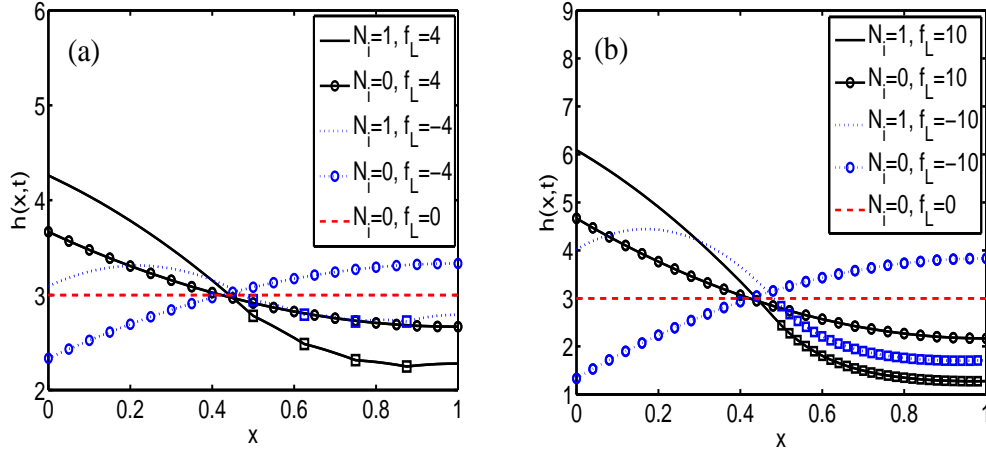


**Figure 5.16:** Membrane steady states under different forces  $f_L$ , for  $L = 1$ ,  $V = 3$ ,  $T = 1$  and (a)  $M = 4$ ; (b)  $M = 25$ . The clusters located at  $X_i = 1/2 + (i - 1)/(2M)$ , and have  $N_i \in \{0, 1\}$  bonds,  $i = 1, \dots, M$ . Squares represent the clusters's ends.

a while, one of the bonds ruptures and the membrane immediately moves towards the next equilibrium. Finally, when all the bonds break, the membrane moves towards the final equilibrium where  $N_i = 0$  (solid lines),  $i = 1 \dots, M$ .

#### Dependence on force and cluster size. Impact on single simulations

The steady states for  $M = 4$  are illustrated in Fig. 5.16 (a), where the dashed line represents the steady state  $f_L = 0$  in the absence of bonds. The positive force  $f_L > 0$  at  $x = 0$ , pulls up the left-end of the membrane, tilting the steady state positions clockwise and bringing them closer to the initial position. The liquid drop contained under the membrane's initial position first relaxes to the steady state  $N_i = 1$ ,  $f_L = 4$ , waiting for a bond to break. When this finally happens, the liquid fills the region corresponding the next steady state, until the membrane reaches the final position, corresponding to  $N_i = 0$ ,  $f_L = 4$ . For negative force  $f_L < 0$  the membrane's left end is pushed downwards, thus the steady states are tilted anti-clockwise. After all the bonds break, the membrane stabilizes to a position in which the right end is significantly over the equilibrium line  $h_{eq}(x) = V$  corresponding to  $f_L = 0$ . It is then sensible to anticipate that cluster's lifetime (when defined) is an increasing function of  $f_L$ .

The steady states for  $M = 25$  clusters and larger forces are plotted in Fig. 5.16 (b). As expected, for a large positive force  $f_L = 10$  the membrane's left end for the steady state corresponding to  $N_i = 1$  stands at a higher position, while the right end is at a lower position than for  $f_L = 4$  and  $M = 4$ . This is an effect of the large number of clusters holding the membrane, but also of the larger force which raises the left end

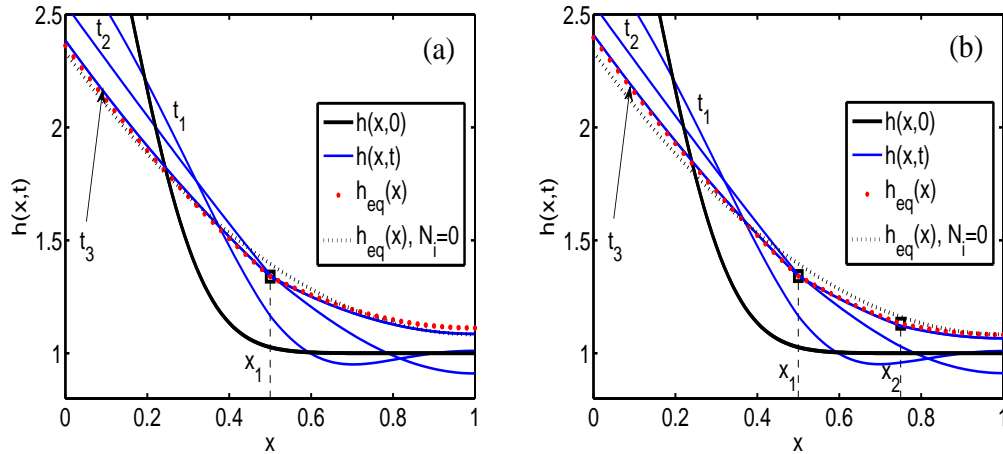


**Figure 5.17:** Membrane motion towards the steady state in the absence of rupture/rebinding. Results obtained for  $f_L = 5$ ,  $T = 1$ ,  $c = 1$ ,  $\sigma = 1/6$ ,  $L = 1$ ,  $V = 1.5$  and (a) one cluster having  $X_1 = .5$ ,  $N_1 = 2$ ; (b) two clusters having  $X_1 = .5$ ,  $X_2 = .75$  and  $N_1 = N_2 = 2$ . Squares represent the clusters's ends at equilibrium, while  $t_1 = 10^{-2}$ ,  $t_2 = 10^{-3}$ ,  $t_3 = 10^{-4}$ .

of the membrane. As the bonds break, the membrane moves towards the position corresponding to  $N_i = 0$ ,  $f_L = 10$ , which is lower than for  $N_i = 0$ ,  $f_L = 4$  in Fig. 5.16 (a), as an effect of the larger force. A large negative force  $f_L = -10$ , can significantly change the cluster's extension from  $N_i = 1$ ,  $f_L = -10$  to  $N_i = 0$ ,  $f_L = -10$ .

The steady states also reveal the pattern of the sequential bond breakage, as the rupture and rebinding rates depends on the cluster's extension. As one can see for  $f_L > 0$ , in each equilibrium position the most stretched cluster is near the left-end, which makes this bond the most likely to rupture, so a peeling pattern could be spotted in the system dynamics. Under  $f_L < 0$ , the situation is more complex, as the maximal membrane displacement moves from the left to the right. It is expected that in a first phase the bonds near the left end break first, while after some time (provided there are still some bonds left ) the peeling starts from the right.

### Validation of membrane trajectories

The numerical solution of the membrane motion is validated by showing that for sufficiently large times the membrane approaches the steady state as depicted in Fig. 5.17.

From (5.1.21) we infer that the drag coefficient  $c$  determines the timescale of the convergence  $h(x,t) \rightarrow h_{eq}(x)$ , but plays no role in the position of the steady state. The steady states are particularly relevant in the zero-drag limit, where following a change in the cluster structure (rupture or rebinding), the membrane reaches the corresponding steady state long before the next event happens.

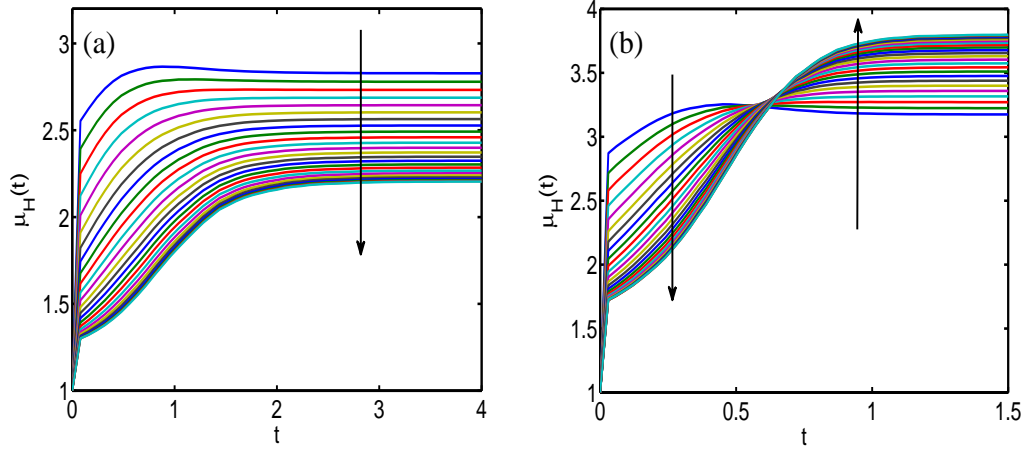


**Figure 5.18:** Stochastic average extension of clusters  $\mu_{H_i}$  under force (a)  $f_L = 10$ ; (b)  $f_L = -10$ , for  $M = 25$  clusters having  $X_i = 1/2 + (i - 1)/(2M)$ , and  $N_i(0) = 1$ , for  $i = 1, \dots, M$ . Results obtained for  $T = 1$ ,  $c = 1$ ,  $L = 1$ ,  $\beta = 1$ ,  $\sigma = 1/8$ ,  $V = 3$  and 1600 simulations. Arrows indicate the direction in which  $i = 1, \dots, M$  increases.

#### 5.4.2 Vanishing rebinding

The application of  $f_L > 0$  at  $x = 0$  lifts up the left membrane's end, and fluid enters to fill the gap. The membrane remains tilted clockwise, as suggested in Fig. 5.17, as it approaches the steady states. Under these geometric constraints, the bonds near the left are on average stretched faster and to a greater extent than the ones located near the membrane's right end, as seen in Fig. 5.18 (a).

The application of a negative force  $f_L < 0$  at  $x = 0$  pushes down the membrane's end, and fluid is squeezed to the right. As bonds rupture, the membrane's steady state profiles are expected to tilt anticlockwise, so in the end the right end of the membrane is at a higher position than the left end. The bonds' extensions depicted in Fig. 5.18(b) show that for a certain time the bonds near the left are more stretched than the ones near the right, while the order is reversed as the bonds rupture and more liquid squeezes in.

As expected, the overall decay of the clusters is faster for negative forces, as illustrated in Fig. 5.19 (a). The decay profiles for positive and negative force are not very much different for small clusters ( $M=4$ ), as the bonds detach due to the fluid flow, and before the effects of force become significant. The difference is considerable for large clusters ( $M=25$ ), which survive long enough to experience the different bond stretching patterns. At the same, the larger clusters decay much slower than the small ones.

The histograms of the membrane detachment times  $T_D$  plotted in Fig. 5.19 (b) are clearly shifting the left with the decrease of force, reflecting the faster clusters' decay.

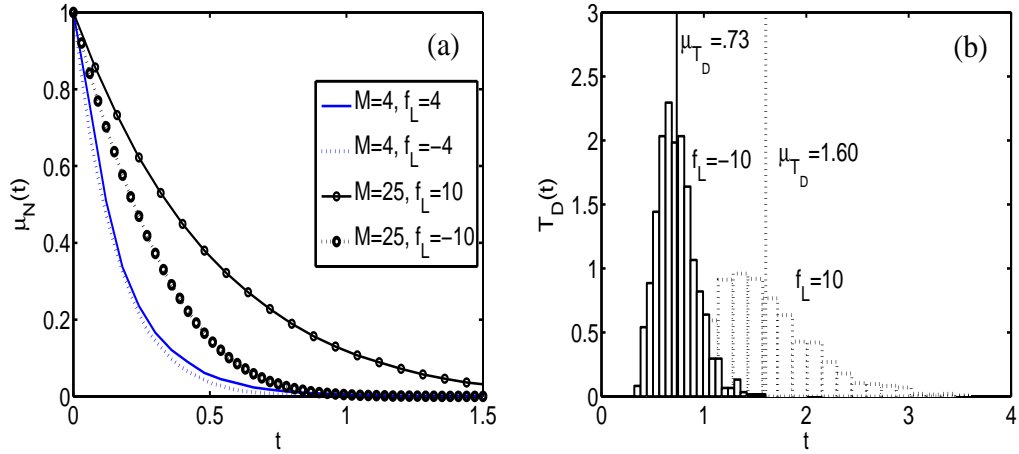


**Figure 5.19:** (a) Overall decay profile  $\mu_N$  (5.3.5a); (b) Histogram of the membrane's detachment time  $T_D(t)$ , from 1600 trajectories for  $M=25$  clusters and force  $f_L = 10$  (dotted line) and  $f_L = -10$  (solid line). Results obtained for  $T = 1, c = 1, L = 1, \beta = 1, \sigma = 1/8$ , and four clusters having  $X_i = 1/2 + (i - 1)/8, N_i(0) = 1$ , for  $i = 1, \dots, 4$ .

### 5.4.3 System dynamics under rupture and rebinding

In the presence of rebinding, the membrane fluctuates around certain equilibrium configurations, depending on the location and composition of the adhesion clusters, and also on the forces applied at the boundary. The membrane positions at the first six events in a single simulation are represented in Fig. 5.20 for positive and negative force. As anticipated, the membrane moves towards equilibrium positions influenced by the force on the boundary, and then fluctuates near a certain position. The membrane's position is generally tilted clockwise for  $f_L > 0$ , and anti-clockwise for  $f_L < 0$ .

The differential extension of bonds under a forced membrane is depicted in Fig. 5.21, where the cluster extensions  $H_i(t)$  are plotted along the first seven rupture and rebinding events. As in the spreading problem depicted in Fig. 5.11, the evolution of the cluster can be divided in three regions dominated by fluid flow (I), bond kinetics (II) and finally (III) by fluctuations near the equilibrium. There is nonetheless a significant difference, as the  $f_L$  forces each cluster to extend differently when in equilibrium.

For positive force  $f_L > 0$ , the extension of the clusters generally satisfies the relation  $H_4(t) < H_3(t) < H_2(t) < H_1(t)$ , most notably at equilibrium, when the membrane's right end is closer to the substrate, as suggested in Fig. 5.21 (a). When a new bond eventually forms, has a significant effect on the extension of adjacent clusters, which rapidly changes. The newly connected bond is suddenly subject to a large loading, and breaks in a short time, allowing the system to occupy its previous equilibrium position.

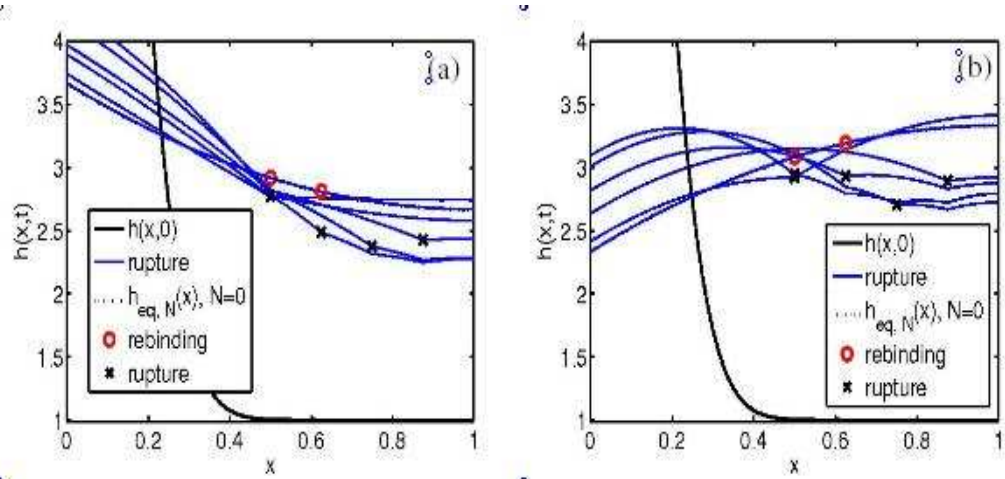


**Figure 5.20:** Position of the membrane during the first 7 rupture and rebinding events for (a)  $f_L = 4$ ; (b)  $f_L = -4$ . Results obtained for  $T = 1, c = 1, L = 1, \beta = 1, \sigma = 1/8, V = 3, \alpha = 1, \gamma = 1$ , and four clusters having  $X_i = 1/2 + (i - 1)/8, N_i(0) = 1$ , for  $i = 1, \dots, 4$ .

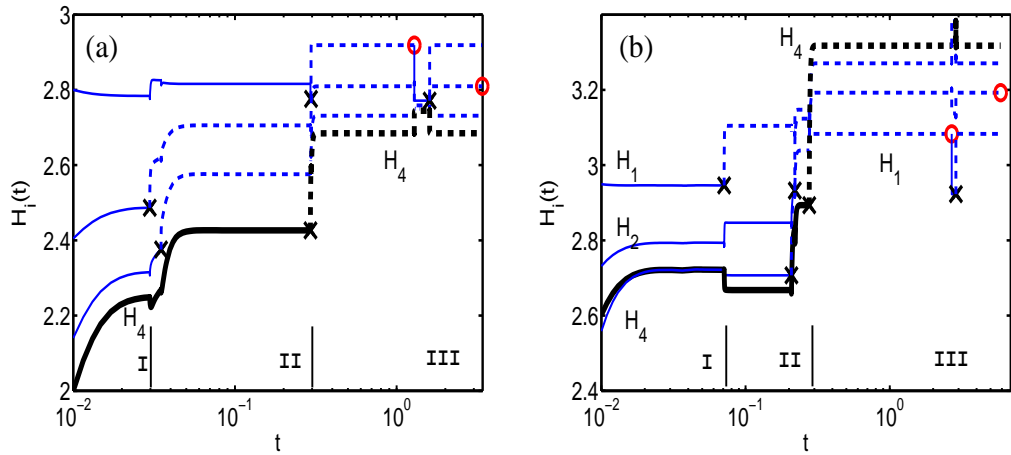


**Figure 5.21:** Plot of cluster extensions  $H_i(t), i = 1, \dots, 4$  under vertical forces (a)  $f_L = 4$ ; (b)  $f_L = -4$ . Connected bonds are represented by solid lines, while dissociated bonds by dashed lines. The rebinding and rupture events are represented by circles and crosses, respectively. Results obtained for  $T = 1, c = 10, L = 1, \beta = 1, \sigma = 1/8, V = 3, \alpha = 1, \gamma = 1$  and four clusters located at  $X_i = 1/2 + (i - 1)/8$ , and having  $N_i(0) = 1$  bonds,  $i = 1, \dots, 4$ . System dynamics dominated by (I) flow; (II) bond kinetics; (III) fluctuations near the equilibrium.

For negative force  $f_L < 0$ , the membrane's motion is initially driven by the spreading of the liquid, which preserves the relation  $H_4(t) < H_3(t) < H_2(t) < H_1(t)$  through region (I), and also in phase (II), as shown in Fig. 5.21. Immediately after the dissociation of the last bond, the force squeezes the liquid near the membrane's right-end, and reverses clusters' extensions to  $H_4(t) > H_3(t) > H_2(t) > H_1(t)$ , at equilibrium. Rarely, a bond is formed and the system leaves the equilibrium (for a much shorter time for  $f_L > 0$ ).

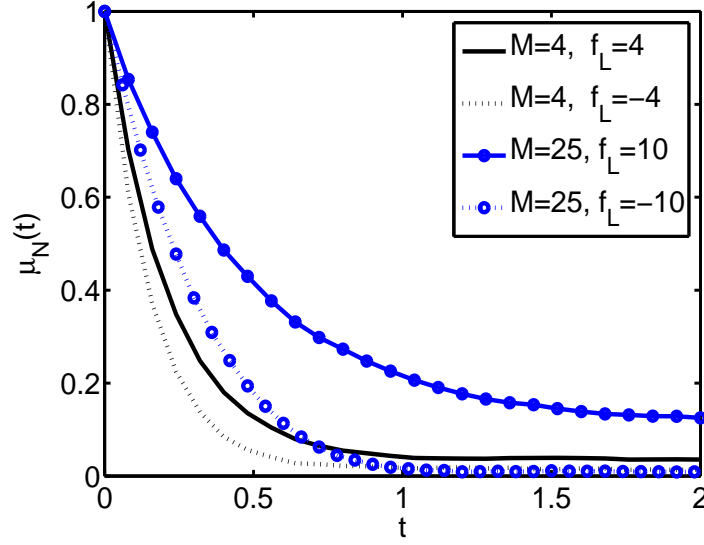


**Figure 5.22:** Overall cluster decay  $\mu_N(t)$  (5.3.5) obtained from the average of 500 simulations. Plot realized for  $T = 1, c = 1, L = 1, \beta = 1, \sigma = 1/8, V = 3, \alpha = 1, \gamma = 1$  and  $M = 4$  or 25 clusters located at  $X_i = 1/2 + (i - 1)/(2M)$ , having  $N_i(0) = 1$  bonds for  $i = 1, \dots, M$ .

One should note that even in the presence of rebinding, the trajectories first hit the boundary  $\sum_{i=1}^M N_i(t) = 0$  at roughly the same time and displacement, mostly because of the spreading fluid, and before the bonds feel the effects of force. This justifies the similar decay pattern observed in for the small clusters ( $M = 4$ ) in Fig. 5.19.

The overall cluster decay  $\mu_N$  as a function of force is illustrated in Fig. 5.22 for fixed rebinding parameters  $\alpha$  and  $\gamma$ , and for two cluster configurations having  $M = 4$  and  $M = 25$  bonds. In all examples, rebinding ensures that a non-zero equilibrium is attained, which is expected to go up as the formation of bonds intensifies.

For the same cluster dimension, the decay trajectories corresponding to positive and negative forces become increasingly different as rebinding becomes more intensive. As opposed to the situation depicted in Fig. 5.19, this effect can now be observed even for small clusters ( $M=4$ ), as rebinding ensures that the clusters are still active beyond the time when membrane dynamics become different for  $f_L > 0$  and  $f_L < 0$ .

The behaviour of large clusters offers two different perspectives. For  $f_L > 0$ , the presence of rebinding is immediately felt by the dissociated bonds, as the membrane's lower position and the higher availability of binding sites is accelerating the formation of new bonds. However, for  $f_L = -10$ , the large cluster ( $M=25$ ) does not benefit of the larger number of available binding sites, as  $\gamma = 1$  is not enough to compensate for the higher extension of the clusters. In the end, the fewer clusters ( $M=4$ ) located at a lower position attain a higher equilibrium value.

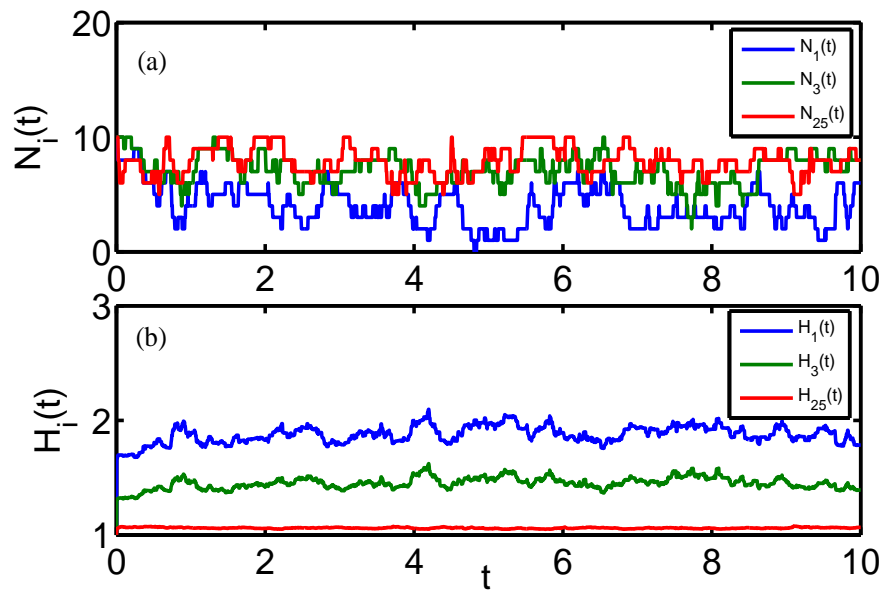


**Figure 5.23:** States of the system (a)  $N_i(t)$  and (b)  $H_i(t)$ ,  $i = 1, 3, 25$  in a single simulation, realized for  $T = 1$ ,  $c = 10$ ,  $L = 1$ ,  $\beta = 1$ ,  $\sigma = 1/8$ ,  $V = 3$ ,  $\alpha = 1$ ,  $\gamma = 5$ ,  $f_L = 10$  and  $M = 25$  clusters located at  $X_i = 1/2 + (i - 1)/(2M)$ , having  $N_i(0) = 10$  bonds for  $i = 1, \dots, M$ . Results for 2000 datapoints.

## 5.5 Analysis of single trajectories and peeling patterns

In this section we examine the behaviour of single trajectories, in the presence of rebinding and force at the boundaries, over longer timescales. The profile of single trajectories estimated at a fine time-grid is compared against the deterministic limit, which accurately predicts the equilibrium states of the system (when they exist), for many clusters ( $M = 25$ ) having multiple bonds. Several cluster statistics are compared using a wavelet-based semblance method, and it is shown that the overall cluster decay and extension are inversely correlated. Finally, we formulate and discuss three types of stochastic membrane peeling.

### 5.5.1 Membrane fluctuations near the equilibrium

As seen in the previous two sections, in the presence of rebinding, the membrane's behaviour consists of three phases. The first phase is flow dominated, in which the bonds are rapidly stretched. The second a slower or faster decay in the number of bonds (depending on  $V$ ,  $c$ ,  $M$ ), while the third is the membrane's fluctuation near an equilibrium position. This is estimated using single trajectories and deterministic approximations.

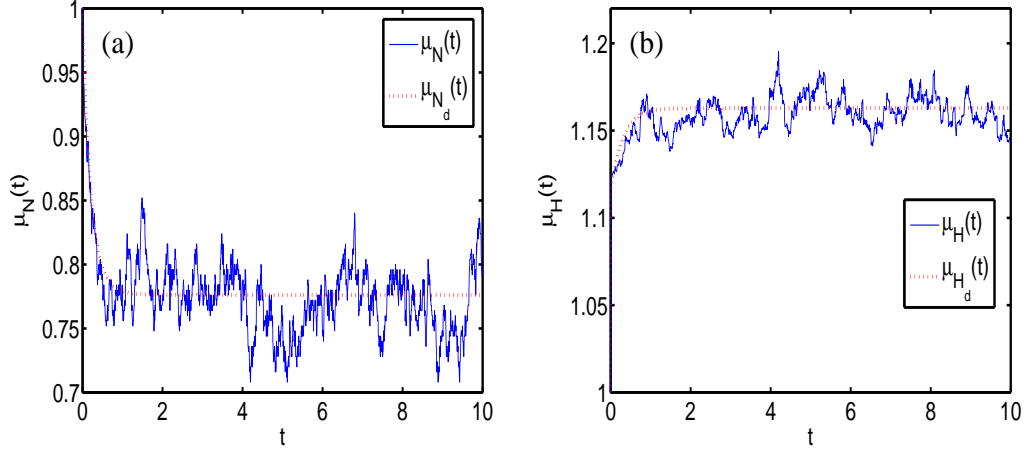


**Figure 5.24:** Stochastic and deterministic (a) overall decay  $\mu_N(t)$  and  $\mu_{N_d}(t)$ ; (b) Average bond extension  $\mu_H(t)$  and  $\mu_{H_d}(t)$  in a single simulation realized for  $T = 1$ ,  $c = 10$ ,  $L = 1$ ,  $\beta = 1$ ,  $\sigma = 1/8$ ,  $V = 3$ ,  $\alpha = 1$ ,  $\gamma = 5$ ,  $f_L = 10$  and  $M = 25$  clusters located at  $X_i = 1/2 + (i - 1)/(2M)$ , having  $N_i(0) = 10$  bonds for  $i = 1, \dots, M$ . The time resolution is 2000 points.

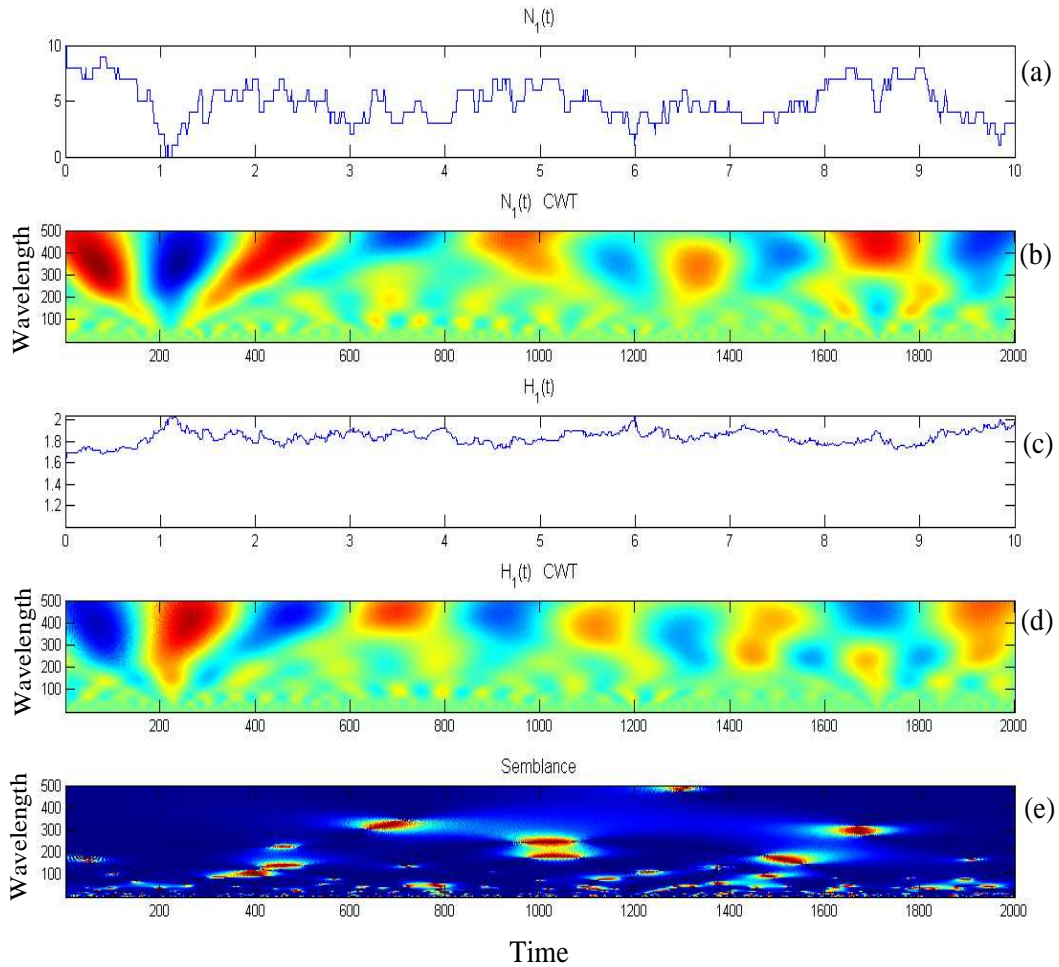
The trajectory of the system  $(N_1, \dots, N_M, H_1, \dots, H_M)$  is completely determined by the time, location and nature of the events. As suggested by Fig. 5.23 (a), the number of bonds in each cluster starts fluctuating, with the largest variations in the cluster located near the left-end. As illustrated in Fig. 5.23 (b), the reason is the bond's larger extension, but the large value  $\gamma$ , does not allow the bonds in  $N_1$  to completely dissociate. Similarly to the overall cluster decay (5.3.5), one can define the stochastic and deterministic clusters' average extension

$$\mu_H(t) = \frac{\sum_{i=1}^M \mu_{H_i}(t)}{M}, \quad (5.5.1a)$$

$$\mu_{H_d}(t) = \frac{\sum_{i=1}^M \mu_{H_{d,i}}(t)}{M}. \quad (5.5.1b)$$

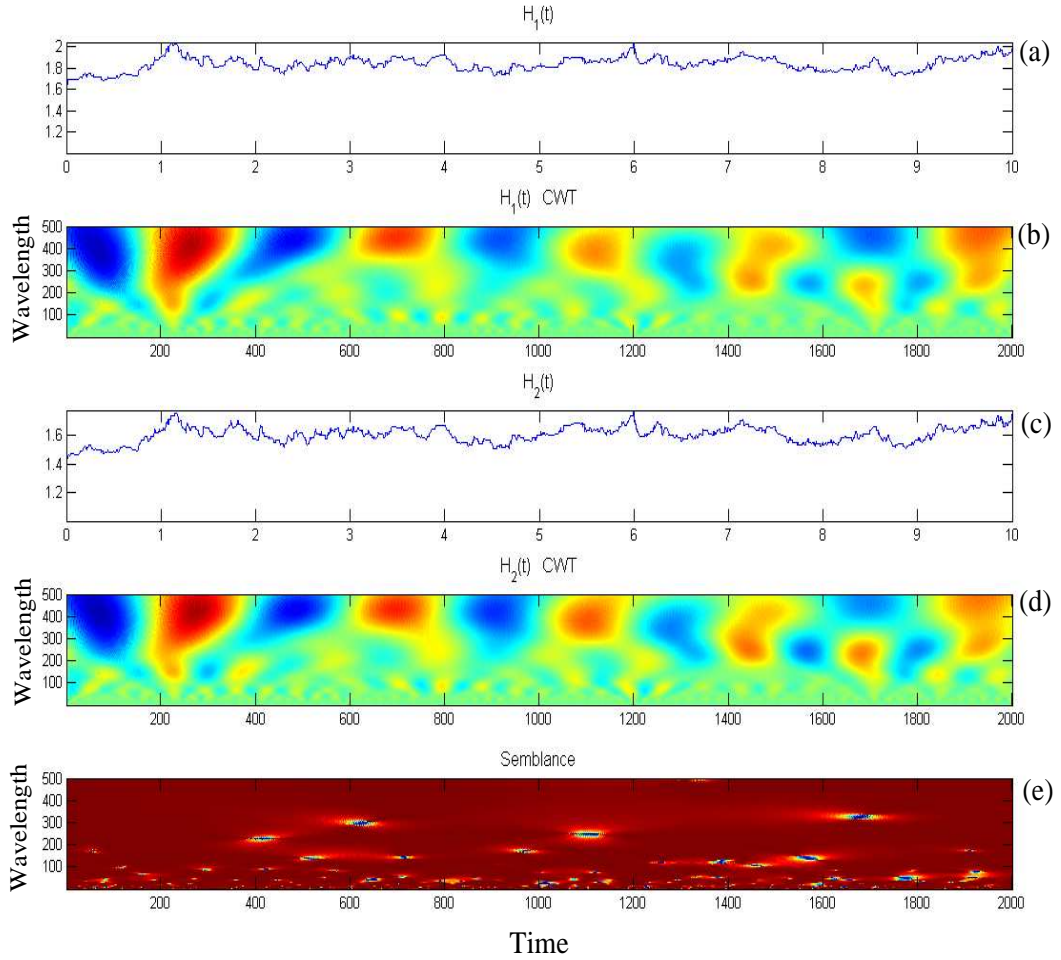
which provides a rough estimate for the membrane's displacement at the clusters' coordinates. The good match between the stochastic and deterministic overall decay and the clusters' average extension can be seen in Fig. 5.24, where the deterministic limit is able to predict the equilibrium values near which the system is oscillating, for bond population and cluster extension.

The interdependence between the variables  $N_1, \dots, N_M$  and  $H_1, \dots, H_M$  is analyzed using the semblance  $S$  (5.2.22), which compares phase angles and ranges from  $-1$  (inversely correlated - dark blue) through zero (uncorrelated - green) to  $+1$  (correlated - red). Unlike the Fourier-transform-based semblance analysis, calculated solely as a function of frequency, the CWT semblance analysis is calculated as a function of both scale (or wavelength - here, length of the time window) and time (or position).



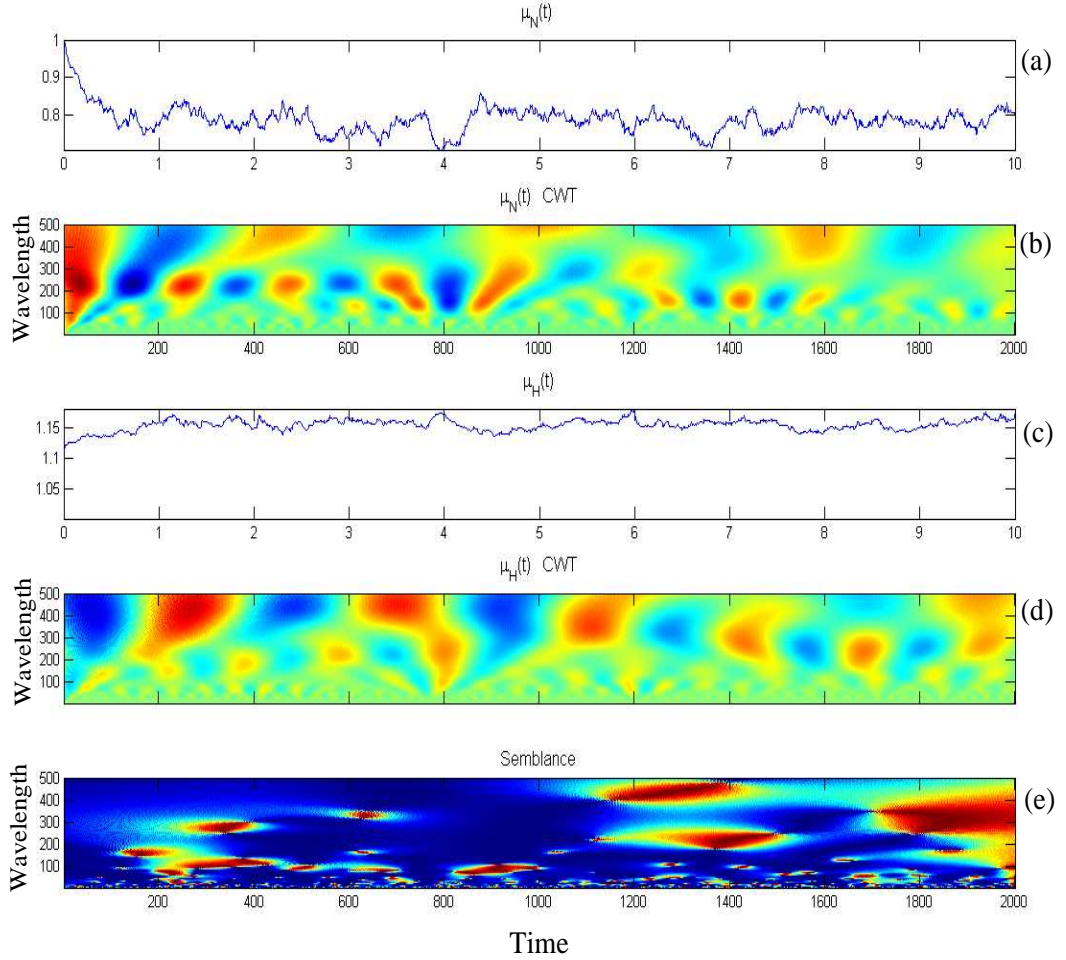
**Figure 5.25:** (a) Dataset containing  $N_1(t)$  at 2000 points. (b) Real part of the complex CWT of dataset in (a). Bright red indicates a large positive amplitude and dark blue indicates a large negative amplitude. (c) Dataset containing  $H_1(t)$  at 2000 points. (d) Real part of the complex CWT of dataset in (c). Bright red indicates a large positive amplitude and dark blue indicates a large negative amplitude. (e) Semblance  $S$  (5.2.22). Bright red corresponds to a semblance of  $+1$ , green to a semblance of zero, and dark blue to a semblance of  $-1$ . Results obtained from a single simulation realized for  $T = 1$ ,  $c = 10$ ,  $L = 1$ ,  $\beta = 1$ ,  $\sigma = 1/8$ ,  $V = 3$ ,  $\alpha = 1$ ,  $\gamma = 5$ ,  $f_L = 10$  and  $M = 25$  clusters located at  $X_i = 1/2 + (i - 1)/(2M)$ , having  $N_i(0) = 10$  bonds for  $i = 1, \dots, M$ . Vertical axes represent the wavelength as in (5.2.17). Code based on [23].

Fig. 5.25 shows the real part of the CWT computed for  $N_1$  and  $H_1$ , and their semblance. As one can see in Fig. 5.25 (b) and (d), the most significant amplitude changes are taking place for large wavelengths, while for smaller wavelength these are close to zero. The rapid variations of small amplitude, generate small and numerous bright spots in the lower part of Fig. 5.25 (e), suggesting rapid changes in the phase for small wavelengths. In general, the two variables tend to be negatively correlated with the increase of the wavelength.



**Figure 5.26:** (a) Dataset containing  $H_1(t)$  at 2000 points. (b) Real part of the complex CWT of dataset in (a). Bright red indicates a large positive amplitude and dark blue indicates a large negative amplitude. (c) Dataset containing  $H_2(t)$  at 2000 points. (d) Real part of the complex CWT of dataset in (c). Bright red indicates a large positive amplitude and dark blue indicates a large negative amplitude. (e) Semblance  $S$  (5.2.22). Bright red corresponds to a semblance of +1, green to a semblance of zero, and dark blue to a semblance of -1. Results obtained from a single simulation realized for  $T = 1$ ,  $c = 10$ ,  $L = 1$ ,  $\beta = 1$ ,  $\sigma = 1/8$ ,  $V = 3$ ,  $\alpha = 1$ ,  $\gamma = 5$ ,  $f_L = 10$  and  $M = 25$  clusters located at  $X_i = 1/2 + (i - 1)/(2M)$ , having  $N_i(0) = 10$  bonds for  $i = 1, \dots, M$ . Vertical axes represent the wavelength, as in (5.2.17). Code based on [23].

Fig. 5.26 shows the real part of the CWT computed for  $H_1$  and  $H_2$ , and their semblance. Again, as seen in Fig. 5.26 (b) and (d), the most significant changes in amplitude are localized at large wavelengths. As  $H_1$  and  $H_2$  represent the extensions of closed neighboring clusters, it is expected that in general their evolution to be correlated, as suggested in Fig. 5.26 (e). There are however numerous small bright spots, particularly over smaller time intervals (wavelengths), which can be explained by the sudden stochastic variation of clusters  $N_1$  and  $N_2$ , which differentially push the membrane above.



**Figure 5.27:** (a) Dataset containing  $\mu_N(t)$  at 2000 points. (b) Real part of the complex CWT of dataset in (a). Bright red indicates a large positive amplitude and dark blue indicates a large negative amplitude. (c) Dataset containing  $\mu_H(t)$  at 2000 points. (d) Real part of the complex CWT of dataset in (c). Bright red indicates a large positive amplitude and dark blue indicates a large negative amplitude. (e) Semblance  $S$  (5.2.22). Bright red corresponds to a semblance of  $+1$ , green to a semblance of zero, and dark blue to a semblance of  $-1$ . Results obtained from a single simulation realized for  $T = 1$ ,  $c = 10$ ,  $L = 1$ ,  $\beta = 1$ ,  $\sigma = 1/8$ ,  $V = 3$ ,  $\alpha = 1$ ,  $\gamma = 5$ ,  $f_L = 10$  and  $M = 25$  clusters located at  $X_i = 1/2 + (i - 1)/(2M)$ , having  $N_i(0) = 10$  bonds for  $i = 1, \dots, M$ . Vertical axes represent the wavelength, as in (5.2.17). Code based on [23].

Finally, in Fig. 5.27 we examine the CWT and the semblance of  $\mu_N$  and  $\mu_H$ , computed from a single trajectory. As before, in Fig. 5.27 (b) and (d), the most significant changes in amplitude are localized at large wavelengths, but the wavelengths where  $\mu_N$  and  $\mu_H$  vary most, are  $\sim 250$ , and  $\sim 400$ , respectively. This indicates that the timescale over which the bond population varies significantly, is shorter than the timescale corresponding to significant variations in the membrane's position. Interpreting accurate results from the semblance graph shown in Fig. 5.27 (e) is not straightforward, as the

track of many effects was lost when we averaged. The two quantities seem to be largely negatively correlated, especially at small wavelengths, with notable exceptions identifiable near  $t = 7$  and  $t = 10$ , where as seen in Fig. 5.25 (a),  $N_1$  is in a low position.

### 5.5.2 Peeling patterns

A significant challenge we are trying to address is the membrane peeling near the boundary of the contact region. The problem has been intensively studied by many authors including Dembo *et al.* [28], Hodges & Jensen [70], or Reboux *et al.* [115], mostly by representing the bonds within a continuum framework, where an adherent cell in a shear flow exhibits genuine tank-treading motion, with a peeling process taking place at the trailing edge of the contact region. In contrast, our model considers that the bonds form at individual binding spots.

The snapshots illustrated in Fig. 5.28, where the states of  $N_i$  are depicted in (a) and membrane's positions  $h(x, t)$  in (b), at four different times, provide preliminary evidence on the existence of peeling pattern in the evolution of the membrane with bonds attached to it. One can see that the bond populations are generally decreasing, while the left-end cluster's coordinates  $X_C(t)$  increases with time.

Here we propose three preliminary types of characterization of a peeling process.

#### Sequential stochastic peeling

As the liquid blob distributes to the right, the bonds to be first stretched are the ones near the left-end boundary, so these bonds are likely to dissociate first. This suggests defining the "stochastic peeling" as the process characterized by the successive dissociation of bonds from the left to the right, as illustrated in Fig. 5.29 (c) and (d). It is clear that such a process is unlikely in the presence of moderate rebinding, so for the moment we shall discuss the vanishing rebinding limit. As the rupture rates depend on cluster extension, the membrane's profile directly influences the peeling frequency.

When the membrane is parallel to the surface, the bonds rupture with the same probability, and the frequency of a stochastic peeling event for  $M$  clusters is easily found to be a discouraging  $1/M!$ , which suggests that even for  $M = 4$  clusters, stochastic peeling is unlikely ( $1/4! \sim 4\%$ ), as seen in Fig. 5.29 (a) and (b).

However, the estimation of sequential peeling events from stochastic simulations, may still indicate parameter regions facilitating the peeling. The peeling frequencies, together with mean and standard deviations of the detachment time  $T_D$  for 2 or 4 clusters and various values of  $f_L$ ,  $V$  and  $\sigma$  can be seen in Table 5.1.

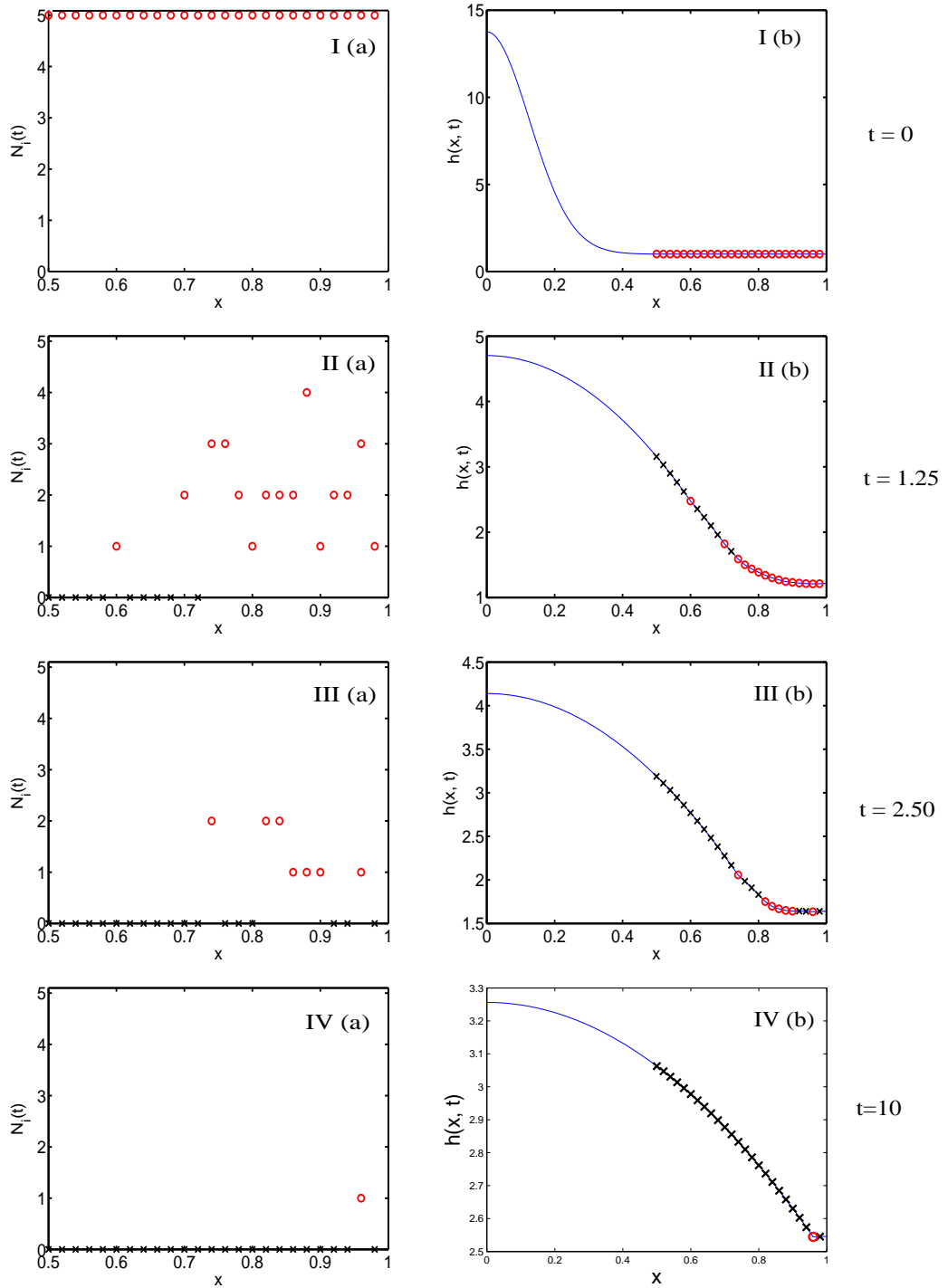


**Figure 5.28:** Peeling behaviour identified from a single simulation. The four time phases *I*, *II*, *III* and *IV* are consistent with the peeling of the membrane and the dissociation of the clusters situated near the left-end boundary. The circles represent connected clusters, the crosses dissociated clusters. (a) Bond population  $N_i(t)$ . (b) Membrane displacement. Plot realized for  $T = 1$ ,  $c = 10$ ,  $L = 1$ ,  $\beta = 1$ ,  $\sigma = 1/8$ ,  $V = 3$ ,  $\alpha = 1$ ,  $\gamma = 1$ ,  $f_L = 0$ , and  $M = 25$  clusters located at  $X_i = 1/2 + (i - 1)/(2M)$ , having  $N_i(0) = 5$  bonds for  $i = 1, \dots, M$ .

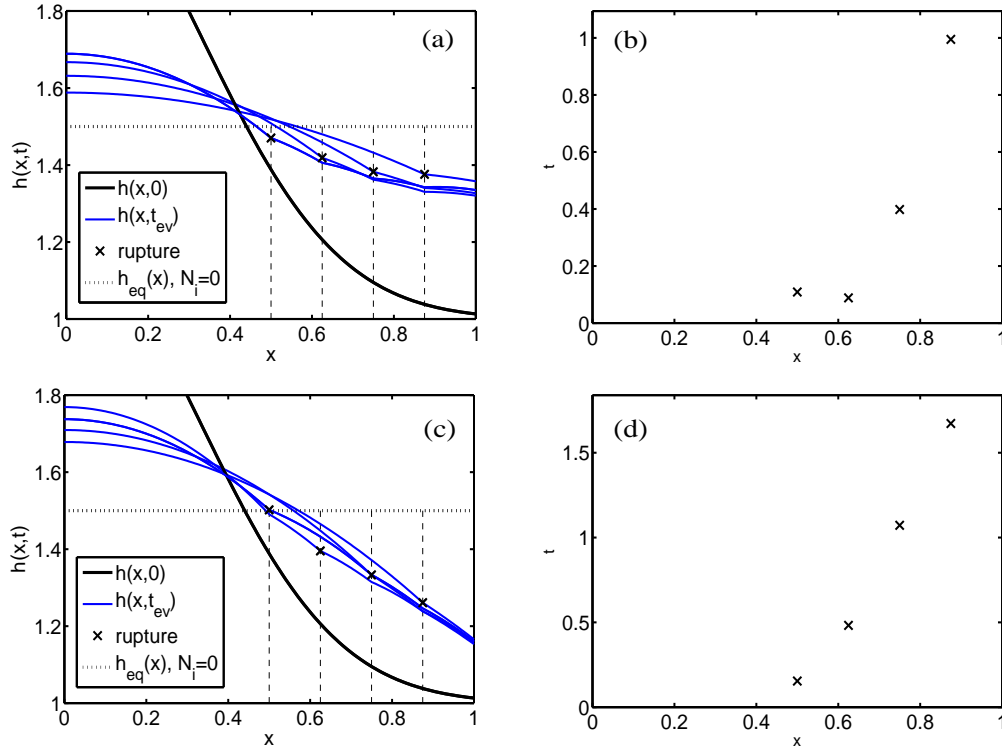


**Figure 5.29:** Single simulation of the stochastic membrane detachment for  $T = 1$ ,  $c = 1$ ,  $\sigma = 1/3$ ,  $L = 1$ ,  $V = 1.5$ , and four clusters having  $X_i = 1/2 + (i - 1)/8$ ,  $i = 1 \dots, 4$  and  $N_1(0) = \dots = N_4(0) = 1$ , plus a fixed cluster at  $x = 1$ , having  $N_{end}$  bonds. (a)  $h(x, t)$  at the rupture times,  $N_{end} = 1$ ; (b) time and location of the rupture event,  $N_{end} = 1$ . (c)  $h(x, t)$  at the rupture times,  $N_{end} = 10$ ; (d) time and location of the rupture event,  $N_{end} = 10$ .

As illustrated in Fig. 5.29, the presence of a large non-breakable cluster at the right boundary tilts the membrane's profile, enhancing the peeling frequency. In a peeling problem, the fixed cluster can be justified by the presence of a large number of bonds in the contact region, at the right of the trailing edge, which keep the membrane tightly attached to the fixed wall. Given the exclusive nature of this definition, we also present some other alternatives.

### Average stochastic peeling

A more inclusive measure of peeling was suggested by the profile of standard deviations  $\sigma_{N_i}$ ,  $i = 1, \dots, M$  depicted in Fig. 5.8 (a). An average stochastic peeling process may be defined as the process in which the times  $T_i$  when  $\sigma_{N_i}$  peaks, verify the relation

$$T_1 \leq T_2 \leq \dots \leq T_M. \quad (5.5.2)$$

As suggested by Fig. 5.13 (a), this definition may be valid even in the presence of rebinding. The averages may represent a much better measure of membrane peeling.

Clusters	$\sigma$	$V$	$f_L$	Peeling %	$\mu_{T_D}$	$\sigma_{T_D}$
2	1/6	1.5	0	53.9375 %	0.92859	0.64162
2	1/3	1.5	0	50.625 %	0.92433	0.62881
2	1/6	3	0	53.4375 %	0.25229	0.18009
2	1/6	1.5	4	57.125 %	1.0937	0.71159
2	1/6	3	4	57.9375 %	0.30472	0.22843
4	1/6	1.5	0	4.875 %	1.3245	0.67344
4	1/3	1.5	0	4.5625%	1.3553	0.68414
4	1/6	3	0	6.125 %	0.41196	0.2342
4	1/6	1.5	4	5.25 %	1.5686	0.78002
4	1/6	3	4	7.1875 %	0.49677	0.30313

**Table 5.1:** Clusters and membrane dynamics: nonbreakable right end cluster  $N_{end} = 1$ , fluid volume  $V$ , the normal-like membrane's initial position (5.1.27) has standard deviation  $\sigma = 1/6, 1/3$ .

### Monotonic left-end peeling

Finally, peeling may also be characterized by the position of the non-dissociated cluster situated closest to the left-end boundary, which we baptize the 'left-end cluster'. An event is called a monotonic left-end peeling if the coordinate  $X_C(t)$  of the left-end cluster is an increasing function with time, as in Fig. 5.30, in the peeling region. Using this definition, in the absence of rebinding any event is a monotonic left-end peeling.

However, things change when rebinding is present. The process can be initially characterized as a monotonic left-end peeling. Initially, the left-end cluster is  $N_1$ , which dissociates at time  $t \sim .48$  when it is replaced the cluster  $N_2$ . An interesting event happens next, when following the rupture of  $N_2$  the left-end cluster coordinate jumps straight to  $X_6$ . This suggests that clusters  $N_1$  and  $N_2$  shielded the rupture of the clusters  $N_3$ ,  $N_4$  and  $N_5$ , which were already dissociated at the time when  $N_2$  vanished. The left-end coordinate then jumps again, this time to  $X_{13}$  at  $t \sim 1.9$ . After time  $t \sim 2.1$  the formation of bonds before the trailing edge may perturb the monotonic left-end peeling profile, as one can see in Fig. 5.30.

Going back to Fig. 5.28, the simulation may still be called monotonic left-end peeling in a broader sense, if the simulation is filtered for a specific timescale, which eliminates the counting of short-lived bonds before the trailing edge.

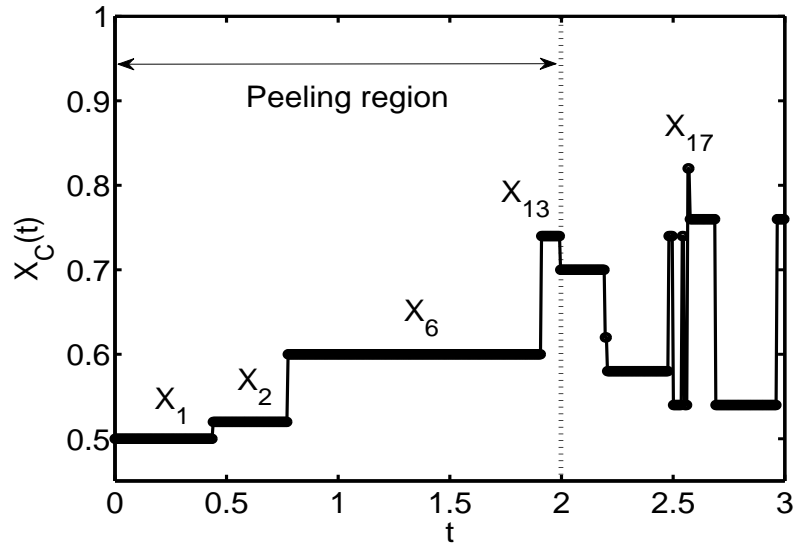


**Figure 5.30:** Peeling region characterized by the position of the left-end non-dissociated cluster. Plot realized for  $T = 1$ ,  $c = 10$ ,  $L = 1$ ,  $\beta = 1$ ,  $\sigma = 1/8$ ,  $V = 3$ ,  $\alpha = 1$ ,  $\gamma = 1$ ,  $f_L = 0$ , and  $M = 25$  clusters located at  $X_i = 1/2 + (i - 1)/(2M)$ , having  $N_i(0) = 5$  bonds for  $i = 1, \dots, M$ . The membrane peels sequentially with clusters dissociating from left to right until time  $t \simeq 2$ .

## 5.6 Summary

In this chapter we have presented a simple description of the coupling between the deterministic continuous motion of a flexible membrane and the stochastic rupture and formation of discrete bonds. The model predicts the relation between the membrane displacement and the evolution of bonds, examines the influence of the relevant parameters.

The first version of the model, ‘spreading membrane’, considered the extension of the bonds as being generated by the spreading of a liquid blob, which widens the gap between the membrane and the substrate. In the absence of rebinding, the membrane detaches completely and stabilizes to an equilibrium position, while the bond’s decay was found to be a function of liquid volume and drag. In the presence of rebinding the system fluctuates near an equilibrium position, which is well solved by the deterministic approximation. The second version of the model considered vertical forces applied at the boundaries, ‘forced membrane’, when the membrane dynamics significantly changed. One of the differences is that in the absence of rupture or rebinding events, the membrane stabilizes to equilibria tilted clockwise for positive, and anti-clockwise for negative force, respectively. The membrane’s profile is also directly dependent on the sign of the force applied.

Finally, we have analyzed single simulation profiles, where the deterministic models were shown to correctly predict the average bond population and cluster extension at equilibrium (Fig. 5.24). A wavelet-based semblance method, was used to show that the displacement of adjacent clusters is positively correlated, while cluster's overall extension and bond population are negatively correlated (Figs. 5.25 and 5.27). Three definitions were proposed for the stochastic membrane peeling. The sequential peeling based on the ordered rupture of bonds was found to be promoted in certain regions of the parameter space, but to occur very rarely even for small clusters. A definition based on stochastic averages, using the differential peaking time of the standard deviations, observed in Fig. 5.8. Finally, for clusters with multiple bonds, and in the presence of rebinding, we have proposed a peeling definition based on the position of the cluster nearest to the left-end, which was found to be more general than the sequential peeling (Fig. 5.28).

The model can be adapted for the study of cell rolling (by applying forces  $f_L < 0$  and  $f_R > 0$  at boundaries) or cell detachment as in the biomembrane force probe (BFP) experiments (by applying  $f_L > 0$ ,  $f_R > 0$ ). At the same time, the generality of the methods ensures that the extension of the model do not require significantly different approaches. The model may be effectively used for the estimation of the number of biological bonds connecting two surfaces. To do this, one needs to know the geometry of the contact region, which allows the modelling of the transition rates. From experiments we can obtain the frequency of rupture/rebinding events using the deflections of the AFM (for example). Simulations could then be used to predict the number of bonds required to attain the measured frequency. Nonetheless, a significant limitation of the model in the current form is the liquid volume constraint.

# Appendix

## 5.A Numerical solution of the membrane's steady states

---

The algorithm for computing the membrane steady states for a given configuration of bonds is detailed below, for the cases of membrane spreading under flow, and membrane spreading under vertically forced boundaries. We also present a more developed model, accounting for lateral membrane motion and rotational moments.

### 5.A.1 Steady states of the membrane: free fluid spreading

For a given cluster configuration  $X_1, \dots, X_M$  and  $K_1, \dots, K_M$ , the membrane's steady state is shown to be formed of parabola arches, which have jumps in their derivative at  $X_1, \dots, X_M$ . The steady state for a single cluster is explicitly solved, and a numerical algorithm for the solution of the general problem are detailed below.

**A single cluster with  $K_1$  bonds attached at  $x = X_1$ .**

Integrating (5.3.3) for  $\epsilon > 0$  over the interval  $[X_1 - \epsilon, X_1 + \epsilon]$  and letting  $\epsilon \rightarrow 0$  one obtains

$$-\left[Th'\right]_{X_1^-}^{X_1^+} + K_1(h-1)\Big|_{x=X_1} = 0. \quad (5.A.1)$$

This suggests that the Dirac just imposes a jump in  $h'$  at  $X_1$ , which is directly proportional to  $K_1$  and inversely proportional to  $T$ . As in the previous case, at the left and right of  $X_1$  the curve  $h$  is still solved by a quadratic. Solving  $h$  is reduced now to matching arcs of parabolas, with prescribed jumps at the nodes and boundary conditions at  $x = 0$  and  $x = L$ . In this particular case an analytical solution can be obtained.

The parameters of the problem are  $T, K_1, h_0, X_1, L, V$ , and the solution has the properties

$$h(x) = \begin{cases} a_0x^2 + b_0x + c_0, & x < X_1, \\ a_1x^2 + b_1x + c_1, & x > X_1, \end{cases} \quad (5.A.2a)$$

$$[h']_{X_1^-}^{X_1^+} = K_1 [h(X_1) - h_0] / T. \quad (5.A.2b)$$

The unknowns are the constants  $a_0, b_0, c_0, a_1, b_1, c_1, C$  and there are several conditions to be fulfilled. The first one is

$$-Th''(x) = C, \quad x < X_1, \quad (5.A.3a)$$

$$-Th''(x) = C, \quad x > X_1, \quad (5.A.3b)$$

which gives  $a_0 = a_1 = -\frac{C}{2T}$ . The boundary conditions at  $x = 0$  and  $x = L$  and give

$$h'(0) = 0 \Rightarrow b_0 = 0, \quad (5.A.4a)$$

$$h'(L) = 0 \Rightarrow -\frac{b_1}{2a_1} = L \Rightarrow b_1 = \frac{LC}{T}. \quad (5.A.4b)$$

The continuity condition of the membrane displacement at  $x = X_1$

$$h^-(X_1) = h^+(X_1), \quad (5.A.5)$$

gives  $c_0 - c_1 = \frac{LC}{T}X_1$ , which together with (5.A.2b) leads to

$$\begin{aligned} c_0 &= \frac{LC}{K_1} + h_0 + \frac{C}{2T}X_1^2, \\ c_1 &= \frac{LC}{K_1} + h_0 + \frac{C}{2T}X_1^2 - \frac{LC}{T}X_1. \end{aligned}$$

So far, the variables  $a_0, b_0, c_0, a_1, b_1$  and  $c_1$  have been obtained in terms of the initial parameters and the constant  $C$ . Finally,  $C$  can be obtained from the conservation of the fluid volume below the membrane

$$V = \int_0^L h(x)dx = \int_0^{X_1} h(x)dx + \int_{X_1}^L h(x)dx. \quad (5.A.6)$$

An important question is whether the system actually has a solution, which can be easily proven, once we reformulate the system in matrix form  $\mathbf{Ax} = \mathbf{b}$ , where  $\mathbf{A}$  is

$$\mathbf{A} = \begin{pmatrix} -X_1 & X_1 & -1 & 1 & 0 & 0 \\ -1 & 1 - \frac{K_1X_1}{T} & 0 & -\frac{K_1}{T} & 0 & -\frac{K_1X_1^2}{T} \\ 1 & 0 & 0 & 0 & 0 & 0 \\ 0 & 1 & 0 & 0 & -\frac{L}{T} & 0 \\ \frac{X_1^2}{2} & \frac{L-X_1^2}{2} & X_1 & L-X_1 & 0 & \frac{L^3}{3} \\ 0 & 0 & 0 & 0 & \frac{1}{2T} & 1 \end{pmatrix} \quad (5.A.7)$$

and the vectors  $\mathbf{x}$  and  $\mathbf{b}$  are

$$\mathbf{x}^T = (b_0 \quad b_1 \quad c_0 \quad c_1 \quad C \quad a) \quad (5.A.8a)$$

$$\mathbf{b}^T = \left(0 \quad -\frac{K_1}{T}h_0 \quad 0 \quad 0 \quad 0 \quad V \quad 0\right). \quad (5.A.8b)$$

Simple computations give

$$\det \mathbf{A} = \frac{L \left[ 3LT + K_1 \left( L - \frac{3}{2}X_1 \right)^2 + \frac{3}{4}X_1^2 \right]}{3T^2} > 0, \quad (5.A.9)$$

so there is a solution of the system for all values of the parameters (as the tension is clearly positive). The general problem can be dealt with in the same way, although a complete proof of the existence of the solution is not available yet.

**General case:**  $K_1, \dots, K_M$  bonds located at the coordinates  $X_1, \dots, X_M$ . The solution of the general problem when  $K_1, \dots, K_M$  bonds located at the coordinates  $X_1, \dots, X_M$  follows the steps suggested before. As the analytical solution is very complicated, the problem is formulated as a linear system of equations, which is then solved numerically when a unique solution exists. The other parameters in the problem  $V, T, h_0, L$  being given, the solution satisfies (5.3.3), where  $C$  is an unknown constant. As mentioned earlier, the steady state solution is composed of the matched parabolic arches  $h(x) = a_i x^2 + b_i x + c_i$ , for  $x \in [X_i, X_{i+1}]$ ,  $i = 0, \dots, M$  where  $X_0 = 0$ ,  $X_{m+1} = L$ .

Inside each interval we have

$$-Th''(x) = C, x \in (X_i, X_{i+1}) \Rightarrow a_0 = a_1 = \dots = a_M = -\frac{C}{2T}. \quad (5.A.10)$$

The continuity of the membrane at  $x = X_i, i = 1, \dots, M$  gives

$$h^-(X_i) = h^+(X_i) \Rightarrow X_i(b_i - b_{i-1}) + c_i - c_{i-1} = 0, \quad i = 1, \dots, M. \quad (5.A.11)$$

Integrating (5.3.3) for  $\epsilon > 0$  over the interval  $[X_i - \epsilon, X_i + \epsilon]$  and letting  $\epsilon \rightarrow 0$  we obtain the jump in the slope of the membrane at the binding site coordinate  $X_i$ , given by

$$[h']_{X_i^-}^{X_i^+} = K_i \frac{h(X_i) - h_0}{T} \Rightarrow b_i - b_{i-1} = \frac{K_i}{T} \left[ a_i X_i^2 + b_i X_i + c_i - h_0 \right]. \quad (5.A.12)$$

The boundary conditions at the right and left ends give

$$h'(0) = 0 \Rightarrow b_0 = 0, \quad (5.A.13a)$$

$$h'(L) = 0 \Rightarrow b_M = -2a_M L = \frac{CL}{T}. \quad (5.A.13b)$$

The last relation comes from the conservation of liquid volume below the membrane, which gives

$$\begin{aligned} \int_0^L h(x)dx &= \sum_{i=0}^M \int_{X_i}^{X_{i+1}} h(x)dx \\ &= a\frac{L^3}{3} + \sum_{i=0}^M b_i \left( \frac{X_{i+1}^2 - X_i^2}{2} \right) + \sum_{i=0}^M c_i (X_{i+1} - X_i) = V. \end{aligned} \quad (5.A.14)$$

The problem can be formulated as a system of  $2m + 4$  equations (one from (5.A.10),  $M$  from (5.A.11),  $M$  from (5.A.12), two from (5.A.13) and one from (5.A.14)). Although  $b_0$  and  $b_M$  can be obtained directly, they still appear in the system for symmetry.

Writing the system in matrix form  $\mathbf{Ax} = \mathbf{b}$ , the matrix  $\mathbf{A}$  is given by

$$\left( \begin{array}{cc|cccc|cc|cc|cc} -X_1 & X_1 & \cdots & 0 & 0 & -1 & 1 & \cdots & 0 & 0 & 0 & 0 \\ \vdots & \vdots & \ddots & \vdots & \vdots & \vdots & \vdots & \ddots & \vdots & \vdots & \vdots & \vdots \\ 0 & 0 & \cdots & -X_M & X_M & 0 & 0 & \cdots & -1 & 1 & 0 & 0 \\ \hline -1 & 1 & -\frac{K_1 X_1}{T} & \cdots & 0 & 0 & -\frac{K_1}{T} & \cdots & 0 & 0 & 0 & -\frac{K_1 X_1^2}{T} \\ \vdots & \vdots & \ddots & \vdots & \vdots & \vdots & \vdots & \ddots & \vdots & \vdots & \vdots & \vdots \\ 0 & 0 & \cdots & -1 & 1 & -\frac{K_M X_M}{T} & 0 & 0 & \cdots & 0 & -\frac{K_M}{T} & 0 & -\frac{K_M X_M^2}{T} \\ \hline 1 & 0 & \cdots & 0 & 0 & 0 & 0 & \cdots & 0 & 0 & 0 & 0 & 0 \\ 0 & 0 & \cdots & 0 & 1 & 0 & 0 & \cdots & 0 & 0 & -\frac{L}{T} & 0 & 0 \\ \frac{X_1^2}{2} & \frac{X_2^2 - X_1^2}{2} & \cdots & \frac{X_M^2 - X_{m-1}^2}{2} & \frac{L - X_M^2}{2} & X_1 & X_2 - X_1 & \cdots & X_M - X_{m-1} & L - X_M & 0 & \frac{L^3}{3} & 0 \\ 0 & 0 & \cdots & 0 & 0 & 0 & 0 & \cdots & 0 & 0 & \frac{1}{2T} & 1 & 0 \end{array} \right) \quad (5.A.15)$$

while the vectors  $\mathbf{x}$  and  $\mathbf{b}$  are

$$\mathbf{x}^T = (b_0 \quad \cdots \quad b_M \quad c_0 \quad \cdots \quad c_M \quad C \quad a) \quad (5.A.16a)$$

$$\mathbf{b}^T = (0 \quad \cdots \quad 0 \quad -\frac{K_1}{T} h_0 \quad \cdots \quad -\frac{K_M}{T} h_0 \quad 0 \quad 0 \quad V \quad 0). \quad (5.A.16b)$$

When  $\det \mathbf{A} \neq 0$  the system has a unique solution.

## 5.A.2 Steady states of the membrane: vertically forced boundaries

The equilibrium position of the membrane general having  $K_1, \dots, K_M$  bonds attached at the coordinates  $X_1, \dots, X_M$  and subject to vertical forces  $f_L$  and  $f_R$  at the left and right membrane ends can be obtained using a modified version of the algorithm used for solving the steady state of the spreading membrane.

The boundary conditions at the right and left ends (5.A.13) of the membrane are replaced by

$$h_x^+(0) = -\frac{f_L}{2T} \Rightarrow b_0 = -\frac{f_L}{2T}, \quad (5.A.17a)$$

$$h_x^-(L) = \frac{f_R}{2T} \Rightarrow 2a_M L + b_M = \frac{f_R}{2T}. \quad (5.A.17b)$$

The solution can be obtained by solving  $\mathbf{Ax} = \mathbf{b}$ , for  $\mathbf{A}$  given by (5.A.15) and  $\mathbf{b}$

$$\mathbf{b}^T = \left( 0 \quad \dots \quad 0 \quad -\frac{K_1}{T}h_0 \quad \dots \quad -\frac{K_M}{T}h_0 \quad -\frac{f_L}{2T} \quad \frac{f_R}{2T} \quad V \quad 0 \right). \quad (5.A.18)$$

## 5.B Membrane model accounting for lateral motion

To begin with, we stress that all the quantities used in this section are dimensional.

Identical hinged plates of length  $2l$ . Midpoint of each plate is at  $(x_i, h_i)$ . The  $i$ -th plate is tilted at the angle  $\theta_i$ , resulting in a tangent vector  $\underline{t}_i = (\cos \theta_i, \sin \theta_i)$  and normal vector  $\underline{n}_i = (-\sin \theta_i, \cos \theta_i)$ . We also have in-plane tension  $T_i$  in each plate, pressure  $p_i$  below each plate and  $p = 0$  above, internal out-of-plane stress resultants  $Q_i \underline{n}_i$ ,  $-Q_i \underline{n}_i$  at the end of each plate.

Hinges lie at coordinates  $(x_i \pm l \cos \theta_i, h_i \pm l \sin \theta_i)$  on plate  $i$ , as seen in Fig. 5.31.

Assume  $k_i$  molecular bonds at the mid-point of the  $i$ -th plate, share the force  $\underline{f}_i = \left( 0, -k_i(h_i - h_0) \right)$ , where  $h_0$  is the unstressed length. The bonds are assumed not to tilt.

Drag on plate  $\underline{d}_i = (d_i^x, d_i^y)$  to be determined using lubrication theory, scaling

$$d_i^x \sim -\mu(lX/h_i^2)dx_i/dt, \quad d_i^y \sim -\mu(lX^2/h_i^3)dh_i/dt,$$

from where we obtain

$$d_i^y \sim lp_i, \quad p_i = \mu(X^2/h_i^3)dh_i/dt.$$

Force balance on the plate is

$$\underline{0} = T_{i+1}\underline{t}_{i+1} - T_{i-1}\underline{t}_{i-1} + \underline{f}_i + \underline{d}_i - Q_{i+1}\underline{n}_{i+1} + Q_{i-1}\underline{n}_{i-1}, \quad (5.B.1)$$

which in vertical and horizontal direction give

$$0 = T_{i+1} \sin \theta_{i+1} - T_{i-1} \sin \theta_{i-1} - k_i(h_i - h_0) + \underline{d}_i^y - Q_{i+1} \cos \theta_{i+1} + Q_{i-1} \cos \theta_{i-1}, \quad (5.B.2a)$$

$$0 = T_{i+1} \cos \theta_{i+1} - T_{i-1} \cos \theta_{i-1} + \underline{d}_i^x + Q_{i+1} \sin \theta_{i+1} - Q_{i-1} \sin \theta_{i-1}. \quad (5.B.2b)$$

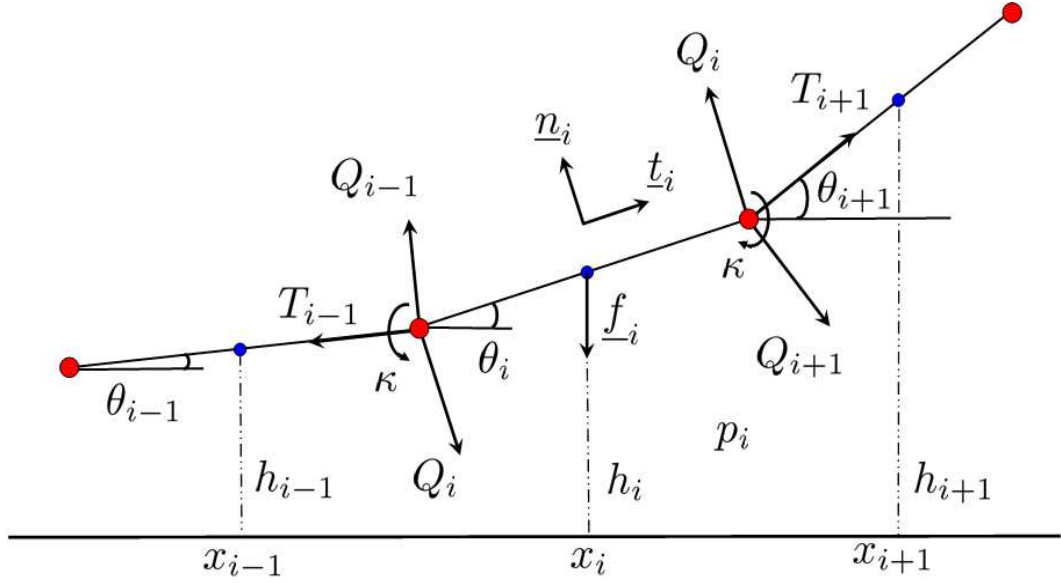


Figure 5.31: The elastic springs are attached at the mid-point of the plates of equal length  $2l$ .

Moment on the plate around mid-point (assume drag exerts no net moment) is

$$\underline{Q} = l\underline{t}_i \times (T_{i+1}\underline{t}_{i+1}) + (-l\underline{t}_i) \times (-T_{i-1}\underline{t}_{i-1}) + \kappa(\theta_{i+1} - \theta_i)\underline{z} - \kappa(\theta_i - \theta_{i-1})\underline{z} \\ + (l\underline{t}_i) \times (-Q_{i+1}\underline{n}_{i+1}) + (-l\underline{t}_i) \times \underline{n}_{i-1}Q_{i-1}, \quad (5.B.3)$$

where  $\underline{z} = \underline{t}_i \times \underline{n}_i$  is a unit vector out of page. So

$$0 = lT_{i+1} \sin(\theta_{i+1} - \theta_i) + lT_{i-1} \sin(\theta_i - \theta_{i-1}) + \kappa(\theta_{i+1} - 2\theta_i + \theta_{i-1}) \\ - lQ_{i+1} \cos(\theta_{i+1} - \theta_i) - lQ_{i-1} \cos(\theta_i - \theta_{i-1}). \quad (5.B.4)$$

Assuming all angles are small, the terms quadratic in  $\theta$  can be discarded in (5.B.2a), (5.B.2b) and (5.B.4), to obtain

$$0 = T_{i+1}\theta_{i+1} - T_{i-1}\theta_{i-1} - k_i(h_i - h_0) + \underline{d}_i^y - (Q_{i+1} - Q_{i-1}) \quad (5.B.5) \\ 0 = T_{i+1} - T_{i-1} + \underline{d}_i^x + Q_{i+1}\theta_{i+1} - Q_{i-1}\theta_{i-1}. \\ 0 = l[T_{i+1}(\theta_{i+1} - \theta_i) + T_{i-1}(\theta_i - \theta_{i-1})] + \kappa(\theta_{i+1} - 2\theta_i + \theta_{i-1}) - l(Q_{i+1} + Q_{i-1}).$$

Further simplification will be possible after rescaling. The distance between  $x_i$  and  $x_{i+1}$  is then  $2l$  (to leading order). Introducing smoothly varying functions  $\Theta(x, t)$ ,  $H(x, t)$ ,  $N(x, t)$ ,  $T(x, t)$ ,  $D^x(x, t)$ ,  $D^y(x, t)$ ,  $Q(x, t)$  such that  $\Theta(x_i, t) = \theta_i$ , where  $l \ll X = \text{length-scale of variation of continuous variables}$ , we obtain

$$T_{i+1} = T(x_{i+1}, t) \approx T(x_i + 2l, t) = T_i + 2lT_x(x_i, t) + 1/2(2l)^2T_{xx}(x_i, t) + \dots$$

and the likes. With these notations (5.B.5) becomes

$$\begin{aligned}
 0 &= (T_i + 2lT_x)(\theta_i + 2l\Theta_x) - (T_i - 2lT_x)(\theta_i - 2l\Theta_x) - N(H - h_0) + D^y - 4lQ_x + \dots \\
 &= 4lT\Theta_x + 4lT_x\Theta - N(H - h_0) + D^y - 4lQ_x + \dots, \quad (5.B.6) \\
 0 &= (T_i + 2lT_x) - (T_i - 2lT_x) + D^x + (Q_i + 2lQ_x)(\Theta_i + 2l\Theta_x) - (Q_i - 2lQ_x)(\Theta_i - 2l\Theta_x) \\
 &= 4lT_x + D^x + 2lQ_x\Theta + 2lQ\Theta_x \\
 0 &= l[(T_i + 2lT_x)2l\Theta_x + (T_i - 2lT_x)2l\Theta_x] + \\
 &\quad \kappa(\theta_i + 2l\Theta_x + 2l^2\Theta_{xx} - 2\theta_i + \theta_i - 2l\Theta_x + 2l^2\Theta_{xx}) - 2lQ_i + \dots \\
 &= 2l^2T\Theta_x + 4\kappa l^2\Theta_{xx} - 2lQ + \dots.
 \end{aligned}$$

At this point we can also relate  $H$  to  $\theta$ :  $h_{i+1} - h_i = 2lH_x + O(l^2) = l(\theta_i + \theta_{i+1}) = 2l\theta_i + O(l^2)$ , so  $H_x = \Theta$ . Replacing  $\Theta_x$  in (5.B.6) we obtain

$$\begin{aligned}
 0 &= 4l(TH_x)_x - N(H - h_0) + D^y - 4lQ_x, \quad (5.B.7) \\
 0 &= 4lT_x + D^x + 2l(QH_x)_x, \\
 0 &= l(TH_{xx} + 2\kappa H_{xxx}) - Q.
 \end{aligned}$$

We can write the scalings

$$\frac{lTh_0}{X^2} \sim N_0 h_0 \sim \mu \frac{lX^2 h_0}{h_0^3 t} \sim \frac{lQ}{X}, \quad (5.B.8a)$$

$$\frac{lT}{X} \sim \mu \frac{lX}{h_0^2} U \sim \frac{lQ h_0}{X X}, \quad (5.B.8b)$$

$$\frac{lTh_0}{X^2} \sim \frac{l\kappa h_0}{X^3} \sim Q, \quad (5.B.8c)$$

where  $H \sim h_0$  and  $U = dX/dt$ . From (5.B.8a) we obtain

$$t \sim \mu \frac{lX^2}{h_0^3 N_0}, \quad X^2 \sim \frac{lT}{N_0}, \quad Q \sim \frac{h_0 T}{X}.$$

Then (5.B.8b) and (5.B.8c) can be written as

$$\frac{lT}{X} \sim \mu \frac{lX}{h_0^2} U \sim \frac{lh_0 h_0 T}{X^2 X} = \frac{lT h_0^2}{X X^2}, \quad (5.B.9a)$$

$$\frac{lTh_0}{X^2} \sim \frac{l\kappa h_0}{X^3} \sim \frac{h_0 T}{X}. \quad (5.B.9b)$$

Since  $l \ll h_0 \ll X$ , the underlined terms are subdominant by  $h_0^2/X^2$  and  $l/X$ , and therefore can be ignored.

Assuming negligible sliding (large mean tension)  $\left(U \ll \frac{Th_0^2}{X^2 \mu}\right)$ , at leading order we have  $T_x = 0$ , so  $T = \text{constant}$ . In the absence of sliding,  $H_t = \left(\frac{H^3}{12\mu} p_x\right)_x$  and  $D^y = pl$ .

The first and third equations of (5.B.6) become

$$\begin{aligned} 0 &= 4lTH_{xx} - N(H - h_0) + D^y - 8l^2\kappa H_{xxxx} \\ Q &= 2l\kappa H_{xxx}. \end{aligned} \quad (5.B.10)$$

Balancing the terms in the first equation we can write

$$\frac{lTh_0}{X^2} \sim N_0h_0 \sim \frac{\mu l X^2 h_0}{h_0^3 t} \sim l^2\kappa h_0 X^4.$$

Let  $X = 2\left(\frac{lT}{N_0}\right)^{1/2} \hat{x}$ ,  $t = \mu \frac{l^2 T}{h_0^3 N^2} \hat{t}$ ,  $p = \frac{N_0}{T} h_0 \hat{p}$ ,  $B = \frac{8\kappa l^2 h_0}{(4lT/N)^2}$ ,  $H = h_0 \hat{H}(\hat{x}, \hat{t})$ ,  $N = N_0 \hat{N}(\hat{x}, \hat{t})$ .

Then

$$\begin{aligned} H_t &= \frac{1}{12} \left( H^3 p_x \right)_x, \\ 0 &= H_{xx} - N(H - 1) + p - BH_{xxxx}, \\ p &= N(H - 1) - H_{xx} + BH_{xxxx}. \end{aligned} \quad (5.B.11)$$

Assume steady peeling such that  $H(x, t) = H(\xi)$ ,  $\xi = x + Vt$ ,  $V$  to be determined.

Then  $VH_\xi = \frac{1}{12} \left( H^3 p_\xi \right)_\xi$  and  $p = N(H - 1) - H_{\xi\xi} + BH_{\xi\xi\xi\xi}$ . This gives  $12V(H - 1) = H^3 p_\xi$ , assuming  $p = 0$  when  $H = 1$  (bonds unstressed), and further  $12V(H - 1) = H^3 [N(H - 1)]_\xi - H^3 H_{\xi\xi\xi} + BH^3 H_{\xi\xi\xi\xi}$ . Assume hinges are weak,  $B \ll 1$  and we can formulate coupled ODEs for solving  $N(\xi)$ .

# Conclusions

THE INTERPLAY between hydrodynamic forces and the stochastic formation and rupture of discrete bonds between moving surfaces has been theoretically investigated. The deterministic motion of the surfaces, solved by lubrication theory and interrupted by the stochastic jumps in the bond population, suggested the formulate the model as a continuous-time piecewise deterministic Markov process. This allowed the simulation of individual trajectories of the system, from which we could obtain important information on cluster lifetime or bond extension. Stochastic simulations were complemented by deterministic approximations valid in the limit of a large number of bonds. These give valuable insight into the behaviour of the system and greatly reduce the mathematical complexity of the problem, as well as the computational cost, but at the expense of not capturing stochastic effects in the evolution of clusters with few bonds. The models under investigation are mostly inspired by dynamic force spectroscopy experiments, which measure force and extension of bonds connecting surfaces at the level of individual molecules.

As a simple coupling between bond kinetics and continuous cell motion, we considered in Chapter 2 a theoretical model for the stochastic adhesion of a cluster of bonds connecting a rigid disk and a flat surface. The model, formulated as a piecewise deterministic Markov process, accounts for the rupture and rebinding of discrete bonds, depending on the disk's motion under applied force. Hydrodynamic forces in the thin layer of viscous fluid between the two surfaces are described using lubrication theory, while inertia at the scales of our model and Brownian motion, were proven to be negligible in the presence of force. Several experiments confirmed the elasticity of bonds under force [98], showing that their length in response to applied force may increase 5- to 6-fold for fibronectin [73], so bonds are modeled as identical, parallel springs, and equally share the load. The coupling between the bond's extension and the nonlinear motion of a disk under force, represents a significant extension over models assuming a

constant displacement using polymeric spacers [35]. Monte Carlo simulations, capturing the stochastic evolution of clusters with few bonds, are complemented by various deterministic approximations, valid in the limit of a large number of bonds.

The model considerably simplified the description of the disk's motion, by squeezing liquid viscosity, disk dimensions and bond's stiffness and unstretched length into a single dimensionless drag coefficient.

Following Erdmann & Schwarz, the zero- and infinite- drag limits of the model were explored in Chapter 3. Several methods were developed specifically for this problem, of which we stress the Fokker-Plank equation (FPE) and a matrix exponential-based the solution of the ME (3.2.2). Using the solutions of the ME (3.2.2) we confirmed the existence of three forcing (small, intermediate, large) and three loading-rate (slow, intermediate, fast) regimes, illustrated in Figs. 3.3 and 3.18, respectively. Our results provide quantitative estimates for the corresponding boundaries, completing the qualitative descriptions discussed in [31] and [33]. A fixed ratio  $f/n$  completely characterizes the deterministic decay for any cluster dimension, while stochastic simulations predict that larger clusters decay faster than smaller ones (Fig. 3.7). Larger clusters may again decay slower than the clusters with fewer bonds, for sufficiently large re-binding (Fig. 3.16). Using stochastic estimates for the mean cluster lifetime, we have established upper and lower bounds for cluster lifetime under drag, depicted in Fig. 3.9. For the constant loading-rate problem we mimicked a DFS experiment, showing that the model is able to predict rupture force as a function of the loading rate [38], [95]. Also, distributions of the rupture force computed for single and multiple bond clusters showed an increasing spread with the increase of the loading rate, while rupture forces for clusters seemed to be normally distributed (see Fig. 3.20).

The effects of drag were investigated in Chapter 4. We identified three distinct regions in the parameter space spanned by force and drag: for large drag, the disk barely moves and the cluster's evolution is largely dictated by bond kinetics; for small drag, bond dynamics are enslaved to the disk's motion; in between, there is a transient regime, where the bonds break as the disk is moving upwards under force. For non-zero re-binding we determined the force required to destabilize the cluster and discussed the stable equilibria of the deterministic approximation.

Drag has an even more profound impact when the disk is under ramped force. Large drag allow the bonds to extend at a slower rate, hence to survive for longer. At the same time, force has the time to build up, resulting in a very abrupt terminal decay. Cluster statistics mimicking dynamic force spectroscopy experiments show that adding drag significantly changes the profile of the rupture force distributions. If in the absence of

drag the distributions were overlapping, adding drag makes the profiles differentiate. The behaviour of clusters is even more different, as large clusters survive longer, being exposed to larger forces, until they eventually break. The expected sudden cluster dissociation for large values of drag and loading rate is evident in Fig. 4.16.

We also examined a PDE formulation for the time-evolution of the probability density of the stochastic process  $(N, H)$ . Solutions of the dCKE with the method of characteristics showed a good agreement with stochastic simulations for large values of drag, but a poor agreement for the late phase of the cluster decay. We have identified two potential reasons for this outcome. The first is the complicated geometry of the solution, which converges to a Dirac distribution with time. In the large-drag limit, this is not a problem, as the characteristics collapse long after the cluster dissociated, so the code shows a good agreement with the stochastic results. We still investigate whether the disagreement for small drag is because of the inaccuracy of the method for the given problem, but preliminary results indicate that increasing the number of characteristic curves does not improve the precision of the results. This fact made us wonder whether the problem may in fact support a PDE formulation. An argument in this sense is the analytical solution obtained for the marginal probability distributions  $P_k$  in Appendix 4.A, which is a  $n + 1 - k$ -dimensional integral, with time-dependent limits. As the densities are some sense differentials of  $P_k$ , we feel it is rather unlikely they would satisfy a PDE. To address this issue, we have developed an integro-differential formula, to be tested against simulations.

The model was extended to include spatial effects and inhomogeneous bonds in Chapter 5, where we considered the stochastic evolution of a bond population connecting a flexible membrane to a rigid wall, accounting for hydrodynamic forces from fluid in the space between the membrane and the wall. The model, formulated as a piecewise deterministic Markov process, accounts for the rupture and rebinding of discrete bonds, depending on the membrane's position. The deterministic motion of the membrane, interrupted by stochastic binding and unbinding events, is formulated as a partial differential equation derived using lubrication theory. Spatial effects were introduced by modeling the bonds as identical and parallel elastic springs, which form at certain binding sites spread over the membrane's surface and which differentially share the load, depending on their extension. Stochastic simulations of the model were compared against solutions of a deterministic approximation, and averages of the bond population and membrane detachment times were examined, showing that cluster dynamics are strongly influenced by the amount and the initial distribution of liquid beneath the membrane. The first version of the model (a "spreading membrane"), considered the

extension of the bonds generated by the spreading of a liquid blob, which widens the gap between the membrane and the substrate. In the absence of rebinding, the membrane detaches completely and stabilizes to an equilibrium position, while the bond's decay was found to be a function of liquid volume and drag. In the presence of rebinding the system fluctuates near an equilibrium position, which is accurately solved by the deterministic approximation. When vertical force was applied at the boundaries (a "forced membrane"), the membrane dynamics significantly change, as in the absence of rupture or rebinding events the membrane stabilizes to tilted equilibria which differentially stretch the connected clusters. The membrane's profile is directly dependent on the sign of the force applied. The model provides preliminary evidence of the nature of the peeling stochastic processes. Subsequently, the model predicts that for clusters with sufficiently many bonds and in the presence of rebinding, the membrane and the bond population fluctuate near equilibria predicted by the deterministic approximation. The average population and extension of clusters are shown to be largely inversely correlated, using a wavelet-based semblance method.

## Future work

---

The results obtained in Chapters 3 and 4 for ramped force (see Fig. 1.4), showed that our theoretical investigation generated results sharing the structure of DFS experiments of Merkel *et al.* [95]. As illustrated in (1.4), Brownian effects play an important role especially for slow loading, so the addition of Brownian noise in the disk-bond system is expected to generate a better rendition of the DFS experiment. After calibrating the model using experimental data obtained from single bond experiments, our model can be used for a better understanding of the experiments for cluster unbinding.

At the same time, the integro-differential forward equation proposed as an alternative to the PDE suggested by Lipniacki [91] can be solved to generate a global description of the joint time-height probability densities characterizing the bivariate Markov process  $(N(t), H(t))$  with discrete and continuous states. Although the model has the merit of coupling discrete bond kinetics to the continuum motion of the disk, its simplicity may not capture many significant physiological processes, as the bonds were treated as an homogeneous population and without spatial effects apart from the vertical motion of the membrane.

The preliminary investigation of the simple membrane model raises interesting questions, one should address before considering more detailed mechanical details, such as membrane bending stiffness, rotational moment, or lateral displacement. A first thing

to do is to consider more realistic boundary conditions, that allow liquid to enter below the membrane. As suggested by the behaviour of the membrane under forced boundaries, one could push one of the membrane's ends while pulling the other, to simulate stochastic rolling or peeling. Also, by applying upwards forces, one could simulate the membrane's detachment as in the DFS experiments. A question which would surely be worth investigating is whether for a force of a given magnitude it is easier to peel, or to detach the membrane of the surface. Another formulation of this problem is to identify the optimal force distribution on the membrane that promotes peeling or detachment.

# References

- [1] Acheson D. J., *Elementary Fluid Dynamics*, Oxford Applied Mathematics and Computing Science Series (1990).
- [2] Ainslie K. M., Bachelder E. M., Sharma G., Grimes A. and Pishko M. V., *Macrophage cell adhesion and inflammation cytokines on magnetostrictive nanowires*, *Nanotoxicology* **1**, Issue 4, 279-290 (2007).
- [3] Ackleh A. S., Banks H. T. and Denga K., *A finite difference approximation for a coupled system of nonlinear size-structured populations*, *Nonlinear Analysis* **50**, 727-748 (2002).
- [4] Alberts B., Johnson A., Lewis J., Raff M., Roberts K. and Walter P., *Molecular biology of the cell*, Garland Science, New York, 4th ed. (2002).
- [5] Alon R., Chen S., Puri K. D., Finger E. B. and Springer T. A., *The kinetics of L-selectin tethers and the mechanics of selectin-mediated rolling*, *J. Cell Biol.* **138**, 1169-1180 (1997).
- [6] Ball F. and Donnelly P., *Interparticle correlation in death processes with application to variability in compartmental models*, *Adv. Appl. Prob.* **19**, 755-766 (1987).
- [7] Barsegov V. and Thirumalai D., *Dynamics of unbinding of cell adhesion molecules: Transition from catch to slip bonds*, *Proc. Nat. Acad. Sci USA* **102**, 1835-1839 (2005).
- [8] Baumgartner W., Hinterdorfer P., Ness W., Raab A., Vestweber D., Schindler H. and Drenckhahn D., *Cadherin interaction probed by atomic force microscopy*, *Proc. Nat. Acad. Sci USA* **97**, 4005-4010 (2000).
- [9] Beckerle M. C., *Cell Adhesion*, Oxford University Press (2002).
- [10] Bell, G. I., *Models for specific adhesion of cell to cells*, *Science* **200**, 618-627 (1978).
- [11] Bell G. I., Dembo M. and Bongrand P., *Cell adhesion: Competition Between Nonspecific Repulsion and Specific Bonding*, *Biophys. J.* **45** (6), 1051-1064 (1984).

- [12] Benoit M., Gabriel D., Gerisch G. and Gaub H. E., *Discrete interactions in cell adhesion measured by single-molecule force spectroscopy*, *Nature Cell Biology* **2**, 313-317 (2000).
- [13] Binnig G., Quate C. and Gerber G., *Atomic force microscope*, *Phys. Rev. Lett.* **56**, 930-933 (1986).
- [14] Blanes S., Casas F., Oteo J. A. and Ros J., *The Magnus expansion and some of its applications*, *Phys. Rep.* **470**, 151-238 (2009).
- [15] Bongrand, P., *Ligand-receptor interactions*, *Rep. Prog. Phys.* **62**, 921-968 (1999).
- [16] Bongrand P., Pierres A., Vitte J. and Benoliel A., *Dissecting individual ligand-receptor interactions with a laminar flow-chamber*, *Biophys. Rev. Lett.* **1**, 231-257 (2006).
- [17] Box G. E. P., Hunter J. S. and Hunter W. G., *Statistics for experimenters*, *Wiley Series in Probability and Statistics*, (1978).
- [18] Chandrasekhar S., *Stochastic problems in physics and astronomy*, *Rev. Mod. Phys.* **15**, 1-89 (1943).
- [19] Chang K. C., Tees D. F. J. and Hammer D. A., *The state diagram for cell adhesion under flow: leukocyte rolling and firm adhesion*, *Proc. Natl. Acad. Sci. USA* **97**, 11262-11267 (2000).
- [20] Clarke R. J., Jensen O. E. and Billingham J., *Three-dimensional elastohydrodynamics of a thin plate oscillating above a wall*, *Phys. Rev. E* **78**, 056310 (2008).
- [21] Coccozza-Thivent C., Eymard R. and Mercier S., *A finite volume scheme for dynamic reliability models*, *IMA Journ. Num. Anal.* **26**, 446-471 (2006).
- [22] Compo G. P. and Torrence C., *A practical guide to wavelet analysis*, *B. Am. Meteorol. Soc.* **79**, 61-78 (1998).
- [23] Cooper G. R. J. and Cowan D. R., *Comparing time series using wavelet-based semblance analysis*, *Comput. Geosc.* **34**, 95-102 (2008).
- [24] Cooper G. M. and Hausman R. E., *The Cell: A Molecular Approach*, *Amer. Soc. Microbiol.*, Washington and Sinauer Assoc., 4th ed., Sunderland, MA (2006).
- [25] Corless, R., Gonnet, G., Hare, D., Jeffrey, D., and Knuth, D., *On the Lambert W function*, *Adv. Comput. Math.*, **5**, 329-359 (1996).

- [26] Cozens-Roberts C., Lauffenburger D. and Quinn J. A., *Receptor-mediated cell attachment and detachment kinetics: I. probabilistic model and analysis*, *Biophys. J.* **58**, 841-856 (1990).
- [27] Davis M. H. A., *Piecewise-deterministic Markov processes: a general class of non-diffusion stochastic models*, *J. R. Stat. Soc. Ser. B* **46**, 353-388 (1984).
- [28] Dembo M., Torney D. C., Saxman K. and Hammer, D. A., *The reaction-limited kinetics of membrane-to-surface adhesion and detachment*, *Proc. R. Soc. Lond. B* **234**, 55-83 (1988).
- [29] DeRoock I. B., Pennington M. E., Sroka T. C., Lam K. S., Bowden G. T., Bair E. L. and Cress A. E., *Synthetic Peptides Inhibit Adhesion of Human Tumor Cells to Extracellular Matrix Proteins*, *Cancer Res.* **61**, 3308-3313, (2001).
- [30] Einstein A., *Über die von der molekularkinetischen Theorie der Wärme geforderte Bewegung von in ruhenden Flüssigkeiten suspendierten Teilchen*, *Ann. Phys-Berlin* **17**, 549-560 (1905).
- [31] Erdmann T. and Schwarz, U. S., *Stochastic dynamics of adhesion clusters under shared constant force and with rebinding*, *J. Chem. Phys.* **121**, 8997-9017 (2004).
- [32] Erdmann T. and Schwarz, U. S., *Stability of adhesion clusters under constant force*, *Phys. Rev. Lett.* **92**, 108-102 (2004).
- [33] Erdmann T. and Schwarz, U. S., *Adhesion clusters under shared linear loading: A stochastic analysis*, *Europhys. Lett.* **66**, 603-609 (2004).
- [34] Erdmann T. and Schwarz, U. S., *Bistability of Cell-Matrix Adhesions Resulting from Nonlinear Receptor-Ligand Dynamics*, *Biophys. J.* **91**, L60-L62 (2006).
- [35] Erdmann T. and Schwarz U. S., *Impact of receptor-ligand distance on adhesion cluster stability*, *Eur. Phys. J. E* **22**, 123-137 (2007).
- [36] Erdmann T., *Stochastic dynamics of adhesion clusters under force*, PhD dissertation, Postdam University (2005).
- [37] Evans E., Berk D. and Leung A., *Detachment of agglutinin bonded red blood cells: I. Forces to rupture molecular-point attachment*, *Biophys. J.* **59**, 838-858 (1991).
- [38] Evans E. and Ritchie K., *Dynamic strength of molecular adhesion bonds*, *Biophys. J.* **72**, 1541-1555 (1997).

- [39] Evans E. and Ritchie K., *Strength of a weak bond connecting flexible polymer chains*, Biophys. J. **78**, 2439-2447 (1999).
- [40] Evans E., Leung A., Hammer D. and Simon S., *Chemically distinct transition states govern rapid dissociation of single L-selectin bonds under force*, Proc. Natl. Acad. Sci. USA **98**, 3784-3789 (2001).
- [41] Evans E. and Williams P., *Dynamic force spectroscopy: I. single bonds*, EDP Sciences, Springer-Verlag In Physics of Bio-Molecules and Cells. Ecoles des HOUCHES d'Ete LXXV: 145-185, (2002).
- [42] Evans E., Leung A., Heinrich V. and Zhu C. *Mechanical switching and coupling between two dissociation pathways in a P-selectin adhesion bond*, Proc. Natl. Acad. Sci. USA **101**, 11281-11286 (2004).
- [43] Ethier S. N. and Kurtz T. G., *Markov Processes: Characterization and Convergence*, Wiley Series in Probability and Statistics (1986).
- [44] Feller W., *On the normal approximation to the binomial distribution*, Ann. Math. Statist., **16**, No. 4, 319-329, (1945).
- [45] Ferm L., Lstedt P. and Hellander A., *A hierarchy of approximations of the Master Equation scaled by a size parameter*, J. Sci. Comput. **34**, 127-151 (2008).
- [46] FitzHugh R., *Statistical properties of the Asymmetric Random Telegraph Signal, with Applications to Single-Channel Analysis*, Math. Biosc. **64**, 75-89 (1983).
- [47] Friddle R. W., Sulchek T. A., Albrecht H., De Nardo S. J. and Noy A., *Counting and Breaking Individual Biological Bonds: Force Spectroscopy of Tethered Ligand-Receptor Pairs*, Curr. Nanosc., **3**, 41-48 (2007).
- [48] Fritz J., Katopodis A. G. , Kolbinger F. and Anselmetti D., *Force-mediated kinetics of single Pselectin/ ligand complexes observed by atomic force microscopy*, Proc. Natl. Acad. Sci. USA **95**, 12283-12288 (1998).
- [49] Gao H., Qian J. and Wang J., *Lifetime and Strength of Adhesive Molecular Bond Clusters between Elastic Media*, Langmuir **24**, 1262-1270 (2008).
- [50] Gardiner C. W., *Handbook of Stochastic Methods*, Springer Verlag, Third Edition (2004).
- [51] Garrod D. and Kimura T. E., *Hyper-adhesion: a new concept in cell-cell adhesion*, Biochem. Soc. Trans. **36**, 195-201 (2008).

- [52] Gillespie D.T., *A general method for numerically simulating the stochastic time evolution of coupled chemical reactions*, J. Comp. Phys. **22**, 403-434 (1976).
- [53] Gillespie D.T., *Exact stochastic simulation of coupled chemical reactions*, J. Phys. Chem. **81**, 2340-2361 (1977).
- [54] Gingras A. R., Ziegler W. H., Bobkov A. A., Joyce M. G., Fasci D., Himmel M., Rothemund S., Ritter A., Grossmann J. G., Patel B., Bate N., Goult B. T., Emsley J., Barsukov I. L., Roberts, Robert J. C. K., Liddington C., Ginsberg M. H. and Critchley D. H., *Structural Determinants of Integrin Binding to the Talin Rod*, J. Biol. Chem. **284**, 8866-8876 (2009).
- [55] Goldman A. J., Cox R. G. and Brenner H., *Slow viscous motion of a sphere parallel to a plane wall. I. Motion through a quiescent fluid*, Chem. Engng Sci. **22**, 637-651 (1967a).
- [56] Goldman A. J., Cox R. G. and Brenner H., *Slow viscous motion of a sphere parallel to a plane wall. II. Couette flow*, Chem. Engng Sci. **22**, 653-660 (1967b).
- [57] Goldstein B. and Wofsy C., *Why is it so hard to dissociate multivalent antigens from cell-surface antibodies ?*, Immunol. Today **17**, 77-80 (1996).
- [58] Gornik O., Dumić J., Flögel M. and Lauc G., *Glycoscience - a new frontier in rational drug design*, Acta Pharm. **56**, 19-30 (2006).
- [59] Gradshteyn I. S. and Ryzhik I. M., *Table of Integrals, Series and Products*, Academic Press, New York, 5th edition, 1994.
- [60] Green J. A., Berrier A. L., Pankov R. and Yamada K. M.,  *$\beta$ 1 Integrin Cytoplasmic Domain Residues Selectively Modulate Fibronectin Matrix Assembly and Cell Spreading through Talin and Akt-1*, J. Biol. Chem. **284**, No. 12, 8148-8159 (2009).
- [61] Hammer D. A. and Lauffenburger D. A., *A dynamical model for receptor-mediated cell adhesion to surfaces*, Biophys. J. **52**, 475-487 (1987).
- [62] Hammer D. A. and Apte S. M., *Simulation of cell rolling and adhesion on surfaces in shear flow: general results and analysis of selectin-mediated neutrophil adhesion*, Biophys. J. **63**, 35-57 (1992).
- [63] English T. E. and Hammer, D. A., *Brownian Adhesive Dynamics (BRAD) for Simulating the Receptor-Mediated Binding of Viruses*, Biophys. J. **86**, 3359-3372 (2004).

- [64] English T. E. and Hammer, D. A., *The Effect of Cellular Receptor Diffusion on Receptor-Mediated Viral Binding Using Brownian Adhesive Dynamics (BRAD) Simulations*, *Biophys. J.* **88**, 1666-1675 (2005).
- [65] Hammer D. A., *Leukocyte adhesion: what's the catch ?*, *Curr. Biol.* **15**, 96-99 (2005).
- [66] Hammer D. A. and Tirell M., *Biological adhesion at interfaces*, *Annu. Rev. Mater. Sci.* **26**, 651-691 (1996).
- [67] Hänggi P., Talkner P. and Borkovec M., *Reaction-rate theory: fifty years after Kramers*, *Rev. Mod. Phys.* **62**, 251-341 (1990).
- [68] Heinrich V. and Ounkmol C., *Force versus axial deflection of pipette-aspirated closed membranes*, *Biophys. J.* **93**, 363-372 (2007).
- [69] Higham D. J., *An algorithmic introduction to the numerical simulation of stochastic differential equations*, *SIAM Rev.*, **43**, No. 3, 525-546 (2001).
- [70] Hodges S. R. and Jensen O. E., *Spreading and peeling dynamics in a model of cell adhesion*, *J. Fluid Mech.* **460**, 381-409 (2002).
- [71] Humphries M. J., *The molecular basis and specificity of integrin-ligand interactions*, *J. Cell Sci.* **97**, 585-592 (1990).
- [72] Humphries M. J., *Integrin structure*, *Biochem. Soc. Trans.* **28**, part 4 (2000).
- [73] Hynes O. R., *The dynamic dialogue between cells and matrices: Implications of fibronectin's elasticity*, *Proc. Natl. Acad. Sci. USA*, **96**(6), 2588-2590 (1999).
- [74] S. Karlin and H.M. Taylor, *A first course in stochastic processes*, 2nd ed. Academic Press, New York (1975).
- [75] S. Karlin and H.M. Taylor, *An Introduction to Stochastic Modelling*, Academic Press (1993).
- [76] Kellermayer M. S. Z., Smith S. B., Granzier H. L. and Bustamante C., *Folding-unfolding transitions in single titin molecules characterized with laser tweezers*, *Science* **276**, 1112-1116 (1997).
- [77] Kerrigan J. J., McGill J. T., Davies J. A., Andrews L. and Sandy I. R., *The role of cell adhesion molecules in craniofacial development*, *J. R. Coll. Surg. Edinb.* **43**, 223-229 (1998).
- [78] King M. R., Sumagin R., Green C. E. and Simon S. I., *Rolling dynamics of a neutrophil with redistributed L-selectin*, *Mathem. Biosc.* **194**, 71-79 (2005).

- [79] Koch A. W., Manzur K. L. and Shana W., *Structure-based models of cadherin-mediated cell adhesion: the evolution continues*, Cell. Mol. Life Sci. **61**, 1884-1895 (2004).
- [80] Kohr M., Pop I., *Viscous Incompressible Flow for Low Reynolds Numbers*, WIT Press: Computational Mechanics Publications, Southampton (UK), Boston, 448 pp. (2004).
- [81] Kortt A. A., Lah M., Oddie G. W., Gruen C. L., Burns J. E., Pearce L. A., Atwell, J. L., McCoy A. J., Howlett G. J., Metzger D. W., Webster R. G. and Hudson P. J., *Single-chain Fv fragments of antineuraminidase antibody NC10 containing five- and ten-residue linkers form dimers and with zero-residue linker a trimer*, Protein Eng. **10**, 423-433 (1997).
- [82] Kramers H. A., *Brownian motion in a field of force*, Physica, **VII** 284-304 (1940).
- [83] Labeau P. E., *A Monte Carlo estimation of the marginal distributions in a problem of probabilistic dynamics*, Reliab. Eng. Sys. Saf. **52**, 65-75 (1996).
- [84] Lahooti S., Yueh H. K. and Neumann A. W., *An image analysis strategy to study cell adhesion*, Coll. Surf. B **3**, 333-342 (1995).
- [85] Laing C. and Lord G. J., *Stochastic Methods in Neuroscience*, OUP Oxford (2009).
- [86] Langston S. and Barlocco D., *Monitor: molecules and profiles*, Drug Disc. Today **6**, 698-699 (2001).
- [87] Lee G., Abdi K., Jiang Y., Michaely P., Bennett V. and Marszalek E., *Nanospring behaviour of ankyrin repeats*, Nature **440**, 246-249 (2006).
- [88] Ley K., Laudanna C., Cybulsky M. I. and Nourshargh S., *Getting to the site of inflammation: the leukocyte adhesion cascade updated*, Nature Rev. Immun. **7**, 678-689 (2007).
- [89] Li F., Redick S. D., Erickson H. P. and Moy V. T., *Force measurements of the  $\alpha_5\beta_1$  integrin-fibronectin interaction*, Biophys. J. **84**, 1252-1262 (2003).
- [90] Liphardt J., Dumont S., Smith S. B. and Bustamante C., *Equilibrium information from nonequilibrium measurements in an experimental test of Jarzynski's equality*, Science **296**, 1832-1835 (2002).
- [91] Lipniacki T., Paszek P. A., Marciniak-Czochra A., Brasier A. R. and Kimmela M., *Transcriptional stochasticity in gene expression*, J. Theor. Biol. **238**, 348-367 (2006).

- [92] Mallat S., *A wavelet tour of signal processing*, Academic Press, New York, Second Edition (1999).
- [93] Marsh J. and Goode J. A., *Cell Adhesion and Human Disease*, Ciba Foundation Symposium 189, Wiley, Chichester (1995).
- [94] Marshall B. T., Long M., Piper J. W., Yago T., McEver R. P. and Zhu C., *Direct observation of catch bonds involving cell-adhesion molecules*, *Nature* **423**, 190-193 (2003).
- [95] Merkel R., Nassoy P., Leung A., Ritchie K. and Evans E., *Energy landscapes of receptor-ligand bonds explored with dynamic force spectroscopy*, *Nature* **397**, 50-53 (1999).
- [96] Merkel R., *Force spectroscopy on single passive biomolecules and single biomolecular bonds*, *Phys. Rep.* **346**, 343-385 (2001).
- [97] Metropolis N. and Ulam S., *The Monte Carlo method*, *J. Amer. Stat. Assoc.* **44**, 335-341 (1949).
- [98] Maruthamuthu V., Schulten K. and Leckband D., *Elasticity and Rupture of a Multi-Domain Neural Cell Adhesion Molecule Complex*, *Biophys. J.* **96** (8), 3005-3014 (2009).
- [99] Morton K. W. and Mayers D. F., *Numerical Solution of Partial Differential Equations*, Cambridge University Press, 2nd Edition (2005)
- [100] Moscona A., *Cell suspensions from organ rudiments of chick embryos*, *Exp. Cell. Res.* **3**, 535- 539 (1952).
- [101] Moy V. T., Florin E. L. and Gaub H. E., *Intermolecular forces and energies between ligands and receptors*, *Science* **266**, 257-259 (1994).
- [102] Nassoy P., *How Accurate are Ultrasensitive Biophysical Force Probes?*, *Biophys. J.* **93**, 361-362 (2007).
- [103] Neuman K. C. and Nagy A., *Single-molecule force spectroscopy: optical tweezers, magnetic tweezers and atomic force microscopy*, *Nature Methods* **5**(6), 491-505 (2008).
- [104] N'Dri N. A., Shyy W. and Tran-Son-Tay R., *Computational Modeling of Cell Adhesion and Movement Using a Continuum-Kinetics Approach*, *Biophys. J.* **85**(4), 2273-2286 (2003).
- [105] Nguyen T. and Strang G., *Wavelets and filter banks*, Wellesley-Cambridge Press, Wellesley (1996).

- [106] Pakdaman K., Thieullen M. and Wainrib G., *Fluid limit theorems for stochastic hybrid systems with application to neuron models*, Adv. Appl. Prob. **42**, 761-794 (2010).
- [107] Palacios J., Benito N., Pizarro A., Suarez A., Espada J., Cano A. and Gamallo C., *Anomalous expression of P-cadherin in breast carcinoma. Correlation with E-Cadherin Expression and Pathological Features*, Am. J. Pathol. **146** No. 3 (1995).
- [108] Paszek M. J., Boettiger D., Weaver V. M. and Hammer D. A., *Integrin Clustering Is Driven by Mechanical Resistance from the Glycocalyx and the Substrate*, PLoS Comput. Biol. **5**(12), e1000604 (2009).
- [109] Perret E., Benoliel A. M., Nassoy P., Pierres A., Delmas V., Bongrand P. and H. Feracci, *Fast dissociation kinetics between individual E-cadherin fragments revealed by flow chamber analysis*, EMBO J. **21**, 2537-2546 (2002).
- [110] Pinchover Y. and Rubinstein J., *An introduction to partial differential equations*, Cambridge University Press, First Edition (2005).
- [111] Postan M., *Dynamics in Logistics : Application of Markov Drift Processes to Logistical Systems Modeling*, Springer Berlin Heidelberg, 443-455 (2008).
- [112] Pozrikidis C., *Effect of membrane bending stiffness on the deformation of capsules in simple shear flow*, J. Fluid Mech. **440**, 269-291 (2001).
- [113] Pozrikidis C., *Modelling and simulation of Capsules and Biological Cells*, CRC Press, ISBN:1584883596 (2003).
- [114] Purcell E. M., *Life at Low Reynold Numbers*, Am. J. Phys. **45**, 3-11 (1977).
- [115] Reboux S., Richardson G. and Jensen O. E., *Bond tilting and sliding friction in a model of cell adhesion*, Proc. R. Soc. A **464**, 447-467 (2008).
- [116] Reboux S., Richardson G. and Jensen O. E., *An asymptotic analysis of the buckling of a highly shear-resistant vesicle*, Eur. J. Appl. Math **20**, 479-518 (2009).
- [117] Risken S., *The Fokker-Planck Equation - Methods of Solution and Applications*, Springer, Second Edition (1989).
- [118] Rief M. and Grubmüller H., *Force spectroscopy of single biomolecules*, Chem. Phys. Chem. **3**, 255-261 (2002).
- [119] Risso F. and Carin M., *Compression of a capsule: Mechanical laws of membranes with negligible bending stiffness*, Phys. Rev., E **69**, 061601 (2004).

- [120] Riveline D., Zamir E., Balaban N. Q., Schwarz U. S., Ishizaki T., Narumiya S., Geiger B. and Bershadsky A., *Focal contacts as mechanosensors: Externally applied local mechanical forces induce growth of focal contacts by an mdia1-dependent and rock-independent mechanism*, J. Cell Biol. **153**, 1175-1185 (2001).
- [121] Ross S. M., Stochastic processes, Wiley, New York (1983).
- [122] Ross S. M., Introduction to probability models, Academic Press, 10th Edition (2010).
- [123] Rudin W., Functional Analysis, McGraw-Hill, Second Edition (1991).
- [124] Schaub H. and Junkins J. L., Analytical Mechanics of Space Systems, AIAA Education Series, 1st Edition Reston, VA (2009).
- [125] Schlierf M. and Rief M., *Single molecule unfolding force distributions reveal funnel-shaped energy landscape*, Biophys. Lett. **90**(4), 33-35 (2006).
- [126] Schwarz U. S., Erdmann T. and Bischofs I. B., *Focal adhesions as mechanosensors: The two-spring model*, BioSystems **83**, 225-232 (2006).
- [127] Seifert U., *Rupture of multiple parallel molecular bonds under dynamic loading*, Phys. Rev. Lett. **84**, 2750 (2000).
- [128] Seifert U., *Dynamic strength of adhesion molecules: Role of rebinding and self consistent rates*, Europhys. Lett. **58**, 792 (2002).
- [129] Silverman B., Density Estimation for Statistics and Data Analysis, Chapman and Hall/CRC, First Edition (1986).
- [130] Smith S. B., Finzi L. and Bustamante C., *Direct mechanical measurements of the elasticity of single DNA molecules by using magnetic beads*, Science **258**, 1122-1126 (1992).
- [131] Smith A. E., Moxham K. E. and Middleberg A. P. J., *On uniquely determining cell-wall material properties with the compression experiment*, Chem. Eng. Sci. **53**, 3913-3922 (1998).
- [132] Sokurenko E.V., Vogel V. and Thomas W. E., *Catch-Bond Mechanism of Force-Enhanced Adhesion: Counterintuitive, Elusive, but ... Widespread?*, Cell Host Microbe, **4**(4) 314-323 (2008).
- [133] Speck T., Reister E. and Seifert U., *Specific adhesion of membranes: Mapping to an effective bond lattice gas*, Phys. Rev. E **82**, 021923 (2010).

- [134] Tees D. F. J., Woodward J. T. and Hammer D. A., *Reliability theory for receptor-ligand bond dissociation*, J. Chem. Phys., 114, 7483-7496 (2001).
- [135] Tha S. P., Shuster J. and Goldsmith H. L., *Interaction forces between red cells agglutinated by antibody. IV Time and force dependence of break-up*, Biophys. J. **50**, 1117-1126 (1986).
- [136] Tsukasaky Y., Kitamura K., Shimizu K., Iwane H. I., Takai Y. and Yanaguda T., *Role of multiple bonds between the single cell adhesion molecules, nectin and cadherin, revealed by high sensitive force measurements*, J. Mol. Biol. **367**, 996-1006 (2007).
- [137] Ullah M. and Wolkenhauer O., *Family tree of Markov models in systems biology*, IET Syst. Biol. **1** (4), 247-254 (2007).
- [138] Van Kampen N. G., *Stochastic Processes in Physics and Chemistry*, Elsevier, Amsterdam (1992).
- [139] Vinogradova O. I. and Yakubov G. E., *Surface roughness and hydrodynamic boundary conditions*, Phys. Rev. E **73**, 045302(R) (2006).
- [140] Wan K., Chan V. and Dillard D. A., *Constitutive equations for elastic indentation of a thin-walled bio-mimetic microcapsule by an atomic-force microscope tip*, Colloids Surf. B **27**, 241-248 (2003).
- [141] Ward M. D., Dembo M. and Hammer D. A., *Kinetics of Cell Detachment: Peeling of Discrete Receptor Clusters*, Biophys. J **67**, 2522-2534 (1994).
- [142] Weekley S. J., Waters S. L. and Jensen O. E., *Transient elastohydrodynamic drag on a particle moving near a deformable wall*, Quart. J. of Mech. Appl. Math. **59**(2), 277-300 (2006).
- [143] Weikl T. R., Groves J. T. and Lipowsky R., *Pattern formation during adhesion of multicomponent membranes*, Europhys. Lett. **59**, 916-922 (2002).
- [144] Williams P. M., *Analytical descriptions of dynamic force spectroscopy: behaviour of multiple connections*, Anal. Chim. Acta **479**, 107-115 (2003).
- [145] Zhang X., Wojcikiewicz E. and Moy V. T., *Dynamic Adhesion of T Lymphocytes to Endothelial cells revealed by atomic force microscopy*, Exp. Biol. Med. **231**, 1306-1312 (2006).
- [146] Zhu C., *Kinetics and mechanics of cell adhesion*, J. Biomech. **33**, 23-33 (2000).